EXPERIMENTAL AND NUMERICAL INVESTIGATION OF POOL BOILING HEAT TRANSFER ON ENGINEERED NANO-FINNED SURFACES

A Dissertation

by

HONGJOO YANG

Submitted to the Office of Graduate and Professional Studies of
Texas A&M University
in partial fulfillment of the requirements for the degree of

DOCTOR OF PHILOSOPHY

Chair of Committee,	Debjyoti Banerjee
Committee Members,	Yassin Hassan
	Robert Handler
	Partha Mukherjee
	Brandon Dooley
Head of Department,	Andreas Polycarpou

August 2014

Major Subject: Mechanical Engineering

ABSTRACT

Pool boiling experiments for nanocoatings (or nanostructured surfaces) show that despite the lower thermal conductivity values than carbon, silicon yielded higher values of CHF (critical heat flux). Subsequently numerical studies showed that the interfacial thermal resistance (Kapitza resistance or "R_k") between a nanofin and fluid molecules is the dominant component of the thermal impedance network. The values of R_k for silicon were predicted to be ~1000 times smaller than that of carbon in these numerical simulations. Since the total thermal impedance of silicon nanofins is lower than that of carbon they cause higher levels of enhancement of CHF.

Surface adsorption of the liquid molecules on a nanofin results in the formation of dense "compressed phase" which in turn induces thermal capacitance and diodic behavior. This is termed as the "nanofin effect": which implies that CHF is more sensitive to R_k than the thermal conductivity of the nanofin. Hence, the objective of this study was to verify the nanofin effect.

Experimental and numerical investigation of transport phenomena during pool boiling were performed in this study for liquid subcooling of 0 ^{o}C, 5 ^{o}C and 10 ^{o}C on horizontal planar heater configuration. Surface temperature was measured using nanosensor (Thin Film thermocouple or "TFT") arrays. Heater surfaces (with or without nanofins of different heights) were composed of ceramic, oxide and metal surfaces. The nanofins were fabricated using Step and Flash Imprint Lithography (SFIL). Contact angle was measured both before and after the experiments.

Nucleate pool boiling heat transfer was enhanced with increase in pillar height. Numerical predictions for R_k obtained from Molecular Dynamics (MD) simulations were found to be consistent with the level of heat flux enhancement observed in the experiments for the different nanofin configurations. Hence this study demonstrates that R_k is the more dominant parameter for heat transfer enhancement during pool boiling – compared to the thermal conduction resistance (or material properties) of the nanofin itself. As an outcome of these investigations future topics of research are also proposed (such as, using temperature nano-sensors for the investigation of controlled fouling on pool boiling phenomena for heaters with micro/nano-structured surfaces).

DEDICATION

To my beloved family and friends for their endless support

ACKNOWLEDGEMENTS

I would like to thank my committee chair, Dr. Debjyoti Banerjee, and my committee members, Dr. Yassin Hassan, Dr. Robert Handler, Dr. Partha Mukherjee and Dr. Brandon Dooley, for their guidance and support throughout the course of this research.

Thanks also go to my friends and colleagues and the department faculty and staff for making my time at Texas A&M University a great experience. Finally, thanks to my mother and father for their encouragement and love.

I would like to thank the National Science Foundation (NSF) for sponsoring the research project for my Ph.D. thesis, and the title of the project is: "FFATA: Exploring New Mechanistic Models for Pool Boiling Experiments on Nano-Fins". While performing research activities towards my Ph.D. thesis at Texas A&M University – I was also supported from the following research projects managed by Dr. Banerjee at the Texas A&M Engineering Experiment Station (TEES) – which I gratefully acknowledge:

1. National Science Foundation (NSF-CBET/TTTP Program), Program Manager: Dr. Sumanta Acharya;
2. Department of Energy (DOE) - Solar Energy Technology Program (SETP);
3. ADA Technologies, Inc. (Denver, CO) through the Office of Naval Research (OSD SBIR Phase I program).
4. Trianja Inc. (subsidiary of Photronics Corp., Allen, TX) and Silicon Values Partners (subsidiary of the venture capital unit of the B G Group) : "Accuflow Project".

My special thanks to Dr. Yordanos Bisrat at Materials Characterization Facility (MCF) at Texas A&M University for her instruction and help for MEMS fabrication and characterization. In addition, I would like to acknowledge the help of Dr. Marylene Palard and Ricardo Garcia as well as other staff members at the Microelectronics Research Center (MRC) of the National Science Foundation (NSF) sponsored National Nanotechnology Infrastructure Network (NNIN) at the University of Texas at Austin for their help in fabricating nano-pillars using SFIL and other micro/nano-fabrication processes.

Finally, I am grateful to everyone who has helped me in some way or another throughout this entire duration of my graduate studies.

NOMENCLATURE

A_c	Top circular area of copper block (m²)
A_w	Test surface area exposed to boiling (m²)
A_n	Total area of the nanofin patterned plan area (m²)
A_{nc}	Total area of the nanofin patterned area (m²)
A_b	Total area of the nanofin non-patterned area (m²)
A_{npb}	Total area of the nanofin base (m²)
A_H	Area of heater (m²)
C_p	Specific heat (J/kg·K)
C_{sf}	Rohsenow coefficient
D	Diameter of circular heater (m)
g	Gravitational acceleration (m/s²)
h_{fg}	Heat of vaporization (J/kg)
k	Thermal conductivity (W/m·K)
L’	Non-dimensional heater size
l_o	The capillary length scale
N_j	Total number of jet on horizontal surface
q''	Heat flux (W/m^2)
q_c''	Heat flux through the copper block (W/m^2)
q_w''	Heat flux through the test surface (W/m^2)
q_n''	Heat flux through the nanofin patterned plan area (W/m^2)

q_{nc}''	Heat flux through the nanofin patterned area (W/m^2)
q_b''	Heat flux through the smooth area (W/m^2)
T_w	Temperature of boiling surface (°C)
T_{sat}	Saturation temperature of working fluid or "boiling point" (°C)
T_∞	Bulk liquid (pool) temperature (°C)
ΔT_e	Wall superheat (°C) or "excess temperature", $\Delta T_e = T_w - T_{sat}$
ΔT_b	Liquid subcooling (°C), $\Delta T_b = T_{sat} - T_\infty$

Greek Symbols

ρ	Density (kg/m^3)
σ	Surface tension (N/m)
λ	Taylor instability wavelength
λ_d	"Most Dangerous" Taylor instability wavelength
μ	Viscosity (Pa·s)

Subscripts

l	Properties of liquid
v	Properties of vapor

Dimensionless parameters

Pr	Prandtl number

TABLE OF CONTENTS

Page

LIST OF FIGURES

Page

LIST OF TABLES

Page

1. INTRODUCTION

Boiling heat transfer is the most efficient transport phenomena that can transport heat and mass at rapid rates at small driving potentials (such as small temperature drops or electrical/ chemical potential differences). Boiling leverages a combination of liquid-to-vapor phase change, conduction, convection and radiation heat transfer as well as mass transfer. The significance of boiling and evaporation is ubiquitous in various applications ranging from domestic appliances (e.g., HVAC systems) to space technologies to industrial components (thermal management in high heat flux devices such as electronic chip cooling and opto-electronics/ Lasers, heat pipes, thermal energy storage, thermal power generation, nucleic acid/ peptide based detection in biotechnology using thermo-cycling for Polymerase-Chain-Reaction/ "PCR", oil-and-gas exploration in deep trek drilling programs, etc.).

The transport mechanisms in pool boiling are very intricate that arise from strong coupling between different parameters such as geometrical effects (size, shape, orientation and surface structure of the heater), material properties (of the heater and fluid materials such as density, thermal conductivity, specific heat capacity, viscosity, etc. for liquid and gas phase as well as the heat exchanging surface) and molecular interactions at the solid-fluid surface (such as surface tension, static/ dynamic contact angle, interfacial resistance to heat and mass transfer, etc.)[1]. The different experimental parameters that are typically used to characterize pool boiling heat transfer (or heat flux) include wall superheat, bubble departure diameter, bubble departure frequency, static/ dynamic contact angle of the liquid-vapor interface and heater size.

During pool boiling heat transfer, the departing bubble absorbs large amount of thermal energy from the solid surface due to phase change. The coupled and intricate mechanisms hidden in pool boiling phenomena, especially for nanostructured surfaces and nanocoatings, are yet to be unraveled for a sufficient level of cognition that could enable reliable prediction of pool boiling performance for different heater configurations. Hence, the nature of pool boiling phenomena is not fully understood yet, despite the literature of pool boiling dating back to 1700s starting with the pioneering work of Johann Gottlob Leidenfrost (1756) [2] and the more systematic study reported by Nukiyama (1934) [3]. Especially the prediction of the pool boiling heat transfer on heaters with nano-structured surfaces is yet to move from the realm of experimental studies to the realm of numerical predictions using models based on first-principles.

1.1. Pool Boiling Curve

When the pool boiling heat flux is plotted as a function of the wall superheat (which is the difference between the value of average surface temperature of the heater and the saturation temperature of the working fluid) – the plot is called the "boiling curve". The theoretical and experimental approach for plotting the boiling curve for a "large" flat horizontal heater surface is a well-established subject [4]. A typical boiling curve consists of four regimes, free convection regime (designated as the onset of nucleate boiling or "ONB"), nucleate boiling regime (designated as the partial nucleate boiling or "PNB" and fully developed nucleate boiling or "FDNB"), transition boiling regime and film boiling regime (which includes the condition at which film boiling

collapses – also designated as the "Ledienfrost point" or "LP"). The transition boiling regime is the least understood pool boiling phenomena. Each regime has characteristic behavior that can be identified by the nature of bubble configuration (bubble formation and growth, bubble diameter at departure, bubble departure frequency, etc.) and the heat flux as a function of wall superheat (i.e., the particular segment of the pool boiling curve). Figure 1-1 shows an example of a typical pool boiling curve. As mentioned before, "Wall Superheat" implies the difference between the temperature of boiling surface or "wall temperature" (T_w) and the saturation temperature of the working fluid at the system pressure (T_{sat}), i.e., the boiling point.

The schematic diagram of bubble (or vapor) departure during boiling heat transfer is shown in Figure 1-2. In the free convection boiling regime, there is insufficient amount of vapor generation (or no vapor bubble formation) to sustain the growth of the bubbles that have just formed (i.e., the onset of nucleate boiling or "ONB") and fluid motion is determined by free convection effects until the experimental system reaches the nucleate boiling regime where the nucleated bubbles depart from the heater surface. This is the juncture where the system is at the cusp of crossing over from single phase heat transfer to multi-phase heat transfer regime. During nucleate boiling, bubble formation (inception), growth and departure occurs resulting in significant enhancement of the wall heat flux (over that of the single phase values).

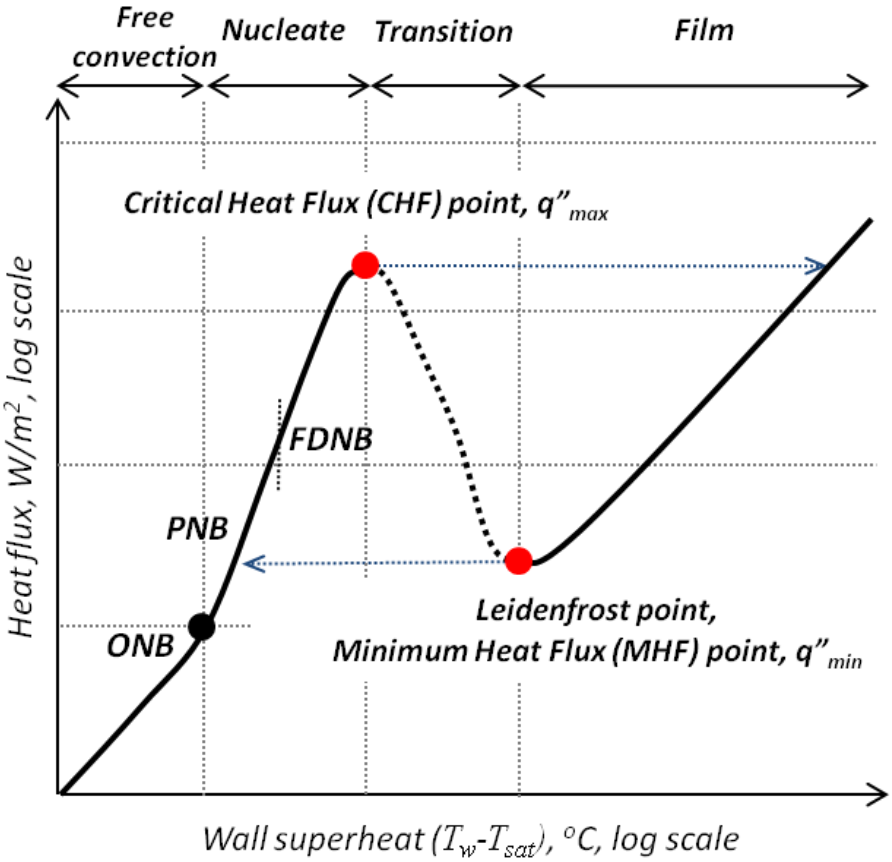

Figure 1-1 Schematic plot of the pool boiling curve showing the various regimes: free convection (ONB), nucleate, transition and film boiling regime; ONB means Onset of Nucleate Boiling, PNB means Partial Nucleate Boiling, and FDNB means Fully Developed Nucleate Boiling.

At the inception of the nucleate boiling regime, isolated vapor bubbles nucleate and depart from the heater surface (this is also called "onset of nucleate boiling" or "ONB"). As the wall heat flux is increased more bubbles nucleate and depart from the surface (i.e., the nucleation site density per unit area increases). On further enhancement of wall heat flux, correspondingly the heater surface temperature (i.e., the wall superheat), and all the nucleation sites available on the heater surface become active. At

this stage the rate of vapor bubble production from the heater surface matches or marginally exceeds the rate of vapor bubble removal from the heater surface (e.g., by terminal velocity of the buoyant vapor bubbles departing from the heater surface). This leads to merger of vapor bubbles in the vertical direction which in turn lead to the formation of isolated jets or columns. This is often termed as the "Fully Developed Nucleate Boiling (FDNB)". A marginal increase in temperature of the heater leads to the "Maximum Heat Flux (MHF)" condition, also known as the "Critical Heat Flux (CHF)" condition. At CHF the vapor generated from the heater surface escapes in the forms of jets that are often modeled to be self-assembled in the form a well-ordered rectangular or circular grid layout (i.e., in a Cartesian or cylindrical coordinate system, respectively) [5].

After the system reaches the Critical Heat Flux (CHF) point (which is the maximum heat flux that can be achieved in pool boiling), a marginal increase in wall heat flux (or wall temperature) will cause the system to be in transition boiling. In transition boiling the heater surface is partially covered by patches of continuous vapor films that are formed by lateral merger of vapor bubbles and jets - since the rate of vapor generation from the surface exceeds the rate of vapor extraction due to bubble escaping from the surface (usually at the terminal velocity), where the patches of vapor films can form and disappear – making the transport phenomena to have a transient character with wide distribution of time constants (which can make the system behave in a fractal/ chaotic fashion). In transition boiling regime the pool boiling system is in an unstable configuration, since the surface is partially covered with vapor film and nucleate boiling is also occurring simultaneously in the remaining part of the heater surface. Therefore

transition boiling regime is also called as partial film boiling regime or unstable film boiling regime. The wall heat flux is substantially lower in regions covered with continuous vapor film compared to the regions where nucleate boiling occurs. In transition boiling, increase in wall temperature causes more of the heater to be covered by the vapor film leading to lower net total wall heat flux.

On increasing the wall temperature substantially beyond the CHF condition, fully developed film boiling condition is achieved where the heater surface is completely covered with a continuous and stable film of vapor. In this regime, heat transfer from the surface to the liquid can take place by a combination of conduction or radiation through the stable vapor film (periodic and transient collapse of the vapor film during stable film boiling has been demonstrated in experimental studies in the literature - which can lead to ephemeral liquid-solid contact resulting in a significant fraction of the total heat transfer to be by transient conduction directly to the liquid phase from the solid phase). After stable film boiling is achieved, reduction in wall temperature leads to reduction in wall heat flux. If the wall temperature (or wall superheat) is reduced substantially, the vapor film can collapse and the pool boiling system can revert to transition boiling or nucleate boiling. The wall superheat (and the corresponding wall heat flux value) for which onset of stable film boiling is achieved by the pool boiling system is called the "Leidenfrost Point" on the pool boiling curve. This is also known as the "Minimum Heat Flux" (MHF) point. Film boiling collapses when the wall superheat is reduced, i.e., below the Leidenfrost point, resulting in lower values of heat flux (for the same wall superheat) – and this phenomena is often termed as "boiling hysteresis" (the directional

dependence of the pool boiling heat flux values are shown by the dashed arrows in Figure 1-1.

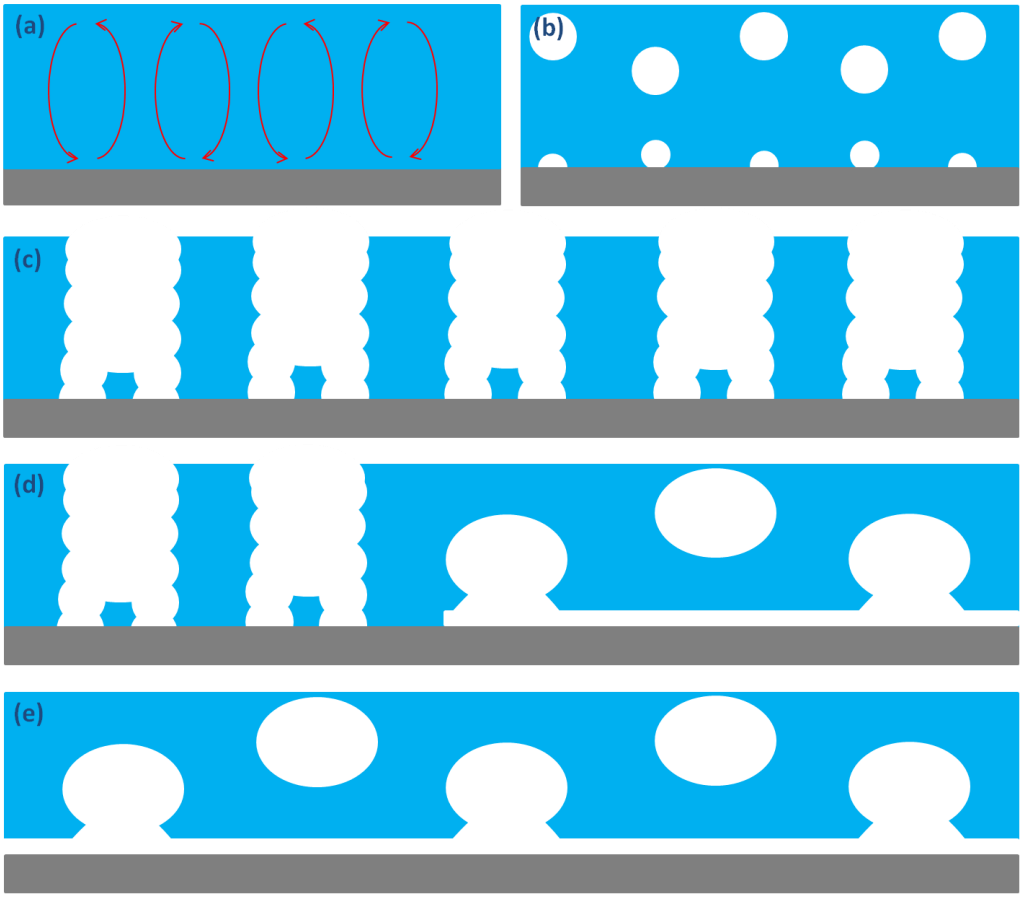

Figure 1-2 Schematic diagrams of different regimes of pool boiling (a) Free convection regime, (b) Nucleate regime, (c) Critical heat flux point, (d) Transition regime, (e) Film regime

1.2. Review of Prior Research

In this section a subset of the pool boiling literature will be reviewed. The focus of this literature review is on effect of heater geometry (size) and surface texturing. Pool

boiling phenomenon has been studied using a parametric approach, since Nukiyama's pioneering study involving a cylindrical metal wire heater [6]. Experimental and analytical approaches for studying pool boiling heat transfer has been developed for various flat surface heater configurations and using various working fluids [7-15].

The effect of surface roughness and cavity configuration on nucleate boiling heat transfer was explored for different heater materials and test fluids [12, 16]. The effect of nanostructured heater surface on pool boiling was also studied [7, 9]. In addition, pool boiling phenomena involving nanofluids as test fluids has also been reviewed in the literature [11].

1.2.1. Micro/Nano Structured Surface

Heater geometry can substantially affect pool boiling heat flux, especially the values of Critical Heat Flux (CHF). The effect of various surface micro-structure configurations on pool boiling heat flux were investigated by Ramaswamy [17], Nakayama [18, 19] and Chien [20]. Different geometrical features were varied parametrically, such as fin, shape, depth and pitch of cavity. The authors reported that as the cavity size was increased or the cavity pitch was decreased, the pool boiling heat flux was enhanced. In these reports the working fluid was varied – such as: FC-72 in the study by Ramaswamy [17], R-11 in the study by Nakayama [18, 19], as well as R-11 and R-123 in the study by Chien [20].

The effect of flat surface with micro-cavity array on pool boiling heat transfer was investigated by Bradley Bon [12]. FC-72 was used as the working fluid. The effect

of crystal plane on boiling surface was investigated for three different silicon surfaces which are 100, 110 and 111. The results show that the consistent increase in heat transfer with planar atomic density of the crystal planes. The author claims that the phonon interaction at the interface is most dominant mode for energy transfer during pool boiling (i.e., the Kapitza resistance). In this study, micro cylindrical cavity was fabricated by the conventional lithography process where the cavity depth and spacing between the cavities were varied parametrically. The author reported that decreasing the cavity spacing (or increasing the cavity density) improved the pool boiling heat flux. The author reported that at very large values of cavity spacing critical heat flux was not affected substantially. In addition, the author reported that deeper cavity resulted in higher values of CHF. However, the heater size in these studies was 1cm × 1cm. Hence, the results reported in this study are affected by the heater size (small heater regime) which would cause the CHF values to be different than on a large heater (infinite heater configuration). Also this study was restricted to only nucleate boiling regime while, the film boiling experiments were not performed in these studies.

The effect of various nanostructured surface configurations on pool boiling was also investigated by Ujereh et al. [21]. The authors reported that critical heat flux (CHF) on a silicon wafer heater surface that was coated with carbon nanotubes was enhanced by 50%, compared to that on a bare silicon surface. The heater size was 1.27 cm × 1.27 cm (which is in the small heater regime where the CHF values are likely to be affected by the size of the heater). The dimensions of the MWCNT were ~30 nm diameter and 20~30 μm length.

Launay performed pool boiling experiment on the hybrid micro-nano structured surfaces, The working fluids used in this study were PF-5060 and water [22]. Carbon nanotubes were synthsized on patterned silicon microstructures. The diameter of carbon nanotubes used in this study was 10~20 nm and the height varied from 40 nm ~ 100 nm. Whole boiling surface area was 1 square cm, and the dimensions of the microstructures were square posts of 200 μm side and 330 μm height. Hence, the CHF values reported in this study are also likely to be affected by the heater size (small heater configuration). For calculating the heat flux values, K-type thermocouples were embedded in the copper heater block. Surprisingly, the highest values of CHF were observed for heaters with microstructures only (i.e., without the carbon nanotube coatings).

Other types of surface modifications were also explored in various literature reports. El-Genk and Parker reported the effect of copper/ porous graphite surfaces on subcooled and saturated pool boiling [23]. In addition, the effect of dimples on the heater surface on pool boiling was studied by Miller et al. [24]. The authors performed pool boiling experiments on an array of hexagonal dimples.

1.2.2. Metal/Non-metal/Carbon Surface

The pool boiling heat transfer characteristics varied substantially with change in the material properties of the heater surface. In pool boiling phenomena energy-exchange interactions between solid surface and liquid molecules is strongly affected by the thermo-physical properties and other material properties of the heater surface.

The effect of silicon and copper nanostructured surfaces on pool boiling heat flux was investigated by Chen et al. [7]. The authors reported that the pool boiling heat flux was enhanced for silicon wafer heater substrates with surface nanostructures composed of silicon or copper nanowire. Water was used as the working fluid in this study. The authors reported significant heat flux enhancement for both cases. The heater size was 1 cm × 1 cm (hence this study also suffered from the deficiency of being in the small heater configuration where the size of the heater potentially affects the values of CHF). Silicon nanowires were synthesized on the silicon substrate by aqueous electroless technique. Copper nanowires were synthesized on commercial porous alumina membranes by electroplating.

In a similar study, TiO_2 (titania) nanotubes were synthesized on a Ti surface [25]. The pool boiling heat flux was enhanced on the heater surface with TiO_2 nanotubes when compared to surfaces without nanostructures, i.e., surfaces with only Ti metal.

El-Genk and Parker measured the pool boiling heat flux for heaters coated with graphite porous structure and involving various organic dielectric liquids as test fluid [23]. Similarly Ahn et al. [8, 9] performed pool boiling experiments using PF-5060 as the working fluid for a horizontal heater coated with Multi Walled Carbon Nanotubes (MWCNT). The results shows MWCNT coated silicon surface enhanced pool boiling heat flux compared to that of a plain (uncoated) surface. The boiling heat flux values for nucleate boiling, was less sensitive to the height of the MWCNT nanocoatings. The boiling heat flux values for film boiling was higher than that of the plain surface when the height of the MWCNT nanocoatings exceeded a threshold value while the boiling

heat flux values were the same (i.e., within the range of measurement uncertainties) for silicon heater substrates with MWCNT nanocoating thickness below the threshold value. The threshold value was found to be consistent with predictions from numerical models for film boiling in prior reports in the literature [26, 27]. The heaters used in these studies were in the "large heater" or "infinite heater" for rectangular heater with a heater size of 31.8 mm × 58.7 mm.

Sriraman (2007) reported that CHF was enhanced by ~120% using silicon nanofins [28]. Hence, despite the lower thermal conductivity values than carbon, silicon yielded higher values of CHF.

1.3. Identification of Issues in Contemporary Boiling Literature

In a substantial number of pool boiling experiments reported in the literature, the effect of heater size was not considered as an important parameter during the design of experiments. The heater size and shape are key parameters that need to be considered for precise understanding of the pool boiling phenomena. For eliminating the complications arising from the dependence of pool boiling heat flux on the heater size, the heater size needs to be in the "infinite heater" configuration, where the heater size should exceed a certain threshold value. The drawback of the pool boiling studies in recent literature is that small heaters were used in a large of number of studies reported in the literature, where the typical heater size was 1cm× 1cm [7, 12, 21, 22]. The pool boiling experiments involving substrates with nanocoatings/ surface nanostructures were typically performed on horizontal flat (planar) surfaces where the heater size was much

smaller than the threshold required for an "infinite heater" configuration. This is a potential cause for the inconsistencies between various literature reports for experimental measurement of pool boiling heat flux on heaters with nanostructures. This and other issues (e.g., lack of steady state conditions, high measurement uncertainty for heater surface temperature or "wall" temperature values) are discussed in the following sections.

1.3.1. Heater Size Effect

Pool boiling of water on the silicon and copper nanowires was conducted by Chen et al. [7]. The authors reported that the CHF was enhanced by 100% compared to that of a plain heater surface. In contrast pool boiling experiments performed on heater surfaces with zinc oxide nanocoating by Hendricks et al. showed that the critical heat flux was enhanced by ~400% compared with the CHF values measured in experiments performed using bare aluminum surface [29]. Wu et al reported that the values of CHF obtained for heaters with Titania nanocoatings were enhanced by 50% for water and 40% for FC-72 [30]. In the experiments performed by Im et al. [31], the pool boiling heat transfer coefficient was increased by ~10 times on the copper nanowire coated surface whereas the critical heat flux was enhanced marginally [31]. These mutually contradictory results for pool boiling experiment on the nanocoated surface, probably arise from the employment of small heaters where the heater size (and edge effects) dominate the boiling phenomena rather than that from the nanocoatings. In addition, the steady state criterion used in these studies is also circumspect where some of the

experiments were performed in 10 minute intervals where the time required for steady state for the pool boiling system is expected to be 2~3 hours.

Lu et al. reported that the critical heat flux on silicon nanowires varied substantially and displayed anomalous behavior with variation in heater size for heater size values less than $2cm^2$ [32]. CHF decreased as the heater size was increased for heater size values of 0.5 cm^2, 1 cm^2, 1.5 cm^2, and 2 cm^2. Lienhard and Dhir measured the critical heat flux values for finite horizontal flat surface heater configurations and developed the theoretical basis for analyzing the effect of heater size on pool boiling phenomena for both nucleate and film boiling regimes [14, 15]. An estimate for determining the appropriate heater size for performing boiling experiments on a horizontal planar surface can be obtained by using the following equations. The capillary length scale (l_o) and the "most dangerous" Taylor instability wavelength (λ_d) are defined in equation (1-1) and (1-2). The non-dimensional heater size, L' is defined using equations (1-3).

$$l_o = \sqrt{\frac{\sigma}{g(\rho_l - \rho_v)}} \tag{1-1}$$

$$\lambda_d = 2\pi\sqrt{3}l_o \approx 11l_o \tag{1-2}$$

$$L' = L / \lambda_d \tag{1-3}$$

The authors argued that when $L' > 5$, it can be considered as a "large heater" or "infinite heater" configuration. For an infinite heater configuration - the heat flux is expected to be independent of the heater size. On the contrary when $L' < 5$, it is considered to be a "small heater" since the heater size is predicted to affect the values of

the pool boiling heat flux. For example, l_o of water is ~2.5 mm and l_o of organic refrigerants (FC-72) is ~0.7 mm. Therefore the pool boiling data of water or FC-72 for heater size smaller than 5 cm (for a square heater), is difficult to interpret. This is because the level of heat flux enhancement at a particular superheat arises from two components – that due to heater size and that due to surface conditions of the heater (such as introduction of surface micro/nanostructures). The proportion of each factor to the resulting enhancement in heat flux is usually unknown. Moreover the λ_d for porous substrate such as for heater with surface nano-fins or nanocoatings, can decrease by as much as ~20% [33, 34]. So it is difficult to interpret the pool boiling data when comparing the heat flux values measured for a plain heater (without engineered surface nanostructures or nanoparticle coatings) to that of a heater surface with nanoparticle coatings/ engineered surface nanostructures. Therefore it is recommended that pool boiling experiments should be performed for a large heater (or an infinite heater) configuration to avoid the confusion in determining the relative contributions from the various sources for the observed enhancements in heat flux in the pool boiling experiments.

A significant number of studies for pool boiling heat transfer in contemporary literature were restricted to the nucleate boiling regime (and the film boiling regime was not explored). The pool boiling heat transfer characteristics for the film boiling regime were not investigated for a majority of these reports involving surface nanocoatings/ engineered surface nanostructures.

Hence, to mitigate some of these deficiencies in the contemporary boiling literature - the effect of heater size (for flat horizontal heater surface configurations) was explored in this study. Experimental characteristics for pool boiling on horizontal heaters (atomically smooth silicon wafers) were studied for two different heater shapes, circular heater and rectangular heater. The experimental results were found to be consistent with predictions from the analytical models, and are presented later in this report.

1.3.2. Steady State Issue

Significant number of studies on experimental measurements for pool boiling heat flux were conducted on small heaters (i.e., L' <5). The authors in these studies erroneously assumed that the steady-state conditions can be easily reached in a few minutes. For measuring heat transfer (and various thermo-physical properties), achieving steady-state conditions prior to measurements is often key to ensuring the validity and repeatability of the measurements. The pool boiling system as a whole, which includes the test liquid, heater apparatus and cooling system (for studying subcooled pool boiling) has a time constant typically of the order of ~1-2 hours for achieving steady state. However, a significant number of experiments reported in the literature, especially those relating to pool boiling on nanostructures (and typically using small heater configuration) were performed using only a few minutes (between consecutive points on the boiling curve) as the criteria for achieving steady state conditions. Hence, these reports suffer from unreliable data sets which are often contradictory when compared with reports for similar experiments conducted by other research groups. For example, the temporal

profile of heat flux or temperature values in a heater apparatus can deceptively display steady state behavior when the test liquid (bulk temperature) and the cooling system (for liquid subcooling) are yet to achieve steady state conditions. This error becomes even more acute when small heaters are used in the experiments. Hence, experiments designed using small heaters often display steady state conditions for the heater temperature - when in reality the whole boiling system is yet to reach steady state conditions – resulting in erroneous data. Therefore, the experiments are often not repeatable due to flawed design of experiments and unreliable criteria for steady state conditions.

1.3.3. Surface Temperature Measurement

For the investigation of transport phenomena in pool boiling, in addition to measurement of heat flux with high fidelity - the measurement of surface temperature with low measurement uncertainty is of paramount importance for generating the boiling curves that afford a reliable comparison between different experiments. However, in a significant number of experimental results reported in the literature, especially for pool and flow boiling studies using surface nanostructures, the pool boiling surface temperature was estimated based on heat flux measurements, and not measured directly. In some studies, wire bead thermocouples were used to measure the surface temperature of the heater – which is also an erroneous approach since the large form factor of these wire beads will cause nucleation of vapor bubbles on the thermocouple junction leading to erroneous fluctuations in the measurement of the surface temperature transients.

Typically the surface temperature (or "wall temperature", T_w) of the solid-liquid interface during pool boiling heat transfer was calculated or estimated erroneously in these studies. The contact resistance between the wire-bead and the boiling surface can vary with each batch of experiments and within a particular experiment, due to repeatability issues depending on how the wire-bead thermocouple is attached to the boiling surface (often using an adhesive with poor and unreliable thermal characteristics). Hence, to obtain a reliable measurement of the surface temperature (with appropriate or acceptable level of measurement uncertainty), nano-scale temperature metrology platforms are needed.

Thin Film Thermocouple (TFT) arrays were used to measure heater surface temperatures at a high spatial resolution by Park and Taya [35]. The authors used T-type thermocouples of 150 nm thickness in a 10 × 10 array for measuring the temperature values. In addition other authors reported the efficacy of different materials for measurement of high temperature values on silicon wafers using Thin Film Thermocouple (TFT) [36, 37].

In this study the heater surface temperature during pool boiling is directly measured using Thin Film Thermocouple (TFT) arrays. This technique has been developed and tested in prior efforts for pool boiling studies on rectangular flat horizontal heaters [9, 10, 28], including for the study of fractal/ chaotic features in pool boiling and flow boiling.

1.4. Molecular Dynamic Simulation

In prior reports in the literature – the thermo-physical properties of nanofluids were studied by analytically and numerically modeling transport phenomena such as nanoparticle clustering, Brownian motion of nanoparticles, interfacial layering of liquid molecules, and interfacial thermal resistance (Kapitza Resistance, R_k) [38-44]. These types of numerical models are gaining popularity in the research community as there is increasing interest in pool boiling on nanostructures. Particularly, the interfacial layering of liquid on a nanofin which in turn affects R_k, inherently dominates the overall thermal resistance of the system and therefore significantly affects the heat flux values during pool boiling on nanostructured surfaces. Therefore for better understanding of the heat transfer mechanism, the interaction between solid nanoparticle and liquid molecules should be studied in depth. The layering of liquid molecules surrounding the surface of solid nanoparticle is key to understanding the transport mechanisms during pool boiling. Therefore molecular dynamic (MD) simulation techniques are often utilized to estimate these parameters that affect transport phenomena on the nanoscale.

The formation of ultra-thin water film on a crystalline surface was studied experimentally by Majumdar et al [45, 46]. The main driving force responsible for the formation of the ultra-thin water films are the intermolecular adhesive forces at the interface between fluid molecules (water) and solid surface. The measurement of the adsorbed layer of liquid molecules on the surface of a solid was reported in various studies [47].

The interfacial thermal resistance is often the dominant parameter affecting the heat flux values on heaters with surface nanostructures [48-51]. The interfacial thermal resistance, which is also known as the thermal boundary resistance (or Kapitza resistance, R_k), is a key parameter for determining the overall thermal resistance of the pool boiling system and the net heat flux values. The interfacial thermal resistance between a single wall carbon nanotube and the octane molecules were measured and reported by Huxtable et al. [52].

Thermodynamic study based on thermal energy transport from a carbon nanotube (CNT) to surrounding water molecules was investigated by Walther et al. [53]. The values of R_k at the interface between silica and water were also reported in a separate study [54]. Molecular dynamics simulation for molten salt materials was conducted for carbonate mixture of Li_2CO_3 and K_2CO_3 by Costa [55]. The structure and themodynamic properties of carbonate mixtures were verified in this study. MD simulations were performed by Swiatla et al. to estimate the thermophysical properties of water [56].

MD simulations were also used to explore the mechanism for specific heat capacity enhancement of molten salt nanofluids by Shin [57-61, 64-66], Jo [62, 63] and Jung [76]. After adding nanoparticles into molten salts at specified mass concentrations (thus forming molten salt based nanofluids), the authors observed that the overall values of the specific heat capacity of nanofluids were increased dramatically by as much as 120%. The authors suggested that the significant enhancement in the value of specific heat capacity arises from several types of transport mechanisms for mass, species and energy. These transport mechanisms are affected by the surface adsorption of the liquid

molecules on the nanoparticle surface which acts as a thermal barrier and as a thermal capacitor (i.e, effectively as a thermal storage device or thermal battery). The numerical simulations predicted that on the surface of the nanoparticles the density of the solvent (liquid) molecules is higher than that of the bulk properties of the liquid. This layer of higher density liquid molecules on the surface of the nanoparticles is called the "compressed phase" or "compressed layer". The authors claimed that this compressed layer acts as a barrier to energy transport and therefore affects the interfacial thermal resistance. In tandem, the compressed layer also affects the thermal capacitance (i.e., serves as an energy storage – akin to a thermal battery). This in turn can cause the enhancement of the specific heat capacity of the nanofluid.

Moreover, the results from the study by Singh for MD simulations involving suspension of nanoparticles showed that the nanoparticles induce the formation of a "compressed phase" of solvent molecules that are adsorbed on the surface of the nanoparticles [67]. The density of the compressed phase was predicted to match the solid phase density of the solvent material.

In this study, molecular dynamic simulations were performed using a free-ware computational/ numerical tool called LAMMPS [68], which was developed at the Sandia National Laboratory. The formulation of the simulation domain was implemented using a commercial tool (Materials Studio® which is marketed by Accelrys Inc., San Diego, CA). Materials Studio also provides several molecular simulation modules, however the simulation speed and computational resources required limit the efficacy of this feature. Therefore after formulation of the simulation domain was performed using Material

Studio and the simulations were performed using LAMMPS. The simulations were performed using parallel computing nodes at the Supercomputing Center at Texas A&M University.

1.5. Synopsis

Recently, experimental results were reported [9, 10, 28, 48-51, 67, 69-75] that involved heater surfaces with nanoparticle coatings and heater surfaces with engineered surfaces (nanostructured surfaces) with roughness in the ~10-100 nm scale. The boiling phenomena for these experiments were found to be mutually inconsistent. Also these results were found to be inconsistent with the predictions from the conventional theories of boiling that have been espoused in the past ~50 years. The underlying assumptions used in these theories (i.e., they are based on continuum assumption) are not applicable for the nano-scale roughness that are involved in the experiments that were performed in the past ~ 5-10 years – since non-continuum flow regimes are expected to occur in these instances. In addition, many of the recent experiments were performed for "small heater" configurations where the size of the heaters can affect the magnitude of the boiling heat transfer, particularly the CHF values. Hence, new paradigms for performing experiments and computer simulations are needed.

In these experimental studies performed in the past decade significant enhancement in pool and flow boiling heat flux were reported for the nanotextured heater surfaces. Ahn et al. (2006) [9] were the first to report enhancement of pool boiling critical heat flux (CHF) by ~60% using nanoparticle coatings (Carbon Nanotube/CNT).

Banerjee and Dhir (2001) [26] reported that non-linear growth of 3-D Taylor instabilities cause temperature transients ("cold spots") on a plain heater surface. Cold spots can drain 60~90% of the total heat flux. Size of cold spots depends on the thermal conductivity of the heater. However, for the nanofin experiments it was not clear if (instead of high thermal conductivity of CNT) the dominant factor was the enhancement of surface area caused by the introduction of nanofin on the flat substrate. Sriraman (2007) reported that CHF was enhanced by ~120% using silicon nanofins [28] . Hence, despite the lower thermal conductivity values than carbon, silicon yielded higher values of CHF. This conundrum was resolved by Singh et al (2012) [51], who argued that the interfacial thermal resistance (Kapitza resistance or "R_k") between silicon nanofins and liquid molecules was ~1000 times smaller than that of carbon. Jo (2012) [47], Jung (2012) [76] and Shin (2011) [61], reported that R_k is the dominant component of the thermal impedance network for the nanofins. Since total thermal resistance of Si-nanofins is lower they cause higher levels of enhancement of CHF.

In addition, the surface adsorption phenomena of the fluid molecules on a nanofin induces additional thermal resistance and thermal capacitance (thermal energy storage) due to the formation of a dense "compressed phase". Singh and Banerjee (2013) [50] termed this combined effect of thermal capacitance due to surface adsorption of fluid molecules, thermal interfacial resistance offered by the surface adsorbed layer of fluid molecules and the heat transfer modulated by the species transport from the solid surface into the bulk fluid (diodic behavior) - as the "nanofin effect". This implies that CHF should scale inversely with the magnitude of R_k (between the nanofin and the

liquid). Thus thermal conductivity of the nanofin material itself plays a secondary role [69].

1.6. Objective of the Study

The goal of this study is to verify if the pool boiling heat flux scales inversely as the Kapitza resistance between a nanofin and working fluid. Hence, numerical models were utilized to estimate the Kapitza resistance for various materials using Molecular Dynamics (MD) simulations. Experimental validation of this hypothesis will be performed by conducting pool boiling experiments on heaters with different material composition containing surface nanostructures that are fabricated by the Step and Flash Imprint Nanolithography (SFIL) technique. The working liquid is a fluorinert refrigerant (PF-5060, Manufacturer: 3M Corp.). The experiments were performed by varying the heater size, material composition of the heaters, and the height of the surface nanofins.

1.7. Significance of Current Study

This study is expected to make fundamental contributions to the field of thermal-fluids sciences in the following ways:

- Design and fabrication of thin film thermocouple sensors (temperature nanosensors) were performed and were applied to the measurement of heater surface temperature in pool boiling experiments with the intention of minimizing the measurement uncertainties.

- The ‘Step and Flash Imprinting Lithography’ (SFIL) technique was optimized to obtain nanoscale fin arrays on the heater surface for enhancement of pool boiling heat transfer.
- The contribution of various parameters on pool boiling heat flux (and the resulting boiling curve) was evaluated - such as liquid subcooling, wall superheat, heater size, material composition of the heater and configuration of the surface nanofins.
- Demonstrated the dependence of the pool boiling heat flux on the interfacial thermal resistance (Kapitza resistance) between the heater material and the working fluid.

1.8. Summary

The pool boiling characteristics for heaters with nanostructured surfaces were investigated by leveraging experimental and computational studies. Thin Film Thermocouple (TFT) arrays were integrated into the experimental apparatus (by in-situ micro/nano-fabrication) for measurement of surface temperature fluctuations at high spatial resolution and using high speed data acquisition apparatus. Pool boiling heat transfer phenomena was explored by varying heater geometry (size and shape), and heaters with surface nanostructures with different morphologies (geometry and materials). These information are categorized into different chapters, as mentioned below:

Chapter 2 provides the information about the fabrication of thin film thermocouple and nanostructured surfaces based on NEMS/MEMS techniques. This

provides information on the fabrication protocols used to prepare the different heater samples for the pool boiling experiments.

Chapter 3 presents the information about the experimental apparatus that was used for investigation of pool boiling phenomena.

Chapter 4 describes the effect of heater size and shape on pool boiling (circular and rectangular shaped heaters). The experimental data were compared with predictions from the analytical models.

Chapter 5 provides information on the effect of material properties of the heater surface on pool boiling. The three different materials explored in this study include: silica, silicon and chromel. The pool boiling curves were compared for each configuration.

Chapter 6 describes the pool boiling phenomena for silicon heaters with nanostructured surfaces. The pool boiling curves were plotted as a function of the geometry of the nanostructures and liquid subcooling.

Chapter 7 describes the results obtained from pool boiling (saturated and subcooled) heat transfer experiments performed on silica heaters with nanostructured surfaces.

Chapter 8 describes the results obtained from pool boiling (saturated and subcooled) heat transfer experiments performed on nickel heaters with nanostructured surfaces.

Chapter 9 provides the comparison between boiling curves for different experimental conditions involving similar height yet different materials properties

(semiconductor/ ceramic/ metal) of the heaters with nanostructures, which are silicon, silica, and nickel, respectively.

Chapter 10 describes the results from the computational studies, which are obtained from the molecular dynamic simulations. The results are used to resolve the conundrums observed in the experimental results.

Chapter 11 provides the analytical basis for estimating the values of capacitance and thermal diode effect for heat transfer between a solid heater surface and molecules of the working fluid.

Chapter 12 summarizes the results obtained in this study.

Chapter 13 addresses the future direction (e.g., using temperature nano-sensors for studying the effect of fouling on pool boiling for heaters with micro/nano-structured surfaces).

2. MICRO/NANO FABRICATION

The goal of this study is to explore the effect of material composition of the heater and the morphology of the surface nanostructures on the pool boiling phenomena. For this purpose the composition of the heater surface was varied using three different classes of materials: ceramic (silica), semiconductor (silicon) and metal (chromel/ nickel), respectively. In addition, engineered surface nanostructures were obtained using nanofabrication techniques. The surface nanostructures consisting of nano-pillars (or nanofins) were obtained in well-defined configurations (i.e., engineered) – with a fixed diameter, pitch and height (unlike prior reports in the literature using carbon nanotube coatings – where the diameter, length, and pitch of the nanotubes were in random order and not well-defined).

2.1. Preparing Boiling Surface

Silicon wafers were procured commercially (from University Wafer Inc., Boston, MA). Single side polished (SSP) and doubled side polished (DSP) wafers with <100> orientation were used. In this study, the surface roughness is expected to significantly affect the pool boiling heat flux. Hence, the atomically smooth surface of the polished silicon wafer is quite adequate for performing the control experiments (baseline case). Silica heater surfaces were obtained by the oxidation of silicon wafer. The silicon wafer is oxidized by LPCVD (Low-Pressure Chemical Vapor Deposition). The help of Dr. Marylene Pallard and the research staff at the NSF sponsored National Nanotechnology

Infrastructure Network (NNIN) of the Microelectronics Research Center (MRC) at the University of Texas at Austin is gratefully acknowledged. Images of the instruments used for processing and obtaining the oxidized silicon wafer are shown at Figure 2-1. After piranha cleaning the silicon wafer is moved into a LPCVD furnace, where thermal oxidation and growth of silica layers with different thicknesses were obtained using a recipe provided by the LPCVD furnace vendor. The thickness of the silica layer was measured to be ~202 nm with a standard deviation of 2 nm by using an ellipsometer (Model: M-2000, Manufacturer J.A. Woollam Co. Inc., Lincoln, NE). To minimize the measurement error, the measurements were performed for five different locations on the processed wafer.

Metal nanocoatings on the heater surfaces were obtained by using thermal evaporation techniques. The target materials used for the metal deposition were: chromel (90% Nickel + 10% Chromium) or nickel. Chromel alloy or nickel were deposited on the top of silicon wafer to a thickness of 200 nm by using an electron beam evaporator (CHA electron beam evaporator, CHA industries, Fremont, CA) as shown in Figure 2-1. The metal deposition was carefully controlled using a slow deposition rate (which typically varied from 0.5 ~ 1.0 Å/s) with the intention of obtaining high quality of the deposited thin films.

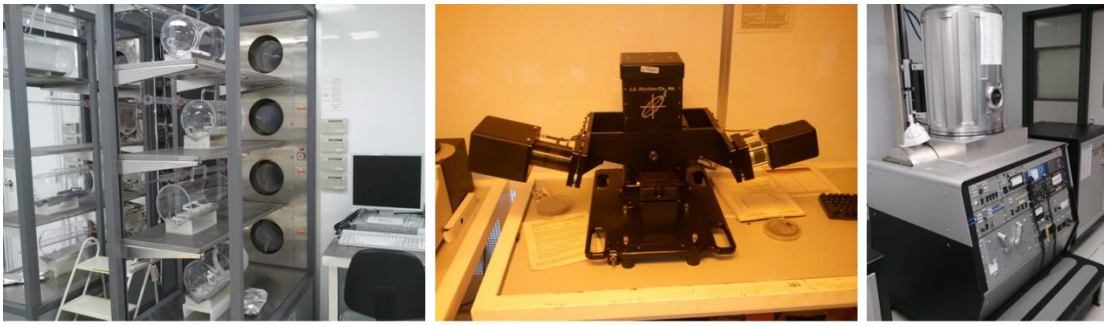

Figure 2-1 Images of instruments used in this study: (a) LPCVD furnace, (b) Ellipsometer, and (c) Electron beam evaporator. These instruments are located at MRC (NNIN, University of Texas at Austin).

2.2. Fabrication of Thin Film Thermocouple

In addition, Thin Film Thermocouple (TFT) arrays were fabricated by using conventional lithography techniques. Thermocouples are widely used for temperature measurement. The operating principle for thermocouples is based on the thermoelectric effect (also called Seebeck effect). Seebeck effect is used to calculate the magnitude of the electric potential that is generated between two junctions of dissimilar electrically conducting materials that are in mutual contact (called thermocouples), due to temperature difference between the two junctions. This phenomenon can be used for measuring temperature where the measured voltage generated by a thermocouple is used to estimate the temperature – typically using results from a calibration experiment. Hence, the junction of two different electrical conductors that is used for the purpose of measuring voltage as a function of temperature difference is known as a thermocouple.

Depending on the type of junction desired, various materials (e.g., pure metal or alloy) can be used for a chosen temperature range of desired operation. In this study, K-

type thermocouples were used, which is the junction of Chromel (90% Nickel + 10% Chromium) and Alumel (95% Nickel + 2% Manganese, 2% Aluminum and 1% Silicon). The operating temperature range of K-type thermocouples are typically between 0 ^{o}C to 1100 ^{o}C. Thin Film Thermocouple (TFT) was chosen for this study where the component materials were that of a K-type thermocouple. Conventional wire bead thermocouples have a large form factor (size) that can cause perturbation of the transport mechanisms when applied for measuring the surface temperature transients of heaters during pool boiling. This would lead to unreliable and erroneous measurements of temperature fluctuations of the heater surface (i.e., the wall temperature values, T_w). Hence, Thin Film Thermocouple (TFT) arrays were fabricated to measure the surface temperature transients in pool boiling with high fidelity (high spatial and temperal resolution). To minimize the perturbation of the transport mechanisms by the TFT the thickness is limited to 200 nm (below a thickness of 200 nm the junction ceases to behave as a thermocouple due to scattering effects). The sequence of the processing steps that were used for the fabrication of TFT arrays are shown in Figure 2-2.

The fabrication of arrays of thin film thermocouple (TFT) and nano-scale pillars were performed at the Materials Characterization Facility (MCF) at the Texas A&M University and the Microelectronics Research Center (MRC/ NNIN) at the University of Texas at Austin, respectively.

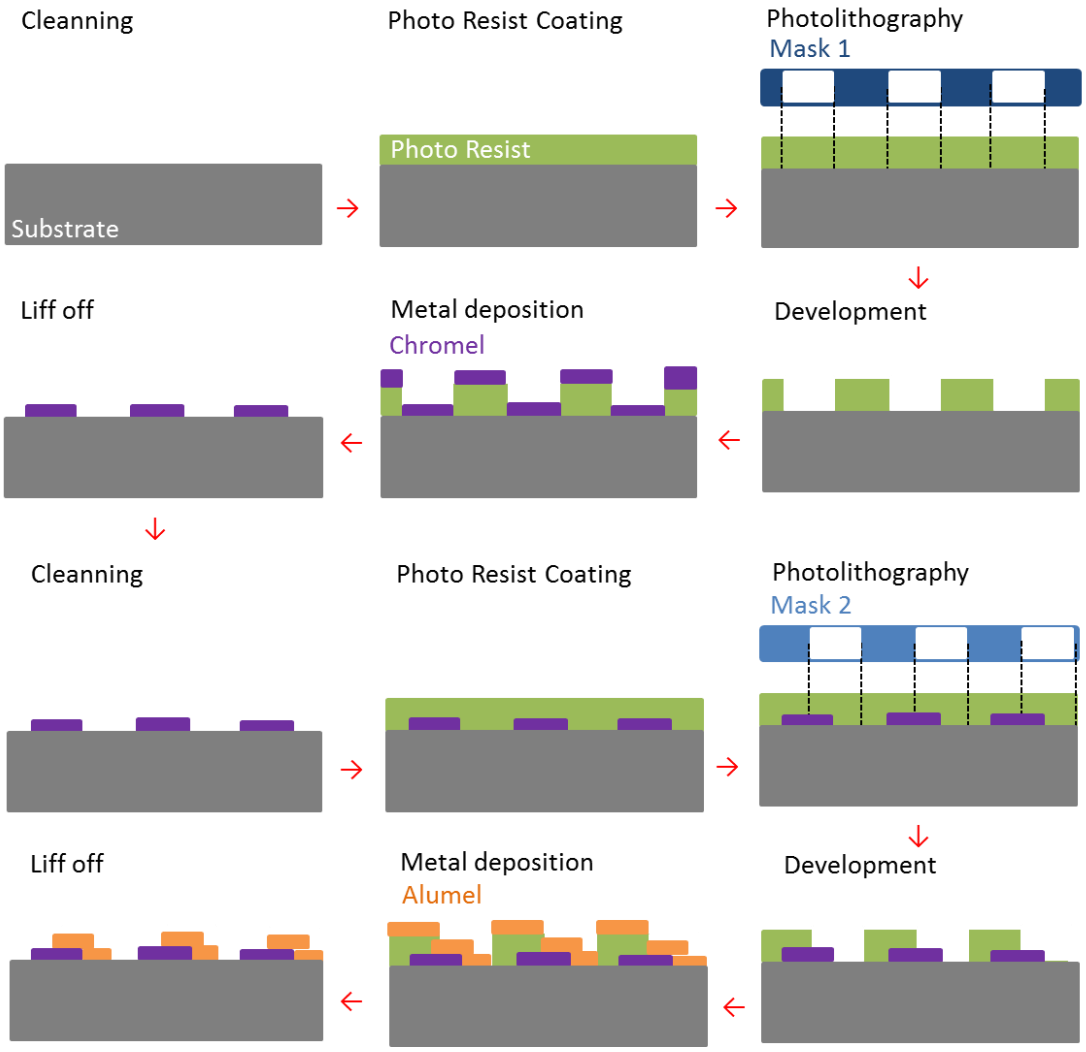

Figure 2-2 Schematic diagram showing the sequence of the processing steps for fabrication of Thin Film Thermocouple (TFT) arrays

2.2.1. Photolithography

Two different photomask layouts were designed for obtaining the arrays of chromel and alumel junctions. The desired photo film mask was printed using commercial printing services (Southwest Printing, Bryan, Texas). Photolithography for

the Chromel and Alumel layers was performed at the Materials Characterization Facility (MCF), at the Texas A&M University.

The steps involved in a typical photolithography include designing the layout for a photoresist pattern, obtaining the mask (e.g., by commercial printing services), wafer cleaning, photoresist spin coating, photo (UV) exposure step, and development. The photolithography process is critical for obtaining the TFT arrays. If the photoresist pattern is not developed properly on the wafer substrate, the resulting chromel or alumel metal pattern obtained from the microfabrication process will be defective leading to potential malfunctioning of the TFT junctions. Details of the processing conditions are listed in Table 2-1.

Table 2-1 Photolithography recipes for fabrication of Thin Film Thermocouple

Dry Cleaning	Reactive Ion Etcher		Bake	Hot Plate	
	Power	350W		Temerature	115 °C
	Time	5 min		Time	1 min
	O_2	20 sccm			
			UV exposure	Mask Aligner	
Spin coating	Spin coater			Power Density	14 mW/m²
	Speed	3000 rpm		Time	1 min
	Time	1 min			
	Acceleration	500 rpm/s	Development	Time	1min

2.2.1.1. Mask Design

Two different mask patterns were used for fabricating the array of chromel and alumel junctions. Typical mask layouts for obtaining chromel and alumel metal patterns

are shown in Figure 2-3, and the black area in the figure is the transparent region in the mask.

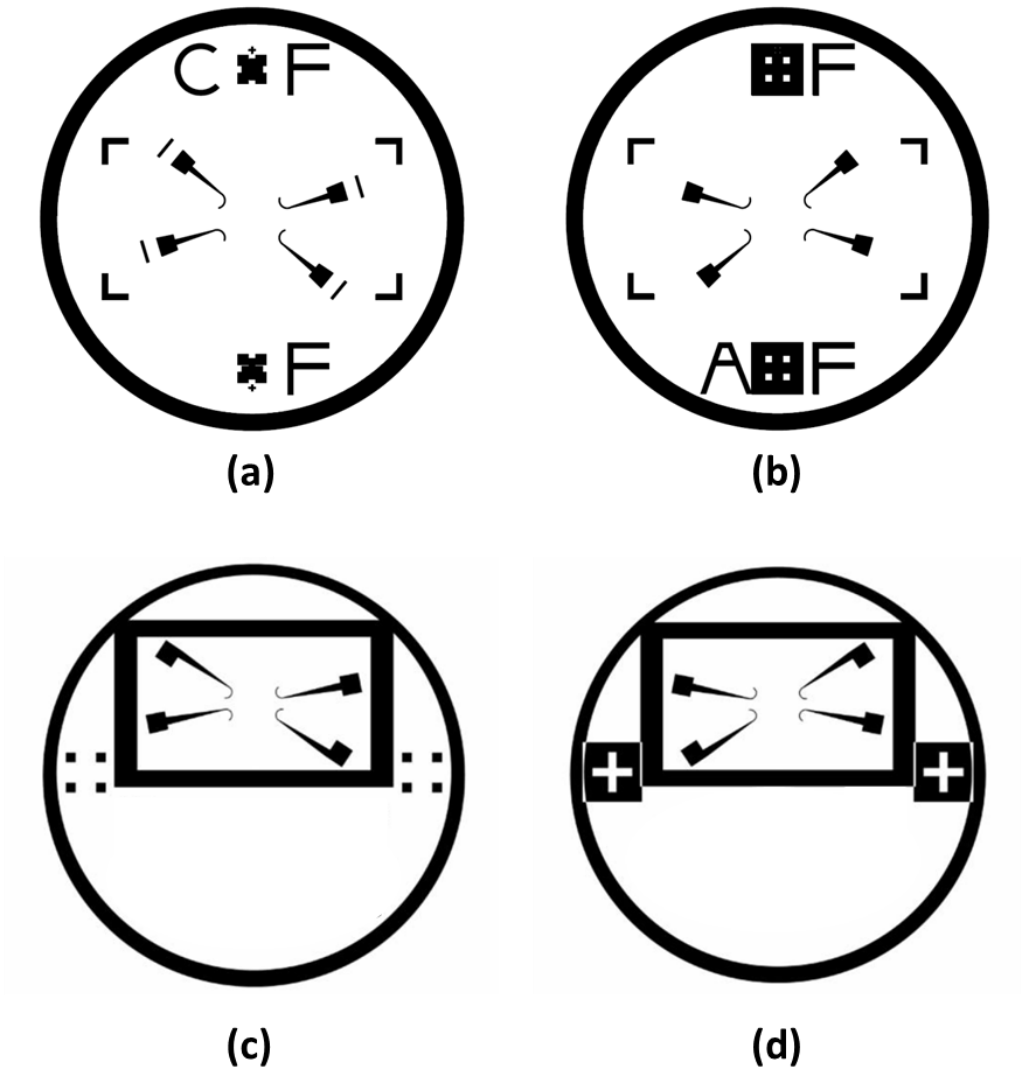

Figure 2-3 Mask layout for 3 inch wafer (a) Chromel layer, (b) Alumel layer; for 4 inch wafer (c) Chromel layer (d) Alumel layer

Different layouts were used for 3 inch wafer (SSP) and 4 inch wafer (DSP) substrates, respectively. The 3 inch wafers were used for performing the control experiments (i.e., without any surface nanostructures). The 4 inch wafers were used for fabricating surface nanostructures for subsequent use in the pool boiling experiments. To align the two metal layers for obtaining the thermocouple junction in the photolithography steps, alignment patterns were designed in the the two mask layouts. Commercial Computer Aided Design (CAD) tools were used for designing the mask layout (e.g., Solidworks v2010, Dassult Systems). The desired critical dimension of the chromel and alumel junctions was 200 nm. An array of bond pads was designed for connecting the thermocouple junctions to the data acquisition system by using wire bonding. The bond pads were designed to be ~1 mm square.

2.2.1.2. Wafer Cleaning Step

The wafers procured from the commercial vendor can potentially be contaminated by dust or undesired chemical exposure, so the wafer should be cleaned before further processing. To remove a potential contamination, the wafer is cleaned initially using acetone, DI water and oxygen plasma Reactive Ion Etch (RIE). The wafer was immersed in acetone and DI water for washing, and then blow dried using compressed nitrogen gas. The wafer was place on the hotplate for ten minutes at 115 ^{o}C to remove residual water. Reactive Ion Etcher (CS-1701, March Plasma Systems) was used to remove organic residue.

2.2.1.3. Photoresist Spin Coating

Photoresist (Positive type, SC 1827, Rohm and Haas Electronic Materials) was spin-coated on the wafer. The spin processor (WS-650S, Laurell) was used, and the desired thickness of photoresist is targeted to be 3μm. Based on the recipe supplied by the photoresist vendor, the wafer was spin coated at 3000 rpm for one minute. Pre-exposure bake was performed by placing the wafer on a hot plate at 115 ^{o}C for one minute as shown in Table 2-1.

2.2.1.4. UV Exposure

The wafer with photoresist coating was then placed on a mask aligner (Q4000, Quintel) for UV exposure. The mask with desired pattern and wafer was aligned using optical microscope in the mask aligner followed by UV exposure for 1 minute. The first mask for chromel pattern does not require alignment step, however the second mask for alumel pattern should be carefully aligned with the wafer with chromel pattern (as well as the mask alignment patterns already printed on the wafer surface from the previous photolithography step). The UV light source intensity was set to a value of 14 mW/cm^2. The details of the recipe are listed in Table 2-1.

2.2.1.5. Development

After UV exposure the wafer was immersed into a developer solution (MF-319, Rohm and Hass Electronic Materials) for one minute, for obtaining the desired photoresist pattern. The exposed photoresist was removed by the developer solution

(since a positive photoresist was used). The wafer was then rinsed in DI water for one minute, followed by blow drying using compressed nitrogen gas.

After completion of the photolithography step, the final photoresist pattern was examined using an optical microscope for confirmation that the process steps did not cause any defects in the desired pattern. If a defect is detected the photoresist is stripped using a photoresist stripper solution and the steps are repeated from the beginning. The equipment used for these processing steps is shown in Figure 2-4.

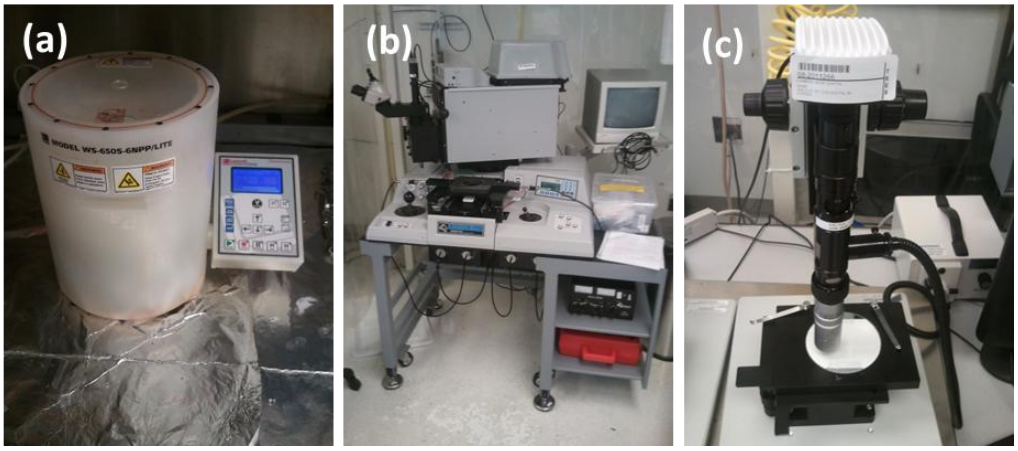

Figure 2-4 Photolithography equipment (a) Spin coater, (b) Mask aligner, (c) Optical microscope.

2.2.2. Physical Vapor Deposition(PVD)

Metals with high melting point are not amenable for deposition using thermal evaporator. So, in this study, metal alloys (which have high melting point) such as chromel and alumel were deposited on a wafer substrate using an electron beam evaporator (CHA electron beam evaporator, CHA industries), which is located at the

MRC/NNIN node in the University of Texas at Austin. The wafer with patterned photoresist was used for deposition of the metal targets.

The adhesion between the deposited metal thin films and the wafer substrate may not be adequate. Therefore an adhesion layer, such as titanium of 20 nm thickness, is typically deposited prior to deposition of the target material. The minimum thickness of vapor film in the film boiling regime is expected to exceed 10 μm [77]. Hence the TFT feature with 200 nm thickness is not expected to cause significant perturbation of the transport mechanisms in pool boiling (the ratio of vapor film thickness to the thickness of the individual metal layers of the TFT array thus exceeds by 50 times). Using previously established fabrication protocols at MRC, the deposition rate of the metals was controlled with a value of 0.5 ~ 1.0 Å/s. Control of the deposition rate of the metals is critical for ensuring effective quality and performance of the TFT arrays. If the deposition rate is too high, the deposited metal has poor adhesion and can peel off during the lift-off process. A typical recipe involves deposition of the metal thin films at 0.5 Å/s up to a thickness of 30 nm, and then the deposition rate is increased to 1.0 Å/s for the remaining part of the metal deposition step.

2.2.3. Lift-off

To obtain the final pattern of the chromel or alumel layers, lift-off process was performed. After physical vapor deposition, the substrate was immersed into a solution containing photoresist remover (PG remover, Supplier: Microchem Corp.) to dissolve the photoresist. In this process the metal deposited on top of the photoresist layer is

removed while the metal deposited on the exposed wafer surface is not removed. The wafer substrate is immersed in the PG remover solution (for obtaining lift-off) and then placed in an ultrasonic bath for 20 minutes until all the undesired metal was lifted off. Finally the substrate was rinsed with DI water and blow dried using compressed nitrogen gas.

2.2.4. Characterization of Samples

The images of the wafer surfaces containing the Thin Film Thermocouple (TFT) arrays are shown in Figure 2-5. TFT arrays on the substrates were sucessfully fabricated using surface micromachining techniques. Optical microscopy image shows the juction between chromel and alumel layers that were deposited sequentially. Details of the procedure for bonding the wires to the bondpads (packaging step) for the purpose of recording the temperature readings obtained from the TFT will be described in the following chapter.

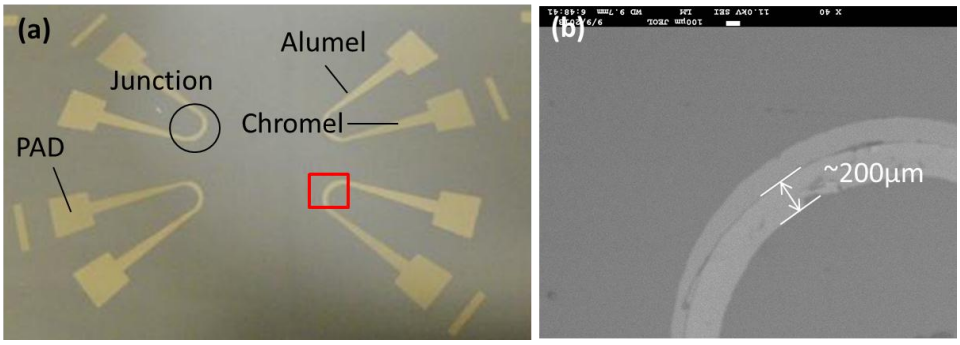

Figure 2-5 (a) Image of Thin Film Thermocouple (TFT) array on a plain silicon wafer substrate, (b) SEM image of the junction between the alumel and chromel layers.

Images of the wafers of Si, SiO_2,Chromel, and Ni with TFT fabricated in-situ are shown in Figure 2-6. The TFT array on SiO_2 substrate was fabricated after oxidation of silicon wafer by LPCVD. For the wafer with metal thin film coatings, only chromel (or nickel) was deposited uniformly on the wafer substrate. Therefore only alumel layer was patterned for effectively obtaining a TFT array, for the purpose of measuring the surface temperature fluctuations.

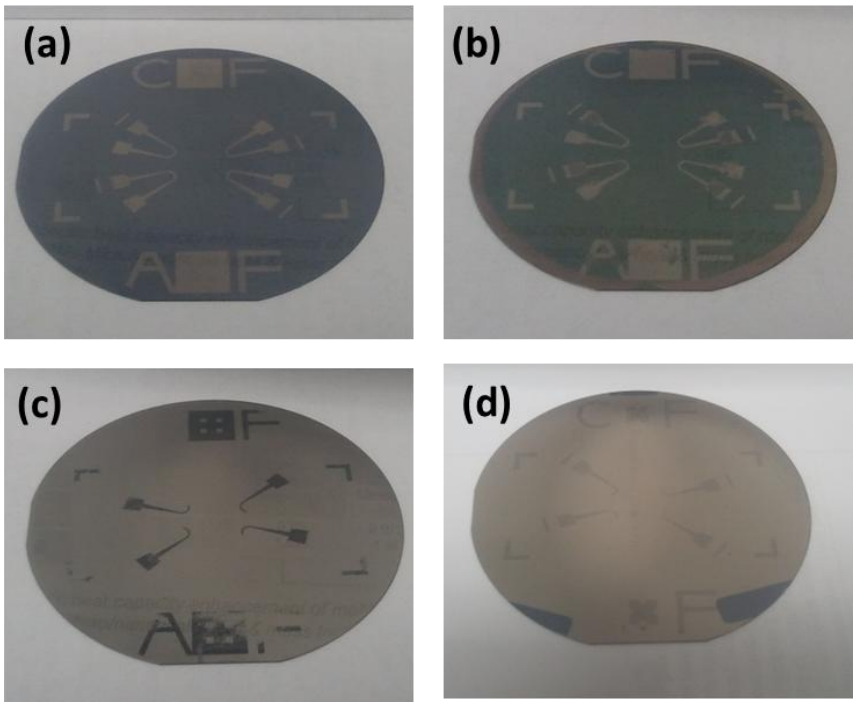

Figure 2-6 Images of Thin Film Thermocouple (TFT) arrays that were fabricated on a: (a) Plain silicon surface, (b) Plain silica surface, (c) Plain chromel surface, and (d) Plain nickel surface

2.3. Fabrication of Nano-pillars (Engineered Nanofins)

For investigating the effect of nanostructures on pool boiling performance, cylindrical pillars with nano-scale dimensions (i.e., nanofins) were fabricated in this study. The target values for the pitch, diameter and height of the nanofins were determined prior to starting the fabrication steps.

The critical dimension (CD) for conventional photolithography is few micrometers, which is limited by the size of the wavelength emanating from the light source (which is approximately 300 nm or less). The CD of final pattern is bigger than the wavelength of light source. Therefore desired nanosized pattern in this study cannot be obtained by conventional photolithography. Electron Beam Lithography (EBL) can be used to obtain nano-scale patterns. EBL enables the realization of nanometer sized patterns with extremely high resolution. However, EBL is cost prohibitive and slow.

To overcome the cost problem of EBL, Nano Imprint Lithography (NIL) can be used for obtaining nano-scale patterns. Typically patterns with 25 nm CD were fabricated by thermal nanoimprint lithography [78]. However, this technique suffers from several drawbacks such as the substrate requires backside heating, and also high pressure is applied to a substrate to fabricate the nanoscale patterns. Thermal and pressure requirements can induce thermal and mechanical stress on the substrate, which eventually affects the alignment and critical dimension during nanofabrication.

Step and Flash Imprint Lithography (SFIL) was developed to overcome the disadvantages of NIL [79-81]. The SFIL technique can be performed at room temperature using low viscosity imprint resist, which is composed of two layers. One is

transfer layer, the other is imprint resist. The processing steps during SFIL for fabricating nano-pillars are illustrated in Figure 2-7.

The mold (also called as template) was prepared by Electron Beam Lithography (EBL). The final mold is patterned to enable the fabrication of 200 nm diameter circular nanofins with ~1μm pitch.

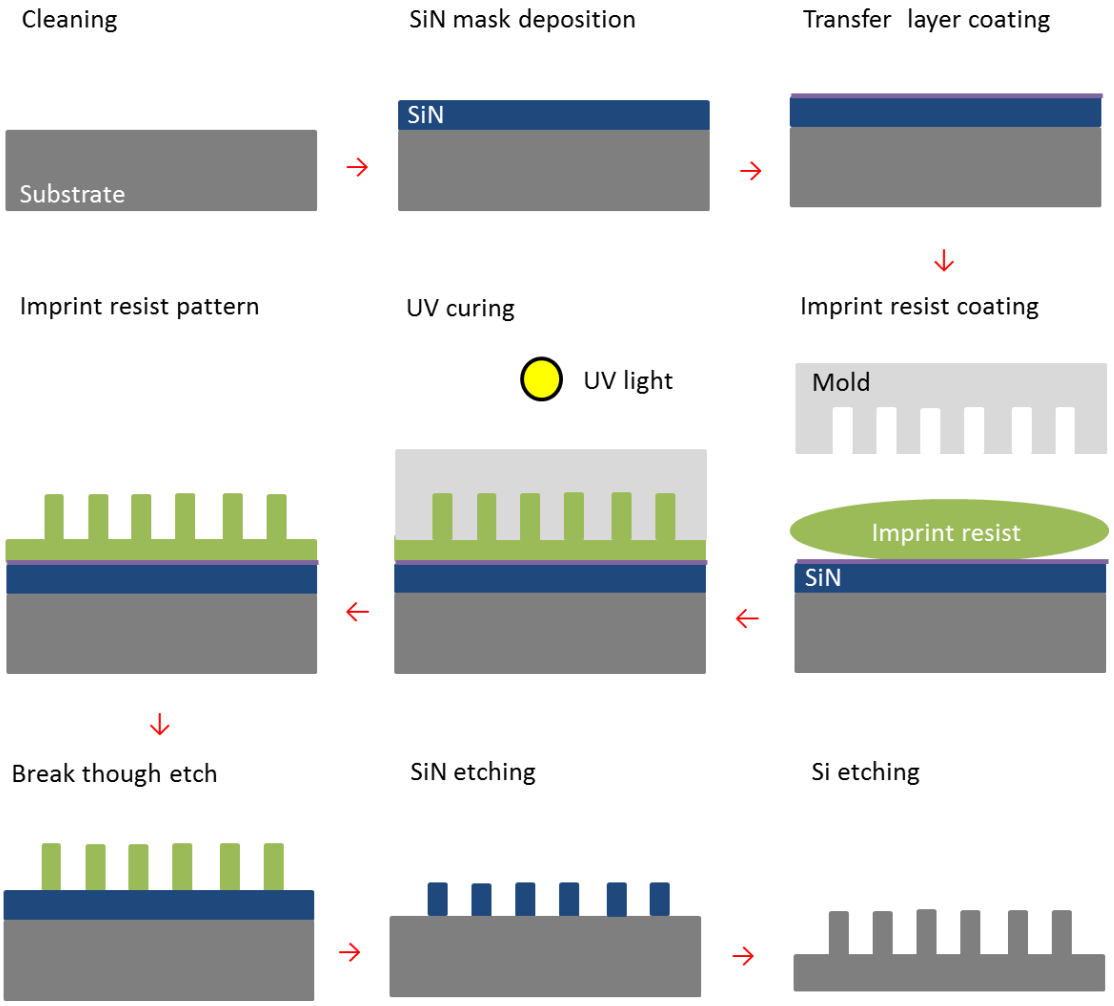

Figure 2-7 Schematic diagram of Step and Flash Imprint Lithography (SFIL) process for fabrication of nanostructure on silicon substrate

2.3.1. Piranha Cleaning

Before the starting the SFIL process, the wafer was cleaned by piranha solution to remove potential organic residues. Piranha solution (also known as piranha etchant) is recommended for cleaning the substrate. Piranha solution is a mixture of sulfuric acid (H_2SO_4) and hydrogen peroxide (H_2O_2) in volume ratio of 2:1. Piranha cleaning is performed in an acid hood (shown in Figure 2-8) with proper protective wear, because the piranha solution is strong oxidizing agent. In addition, if the imprint resist pattern on substrate is not successful, the organic imprint resist can be removed by piranha cleaning and the substrate can be reused for SFIL.

To prepare fresh piranha solution, 1650 ml sulfuric acid (H_2SO_4) was dispensed into quartz bath. Then 825 ml of hydrogen peroxide (H_2O_2) was added carefully and slowly. The mixture of sulfuric acid and hydrogen peroxide generates bubbles and heat because of exothermic chemical reactions. The piranha solution is stabilized after waiting for 5 minutes. The wafer substrate was then immersed into the piranha solution for 10 minutes. Piranha solution is used to remove potential organic contaminants from the surface of the wafer substrate.

After finishing the piranha cleaning, the substrate was rinsed with DI water 5 times in the cascade washer in acid hood. To remove the DI water, the substrate was moved to spin drier (SRD, Verteq), which is shown in Figure 2-8.

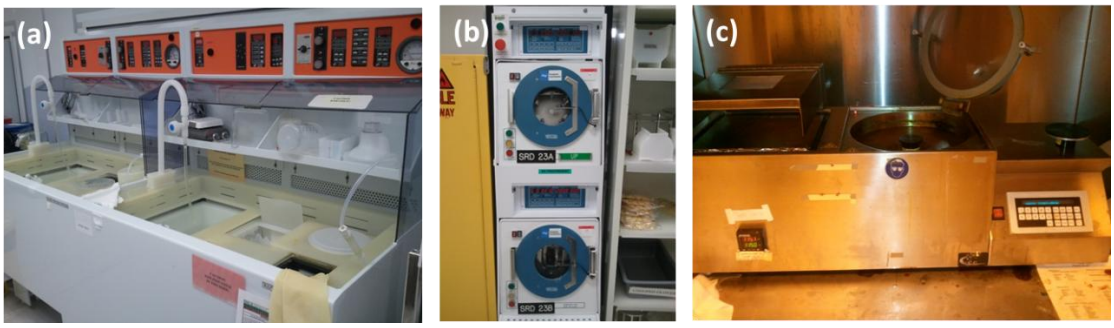

Figure 2-8 Image of instruments: (a) Acid hood, (b) Spin dryer, and (c) Brewer science spin coater.

2.3.2. Silicon Nitride Deposition

The imprint resist pattern is composed of soft organic material and it does not possess enough mechanical strength (or etch selectivity) to endure the harsh environment of the Deep Reactive Ion Etch (DRIE) process that is required for etching silicon in order to obtain nanofins in the silicon substrate. The imprint resist enables patterns that are less than 100 nm depth in silicon. Therefore silicon nitride was chosen for hard mask, in order to obtain better selectivity for dry etch. The silicon nitride layer is deposited to a thickness of 200nm by LPCVD.

2.3.3. Transfer Layer Coating

Transfer layer is used for realizing better adhension between imprint resist and substrate. It also provides high etch selectivity for the silicon wafer substrate. To obtain anti-relfective layer for SFIL, transfer layer (AP410, obtained from MRC staff) is spin coated on 4 inch silicon wafer by spin coater (Brewer Scinece Spinner) as shown Figure

2-8. AP410 is spin coated at 2600 rpm for 60 second, and then baked at 180 ^{o}C for one minute (based on standard recipe provide by MRC staff).

2.3.4. Step and Flash Imprint Lithography

The wafer substrate coated with the transfer layer is moved to the instrument used for Step and Flash Imprint Lithography (IMPRIO 100, Manufacturer: Molecular Imprints, located at MRC). In addition, the mold (or template) is loaded into the SFIL instrument after cleaning with IPA and DI water. After loading, leveling step for the mold is conducted. Even though this step is time consuming, it's a critical step to obtaining the uniform and well defined imprint resist pattern during the SFIL process. In the leveling step four point measurement was used to make the mold perfectly horizontal (and parallel to the wafer substrate). Each of the four measurement points were located on the area that was outside of extent of the mold and the measurements were repeated. After obaining the required level of alignment specified by the instrument vendor, the four inch wafer was loaded and the substrate and mold were aligned with each other.

After aligning the mold and the substrate, the imprint resist was selectively dispensed to the desired area on the substrate. At this time, the volume, position and droplet size of the imprint resist was controlled to obtain the optimized imprint resist pattern for the desired array of nanofins. The shape, size and material of mold or substrate is different for each user, and hence the specified recipe should be optimized by each user of the instrument. After multiple efforts involving trial and error, the recipe for this study was optimized, specified and fixed.

To obtain the imprint resist pattern, the mold was on to the wafer substrate with a force of 9 N. Exposure to ultra violet light source is performed for 10 seconds for curing the photoresist (provide mechanical rigidity) and to make a firm imprint resist pattern. The mold is then stepped to the nighboring location on the wafer substrate. Dispensing, exposing and curing of the imprint resist is repeated at the new position. The process is repeated until the entire area of the desired area on the wafer surface is imprinted. During SFIL, any dust particle contaminant deposited from the ambient can affect the process yield, which means the imprint resist pattern is not formed because of the poor contact between the mold and the wafer substrate. So the user should check the surface of the substate in each step, and any observed dust particle can be removed by using kapton tape.

After SFIL, the surface topology of the imprint resist pattern was measured by using Atomic Force Microscope (AFM) as shown in Figure 2-9. To estimate the thickness of the imprint resist layer, a line was scratched on the imprint resist at a location outside of the heater area of the substrate by using a sharp pen tip. This enabled the measurement of the thickness of the imprint resist layer. AFM (AFM 3000, Digital Instruments) was used to measure the thickness of the imprint resist and the pattern thickness as well. As shown at Figure 2-9, the thickness of the imprint resist layer is approximately 114nm and the imprint resist pattern (nanopillar or nanofin pattern) is approximately 65nm, respectively. Gwyddion, AFM analysis freeware was used for analyzing the measured data [82].

2.3.5. Pattern Transfer

Dry etching technique such as Reactive Ion Etching (RIE) or Deep Reactive Ion Etching (DRIE) was used for pattern transfer on the substrate. The imprint resist pattern was already obtained on the substrate from the SFIL process. This can be utilized to selectively etch the imprint resist pattern on the silicon nitride layer and the silicon wafer substrate. After dry etching of the imprint resist layer and silicon nitride layer, the nanoscale features of the patterns were investigated by using Atomic Force Microscope (AFM). AFM allowed the verification of the patterned surfaces without causing any damage to the test samples. The images for the instruments used for RIE, AFM and DRIE are shown in Figure 2-10.

First of all, the imprint resist with adhesion layer is removed for breakthrough etching by RIE (Plasma Therm #2) with O_2 plasma, using the recipe listed in Table 2-2. Since the imprint resist layer is coated on the substrate, breakthrough etch is essential to ensure that the silicon nitride layer is exposed. After that, silicon nitride layer also can be etched away by RIE (Plasma Therm #2) with CHF_3 and O_2 plasma, using the recipe listed in Table 2-2. During silicon nitride etching, 30 % over etching is recommended to ensure that the silicon nitride layer was removed completely.

Table 2-2 Recipe for breakthrough etching and silicon nitride etching

	Plasma Therm #2	
Breakthrough Etching	Recipe	YJ_O2.prc
	DC	400W
	Time	30 ~ 45 sec
	Gas	O_2 8 sccm

	Plasma Therm #2	
Silicon Nitride Etching	Recipe	TA_N1T1.prc
	Power	400W
	Time	110 sec
	Gas	CHF_3 40 sccm + O_2 2 sccm

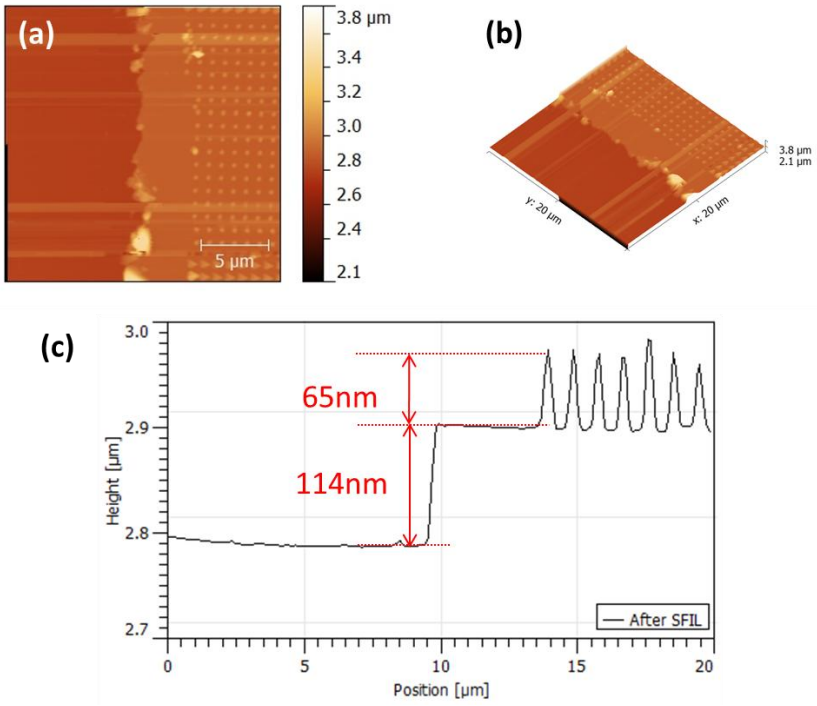

Figure 2-9 Surface topology measurements by AFM of the imprinted wafers after performing SFIL: (a) Plan view, (b) Topography view, and (c) Section analysis for obtaining the height of the imprint resist pattern and the imprint layer.

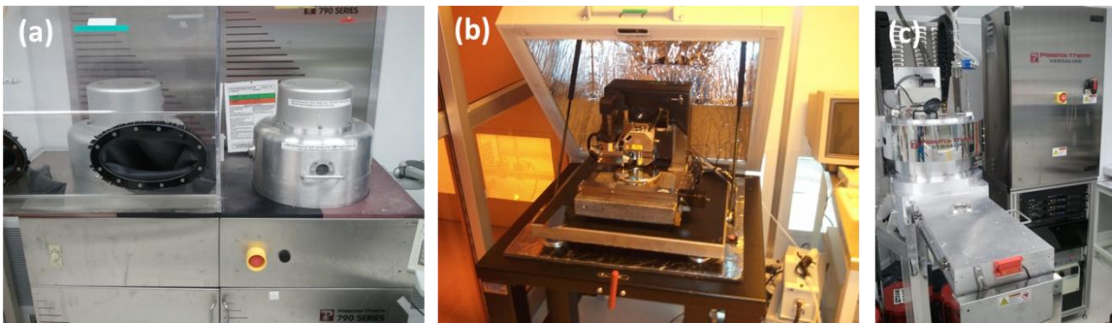

Figure 2-10 Images of instruments: (a) Reactive Ion Etcher (RIE), (b) Atomic Force microscope (AFM), (c) Deep Reactive Ion Etcher (DRIE).

The imprint resist pattern should be etched completely during the breakthrough etch step. However, this is difficult to estimate. This can be verified by AFM as shown in Figure 2-11. The height of the imprint resist pattern is approximately 63 nm (as shown in the figure). The AFM measurements are also used to check if the silicon nitride layer is etched completely. If the silicon nitride layer is not etched completely, the breakthrough etch step is repeated and the AFM measurements are performed again for verification.

In the same way, the breakthrough etch of the silicon nitride layer can also be verified by AFM (after RIE) as shown in Figure 2-12. The image shows the patterned silicon nitride etch-mask (to be used subsequently for DRIE), and the height of silicon nitride pattern is measured to be approximately 67 nm. Since the thickness of the silicon nitride (which is grown by LPCVD) is 100 nm, and the thickness of the etched features is less than 100 nm, this implies that theunderlying silicon wafer was exposed. Once the silicon nitride layer (which has a blue or purple color depending on the thickness of the

silicon nitride film) is etched sucessfully, the substrate color changed to gray (which is the same color as silicon). During breakthrough etch and SiN etch, most of the imprint resist was removed. However, to ensure the removal of all potential imprint resist on the substrate, RS 111 solution was used. The substrate was immersed into RS 111 solution at 50 ^{o}C for 20 minutes.

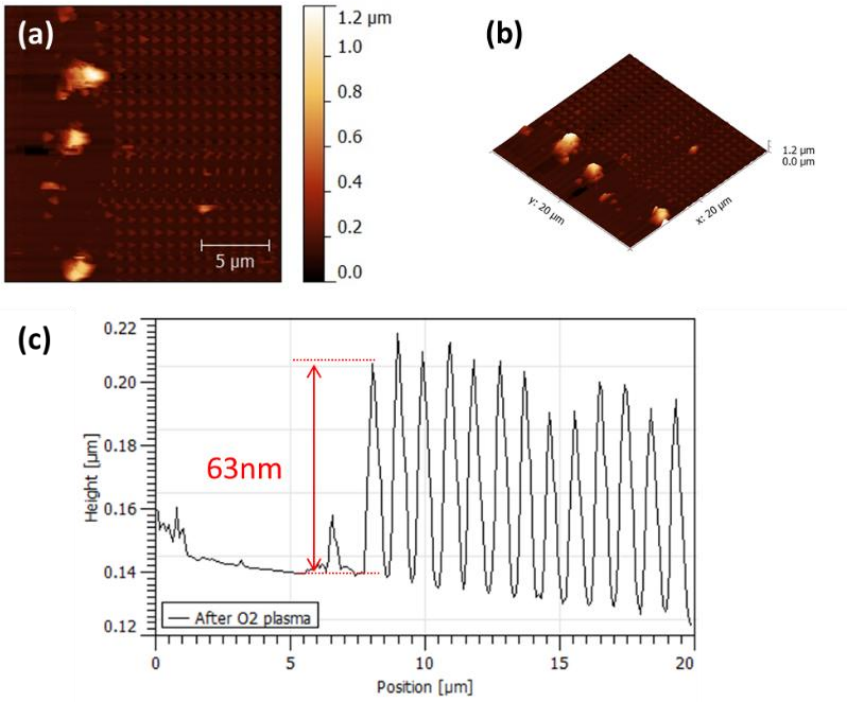

Figure 2-11 Surface topology measurements by AFM of the imprinted wafers after performing breakthrough etch: (a) Plan view, (b) Topography view, and (c) Section analysis for obtaining the height of the etched nanostructures.

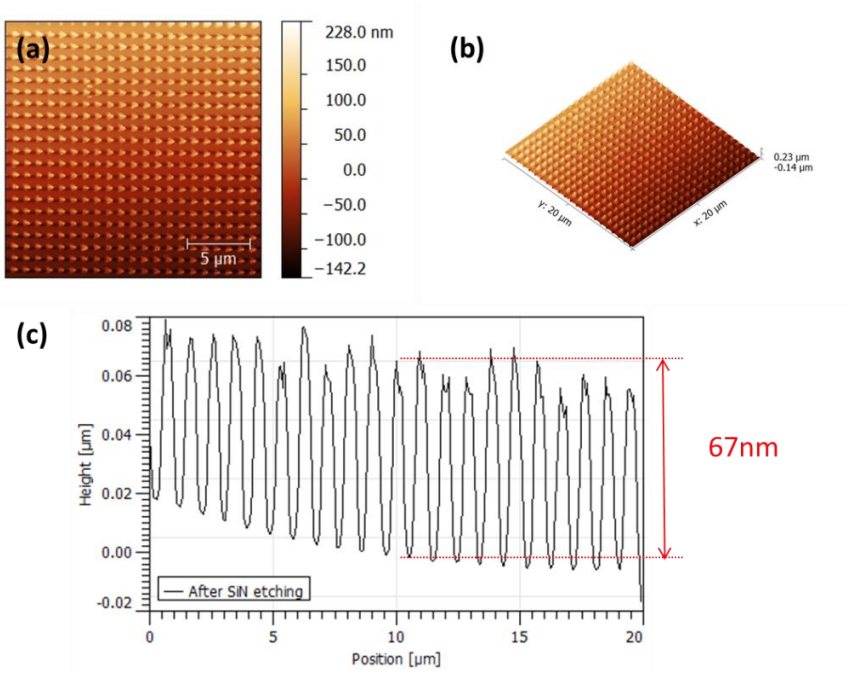

Figure 2-12 Surface topology measurements by AFM of the imprinted wafers after performing breakthrough etch of the Silicon nitride film: (a) Plan view, (b) Topography view, and (c) Section analysis for obtaining the height of the etched nanostructures.

To obtain the high aspect ratio of the silicon nanostructures, DRIE (Plasma Therm DSE, Manufacturer: Plasma Therm) was performed. By changing the number of processing cycles in DRIE, it is possible to control the height and aspect ratio of the surface nanostructures. If number of cycles is increased the height of the silicon nanofins is also increased. Hence the fabrication of silicon nanofins can be successfully accomplished along with the desired dimensions. The nanofin arrays on silicon substrate were successfully fabricated as shown in Figure 2-13. After the DRIE step, the morphology of the silicon nanofins was measured by using AFM and Scanning electron microscope (SEM).

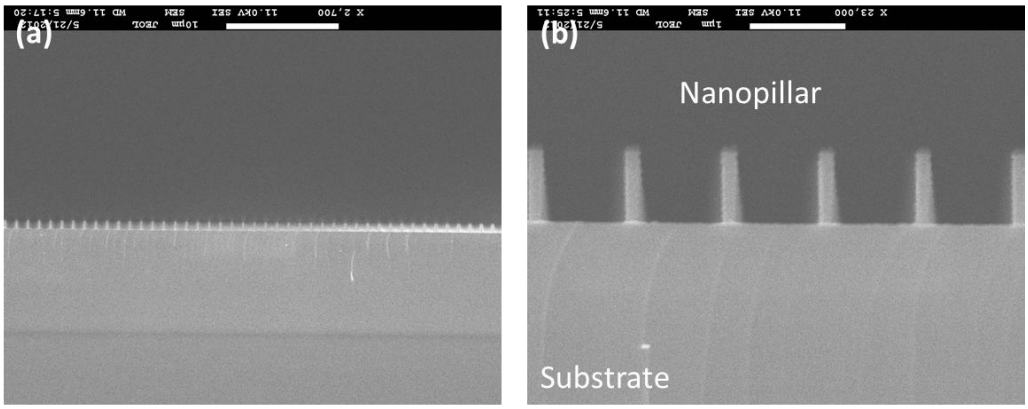

Figure 2-13 Cross sectional view of nanofins obtained from SEM image: (a) Silicon nanofins on silicon substrate, (b) Magnified view.

2.3.6. Silica and Nickel Nanofin, TFT Fabrication and Dicing

The silica nanofins can be obtained by thermal oxidation of the silicon nanofins (that were obtained by SFIL process). The thermal oxidation is accomplished by using LPCVD furnace located at the MRC. The process recipe was provided by the vendor. In addition, Thin Film Thermocouple (TFT) could be fabricated on the nanofin arrays - as described in previous chapter. Once the fabrication of both nanofin and TFT arrays are complete, the substrate can be cut by dicing saw (Dicing Saw, ADT) for the desired shape and size.

The metal nanofins can be obtained by thermal deposition of target materials (nickel) onto the substrate containing the silicon nanofins. After that, TFT arrays were fabricated using the process steps as described in previous chapters. The images of the silicon, silica, and nickel nanostructures (along with the TFT arrays) are shown in Figure 2-14. In addition, SEM image of nanofins with thin film thermocouple (TFT) is shown

in Figure 2-15. Thin film thermocouple (TFT) was deposited on top of these substrates (with surface nanostructures) as shown in Figure 2-15(b).

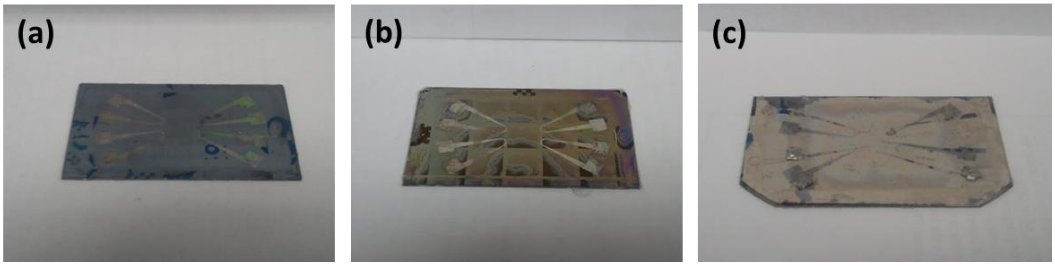

Figure 2-14 Image of surface nanostructures on wafer substrates with Thin Film Thermocouple (TFT) arrays for: (a) Silicon, (b) Silica, and (c) Nickel.

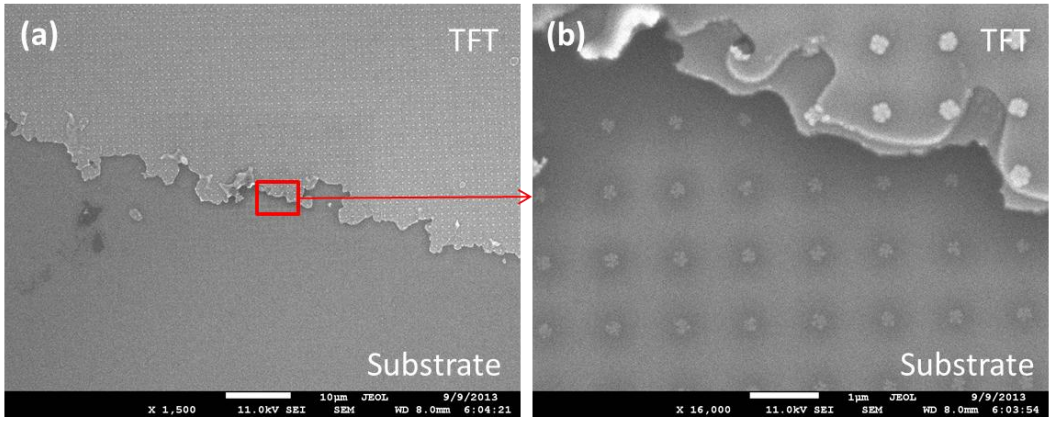

Figure 2-15 (a) SEM image of nanofin array at the junction of a Thin Film Thermocouple (TFT), (b) Magnified view

2.3.7. Characterization of Samples

The morphology of the surface nanostructures were verified by Atomic Force Microscopy (AFM) and Scanning Electron Microscopy (SEM), such as for the measurement of the dimension of nanofins (e.g., height, diameter and pitch).

The SEM images were used to obtain the top-view of fabricated nanofins, which enabled the measurement of the diameter and pitch of the nanofins. In addition, the information about nanofin height could be obtained by AFM. For example, the image of the fabricated silicon nanopillars is shown in Figure 2-16. SEM and AFM images show that the silicon nanofin array was successfully fabricated with the desired dimensions. From the SEM measurements, the diameter of nanopillar was measured to be 187.3 nm, 200.4 nm and 184.7 nm. Therefore the mean diameter is 191 nm, and standard deviation is 6.9 nm. Moreover, the height of the nanofin was obtained by using AFM, which is 106 nm.

The heights of nanofins with high aspect ratios were not amenable for characterization by AFM. The AFM tip cannot reach the bottom of pillars, because of the constraints imposed by the size of the AFM tip. Hence SEM measurements using a tilted platform enabled the measurement of the height of the nanofins - as shown in Figure 2-17. At 45^{o} tilt angle, the distance between top and bottem of nanofin was measured to be 236 nm, 257 nm, 251 nm, 256 nm and 241 nm. The mean height (with tilt) was measured to be 248.2 nm, and therefore the corresponding height of the silicon nanofins was estimated to be 354 nm. In addition, the diameter of nanofins was also obtained from the SEM images. The dimensions of the silica nanofins can also be

obtained by SEM and AFM, as shown in Figure 2-18. After the fabrication of the silicon nanofins, the SEM/AFM characterization was performed. The mean diameter obtained from SEM image is 201 nm and the height from AFM image is 210.4 nm. Subsequently the silicon substrate was moved into LPCVD furance for oxidation. The results from the SEM/AFM characterization for other samples are described in Appendix A. The nickel nanofins were obtained by deposition of nickel thinfilm onto silicon nanofins, and are shown in Figure 2-19. The dimensions of the silicon nanofins on silicon wafer surface and silica/ nickel nanofins (which are used in this study), are summarized in Table 2-3 and Table 2-4, respectively. Occasionally the fabrication of nanofins was not successful due to unexpected factors. Particularly, unexpected deposition of dust particles often would disturb the fabrication process during SFIL. For silicon nanofin sample, the number of "steps" with successful nanofin pattern is 11 for nanofin height of 10 nm, 14 for nanofin height of 46 nm, 11 for nanofin height of 106 nm, 14 for nanofin height of 351 nm, 8 for nanofin height of 464 nm, and 9 for nanofin height of 750 nm, respectively. For silica samples, the number of "steps" with successful nanofin patterns is 15 for nanofin height of 108 nm, 15 for nanofin height of 210 nm. For nickel, the number of "steps" with successful nanofin patterns is 8 for nanofin height of 93 nm.

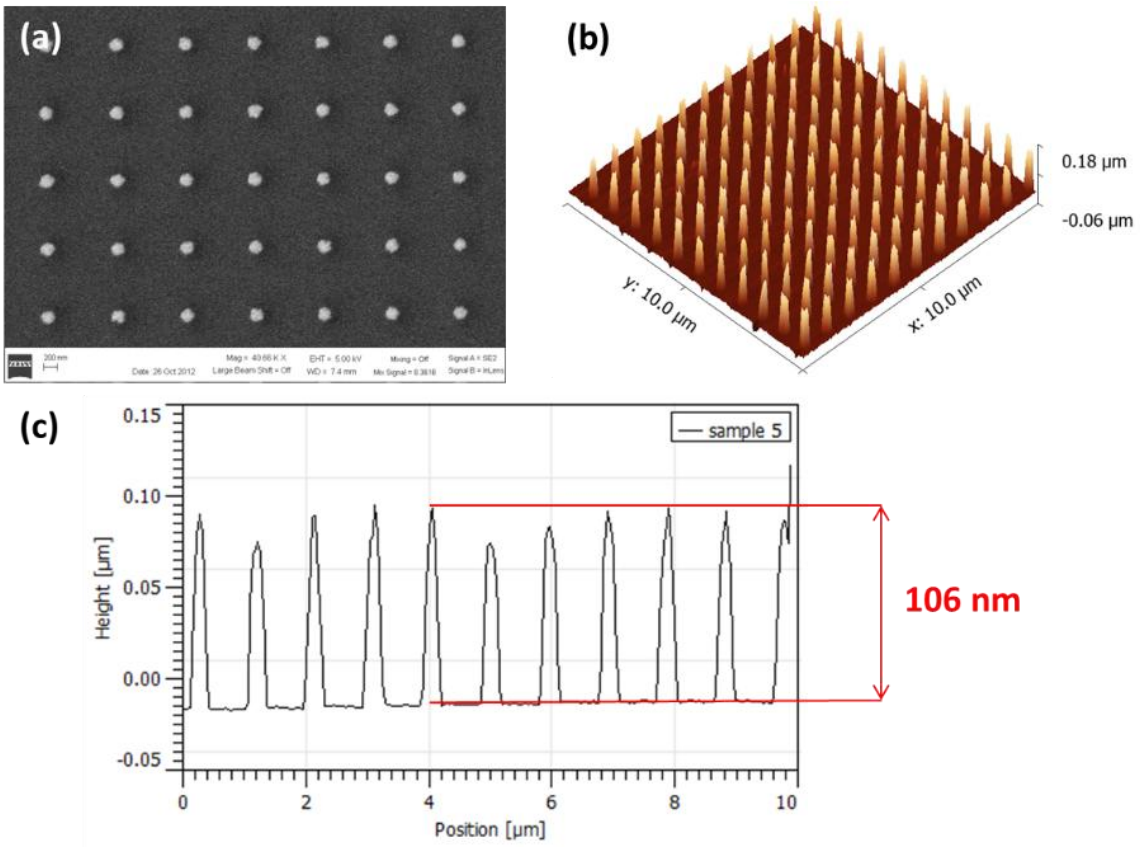

Figure 2-16 AFM and SEM measurements for silicon nanofins with height of 106 nm and diameter of 225 nm. (a) SEM image, (b) Topography view obtained from AFM measurements. (c) Section analysis using data obtained from AFM measurements.

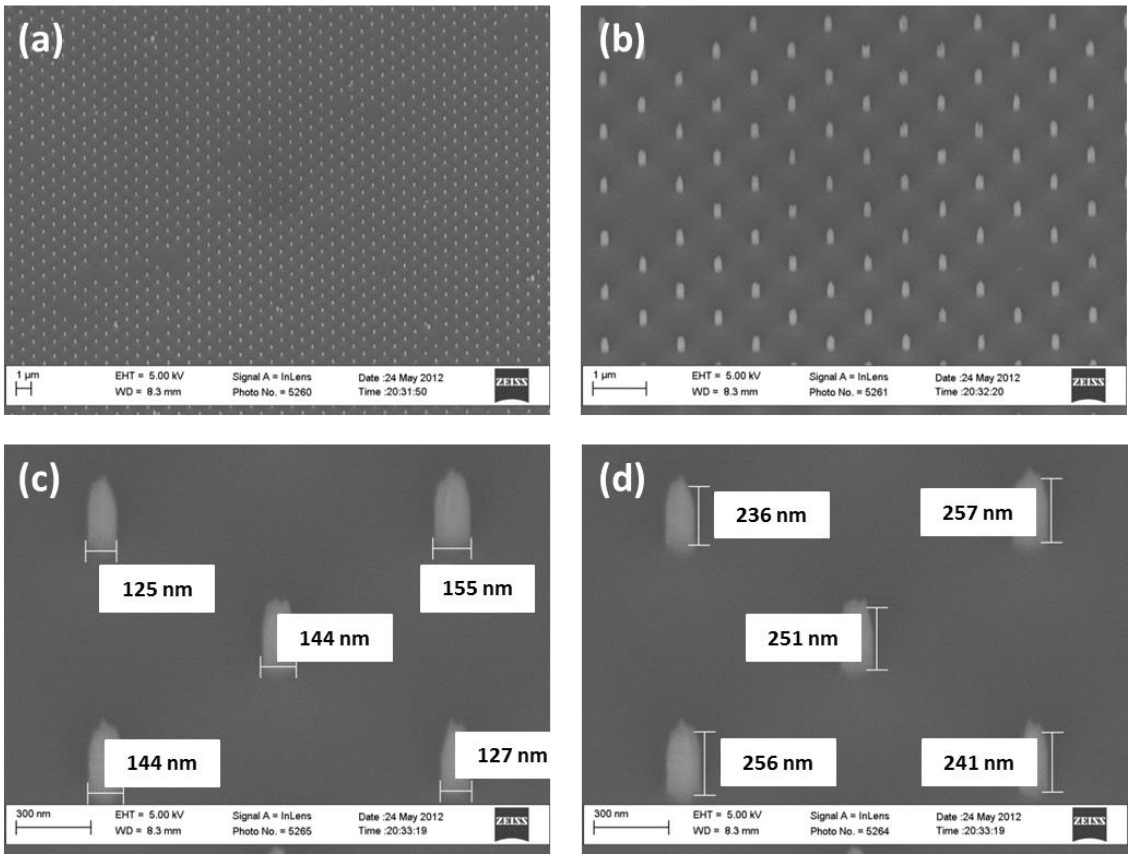

Figure 2-17 SEM image of silicon nanofins with a height of 354 nm and diameter of 139 nm (image obtained at a tilt angle of 45^{o}). (a) SEM image, (b) Magnified image, (c) Measurement of diameter, (d) Measurement of height.

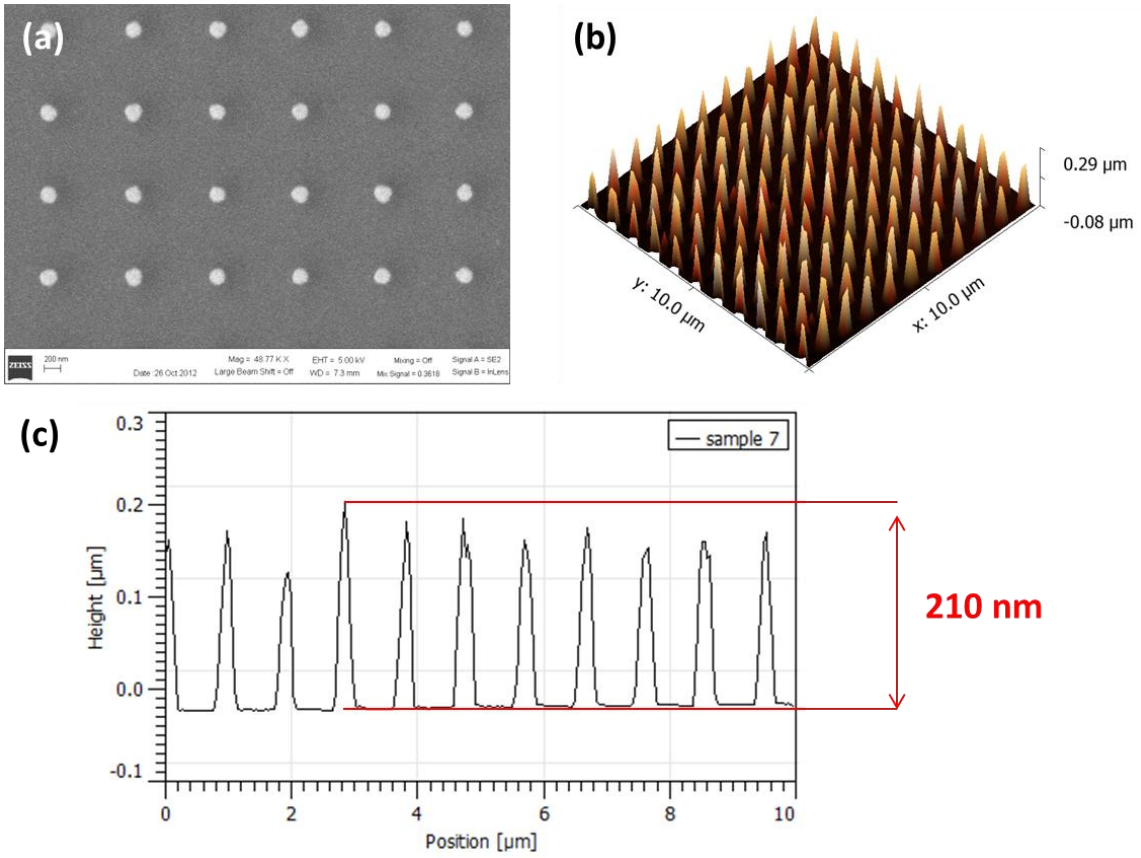

Figure 2-18 AFM and SEM measurements for silica nanofins with height of 210 nm and diameter of 201 nm. (a) SEM image, (b) Topography view obtained from AFM measurements, (c) Section analysis using data obtained from AFM measurements.

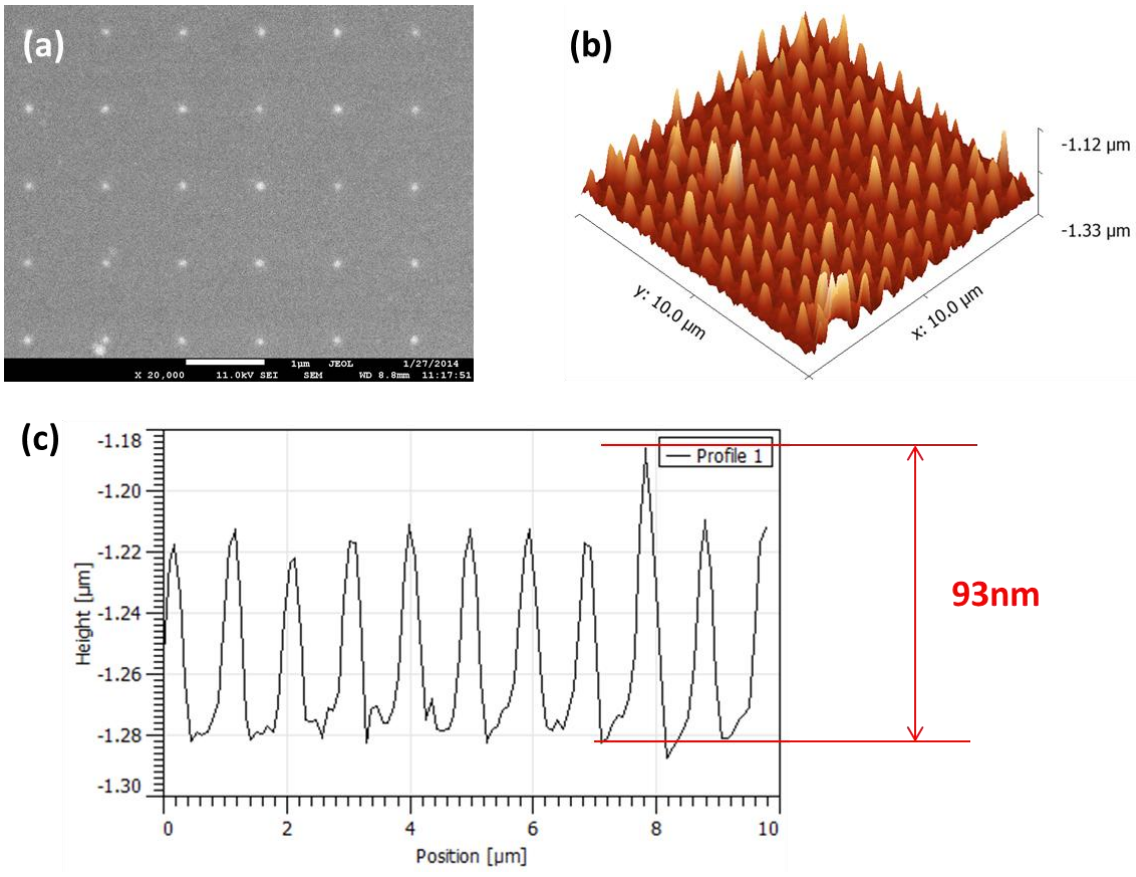

Figure 2-19 AFM and SEM measurements for nickel nanofins with height of 93 nm and diameter of 191 nm. (a) SEM image, (b) Topography view obtained from AFM measurements, (c) Section analysis using data obtained from AFM measurements.

Table 2-3 Summary of silicon nanofin dimensions

Pillar	Height, nm	Diameter,nm
Silicon	10	164
	46	173
	106	191
	354	139
	464	165
	750	104

Table 2-4 Summary of silica/ nickel nanofin dimensions

Pillar	Height, nm	Diameter,nm
Silica	108	225
	210	201
Nikel	93	191

3. EXPERIMENTAL APPARATUS AND PROCEDURE

The packaging of thin film thermocouple (TFT), calibration, experimental setup and experimental procedures are discussed in this chapter. The objective for performing the experiments is to obtain the pool boiling curves using the test fluid (PF-5060).

3.1. Packaging and Calibration of Thin Film Thermocouples (TFT)

3.1.1. Packaging of TFT

Several methods can be employed for packaging of thin film thermocouple (TFT) for the purpose of connecting the TFT arrays to the Data Acquisition (DAQ) system. Wires were soldered to the bond-pads of the TFT array for the packaging step. Conventional soldering materials were used in this study.

The fabrication procedure for TFT arrays is described in Chapter 2. Using lead soldering the K-type thermocouple wires (Chromel and Alumel, Supplier: Omega) were connected to the corresponding bond-pads of the TFT arrays. The silicon wafer substrate containing the TFT array was placed on a hotplate, and then the substrate was heated to approximately ~170^{o}C, which is the melting point of the solder materials. After making electrical connection between the individual bond-pad and the corresponding thermocouple wire (K-type, consisting of chromel and alumel), the substrate was cooled down to room temperature. At this time, the chromel bond-pad was connected to chromel wire, and the alumel bond-pad was connected to alumel wire, respectively.

The electrical connection between the bond-pad and thermocouple wire is quite delicate, and the soldered junctions are susceptible to breakage during handling. Therefore the thermocouple wires are fixed on to the clamp as shown in Figure 3-1.

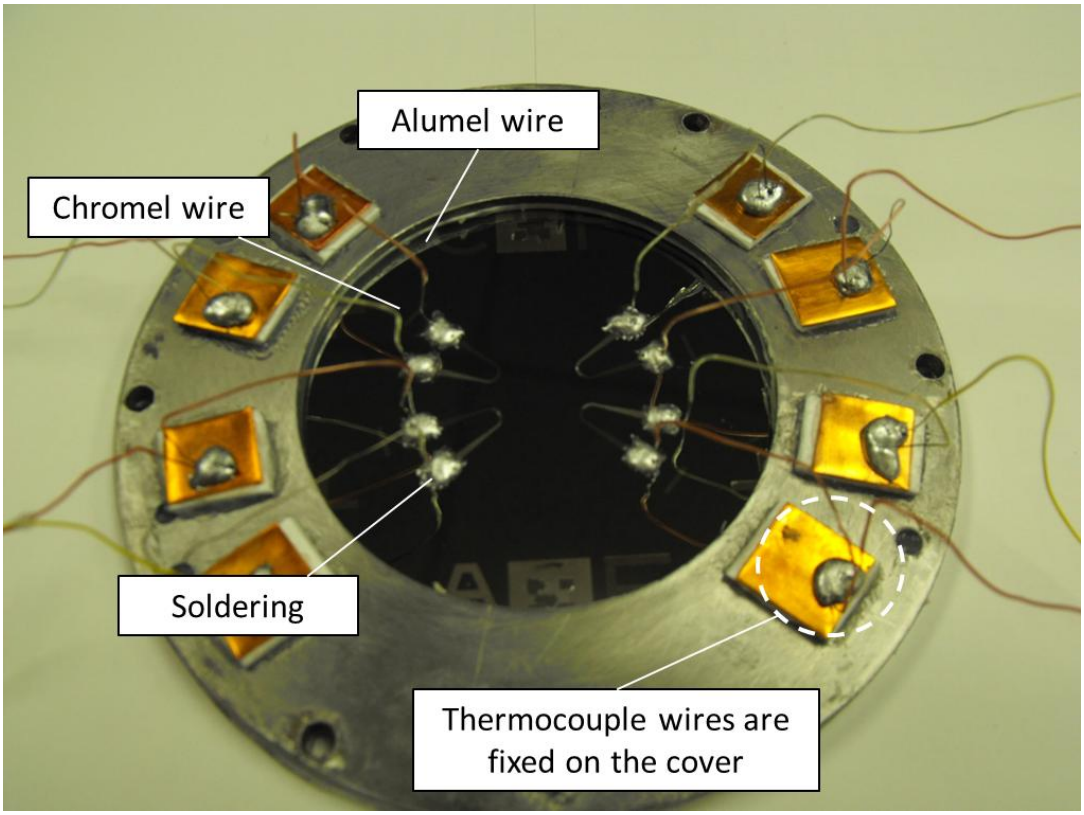

Figure 3-1 Image of wafer substrate mounted on steel clamp after packaging of the thin film thermocouple (TFT) arrays.

3.1.2. Calibration of TFT

After the packaging step, each Thin Film Thermocouple (TFT) was calibrated by using a commercial IR camera (FLIR i50, FLIR Systems) as shown in Figure 3-2. The emissivity of silicon wafer is selected in the camera software using literature data [83].

To perform the calibration experiments the silicon wafer substrate was placed on a hotplate and the surface temperature profile was obtained by TFT and imaged at the same time using the IR camera. The temperature data recorded by the TFT and IR camera were observed to be consistent. In addition, the calibration curve is observed to be linear and consistent for the range of temperatures considered in this study i.e., from room temperature (~ 290 K or 20 °C) to a maximum temperature not exceeding 573K (~ 200 °C). The slope of the calibration curve was close to unity and the R^2 value exceeded 0.99 (but was less than 1).

3.2. Description of Experimental Setup

The test chamber that was used for the pool boiling experiments has a cubic shape (of ~15-20 cm side). This apparatus was used in previous studies and the description of the experimental apparatus is available in previous publications in the literature [8, 10, 28, 84]. The pool boiling test chamber consists of the following components: 1) Cube shaped test chamber with transparent glass window for viewing ports; 2) an immersion cooling coil connected to a chiller apparatus for maintaining a fixed subcooling of the liquid pool; 3) a calorimeter apparatus consisting of power supply units that are connected to cartridge heaters which are embedded in a copper block containing an array of wire-bead thermocouples for estimating the heat flux to the boiling surface (the silicon wafer containing TFT array and surface nanostructures are placed on top of the copper block/ calorimeter and secured using a stainless steel clamp that is secured by screws on a concentric steel jacket); 4) an automated/ computerized data acquisition system (DAQ) for recording temperature at high-speeds and with high

spatial resolution using the TFT array and the thermocouples embedded in the calorimeter apparatus (copper block).

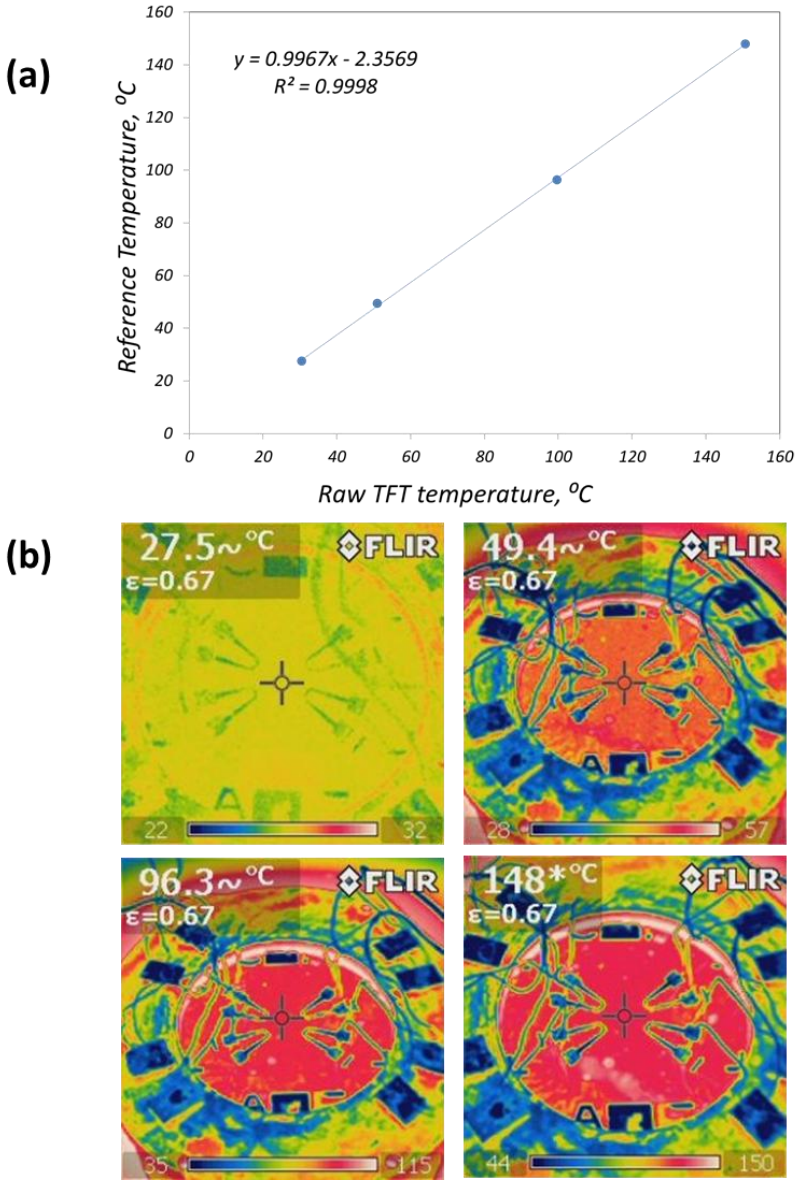

Figure 3-2 (a) Calibration curve of Thin Film Thermocouple (TFT) generated by using images from IR camera (b) Images recorded by IR camera for various values of the wafer surface temperature.

Figure 3-3 shows the schematic diagram of the apparatus used for the pool boiling experiments. In addition, a high-speed camera (Fastec Imaging Corporation, Troubleshooter TSHRMS) was used for performing high speed visualization experiments to record the bubble nucleation, growth and departure.

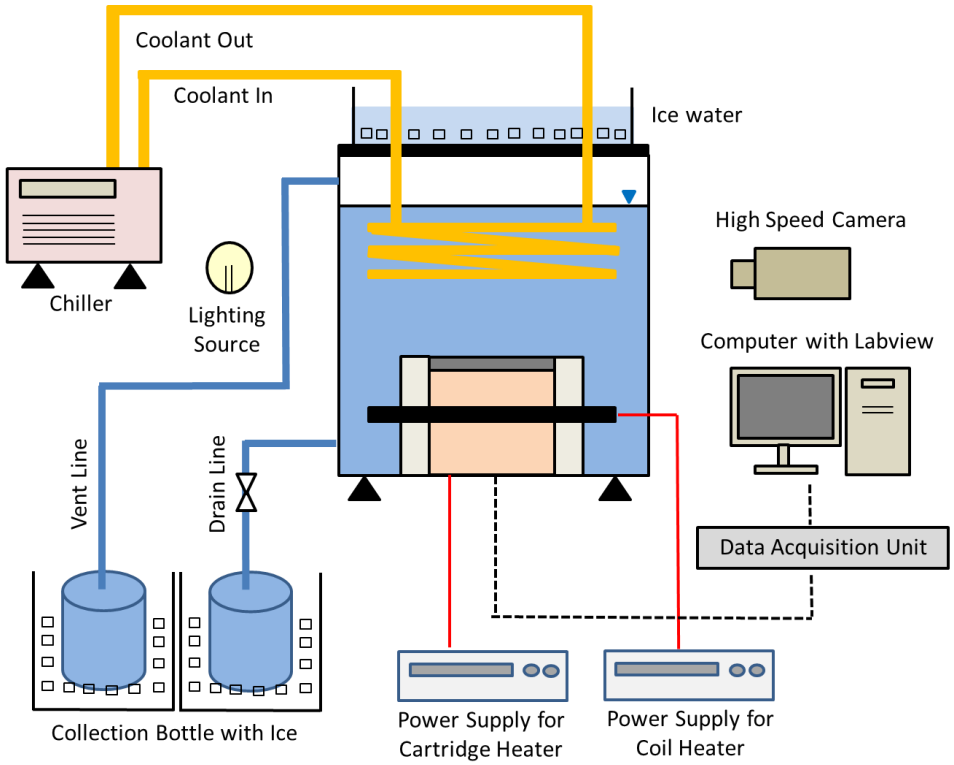

Figure 3-3 Schematic diagram of apparatus used for pool boiling experiments

3.2.1. Pool Boiling Chamber

The cylindrical copper block is 8. 9cm diameter and 5.1cm height as shown in Figure 3-4. The copper block was enclosed within a concentric hollow stainless steel jacket with an air gap (for insulation). Five cartridge heaters (three for 500W, two for

300W) were installed to generate heat within the copper block. To measure the heat flux, K type bead thermocouples were embedded at various distances from the top flat surface of the copper cylinder as shown in the figure. The copper block and the steel cylinder were tightly secured to the bottom steel plate of the test chamber by six screws (as well as gaskets to make it leak-proof and provide better thermal insulation to the heated copper block).

A coil heater was installed outside the steel jacket and concentric with the steel jacket within the pool boiling chamber. The coil heater was used for boiling the test liquid prior to start of the experiment for degassing step. Also, at low heat flux values within the copper block (calorimeter apparatus), power input to the coil heaters can be used to reach the desired bulk temperature of the test liquid in the event the heat supplied by cartridge heater is not sufficient.

On the outside top surface of the chamber, ice water is placed for condensing the test liquid and recovering the condensed test liquid (since the test fluid, PF-5060 is highly volatile and expensive). The melted ice is replenished periodically. The outlet port of the test chamber is also connected to a collection bottle that is placed in a container packed with ice outside for recovery of any effluent refrigerant from the test chamber (which means that the test chamber is open to the ambient and therefore it is maintained at atmospheric pressure). In addition, digital cameras (a low speed digital camera as well as a high speed digital camera) were used for visualization of the boiling surface periodically during the experiment, usually after steady state conditions were achieved (to record parameters such as bubble inception, spatial density of bubble

nucleation, bubble growth as a function of time, bubble diameter at departure, bubble departure frequency, etc.).

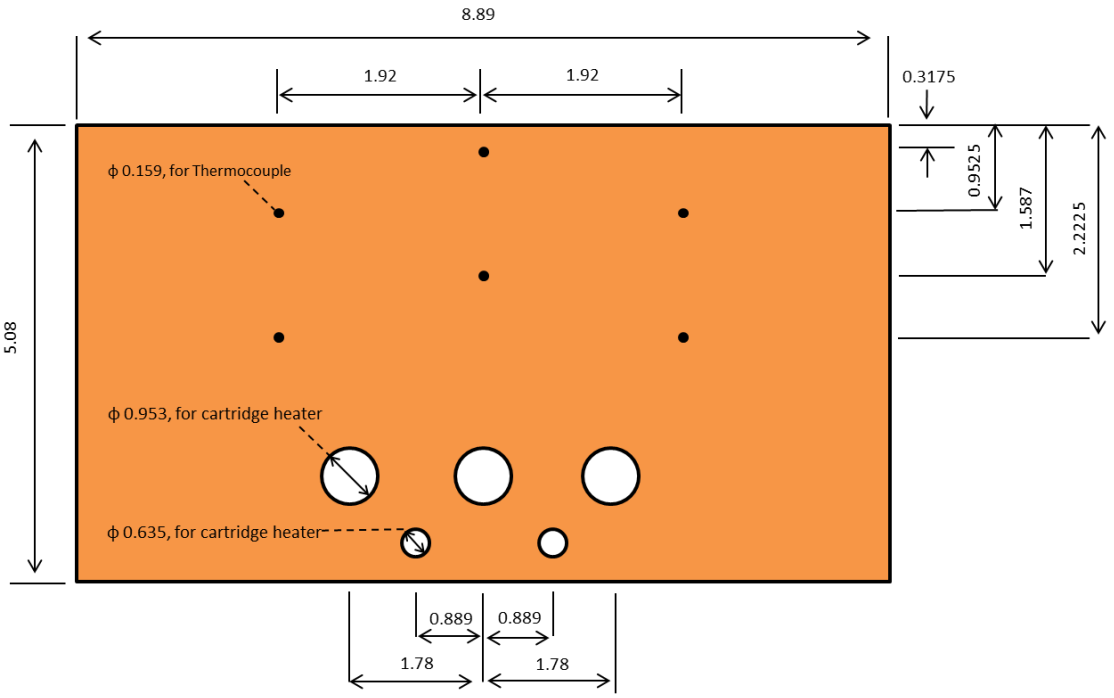

Figure 3-4 Schematic diagram of the cylindrical copper block heater (calorimeter) apparatus (figure not to scale, unit: cm)

3.2.2. Subcooling Appratus

For the subcooling experiments, the test fluid is maintained at fixed temperature below the saturation temperature by immersing a cooling coil (i.e., a coiled copper tube with chilled liquid flowing inside) into the liquid pool. The temperature difference between the saturation temperature and the bulk liquid temperature (or liquid pool temperature) is called the "liquid subcooling". The cooling coil is connected to a chiller

unit (Model: 9612, Manufacturer: Polyscience) which has automated temperature control. This enables the pool temperature of the test liquid to be maintained at 51^{o}C (for liquid subcooling of 5 ^{o}C) and 46 ^{o}C (for liquid subcooling of 10^{o}C). Tap water is used as the chilled liquid which flows in the cooling coil. The pool temperature was measured by placing a wire-bead thermocouple inside the test chamber, which is – in turn, connected to the controller of the chiller apparatus.

3.2.3. Power Supply Unit

As mentioned before, a silicon wafer (with TFT array and the surface nanostructures) was clamped on top of the copper heating block (calorimeter apparatus). The cylindrical copper block is placed inside a concentric steel jacket. The air gap between the copper block and the steel jacket acts as a thermal insulator and minimizes heat loss in the horizontal direction. The diameter of copper block is 3.5 inches and height is 2 inches. Five cartridge heaters (3EA of 500W and 2EA of 300W) were embedded in the copper block (near the bottom portion of the copper block) to serve as the heat source for the boiling surface. The cartridge heaters were connected to a power supply (Manufacturer: Amrel, Model No.: SPS120-10-0020, Power rating: 1 kW). The coil heater (that was placed outside the steep jacket and concentric with the steel jacket) was connected to a rheostat for modulating the energy input into the coil heater.

To measure the heat flux, commercial K-type wire bead thermocouples were embedded in the copper block. These commercially sourced thermocouples were

calibrated by a NIST calibrated mercury thermometer (both were placed in a water bath for performing the calibration experiments).

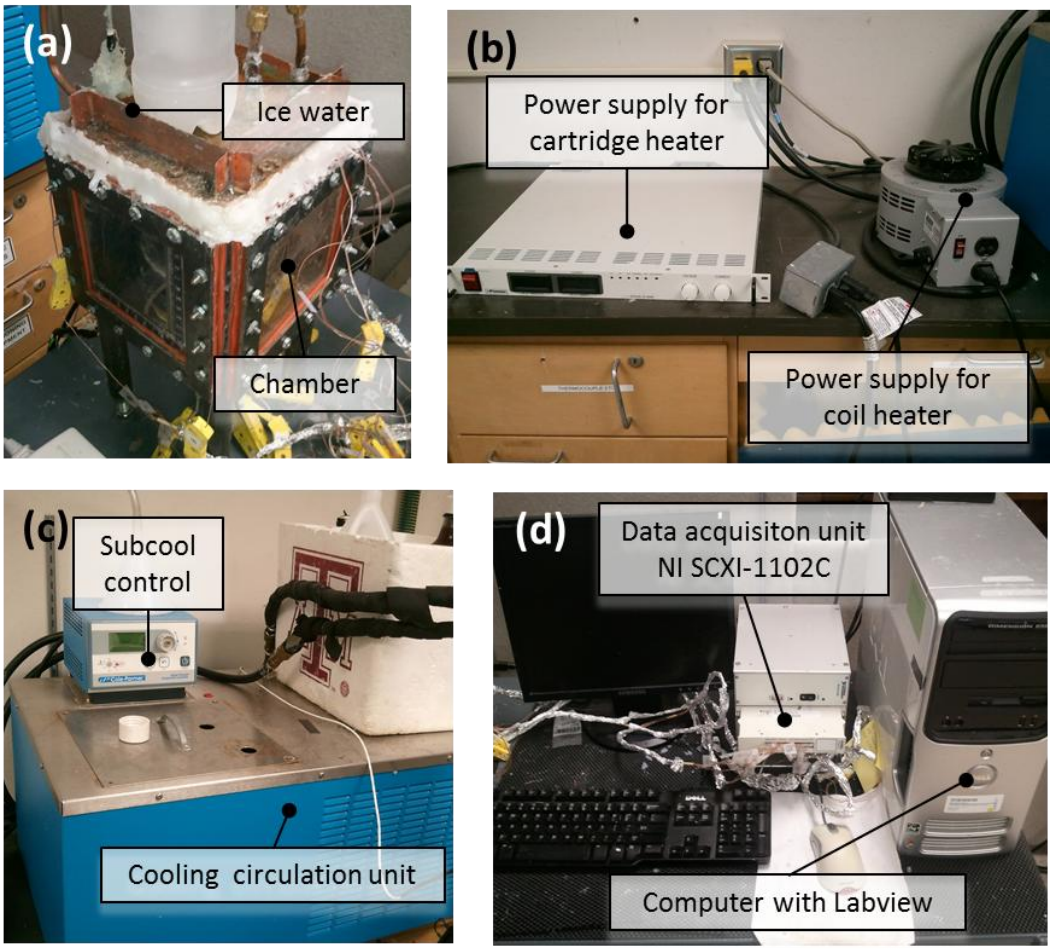

Figure 3-5 Images of experimental apparatus used for the pool boiling experiments, consisting of: (a) Pool boiling chamber, (b) Power supply unit, (c) Coolant circulation unit (chiller apparatus), and (d) High-speed data acquisition (DAQ) unit

3.2.4. Data Acquisition Unit

The temperature data from these thermocouples are periodically recorded by a computer through an automated high-speed data acquisition (DAQ) system. The DAQ

consists of NI SCXI-1102C and PCI-6251 DAQ board (Manufacturer: National Instruments, Austin, TX). The software codes for automating the high-speed data acquisition was programmed using a graphical user interface (GUI) based on Labview 7.1 (Manufacturer: National Instruments, Austin, TX). The temperature data from the thermocouples embedded inside the copper block were recorded at 200 Hz. Simultaneously the temperature of the test surface was recorded using TFT and the temperature of the liquid pool were also monitored in real time and recorded by the DAQ system. An image of the boiling apparatus is shown in Figure 3-5. The figure shows the components of the apparatus – such as the pool boiling chamber, the chiller unit, power supply unit and data acquisition unit.

3.3. Experimental Procedure

3.3.1. Test Surface Assembly

A steel clamp was used for mounting the silicon wafer (containing the TFT array and nanostructured surface) on the copper block (i.e., the calorimeter apparatus). The test chamber was filled with the test fluid (PF-5060, Manufacturer: 3M Corp.) and came in contact with the hot silicon substrate (boiling surface). Teflon gaskets were used for preventing the leakage of liquids from the experimental apparatus, particularly from the steel clamp, the steel jacket and the bottom surface of the copper block (calorimeter apparatus).

High thermal conductivity grease (Model: 340 Heat Sink Compound, Manufacturer: Dow Corning) was used for achieving better thermal contact between the

copper block and the silicon wafer. A torque wrench was used for uniformly tightening the screws used for mounting the steel clamp on the silicon wafer. The schematic diagram for the assembly of the test surface is shown in Figure 3-6.

Two different shapes of circular steel clamps are used in this study. The opening in the steel clamp determines the size of the boiling (heater) surface. One of the clamp configurations has a rectangular window (31.75 mm × 58.73 mm), while the other has a concentric circular window (63.5mm diameter).

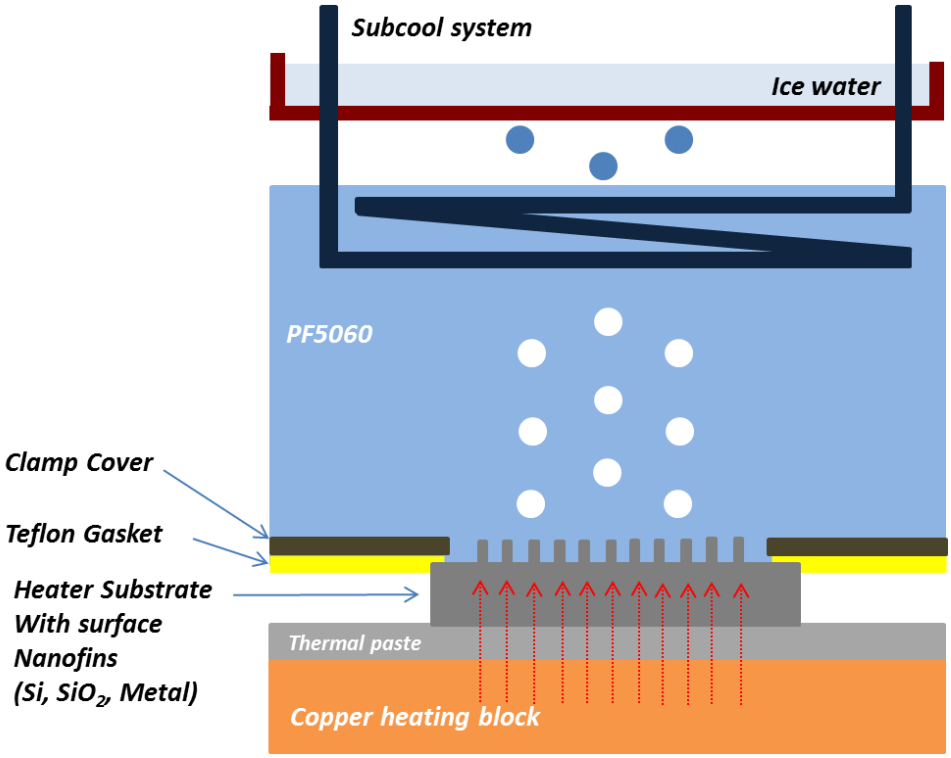

Figure 3-6 Schematic diagram for assembly of the test surface used in the pool boiling experiments.

3.3.2. Leakage Test and Degassing Step

The pool boiling chamber was tested for leaks before every experiment. During leak test, DI water was used instead of PF-5060, since PF-5060 is expensive and highly volatile (which makes it difficult to check for leaks). After assembly of the test surface, the chamber was filled with the DI water and the bottom of the test chamber was monitored for any leaks. A set of six screws that are placed on each face of the optical windows as well as the steel jackets were tightened using a torque wrench to close any of the water leaks. After eliminating any leaks from the chamber, the water is drained and the chamber was left open for several tens of minutes to dry. The top steel cover was then assembled with screws. To minimize vapor loss, silicone glue was applied for enhanced sealing during the assembly of the top steel cover.

The test liquid (PF-5060, 3M Corp.) has the propensity to dissolve air (particularly oxygen), which may cause unexpected nucleation during the execution of the pool boiling experiments. Therefore, degassing of the test liquid was performed before resuming any pool boiling experiments. The test liquids were heated to the boiling point of 56^{o}C (saturation temperature) by the cartridge heaters and the coil heater as well, to achieve pool boiling of the test liquid in the test chamber. This condition was maintained for a minimum of three hours to potentially remove any trapped gasses in the cavities on the surface of the heater or to eliminate any dissolved gasses in the test fluid.

3.3.3. Heat Flux Calculation

The heat flux values in the copper block for the pool boiling experiments were calculated using the Fourier's law of heat conduction, as shown in the following equation [85]:

$$q_c'' = k\frac{T_1 - T_2}{L_c} = k\frac{\Delta T}{L_c} \tag{3-1}$$

Where q_c'' is the heat flux through the copper block in the vertical direction, and k is the thermal conductivity of copper; T_1 and T_2 are the temperature values recorded by the wire-bead thermocouples that are embedded in the copper block; ΔT is the temperature difference between a pair of wire-bead thermocouples lying in the same vertical plane; and L_c is the distance between a pair of wire-bead thermocouples located in the same vertical plane. The heat flux, q_c'' is calculated using the equation above (Equation 3-1) after each set of steady state conditions are achieved. The copper block (k = 401 W/m·K) is surrounded by air (k = 0.024 W/m·K) which serves as a good thermal insulator, as described previously. Therefore it can be assumed that heat passing through the copper block (in the vertical direction, neglecting losses) is equal to the heat lost through the test surface. Hence applying the law of the energy conservation in the vertical direction, $Q_c = Q_w$; where Q_c is the heat loss through the copper block in the vertical direction and Q_w is the heat loss through the test surface (boiling surface). This equation can be expressed in an alternate form as:

$$q_c'' A_c = q_w'' A_w \;;\; q_w'' = q_c'' \frac{A_c}{A_w} \tag{3-2}$$

Where, q_w'' is the wall heat flux through the test surface, A_c is the projected area (or cross section area) of the cylindrical copper block and A_w is the area of the test surface (wall) in contact with the test fluid. The measurement uncertainty of the heat flux values were obtained by using the Klein and McClintock method, as shown in the following equation:

$$\frac{\omega_{q''}}{q''} = \sqrt{\left(\frac{\omega_{\Delta T}}{\Delta T}\right) + \left(\frac{\omega_{\Delta y}}{\Delta y}\right) + \left(\frac{\omega_K}{K}\right)} \tag{3-3}$$

Where, ω is the statistical uncertainty for each variable; ΔT and Δy represent the temperature difference and the spatial distance between two wire-bead thermocouples located in the same vertical plane that are placed inside the copper heating block (i.e., the calorimeter apparatus). An uncertainty value of ±1.0% was assumed for the thermal conductivity of copper in the heating block and ±3.0% for the uncertainty in the distance between two thermocouples that were used in this study. The experimental error in the heat flux measurement and the wall superheat values were also plotted in the boiling curve with a confidence of 1σ (where σ is the standard deviation calculated from the statistical analysis of the measured temperature and heat flux data).

3.3.4. Experimental Procedure

The temperature data from pool boiling experiments were obtained under steady state conditions. After the leakage test and degassing step, the power source is switched on resulting in heat being generated by cartridge heater and coil heater. At same time, the temperature of the liquid pool is maintained at a constant level of subcooling by the

chiller unit (at 46^{o}C for subcooling of 10^{o}C; at 51^{o}C for subcooling of 5^{o}C and at 56^{o}C for saturated condition). In addition, the ice is replenished regularly for recovering the condensates from the pool boiling apparatus. Typically four different data points were established for steady state conditions and were measured until Critical Heat Flux (CHF) point, and four different data points were measured after Minimum Heat Flux (MHF) point (or Leidenfrost point). The detailed steps for data acquisition leading to the plotting of the pool boiling curve are shown in Figure 3-7.

Once the steady state conditions are achieved in the experimental apparatus - data acquisition for the temperature measurements is performed using the DAQ. The temperature data is then analyzed for obtaining the wall heat flux and wall superheat values for the purpose of plotting the boiling curve for different subcooling conditions and different test surface conditions. Typically it takes over two hours to reach the steady state conditions (defined as less than 1 °C variation in the temperature of the wire-bead thermocouples in the copper calorimeter apparatus over a 5 minute period). After the steady state conditions are established the temperature data measured by the wire-bead thermocouples in the copper block, the temperature of test surface measured by the TFT array and the temperature of the liquid pool are recorded by the data acquisition system. Moreover flow visualization of the pool boiling experiments are also performed using both a low-speed camera and a high speed camera.

After obtaining the desired wall heat flux data and the wall superheat values on the test surface, the power (heat) input to the experimental apparatus is raised by increasing the voltage of the cartridge heater with the intention of obtaining the next

steady state data point. The cooling circulation unit (chiller unit) is also carefully controlled while monitoring the temperature of the liquid pool. This process is repeated until the Critical Heat Flux (CHF) condition is obtained (i.e., until point 4 in Figure 3-7).

After obtaining the CHF data, the power input (or voltage supply to the cartridge heaters) is increased marginally (to obtain film boiling conditions) and then the power input is decreased progressively to prevent the apparatus from exceeding the maximum temperature set point (which is 200 °C, since this is the maximum rating for operating temperature of the cartridge heaters). In this study the pool boiling experiment system is controlled by leveraging the heat flux values (which is called as "power control"). In this strategy the temperature of the test surface increases rapidly during the transition from CHF to steady state film boiling conditions, because the continuous and stable vapor film that forms on the test surface effectively acts like a vapor-blanket (i.e., as a very effective insulating vapor film). Therefore once it reaches the film boiling regime, the voltage (and power) supply to the cartridge heater was reduced to prevent burnout and to protect the pool boiling experimental apparatus from damage. In other words the system transitions from point 4 to point 5' when the input power (voltage) to the cartridge heaters is held constant. This would lead to unacceptably high values of the wall superheat and is therefore avoided in the experiments. However, the system transitions from point 4 to the point 5 when the power (or voltage) input to the heaters is decreased. During this time the temperature and flow rate of the chilling fluid from the chiller unit was also modulated to maintain the desired temperature (and liquid subcooling) of the liquid pool. After steady state conditions are achieved for all the components in the

experimental apparatus, data acquisition is performed (the data is then utilized for post-processing, such as for plotting the boiling curve).

After steady state film boiling conditions are established, the power input (and voltage supply) to the cartridge heaters is reduced step by step until the Leidenfrost point condition is established (i.e., the system transitions from point 5 to point 8 in the boiling curve). After obtaining the experimental data at the Leidenfrost point, the system is cooled down and whole process is repeated again to check for the repeatability of the experiments.

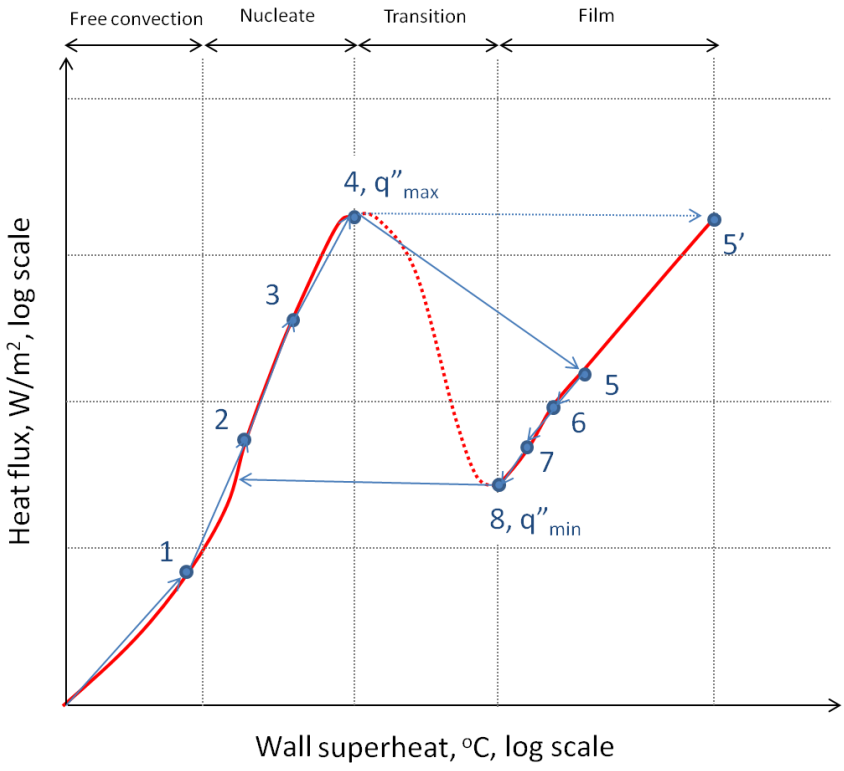

Figure 3-7 Schematic showing the experimental procedure for obtaining the boiling curve

4. EFFECT OF HEATER SIZE ON POOL BOILING

In this chapter, experimental validation of theoretical predictions (obtained using analytical models) will be performed for exploring the effect of heater size on the peak heat flux (i.e., Critical Heat Flux or "CHF") during pool boiling on a horizontal heater surface. Three different shapes of the flat horizontal heater are chosen for this investigation: the square heater, the rectangular heater and the circular heater. The analytical model for predicting the maximum (peak) heat flux for the square heater (or critical heat flux) was obtained from previous reports in the literature, and the analytical model was modified in this study for a rectangular and a circular heater. After development of the theoretical model, experimental validation of the theoretical prediction was performed in this study.

4.1. Analytical Approach

The theoretical approach for pool boiling phenomenon has been summarized in several heat transfer textbooks (e.g., [4]). The thermo-physical property values and parameters utilized in this study are listed in Table 4-1 [5]. The liquid properties can be obtained from product data sheet distributed by the manufacturer (3M Corp., Minneapolis, MN). In addition, the kinematic viscosity of the vapor phase was estimated from that of FC-72. Since PF-5060 has similar chemical composition and liquid-phase property values as FC-72, hence the density and the specific heat capacity values of FC-

72 in the vapor phase (available in the literature) has been used in this study for that of PF-5060.

Table 4-1 Thermophysical property values for PF-5060

Property	Units	Liquid	Vapor
Density	kg/m³	1610	13.01
Kinematic viscosity	m s	3.8 X 10^{-7}	8.8 X 10^{-8}
Specific Heat	J/kg K	1050	651
Thermal Conductivity	W/m K	0.057	0.0124
Latent Heat of Vaporization	J/kg	8800	N/A
Surface Tension	N/m	0.00848	N/A
Saturation Temperature	°C	56	N/A

The prediction of the wall heat flux (q_w'') as a function of wall superheat, $(\Delta T)_{sup}$ or $(\Delta T)_w$ or (ΔT), in the fully developed nucleate boiling regime is provided by the Rohsenow [86] correlation:

$$q_s'' = \mu_l h_{fg} \left[\frac{g(\rho_l - \rho_v)}{\sigma} \right]^{1/2} \left(\frac{C_{p.l} \Delta T}{C_{s.f} h_{fg} \, \mathrm{Pr}_l^n} \right)^3 \qquad (4\text{-}1)$$

Where μ is the viscosity, h_{fg} is the latent for liquid-vapor phase change, g is the acceleration due to gravity, ρ is the density, C_p is the specific heat capacity, σ is the

surface tension, Pr is the Prandtl number, $C_{s,f}$ is the surface constant, n is a constant, subscript l stands for liquid properties and subscript v stands for vapor properties.

In the film boiling region, Berenson correlation is typically used for predicting the wall heat flux or wall heat transfer coefficient (h) as a function of wall superheat [87] as:

$$h = 0.425\left[\frac{k_v^3 h_{fg}\rho_v g(\rho_l-\rho_v)}{\mu_l \Delta T\sqrt{\frac{g_0\sigma}{g(\rho_l-\rho_v)}}}\right]^{1/4} \tag{4-2}$$

The minimum and maximum heat flux values were predicted by Zuber [88, 89], as shown in equations (4-3) and (4-4), respectively as:

$$q''_{\min} = \frac{\pi^2}{60}\sqrt[4]{\frac{4}{3}}h_{fg}\rho_v\sqrt[4]{\sigma g\frac{(\rho_l-\rho_v)}{(\rho_l+\rho_v)^2}} \tag{4-3}$$

$$q''_{\max} = \frac{\pi}{24}h_{fg}\rho_v\left[\frac{\sigma g(\rho_l-\rho_v)}{\rho_v^2}\right]^{1/4}\left(\frac{\rho_l+\rho_v}{\rho_l}\right)^{1/2} \tag{4-4}$$

Where μ is the viscosity of liquid, h_{fg} is the latent heat of vaporization, g is gravitational acceleration, ρ is density, and σ is the surface tension. Subscript v refers to vapor properties, while the subscript l refers to liquid properties. These correlations are derived for "infinite heater" configurations where the heat flux values are not affected by the size of the heater. However, below a critical size (called the "small heater" regime), the heater size can affect the pool boiling heat flux values.

4.2. Experimental Results

4.2.1. Circular Heater

The boiling curve for a plain (flat) circular heater was obtained from experiments performed in this study and is plotted in Figure 4-1. For example, the Critical Heat Flux (CHF) is measured to be 8.32×10^4 W/m^2 at a temperature of 17.9^{o}C, and Minimum Heat Flux (MHF) is measured to be 4.03×10^4 W/m^2 at 75.2^{o}C for liquid subcooling of 10^{o}C. In addition, CHF is measured to be 7.39×10^4 W/m^2 at 19.7^{o}C, and MHF is measured to be 4.37×10^4 W/m^2 at 72.3^{o}C for subcooling of 5^{o}C. The experimental data obtained in this study for the circular heater configuration are listed in Appendix B.

As expected, the CHF values for subcooling of 10^{o}C are marginally higher than that of 5^{o}C. Moreover, in the nucleate boiling regime, the measured data is found to be consistent with the predictions from the Rohsenow correlation. Also for the film boiling regime, the measured data are found to be consistent with the predictions from the Berenson correlation. However, the experimental measurements for CHF values are significantly higher than the predicted values of CHF obtained from Zuber's correlations. This inconsistency will be discussed later in this chapter.

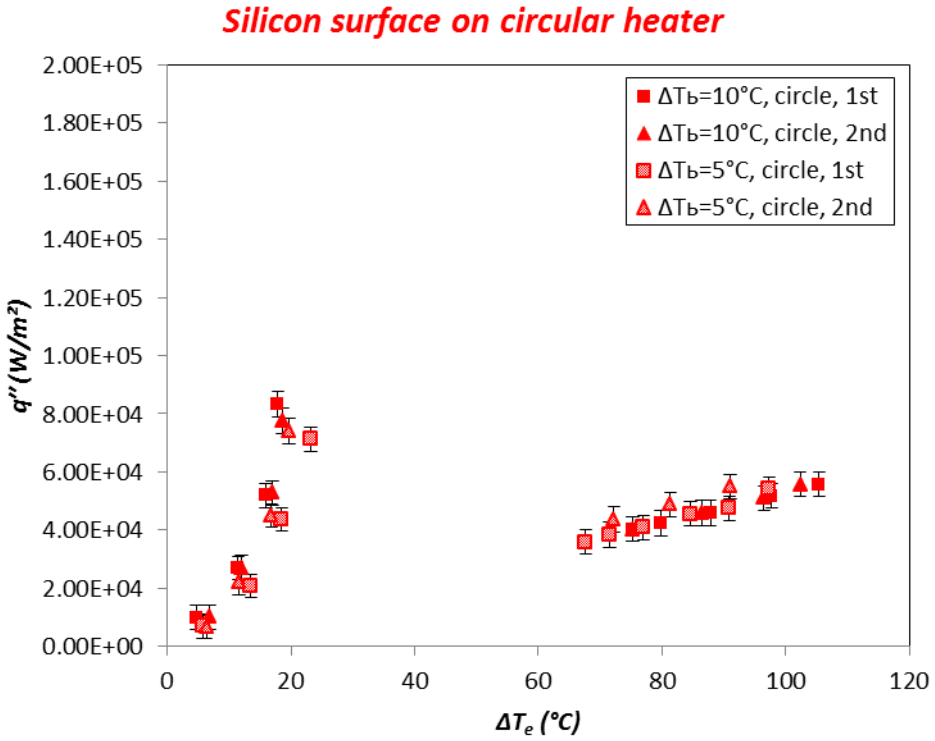

Figure 4-1 Pool boiling curve for a plain (flat) circular horizontal silicon wafer at different values of liquid subcooling.

Figure 4-2 shows the images obtained for different pool boiling regimes of test fluid (PF-5060) on a circular heater. In the nucleate boiling regime, as the wall superheat is increased, the bubble nucleation density, growth and departure (bubble release frequency as well as bubble diameter at departure) increases consistently. However the shape of bubble at departure (departure diameter, bubble release frequency, bubble departure site density) is not observed to change significantly with the increase in wall superheat during the film boiling regime.

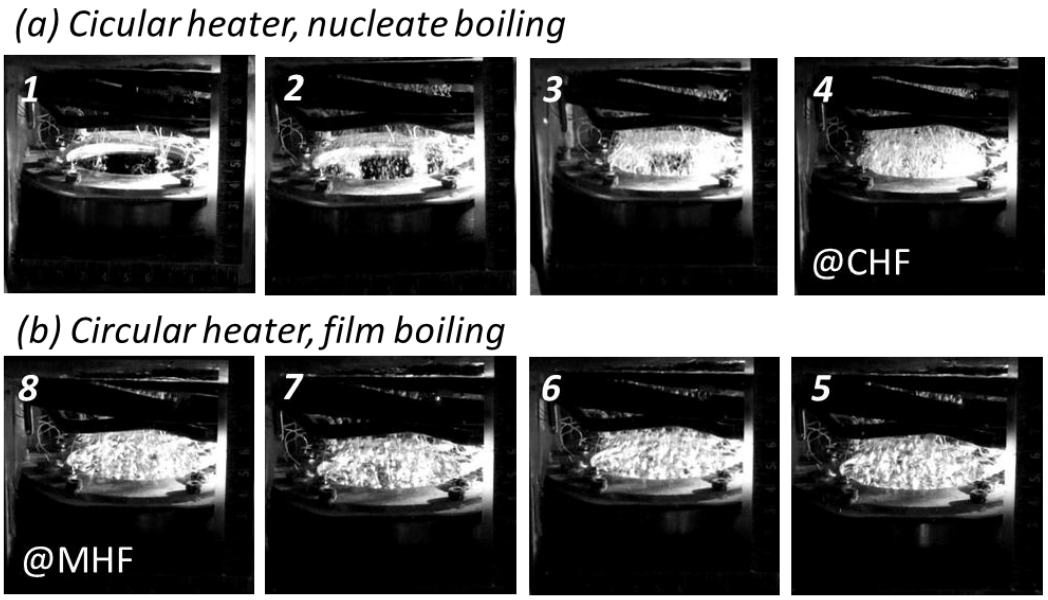

Figure 4-2 Images obtained from pool boiling experiments performed on a plain (flat) circular silicon wafer heater in horizontal orientation for a subcooling of 5 ^{o}C in the (a) nucleate boiling regime for Image Numbers 1 to 4, and (b) film boiling regime for Image Numbers 5 to 8

4.2.2. Rectangular Heater

The boiling curve for a plain (flat) rectangular heater was obtained from experiments performed in this study and is plotted in Figure 4-3. For example, the CHF is measured to be 1.42×10^{5} W/m^{2} at a wall superheat of 26.8^{o}C, and Minimum Heat Flux (MHF) is measured to be 7.49×10^{4} W/m^{2} at a wall superheat of 89.3^{o}C for a liquid subcooling of 10^{o}C. In addition, CHF is measured to be 1.33×10^{5} W/m^{2} at a wall superheat of 26.8^{o}C, and MHF is measured to be 7.05×10^{4} W/m^{2} at a wall superheat of 88.4^{o}C for liquid subcooling of 5^{o}C. The experimental data obtained in this study for the rectangular heater configuration are listed in Appendix B.

The measured data for the nucleate boiling regime are consistent with the predictions from the Rohsenow model. However, in contrast to the experimental data for wall heat flux obtained for the circular heater, the experimental data obtained for the rectangular heater have higher values than the predicted values obtained from the Berenson correlations for the film boiling regime. This will be discussed later in this chapter.

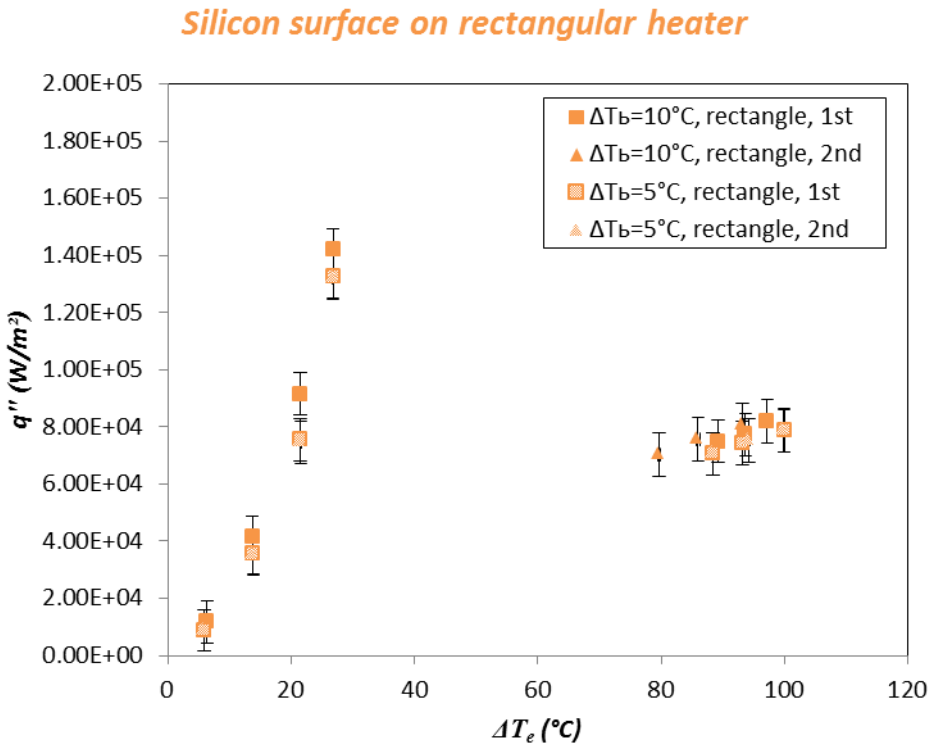

Figure 4-3 Pool boiling curve for a plain (flat) rectangular horizontal silicon wafer at different values of liquid subcooling.

Figure 4-4 shows the images obtained for different pool boiling regimes of test fluid (PF-5060) on a rectangular heater. In the nucleate boiling regime, as the wall superheat is increased, the bubble nucleation density, growth and departure (bubble release frequency as well as bubble diamter at departure) increases consistently. However the shape of bubble at departure (departure diameter, bubble release frequency, bubble departure site density) is not observed to change significantly with the increase in wall superheat during the film boiling regime.

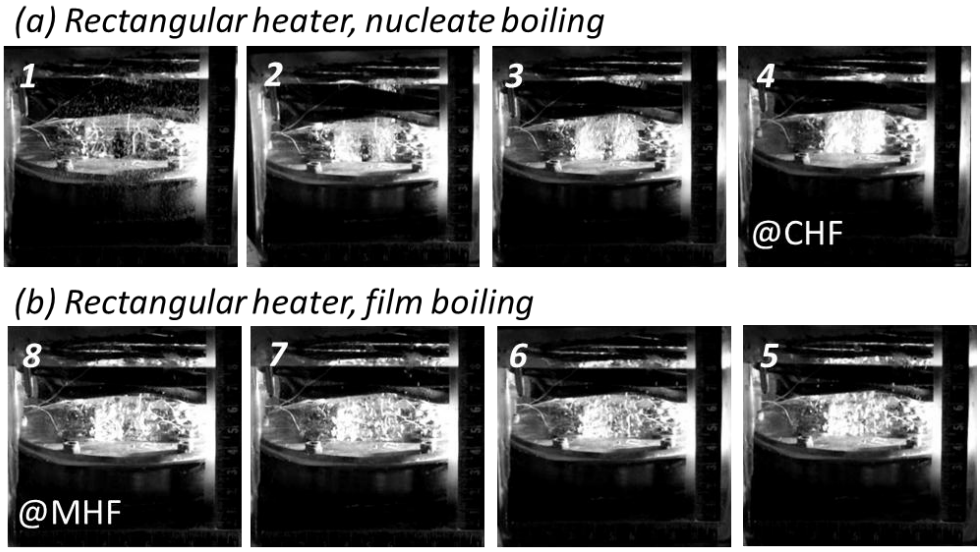

Figure 4-4 Images obtained from pool boiling experiments performed on a plain (flat) rectangular silicon wafer heater in horizontal orientation for a subcooling of 5 oC in the (a) nucleate boiling regime for Image Numbers 1 to 4, and (b) film boiling regime for Image Numbers 5 to 8.

The comparison for CHF and MHF values between circular and rectangular heaters at subcooling of 10^{o}C and 5^{o}C are summarized in Table 4-2. The pool boiling

curves for the circular and rectangular heaters are plotted in Figure 4-5 for comparison. The heat flux for the rectangular heater (with a smaller total area) is higher than that of the circular heater (which has a larger total area than that of the rectangular heater). The CHF and MHF values for the rectangular heater are higher than that of the circular heater.

In summary, boiling heat transfer experiments were performed on plain (flat) horizontal silicon wafer for both circular and rectangular heaters. The temperature of the silicon wafer surface was measured by using thin film thermocouple (TFT) array. The TFT thermocouples can read the surface temperature with high spatial and temporal precision at high speeds and with high spatial resolution. It is expected that the disruption of the transport mechanisms during pool boiling are minimized due to the use of nano-scale thickness of the temperature nanosensors (TFT array). For the circular and rectangular heaters, the experimental measurements are consistent with the Rohsenow correlation (for nucleate boiling regime) and the Berenson correlation (for film boiling regime). The result shows that the heat flux values for the rectangular heater are consistently higher than that of the circular heater for both the nucleate boiling regime and the film boiling regime.

Table 4-2 Summary of CHF and MHF for plain flat horizontal heaters (circular and rectangular shapes) at liquid subcooling of 10 °C and 5 °C

subcooling 10°C	Critical heat flux		Minimum heat flux	
	Wall superheat, °C	Heat flux, W/m²	Wall superheat, °C	Heat flux, W/m²
Circular heater	17.9	8.32E+04	75.2	4.03E+04
Rectangluar heater	26.8	1.42E+05	89.3	7.49E+04
subcooling 5°C	Critical heat flux		Minimum heat flux	
	Wall superheat, °C	Heat flux, W/m²	Wall superheat, °C	Heat flux, W/m²
Circular heater	19.7	7.39E+04	72.3	4.37E+04
Rectangular heater	26.8	1.33E+05	88.4	7.05E+04

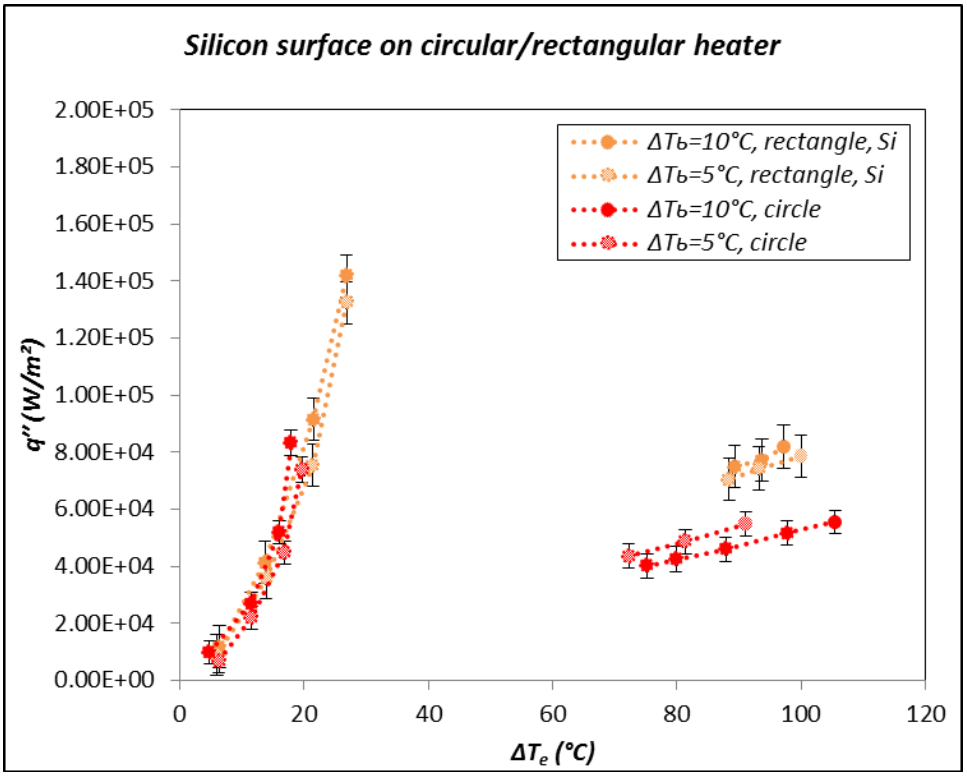

Figure 4-5 Comparison of pool boiling curves on a plain (flat) horizontal silicon wafer between circular and rectangular heater

4.3. Effect of Heater Size and Shape on Pool Boiling Heat Flux

For a fixed set of heater material properties the heat flux values in pool boiling can change with heater size or shape if the heater size is below a certain critical size. For a dimensionless heater size less than 5 (i.e., the ratio of heater characteristic dimension, L, to the "most dangerous" Taylor instability wavelength, λ_d, – corresponding to the highest growth rate of the instability waves), as shown in Figure 4-6, the pool boiling regime is considered to be in the "small heater" regime where the heat flux values scale inversely as the heater size. As the dimensionless heater size ($L' = L/\lambda_d$) increases progressively and exceeds the critical value of 5, the heater size has minimal effect on the pool boiling heat flux, and the pool boiling regime is therefore considered to be in the "large heater" or "infinite heater" configuration. During critical heat flux (CHF) condition, the vapor production marginally exceeds the vapor removal limit (due to terminal velocity of escaping bubbles) resulting in the merger of bubbles in the vertical direction causing the formation of vapor jets where the jets are modeled to self-organize in a certain "jet configuration". The fluid instabilities are believed to cause the jets to be arranged on a grid where the grid size scales as the Taylor instability wavelengths. The critical heat flux (CHF) condition during pool boiling is believed to be strongly dependent on this jet configuration. Figuratively speaking, if each jet delivers 1 unit power/ jet (if it is assumed, say, that it is 1 W/ jet) with a jet spacing of λ_d then for a given heater size *(*say, a square with size λ_d*)*, the critical heat flux increases as the heater size decreases (since one single jet per unit area still continues to dissipate the same amount of heat from the boiling surface even though the net area has gone down). On the

other hand, the CHF decreases as the heater size increases until the heater size reaches *(~1.5 λ_d)* The analysis shows that the heat flux can be lowered by as much as ~55% or increased by ~75% just my tweaking the heater size from a value of *(~1.5 λ_d)* to *(~0.75 λ_d)*, respectively.

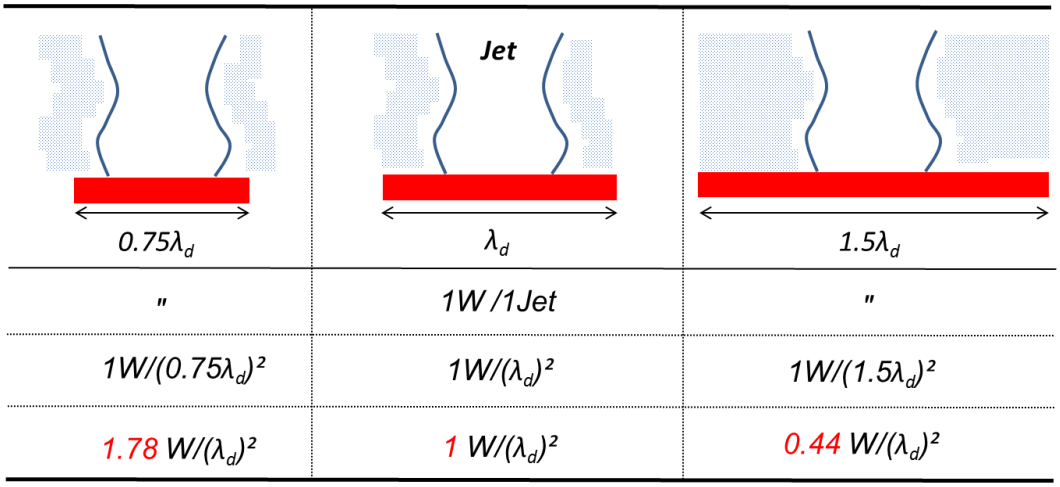

Figure 4-6 Schematic diagram of jet distribution at critical heat flux (CHF) assuming that each jet disspates 1 unit power/ jet (say 1W/jet)

The pool boiling heat flux values on a flat surface are therefore highly sensitive to the heater size and shape, especially in the "small heater" regime. However, in contemporary literature on pool boiling, the heater size and shape effects are often disregarded in the design of experiments, resulting in a large number of studies being reported in the "small heater' regime. As a result, it is not clear whether the pool boiling heat flux enhancement values reported in these studies are caused by the heater size/ shape issues or other experimental parameters (e.g., on heater with nanostructured

surfaces or heaters with nanocoatings). As a consequence, similar experiments performed by different research groups yield inconsistent results.

Assuming that the jets are spaced apart with a jet spacing of λ_d then, for a given heater size and shape it is possible to predict the total number of jets that can be formed at the CHF condition. This in turn enables the calculation (or prediction) of the critical heat flux values for a given set of fluid properties and heater size/shape. Prior reports in the literature enable the prediction of these values (number of jets, CHF, etc.) for horizontal flat (plain) heaters with square shape [5, 26, 27]. Theoretically it is possible to predict the number of jets for a given heater with specified dimensions, and therefore it is possible to predict the anticipated value of the critical heat flux (CHF). The analytical model for the number of jets for a square heater was reported by Lienhard et al. [90]. However, the analytical prediction for the number of jets on a circular or rectangular heater has not yet been reported in the literature. The experimental validation of the prediction for the number of crests (and by extension, the number of bubbles) formed during film boiling on a flat (plain) horizontal circular heater was performed by Banerjee and Dhir [26, 27]. They reported that the crests plotted using analytical predictions and the actual number observed in pool boiling (under high subcooling conditions) were in good agreement with each other for a circular heater (as shown at Appendix B).

As mentioned before, no reports were found in the literature on the effect of other shapes of heater (such as circular or rectangular heater), on the critical heat flux values. Hence, the motivation of this study was to explore the effect of heater size and shape on the CHF values, while keeping the heater and fluid material properties to tbe the same.

The aim of this study was to develop an analytical model for predicting the number of jets that may form on a heater with different shapes and sizes (e.g., rectangular and circular) and to extend this analysis to the prediction of the total heat flux during CHF condition on these heaters. The results show that the values for the peak heat flux are modulated dramatically as the heater size and shape are changed. The experimental validation is found to be consistent with the predictions from the analytical model.

4.4. Numerical Analysis

4.4.1. Analysis of Dimensionless Heat Flux

The "most dangerous" Taylor instability wavelength (λ_d) – corresponding to the instability wavelength that has the highest growth rate - can be obtained from the following equation (4-5),

$$\lambda_d = 2\pi\sqrt{\frac{3\sigma}{g(\rho_l - \rho_v)}} \tag{4-5}$$

Where, σ is the surface tension, g is the gravitational acceleration, ρ_l is the density of the liquid phase and ρ_v is the density of the vapor phase. Liquid PF-5060 was used in this study. The expression for the dimensionless critical heat flux (CHF) on a horizontal flat infinite heater configuration can be expressed using the following equation [14].

$$\frac{Q_{\max.infinite}}{Q_{\max.zuber}} = C \tag{4-6}$$

Where, C is a function of various variables (including instability wavelength) – corresponding to the experimental value ($Q_{max.infinite}$) and theoretical value estimated using Zuber's correlation ($Q_{max.zuber}$), respectively [88]. This equation can be also expressed as a function of the non-dimensional heater size ($L' = L / \lambda_d$) as:

$$\frac{Q_{\max}}{Q_{\max.zuber}} = f(L/\lambda_d) = f(L') \tag{4-7}$$

The value of this function can be estimated as a function of the total number of jets that are formed at the CHF condition. The heater area, A_H, typically can be expressed as the number of multiples of λ_d^2, which means that the actual value of CHF on a flat surface can be influenced by the total number of jets that are formed on the boiling surface. Finally the dimensionless heat flux on finite surface can be expressed using the following equation which was suggested by Lienhard [13].

$$\frac{Q_{\max}}{Q_{\max.zuber}} = C' \frac{N_j}{A_H / \lambda_d^2} \tag{4-8}$$

Where, N_j is the calculated value for the total number jets that are formed at the critical heat flux (CHF) condition and C' was predicted to be 1.14 [14].

4.4.2. Analysis of Total Number of Jet

The schematic diagram of the jet configuration on the flat plate with vertical side wall is shown in Figure 4-7. The finite heater contains a limited number of jets, and the pitch between the centers of two consecutive jets is most likely to be the most dangerous Taylor wavelength, λ_d. Moreover, due to the presence of vertical side walls, the

minimum distance between the center of the jet to that of the side walls, can be assumed to be $\lambda_d/2$. The total number of jets for these assumed configurations corresponding to the square heater and circular heater corresponding to the experiments performed in this study (and the values of the dimensionless critical heat flux) are listed in Appendix B.

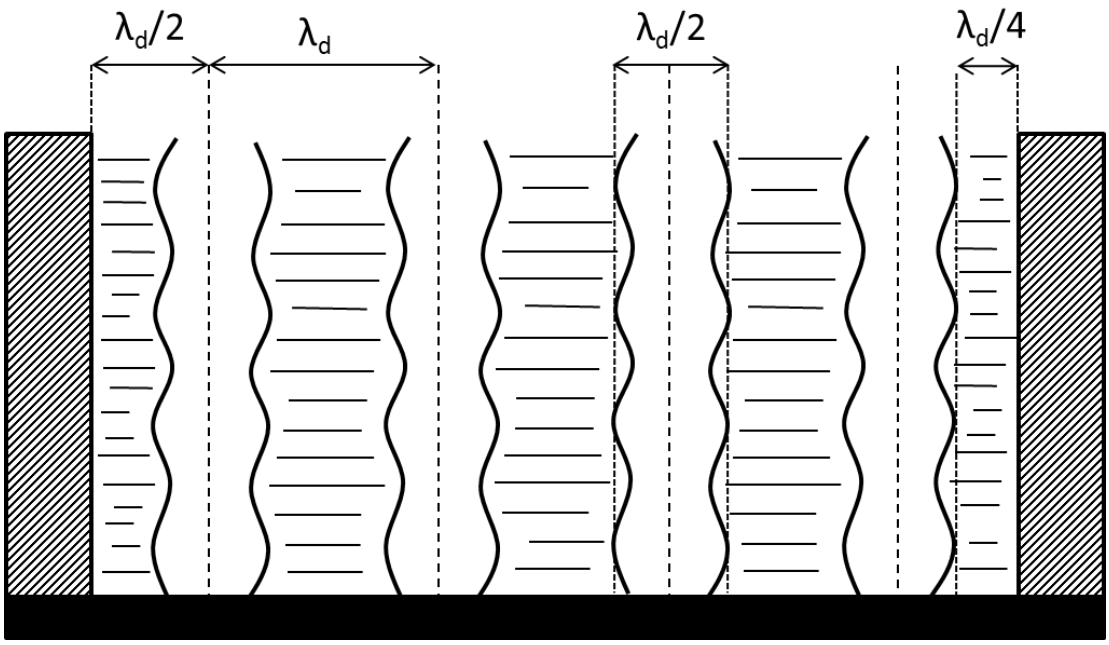

Figure 4-7 Horizontal flat plate jet configuration with vertical side wall

Note : reprinted with permission from " Peak pool boiling heat-flux measurements on finite horizontal flat plates" by J. H. Lienhard, V. K. Dhir, D. M. Riherd, Journal of Heat Transfer, 95(4), 477-482, 2001, Copyright 2001 by the American Society of Mechanical Engineers (ASME)

4.4.2.1. Total Number of Jets on Rectangular Heater

The jet configuration at CHF condition on the rectangular heater (corresponding to the heater that was used in the experiments performed in this study) is shown in Figure 4-8. This configuration was generated using a CAD program (Solidworks 2012,

Dassault Systems). For the dimension of the rectangular heater that was used in the experiments (31.75 mm × 58.73 mm), the maximum possible number of jets with a pitch of λ_d, is 21.

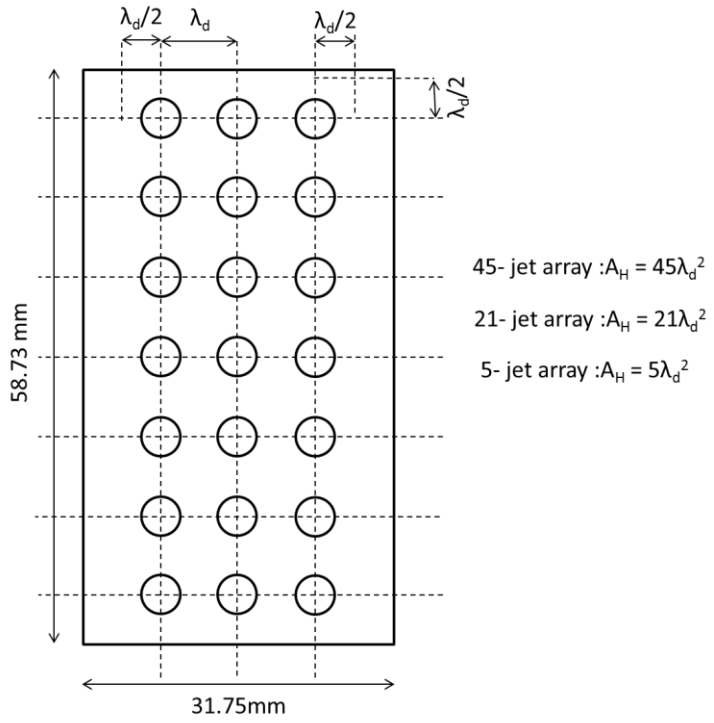

Figure 4-8 Schematic showing the rectangular heater with the total available number of jets and jet configuration.

4.4.2.2. Total Number of Jets on the Circular Heater

Determination of the jet configuration for circular heater is more complicated, since direct application of the Cartesian configuration to a circular (or cylindrical configuration) is not possible. The circular heater has a different jet configuration

compared to that of the square and rectangular heaters. The first step is to calculate the jet position and the number of jets in the cylindrical heater.

The analytical and numerical study for film boiling on horizontal flat-plate heaters with circular shapes (disc shaped heaters) has been reported in the literature [5, 26, 27]. The continuity equation for potential flows can be expressed as:

$$\nabla^2\phi = \frac{1}{r}\frac{\partial}{\partial r}\left(r\frac{\partial\phi}{\partial r}\right)+\frac{1}{r}\frac{\partial^2\phi}{\partial r^2}+\frac{\partial^2\phi}{\partial y^2}=0 \tag{4-9}$$

The solution of Equation (4-9) can be expressed by the following expression:

$$\phi(r,\theta,y,t) = C_{mn}J_m(k_n r)\cos(m\theta)e^{(-k_n\nu)}e^{(-i\omega_n t)} \tag{4-10}$$

Where, J_m is the Bessel function of the first kind of order m; Also, m and n are the eigenvalues of Equation (4-9); and k_n denotes the wavenumber corresponding to mode number n. At the radial location $r = r_n$, we can apply the boundary condition $u|_{\bar{\eta}} = 0$. This enables the derivation of the following set of equations:

$$\frac{\partial}{\partial r}J_m(k_n r)\Big|_{r=r_n} = 0 \tag{4-11}$$

$$k_n = \alpha_{m,n}/r_n \tag{4-12}$$

$$k_n = \frac{1}{l_o}\left[\left(\frac{m}{2r/l_o}\right)^2+1\right]^{\frac{1}{2}} \tag{4-13}$$

Where, $\alpha_{m,n}$ is the n^{th} root of the Bessel function.

The most probable configuration with the maximum number of crests (with the corresponding ring diameter in film boiling regime) was calculated and is summarized in

Table 4-3. From this investigation, the total number of jets in the nucleate boiling regime can also be estimated. In the film boiling regime on circular heaters, each crest is surrounded by two troughs on either side [87, 91, 92]. Hence, for nucleate boiling, close to the CHF condition, the total number of the jets was estimated to be half of the maximum possible number of crests. Moreover the cutoff size of the circular heater for a given ring number can be expressed in two different ways. One way can be expressed by $D_i + \lambda_d$, because the minimum gap between jet and side walls is known as $\lambda_d/2$. The other way is the average value of D_i and D_{i+1} (i.e., midway between two different rings of jets).

Table 4-3 The number of crests and the diameter of each ring on circular heater

Number of ring	Number of crest	Ring diameter, D, mm	Number of jet	$D+\lambda_d$, mm	$(D_i+D_{i+1})/2$, mm
1	4	7.25	2	15.26	13.58
2	8	19.92	6	27.93	28.41
3	15	36.90	14	44.91	44.59
4	21	52.28	24	60.29	56.98
5	27	61.67	38	69.68	67.03

For better understanding, schematic of the jet arrangements is shown in Figure 4-9. In the first method the circular heater size is represented as $D_i+\lambda_d$ and is plotted in the schematic using a dashed red line. Similar jet configuration is also illustrated on circular heater, but the circular heater size is represented as $(D_i+D_{i+1})/2$ and is plotted in the schematic using a dashed blue line.

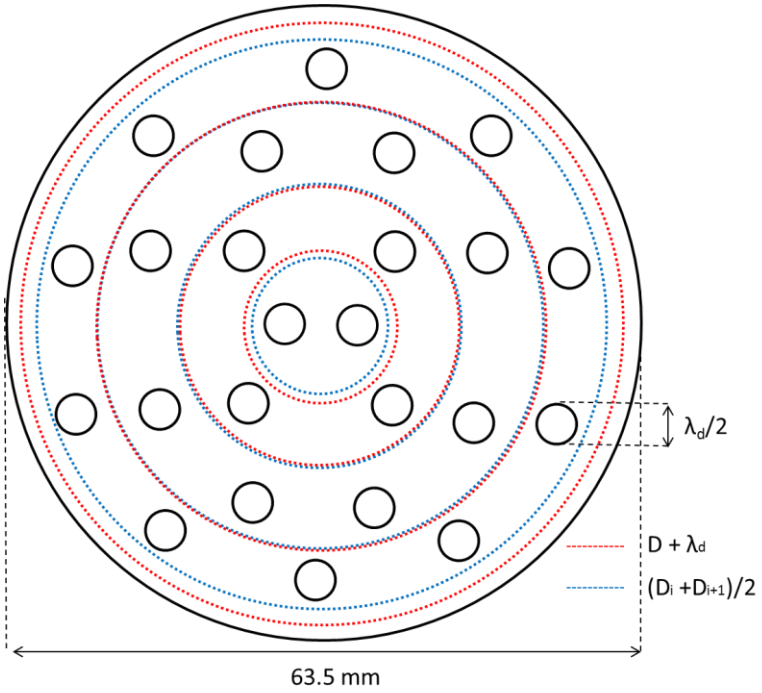

Figure 4-9 Total available number of jets on circular heater is represented using two different methods. Method 1: red dashed line representing $D + \lambda_d$. Method 2: blue dashed line representing $(D_i+D_{i+1})/2$

In addition, the dimensionless heater width can be obtained by the following equation (4-14), which is modified from equation (4-13) for rectangular or circular shape.

$$\frac{Q_{\max}}{Q_{\max.zuber}} = C\frac{N_j}{A_H / \lambda_d{}^2} = C\frac{N_j}{(L^*/\lambda_d)^2} \tag{4-14}$$

Here L^* is the corresponding length scale based on the total heater area. $L^*$is obtained using Equation (4-15) for rectangular heater, and Equation (4-16) for circular heater. The non-dimensional heater length, $L' = L^*/\lambda_d$ along with total number of jets is listed in Table 4-4 are also listed in the table.

$$L^* = \sqrt{W \times L} \tag{4-15}$$

$$L^* = \sqrt{\pi R^2} \tag{4-16}$$

Where, W represents the width and L represents the length for rectangular shaped heater flat horizontal heater; and R is the radius of the circular heater.

Table 4-4 L^* and L^*/λ_d for rectangular and circle heaters

Heater	Area, m²	L*, m	Nj	L*/λd
Rectangle	1.86E-03	4.32E-02	21	5.39
Circle	3.17E-03	5.63E-02	24	7.03

4.5. Results and Discussion

The theoretical prediction for the dimensionless peak heat flux values as a function of heater size is plotted in Figure 4-10 for a rectangular heater. As expected, the values for the dimensionless peak heat flux converge as the heater size is increased. Also the change in the value of dimensionless peak heat flux is larger for smaller sized heaters. Depending on the total number of jets (N_j) and the dimensionless heater size that is expressed in multiples of wavelength (L^*/λ_d), the dimensionless peak heat flux varies significantly – showing that for smaller heaters the heat flux values are strongly sensitive to the variation in heater size . Each line in the plot represents the value of dimensionless heat flux as a function of non-dimensional heater size at a fixed value of N_j. The experimental data point measured in this study is found to be consistent with the theoretical plots within the bounds of the measurement uncertainty.

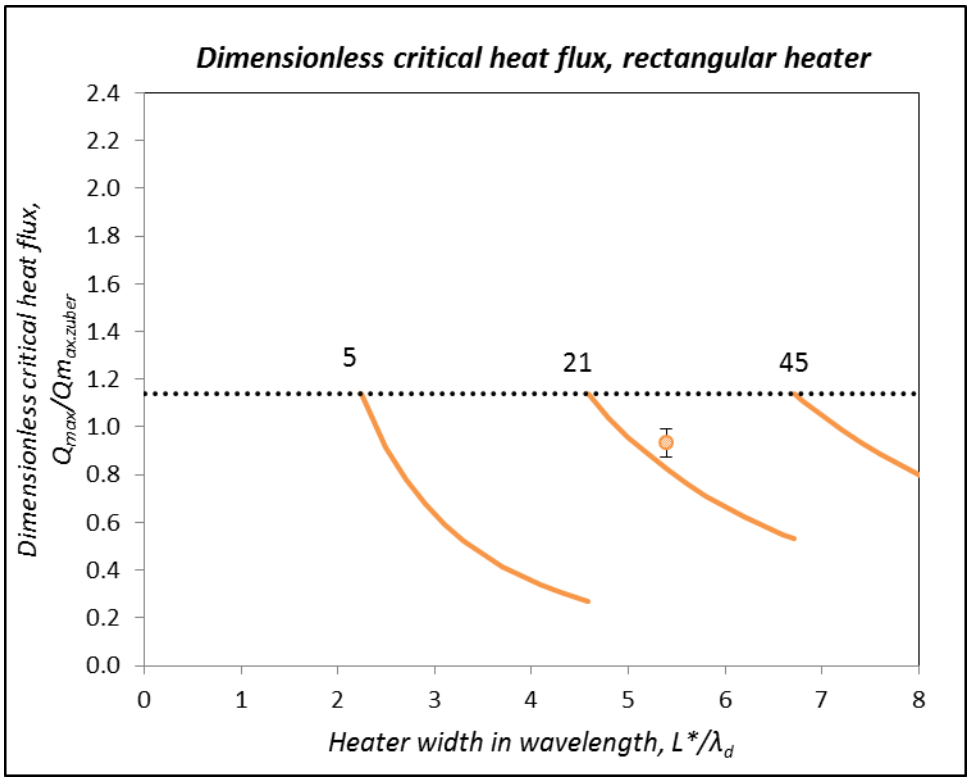

Figure 4-10 Dimensionless critical heat flux plotted as a function of dimensionless heater width for a rectangular heater. Numbers in the graph represent the total number of jets for each configuration.

The theoretical prediction for the dimensionless peak heat flux values as a function of heater size is plotted in Figure 4-11 for circular heater. Two sets of plots are shown in this figure for the two different analytical models that were explored in this study. The first model (plotted in Figure 4-11(a)) corresponds to a cutoff value of (D_i+λ_d). The second model (plotted in Figure 4-11(b)) corresponds to a cutoff value of (D_i+D_{i+1})/2. As expected, for both plots in Figure 4-11, the dimensionless peak heat flux converges as the heater size is increased. Also the change in the value of dimensionless peak heat flux is larger for smaller heater size. Depending on the total number of jets (N_j)

and the dimensionless heater width that is expressed in multiples of wavelength (L^*/λ_d), the dimensionless peak heat flux varies significantly – showing that for smaller heaters the heat flux values are strongly sensitive to the variation in heater size . Each line in the plot represents the value of dimensionless heat flux as a function of non-dimensional heater size at a fixed value of N_j. The experimental data point measured in this study is found to be consistent with the theoretical plot within the bounds of the measurement uncertainty for the first model, as shown in Figure 4-11(a). Therefore cutoff value of ($D_i + \lambda_d$) for (L^*/λ_d) is more appropriate for estimating the value of dimensionless critical heat flux.

To enable a proper comparison, the predictions for the dimensionless heat flux as a function of dimensionless heater size were plotted in Figure 4-12 for both rectangular and circular heater; along with the experimental data points for each case that were obtained in this study. The results show that for similar values of the total number of jets that are expected to form at the CHF condition the smaller heater (rectangular heater) affords a higher value of heat flux than that of the larger heater (circular heater).

Ironically, even though the size of circular heater is 1.7 times bigger than the size of rectangular heater, the critical heat flux of circular heater is smaller. Also, it might be noted that the total number of jets for the circular heater ($N_j = 24$) is marginally higher than that of the rectangular heater ($N_j = 21$).

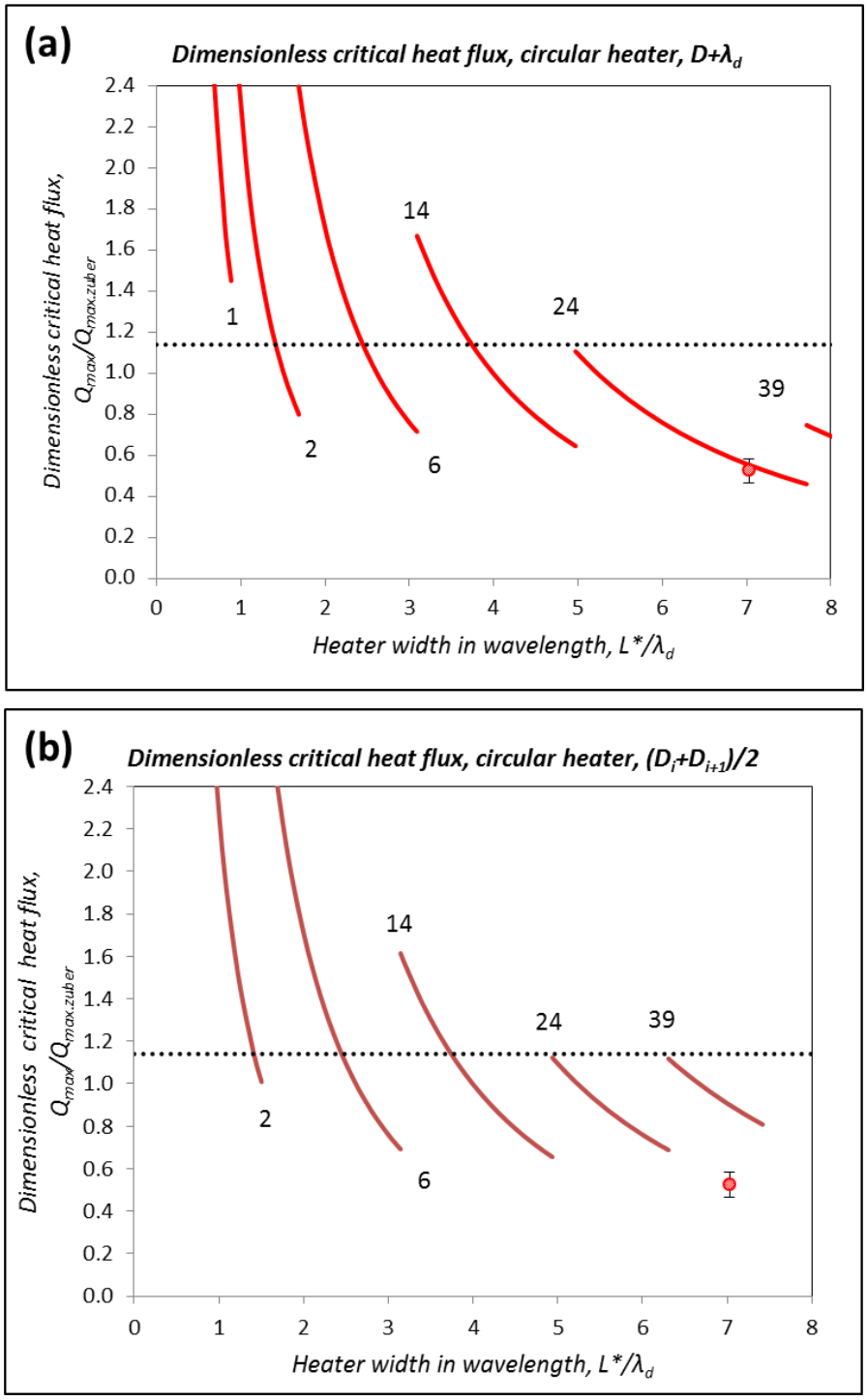

Figure 4-11 Dimensionless critical heat flux plotted as a function of dimensionless heater width for a circular heater. Numbers in the graphs represent the total number of jets for each configuration. The cutoff value of dimensionless diameter is: (a) ($D_i+\lambda_d$), and (b) (D_i+D_{i+1})/2.

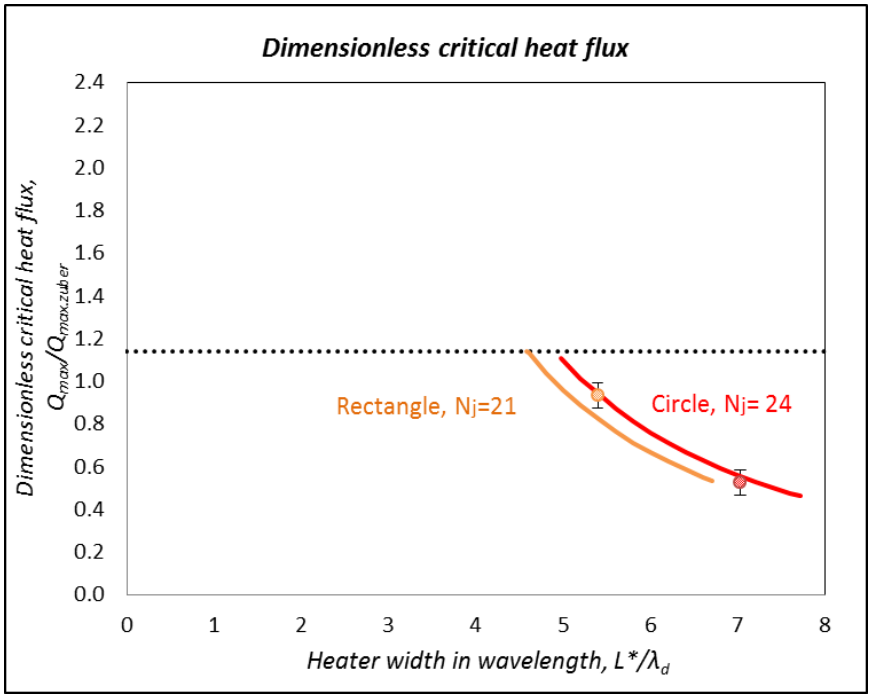

Figure 4-12 Dimensionless critical heat flux plotted as a function of dimensionless heater width for a circular heater. Numbers in the graphs represent the total number of jets for each configuration. The value of dimensionless cutoff diameter is (D_i+λ_d)

4.6. Summary

The sensitivity of the values of Critical Heat Flux (CHF) on the phenomena of vapor jet formation (by merger of departing vapor bubbles in the vertical direction near the CHF condition) as a function of heater size and thereby the number of jets - is explored in this chapter. The plausible jet configuration and maximum number of jets that can be accommodated on a heater were estimated based on the variation in the heater size and shape. It is remarkable that the dimensionless values of critical heat flux varies significantly with heater size and shape, especially for smaller size heaters. The

experimental results show that the predictions from the analytical model are consistent with the experimental measurements for both circular and rectangular heaters.

5. EFFECT OF HEATER MATERIAL PROPERTIES FOR POOL BOILING ON HORIZONTAL FLAT (RECTANGULAR) HEATER SURFACE

In this chapter, the pool boiling phenomena on a flat (rectangular) horizontal heater surface is explored. The effect of the material properties of the heater surface on the pool boiling performance were explored in this study. A flat, polished silicon wafer was used as the heater substrate and the surface was left uncoated (i.e., a semiconductor surface) or coated with ceramic (SiO_2) and metal (Chromel). This corresponds to different class of materials (i.e., semiconductor, ceramic and metal surfaces, respectively). The details of the fabrication procedure are discussed in Chapter 2.

The pool boiling literature is replete with experiments conducted on bare metal surfaces (typically on a copper surface), because of the ease of temperature measurement of the boiling surface using an array of wire-bead thermocouples that are placed a few millimeters below the exposed surface. However, in this study the temperature of the boiling surface is measured by using an array of thin film thermocouples (TFT) that are surface micromachined (using Physical Vapor Deposition/ PVD and the lift-off process) on the wafer substrate. This enables the use of non-metallic surfaces for pool boiling studies with measurement of surface temperature fluctuations with high precision (i.e., high-speed and high spatial density of measurements). The goal of the studies described in this chapter is to investigate the effect of the material properties of the heater surface on the pool boiling curve for various materials (i.e., metals, ceramic and semi-conductor materials).

5.1. Experimental Results

The pool boiling curves were obtained for two different shapes for the silica heaters: rectangular and circular. The experiments were performed for liquid subcooling of 10 ^{o}C and 5 ^{o}C.

5.1.1. Pool Boiling on Silica Heater

The pool boiling curve for the silicon dioxide surface is shown in Figure 5-1. In the figure, the green colored icons represent the experimental data for a rectangular heater and the gray colored icons represent the experimental data obtained from a circular heater. The trends for the pool boiling curve on the silica surface are similar to that of the silicon surface. The surface temperature measurements were performed using thin film thermocouple (TFT). The details of the pool boiling data, including 1st and 2nd run for each experiment for silica are shown in Appendix C. The results show that the rectangular heater (smaller area) enables higher values of pool boiling heat flux compared to that of the circular heater (which has a larger area) for both nucleate and film boiling.

5.1.2. Pool Boiling on Metal (Chromel) Heater

The pool boiling curve for experiments performed using a chromel heater surface is shown in Figure 5-2. The brown colored icon represents data from a rectangular heater and the pink colored icon represents data from a circular heater. The surface temperature measurements were performed using thin film thermocouple (TFT). The

details of the pool boiling data, including 1st and 2nd run for each experiment for Chromel are shown in Appendix C. The results show that the rectangular heater (smaller area) enables higher values of pool boiling heat flux compared to that of the circular heater (which has a larger area) for both nucleate and film boiling.

Hence, it can be concluded that regardless of the material composition of the heater surface, as discussed in the previous chapter, the heat flux for a rectangular heater (with smaller heater area) was higher than that of the circular heater (with larger heater area) for all three heater materials considered in this study: silicon, silica and chromel.

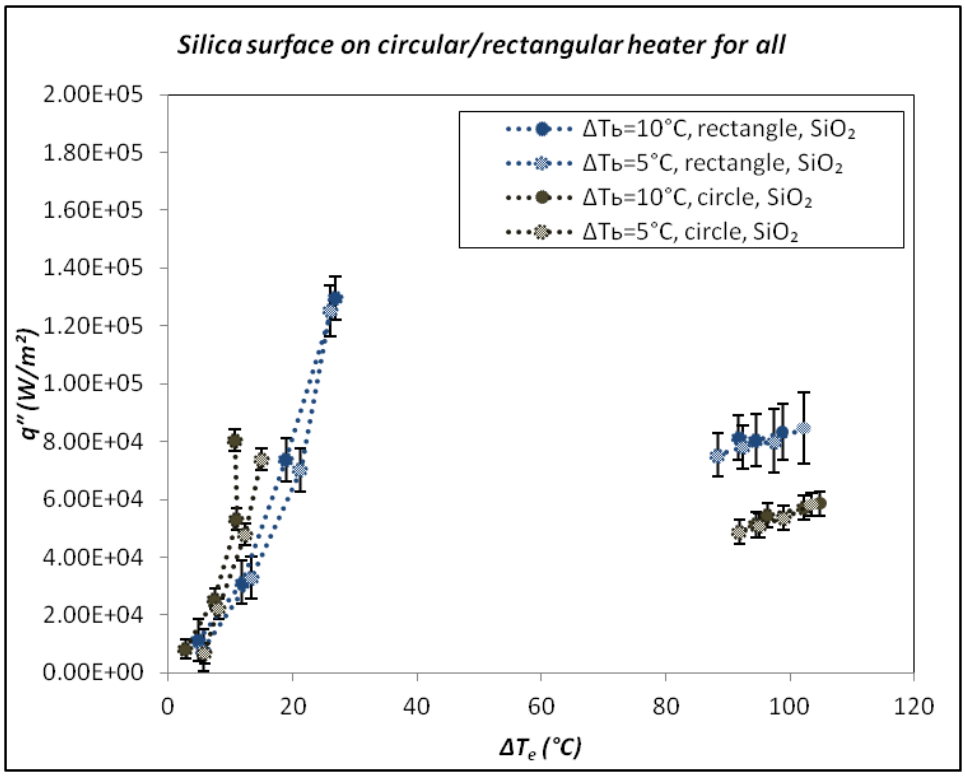

Figure 5-1 Pool boiling curve on rectangular and circular heater for a silica heater.

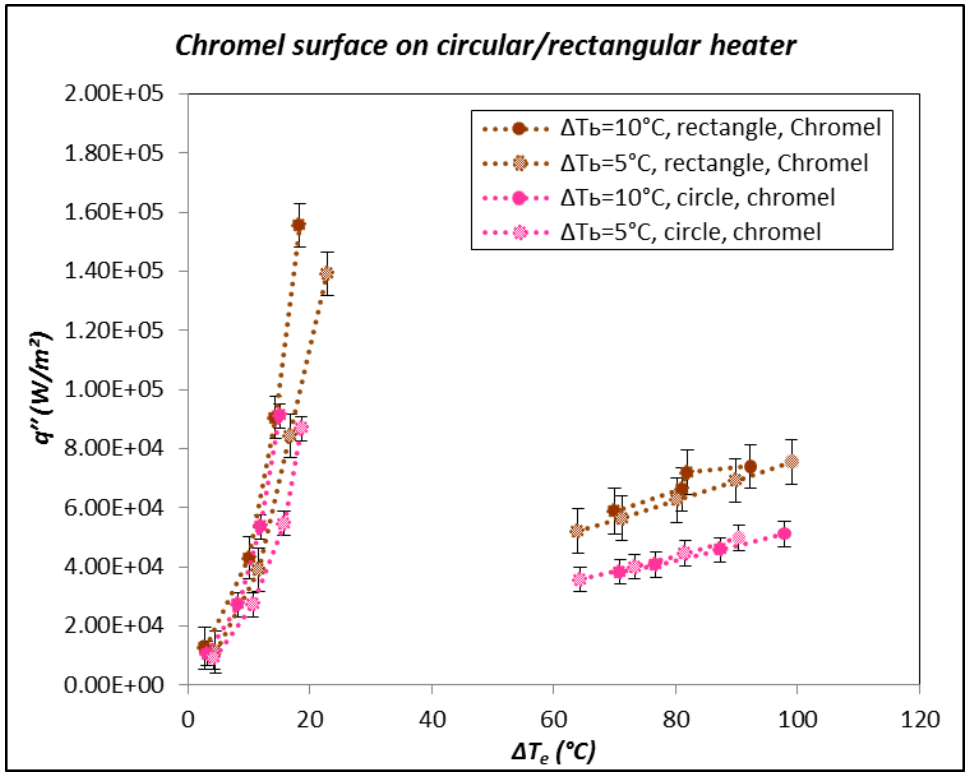

Figure 5-2 Pool boiling curve on rectangular and circular heater for a chromel heater.

5.2. Analysis and Discussion

5.2.1. Rectangular Heater

The experimental data used for plotting the pool boiling curve for rectangular heater with heater materials consisting of silicon, silica and chromel are shown in Figure 5-3. Regardless of the level of liquid subcooling the following trends are observed. First of all, the critical heat flux (CHF) for chromel surface is highest, while CHF for silicon is of intermediate level and CHF for silica is lowest. Secondly, the minimum heat flux (MHF) value for silica is highest, MHF for silicon is of intermediate value and MHF of

silica is lowest. Finally, when the pool boiling curves are compared for each value of liquid subcooling, the pool boiling curve for chromel is on the left side and that of silica is on the right while that of silicon is in the middle. This will be discussed in additional details in the following sections. The values of CHF and MHF for a rectangular heater for different heater materials are summarized in Table 5-1.

Critical heat flux (CHF) values were normalized by that of silica and plotted in Figure 5-4(a). Similarly the values of MHF were normalized by that of silica and plotted in Figure 5-4(b). In these figures, darker colors represent subcooling of 10 ^{o}C and lighter color represents subcooling of 5 ^{o}C; while orange color represents CHF and blue color represents MHF. The CHF of silicon heater is higher than that of silica heater by 9% for liquid subcooling of 10 ^{o}C and 7% for liquid subcooling of 5 ^{o}C. The CHF of chromel surface is higher than that of silica surface by 20% for liquid subcooling of 10 ^{o}C, and by 6% for liquid subcooling of 5 ^{o}C. In addition, The MHF of silicon surface is smaller than that of silica surface by 14% for liquid subcooling of 10 ^{o}C, and by 7% for liquid subcooling of 5 ^{o}C. The CHF of chromel is larger than that of silica by 23% for liquid subcooling of 10 ^{o}C, and by 32% for liquid subcooling of 5 ^{o}C.

The results show a consistent trend. The CHF values are highest for metal (chromel) surface, lowest for ceramic surface (silica) and of intermediate value for semiconductor (silicon) surface. The MHF values are highest for ceramic (silica) surface, lowest for metal (chromel) surface, and of intermediate value for semiconductor (silicon) surface.

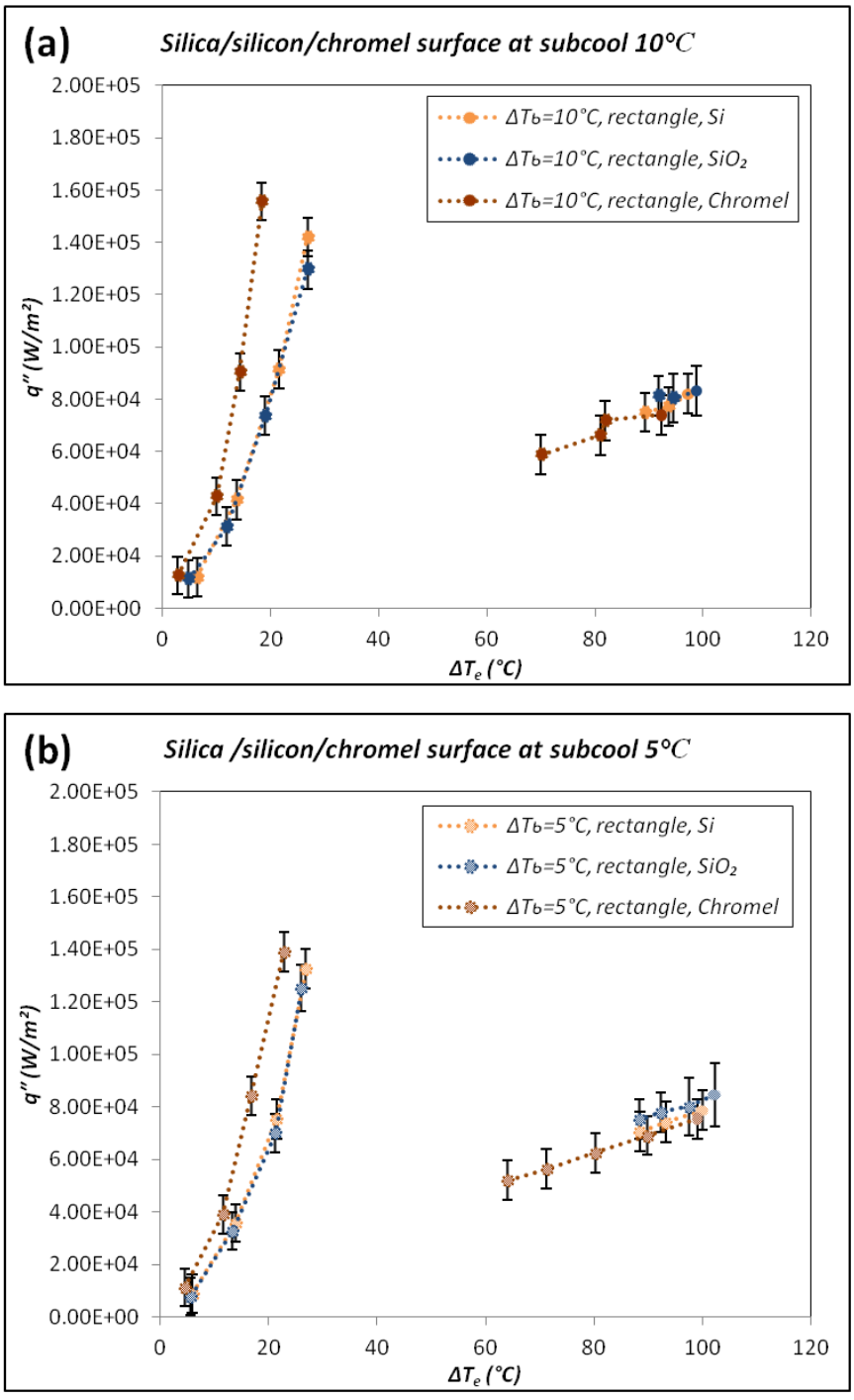

Figure 5-3 Pool boiling curve for a rectangular heater for different heater materials (silicon, silica, and chromel) at liquid subcooling of: (a) 10°C; and (b) 5°C.

Table 5-1 CHF and MHF values along with the corresponding values of wall superheat for a rectangular heater at liquid subcooling of 10 °C and 5 °C

Rectangular heater subcooling 10°C	Critical heat flux		Minimum heat flux	
	Wall superheat, °C	Heat flux, W/m²	Wall superheat, °C	Heat flux, W/m²
SiO_2	26.8	1.30E+05	91.7	8.13E+04
Si	26.8	1.42E+05	89.3	7.49E+04
Chromel	18.4	1.56E+05	70.0	5.88E+04
Rectangular heater subcooling 5°C	Critical heat flux		Minimum heat flux	
	Wall superheat, °C	Heat flux, W/m²	Wall superheat, °C	Heat flux, W/m²
SiO_2	26.0	1.25E+05	88.4	7.53E+04
Si	26.8	1.33E+05	88.4	7.05E+04
Chromel	22.8	1.39E+05	64.0	5.21E+04

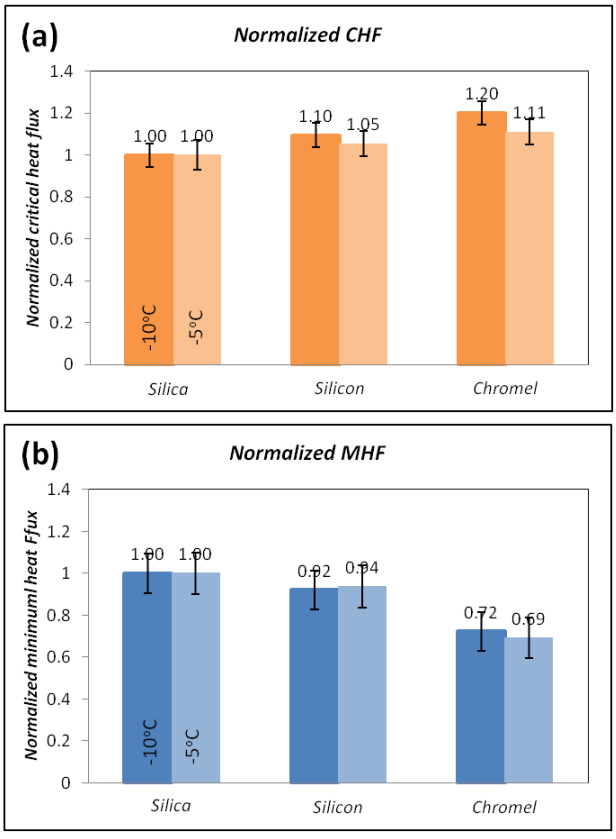

Figure 5-4 CHF and MHF values at liquid subcooling of 10 °C and 5 °C for rectangular heater: (a) normalized CHF based on that of silica heater surface; and (b) normalized MHF based on that of silica heater surface.

The wall superheat values for CHF and MHF condition were also investigated and are plotted in Figure 5-5. Figure 5-5(a) shows the wall superheat temperature at the CHF point (T_{CHF}), and Figure 5-5(b) shows the wall superheat temperature at MHF point (T_{MHF}). The result shows that T_{CHF} for silica is highest, T_{CHF} for chromel is the lowest and T_{CHF} for silicon is of intermediate magnitude. T_{MHF} for silica is highest, T_{MHF} for chromel is lowest and T_{MHF} for silicon is of intermediate value. The results show that the CHF and MHF conditions are affected by the material properties of the heater surface.

The difference between the values of T_{MHF} and T_{CHF} was plotted in Figure 5-5(c). The figure shows the temperature range for the transition boiling regime. The chromel surface has the smallest temperature (or wall superheat) range for the transition regime, and silica has the largest temperature (or wall superheat) range for the transition regime. The range of the transition regime is more sensitive to the value of T_{MHF} rather than that of T_{CHF}, since the variation in T_{MHF} is much larger than that of T_{CHF} as the material property of the heater is changed.

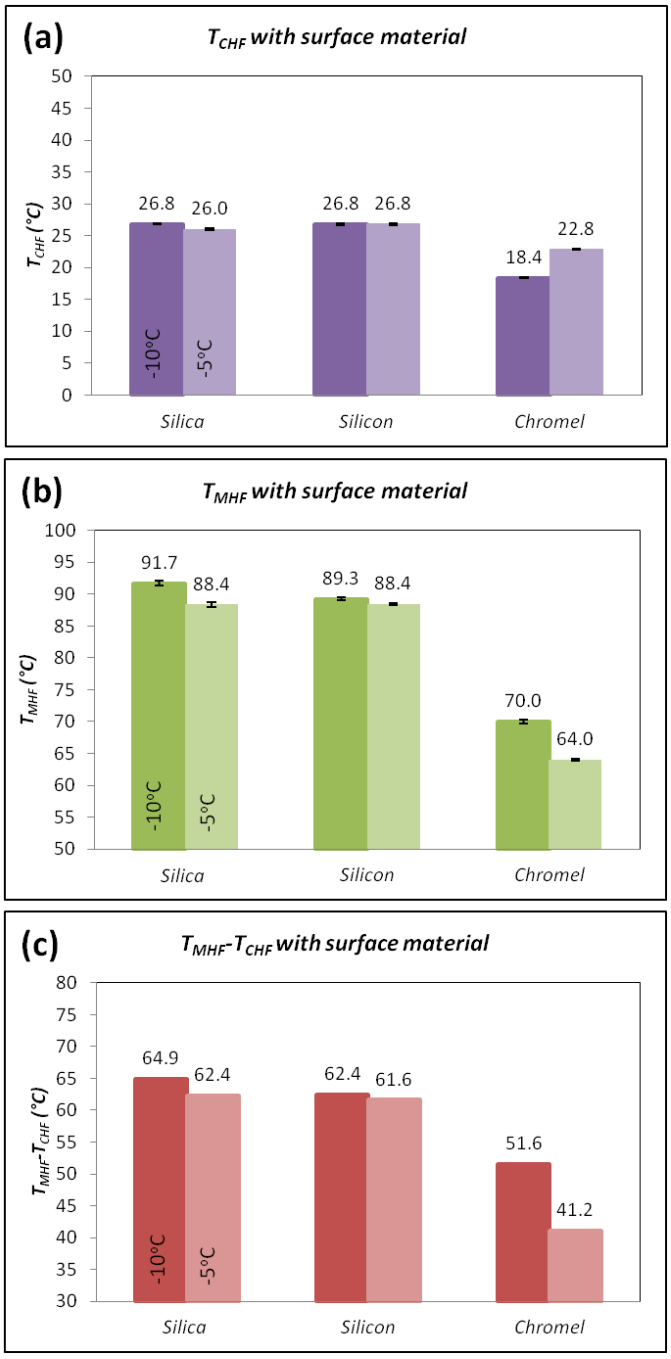

Figure 5-5 Wall superheat temperature for rectangular heater (a) at CHF point and (b) MHF point. (c) Temperature difference between T_{MHF} and T_{CHF} showing the range of temperature (or wall superheat) for the transition boiling regime.

5.2.2. Circular Heater

Similar investigations were also conducted for circular heater configuration. Figure 5-6 shows the experimental pool boiling curve for the silicon, silica and chromel surface for a circular heater configuration. Similar trends are observed for the circular heater case to that of the rectangular heater case. When considering CHF values, it is highest for that of chromel, lowers for that of silica and of intermedicate value for that of silicon. When considering the MHF values, it is highest for that of silica, lowest for that of chromel and of intermediate value for that of silicon. The CHF and MHF values as well as the corresponding wall superheat values are listed in Table 5-2 for liquid subcooling of 5 ^{o}C and 10 ^{o}C.

Critical heat flux (CHF) values were normalized by that of silica and plotted in Figure 5-7. Similarly the values of MHF were normalized by that of silica and plotted in Figure 5-7(b). In these figures, darker colors represent subcooling of 10 ^{o}C and lighter color represents subcooling of 5 ^{o}C; while orange color represents CHF and blue color represents MHF. The CHF of silicon heater is higher than that of silica heater by 3% for liquid subcooling of 10^{o}C. The CHF of chromel surface is higher than that of silica surface by 13% at liquid subcooling of 10^{o}C, and by 17% at liquid subcooling of 5^{o}C. In addition, the MHF of silicon surface is smaller than that of silica surface by 22% at liquid subcooling of 10^{o}C, and by 11% for liquid subcooling of 5^{o}C. The CHF of chromel is smaller than that of silica by 25% for liquid subcooling of 10^{o}C, and by 27% for liquid subcooling of 5^{o}C.

The results show a consistent trend. The CHF values are highest for metal (chromel) surface, lowest for ceramic surface (silica) and of intermediate value for semiconductor (silicon) surface. The MHF values are highest for ceramic (silica) surface, lowest for metal (chromel) surface, and of intermediate value for semiconductor (silicon) surface.

The wall superheat values for CHF and MHF condition were also investigated and are plotted in Figure 5-8. Figure 5-8(a) shows the wall superheat temperature at the CHF point (T_{CHF}), and Figure 5-8(b) shows the wall superheat temperature at the MHF point (T_{MHF}). The result shows that T_{CHF} for silica is highest, T_{CHF} for chromel is the lowest and T_{CHF} for silicon is of intermediate magnitude. T_{MHF} for silica is highest, T_{MHF} for chromel is lowest and T_{MHF} for silicon is of intermediate value. The results show that the CHF and MHF conditions are affected by the material properties of the heater surface. The difference between the values of T_{MHF} and T_{CHF} was plotted in Figure 5-8(c). The figure shows the temperature range for the transition boiling regime. The chromel surface has the smallest temperature (or wall superheat) range for the transition regime, and silica has the largest temperature (or wall superheat) range for the transition regime. The range of the transition regime is more sensitive to the value of T_{MHF} rather than that of T_{CHF}, since the variation in T_{MHF} is much larger than that of T_{CHF} as the material property of the heater is changed. These results are similar to that of the rectangular case.

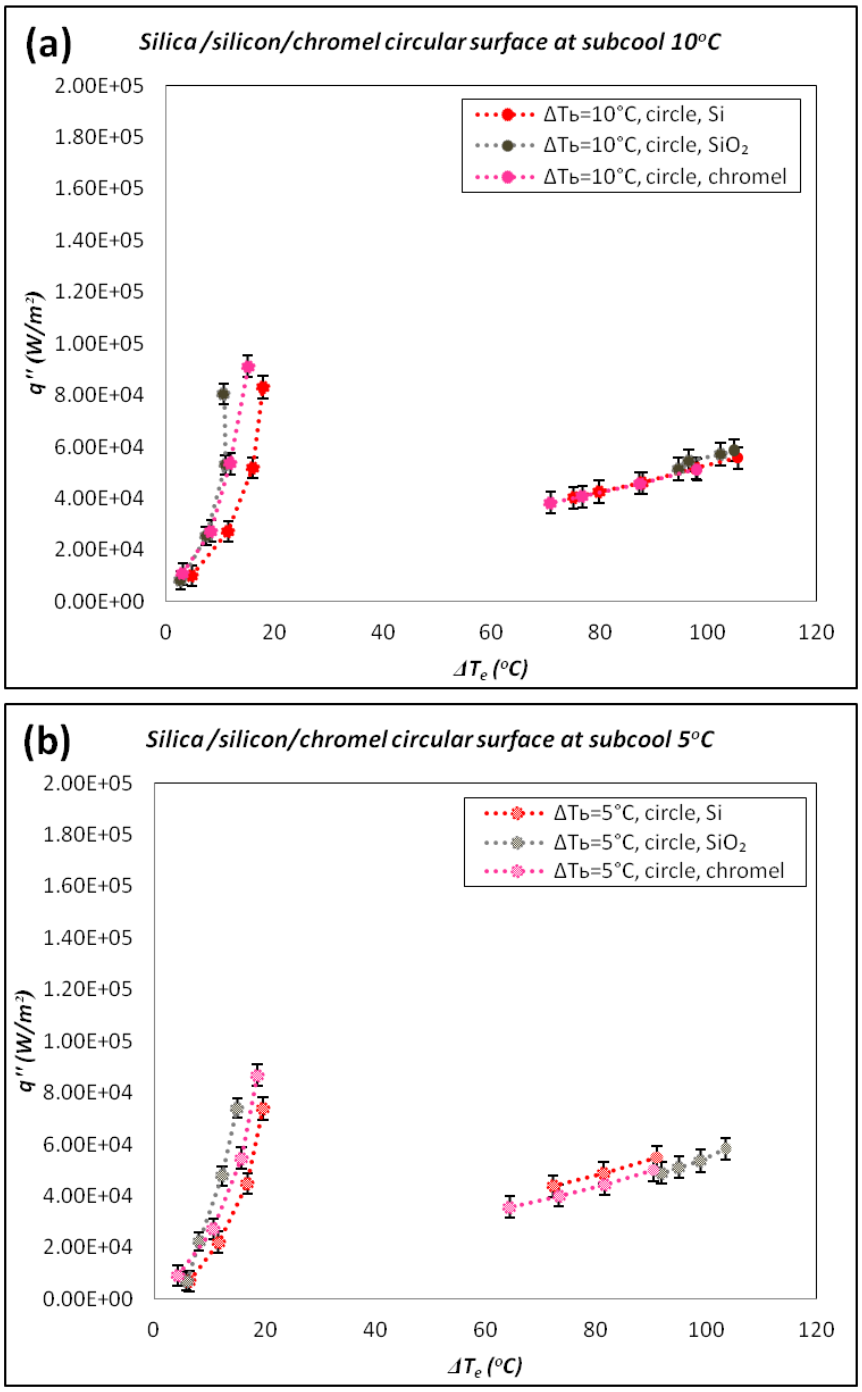

Figure 5-6 Pool boiling curve for a circular heater for different heater materials (silicon, silica, and chromel) at liquid subcooling of: (a) 10°C; and (b) 5°C.

Table 5-2 CHF and MHF values along with the corresponding values of wall superheat for a circular heater at liquid subcooling of 5 °C and 10 °C.

Circular heater subcooling 10°C	Critical heat flux		Minimum heat flux	
	Wall superheat, °C	Heat flux, W/m²	Wall superheat, °C	Heat flux, W/m²
SiO_2	10.7	8.05E+04	94.5	5.13E+04
Si	17.9	8.32E+04	75.2	4.03E+04
Chromel	15.1	9.10E+04	70.9	3.83E+04
Circular heater subcooling 5°C	Critical heat flux		Minimum heat flux	
	Wall superheat, °C	Heat flux, W/m²	Wall superheat, °C	Heat flux, W/m²
SiO_2	15.0	7.40E+04	91.9	4.89E+04
Si	19.7	7.39E+04	72.3	4.37E+04
Chromel	18.6	8.68E+04	64.3	3.56E+04

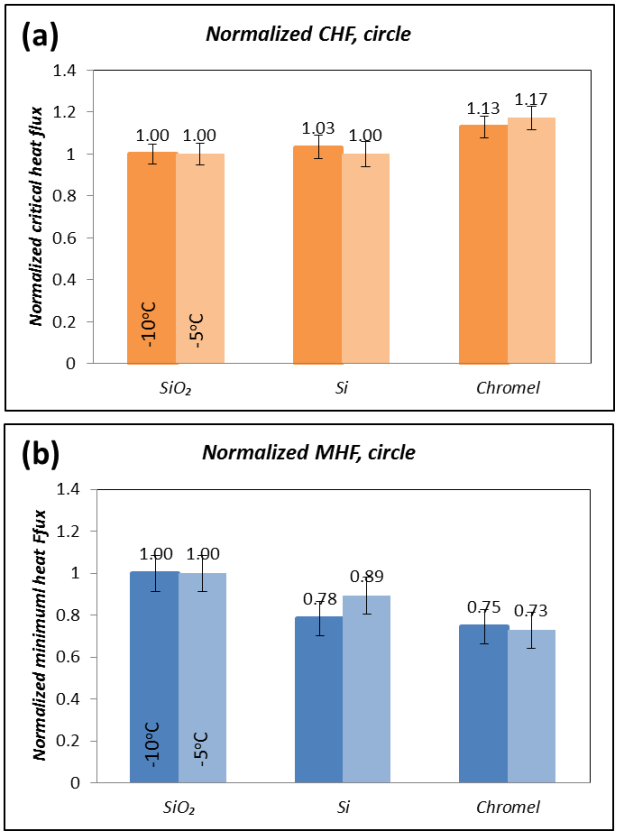

Figure 5-7 CHF and MHF values at liquid subcooling of 10 °C and 5 °C for circular heater: (a) normalized CHF based on that of silica heater surface; and (b) normalized MHF based on that of silica heater surface.

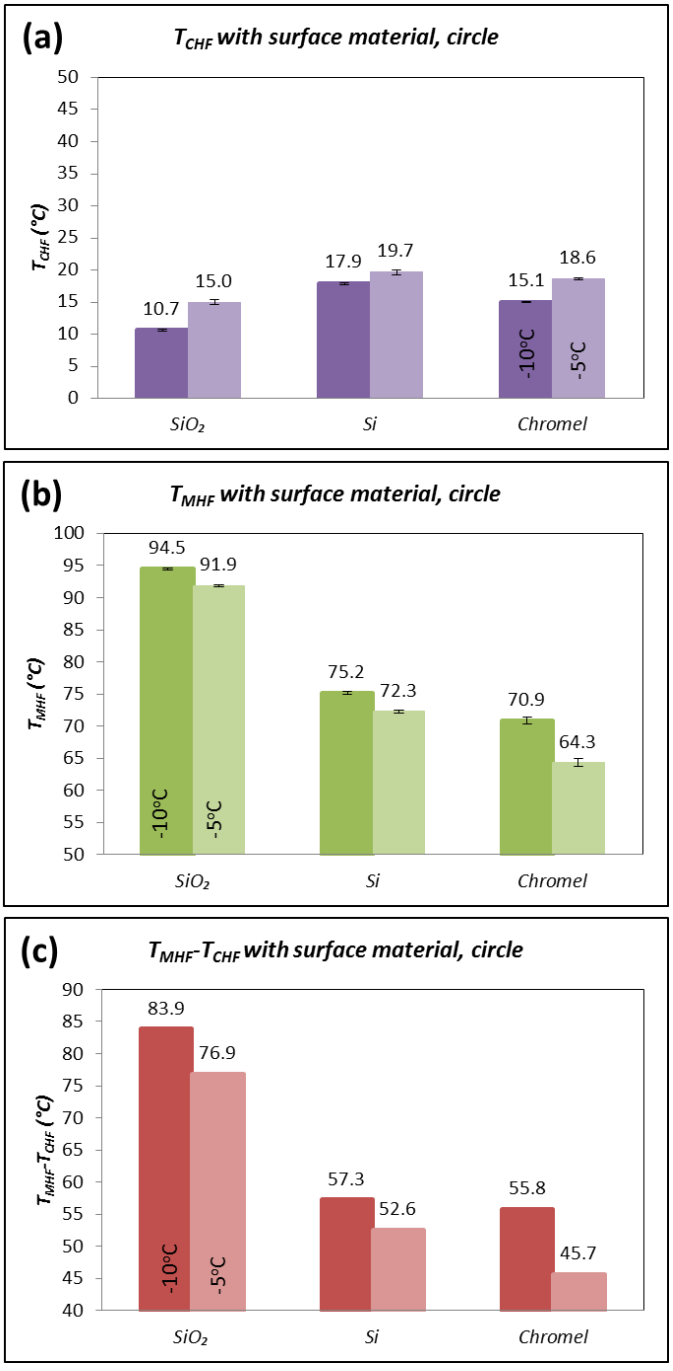

Figure 5-8 Wall superheat temperature for circular heater (a) at CHF point and (b) MHF point. (c) Temperature difference between T_{MHF} and T_{CHF} showing the range of temperature (or wall superheat) for the transition boiling regime.

5.3. Analysis of Dimensionless Heat Flux for Different Surface Materials

The dimensionless heat flux on flat horizontal surface for silica, silicon and chromel are plotted in Figure 5-9. As expected, the dimensionless heat flux value is highest for chromel surface regardless of the shape of the heater.

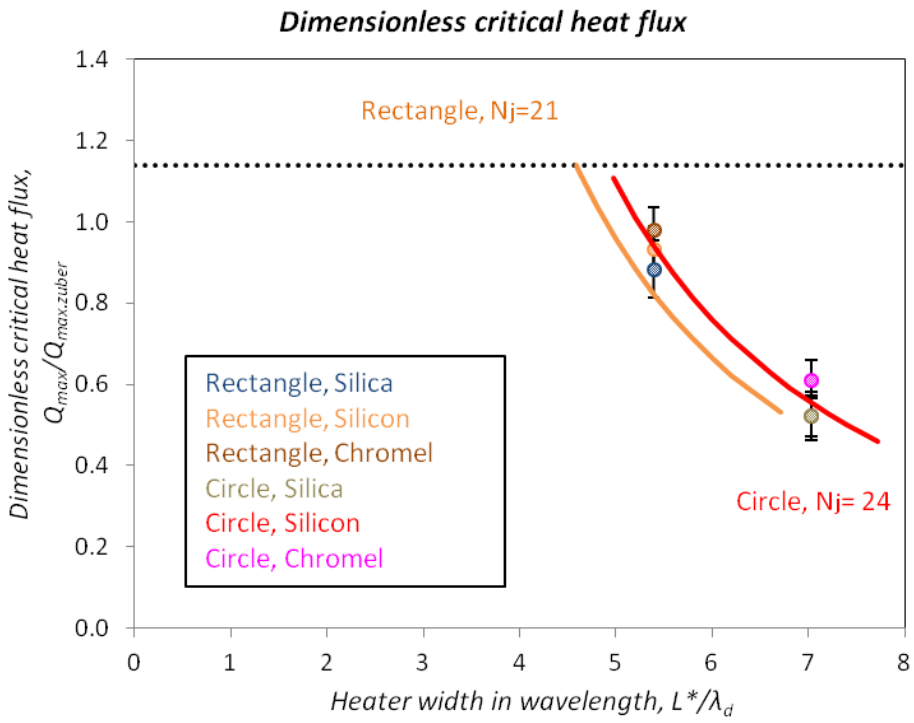

Figure 5-9 Plot of dimensionless critical heat flux for heaters with different surface materials

5.4. Contact Angle

The contact angle (static and dynamic) of the test fluid with the heater surface is one of the significant parameters that influences the values of the pool boiling heat flux

[93]. For example, higher critical heat flux values can be obtained by decreasing the contact angle (e.g., by adding surfactants at very minute concentration). Therefore, the contact angles of test fluid (PF-5060) on the different heater surfaces (silica, silicon and chromel) were investigated in this study.

The image of PF-5060 droplet on the heater surface (for the purpose of measuring the contact angle) was obtained before and after the pool boiling experiment. To measure the contact angle, digital image processing of the picture of the droplet was performed (using the freeware tool Image J). Figure 5-10 shows an example of the measurement procedure for the contact angle, where three different measurements of the contact angle for a droplet was conducted for each case. The measured values of the contact angle are shown in Figure 5-10(b). For silicon surface after boiling, the contact angle is measured 14°, 13.6° and 13.6°, which means the average contact angle is 13.8° and standard deviation is 0.2°.

Contact angle measurements for silica, silicon, and chromel surface before and after pool boiling experiments are shown in Figure 5-11. The contact angle measurements for silica, silicon and chromel heater surfaces are listed in Table 5-3, where the measurements were performed before and after the pool boiling experiments.

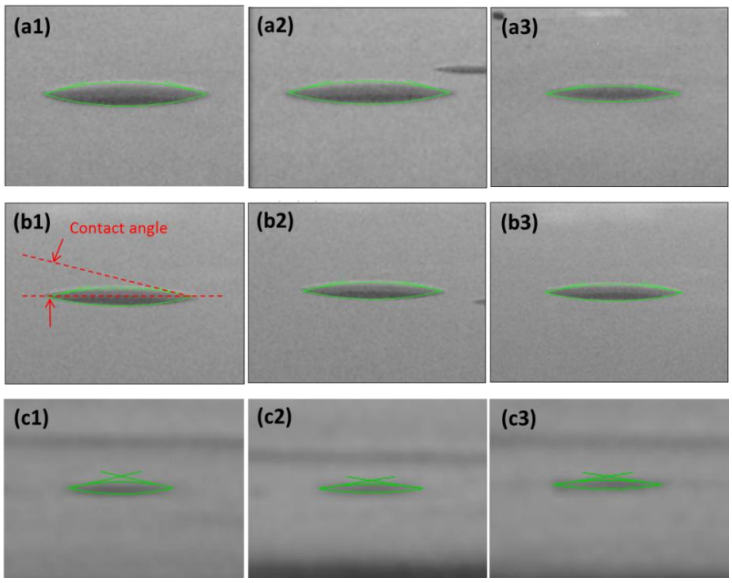

Figure 5-10 Contact angle measurement for PF-5060 droplets after boiling experiment for (a) Silica, (b) Silicon and (c) Chromel surface. Contact angle was measured 3 times for each surface. For example on the silicon heater surface, (b1) 14.070° (b2) 13.604° (b3) 13.590° : therefore average contact angle is 13.8° and the standard deviation is 0.22°. Contact angle was measured by using the freeware tool "Image J".

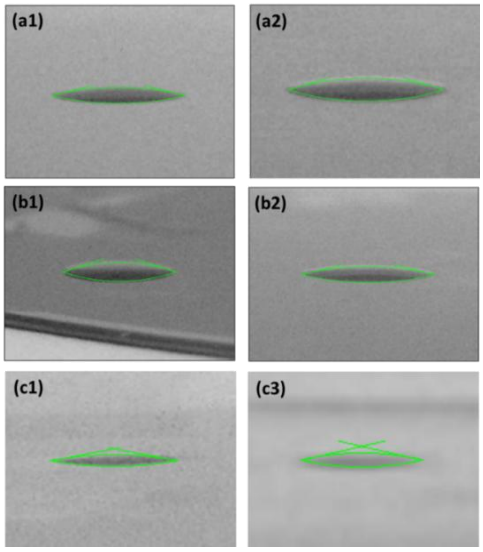

Figure 5-11 Contact angle measurement for PF-5060: silica before boiling (a1), and after boiling (a2); silicon surface before boiling (b1), and after boiling (b2); chromel surface before boiling (c1) and after boiling (c2).

Table 5-3 Summary of contact angle measurements

Material	Before pool boiling		After pool boiling	
	Average, °	STD	Average, °	STD
Silica	17.5	0.18	19.2	1.54
Silicon	17.8	0.75	13.8	0.22
Chromel	9.8	1.40	10.3	1.87

The contact angle (static and dynamic) of the test fluid with the heater surface is one of the significant parameters that influences the values of the pool boiling heat flux and it has been reported in the literature that higher values of critical heat flux were obtained for heater surfaces with lower values of contact angle [93-95]. The critical heat flux for water was observed to increase with decrease in contact angle where the contact angle was controlled by controlling the oxidation of a copper disc [94]. In addition, it was reported that the organic liquids such as R-113 also enabled higher values of critical heat flux with decrease in contact angle [95]. For low values of contact angle, the surface energy is higher resulting in strong inter-molecular coupling at the solid-liquid interface resulting in better heat transfer. Hence, it is expected that higher values of critical heat flux can be obtained for surfaces with lower values of contact angle.

To enable a better comparison - the values of contact angle (before and after boiling experiments) were plotted along with the values of normalized heat flux (both normalized CHF and normalized MHF) for each heater material, as shown in Figure 5-12 for liquid subcooling of 10^{o}C. The contact angle of PF-5060 is highest for silica, lowest for chromel and of intermediate value for silicon. The plot shows that the

normalized CHF for PF-5060 increases with decrease in contact angle, while normalized MHF decreases with decrease in contact angle. This trend is consistent with earlier reports in the literature.

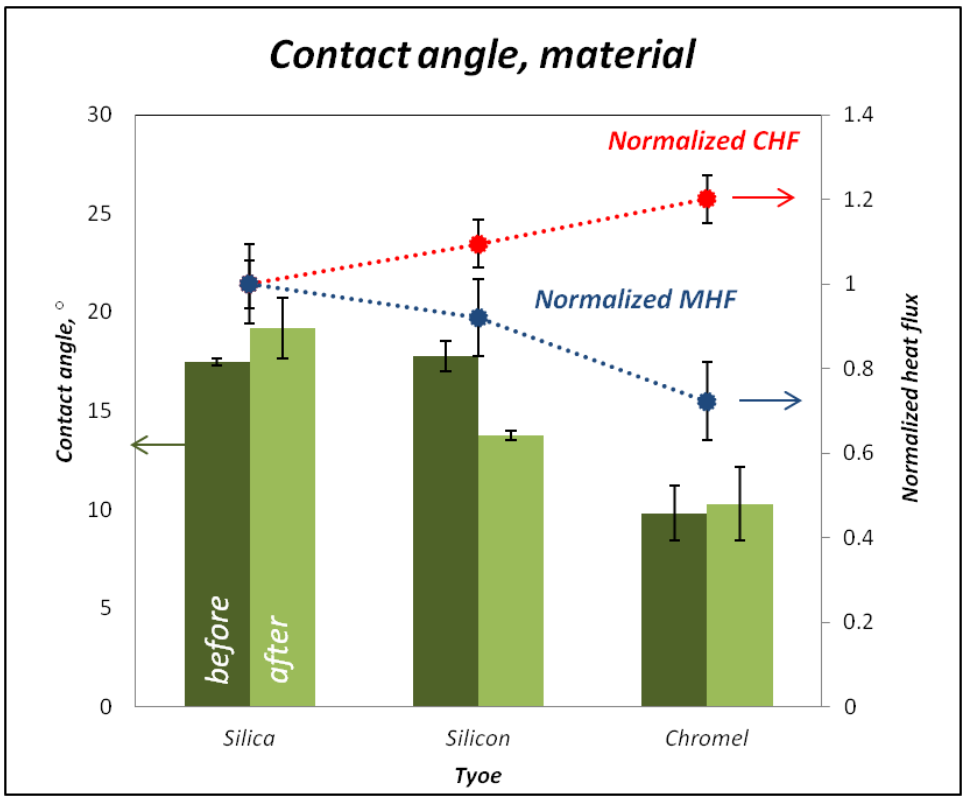

Figure 5-12 Plot showing variation of contact angle and normalized heat flux for each heater material.

5.5. Summary

In this chapter, the effect of the material properties of the heater surface on the pool boiling was explored for three different materials: ceramic (silica), semiconductor (silicon) and metal (chromel). By thin film deposition techniques (physical vapor

deposition, lift-off, oxidation, etc.) – both the heater surface coatings as well thin film thermocouples (TFT) were obtained. The TFT arrays enable successful measurement of surface temperature during pool boiling (both for nucleate and film boiling). This enabled the generation of pool boiling curves for each heater material using PF-5060 as the test liquid. The results show that the pool boiling curve is strongly influenced by the material properties of the heater surface. Consistent with earlier reports in the literature it was observed that the values of critical heat flux (CHF) and minimum heat flux (MHF) were also affected by the material properties of the heater surface. In addition the value of heater temperature (or wall superheat) at which CHF and MHF conditions are achieved – also vary with the change in the material properties of the heater surface, This also indicates that the range of wall superheat values for the transition boiling regime also changes with change in the material properties of the heater surface. In addition, the contact angle between PF-5060 droplet and the heater surface is also measured. The values of CHF increases and the values of MHF decreases with decrease in contact angle. Hence, metal surface has the highest critical heat flux and lowest minimum heat flux since it has the lowest contact angle. Similarly, ceramic (silica) surface has the lowest CHF and highest MHF values – since it has the highest contact angle.

6. POOL BOILING EXPERIMENTS ON HORIZONTAL FLAT HEATERS WITH SILICON NANOFINS

In this chapter, the results from pool boiling experiments are reported for a horizontal flat silicon heater with surface nanostructures. The nanostructures consist of an array of cylindrical protrusions (nanofins) with a diameter of 100 ~ 200 nm and pitch of 800 ~ 900 nm with height of nanofins being fixed for each heater substrate. Different substrates were fabricated with nanofin heights ranging from 10 nm ~ 750 nm. The silicon nanofin arrays were realized by using micro/nano-fabrication techniques borrowed from the MEMS/NEMS literature (MEMS: Micro-Electro-Mechanical Systems; NEMS: Nano-Electro-Mechanical Systems). In this study fabrication methods such as Scanning Flash Imprint Lithography (SFIL), Physical Vapor Deposition (PVD), dry-etching and lift-off process were used primarily for the fabrication of the surface nanostructures as well as the temperature nanosensor arrays in the form of Thin Film Thermocouples (TFT). These fabrication techniques were discussed in Chapter 2. The pool boiling curve on the horizontal silicon heater surface with different nanofin heights were obtained experimentally and the results are discussed in this chapter. The objective of these experiments was to study the sensitivity of the boiling curve to the height of the nanofins for different values of liquid subcooling. In addition, the values of the experimental parameters (such as contact angle and effective surface roughness) were also measured, both before and after the boiling experiments, as the heights of nanofins were varied in each experiment.

6.1. Experimental Results

The silicon wafer substrates with different nanofin heights were fabricated and mounted on the calorimeter apparatus (copper block with embedded cartridge heaters and wire-bead thermocouples) using a rectangular clamp, which was followed by pool boiling experiments that were conducted using PF-5060 as the test fluid. The boiling curve for each experiment was plotted and analyzed in this study. The height of silicon nanofin for each wafer substrate was fixed at a given value. The height of the nanofins used for the different substrates are listed as follows: 10nm, 46nm, 106nm, 354nm, 464nm and 750nm. The details of the fabrication procedure and the geometrical dimensions of each pillar array are discussed in Chapter 2. The surface temperature of silicon wafers with the nanofin surfaces were measured by an array of thin film thermocouple (TFT), except in the case of the silicon surface with nanofin height of 46 nm for which the surface temperature was measured by a wire-bead thermocouple. The pool boiling curves were obtained for these wafer substrates for a rectangular heater configuration for liquid subcooling values of 10 ^{o}C and 5 ^{o}C, where each experiment (for a given liquid subcooling and nanofin height) was conducted twice to check the repeatability of the experimental data within the bounds of the measurement uncertainty.

The pool boiling curves are plotted in the following figures for each value of height of the nanofin array. The colors used in the plots are used to depict the following: sky blue for nanofin array with a height of 10 nm as shown in Figure 6-1, brown for nanofin array with a height of 46 nm as shown in Figure 6-2, purple for nanofin array with a height of 106 nm as shown in Figure 6-3, blue for nanofin array with a height of

354 nm as shown in Figure 6-4, green for nanofin array with a height of 464 nm as shown in Figure 6-5 and black for nanofin array with a height of 750 nm as shown in Figure 6-6, respectively. In addition, icons with solid (filled) icons represent experimental data for liquid subcooling of 10^{o}C, while icons with patterned dots represent experimental data for liquid subcooling of 5^{o}C, and hollow icons represent experimental data for saturated liquid. Moreover, the pool boiling experiments for a given value of liquid subcooling and for a given value of nanofin height were repeated twice (the values for both Run 1 and Run 2 for these experiments are plotted in Appendix D).

The pool boiling curves for the nanostructured surfaces show similar trends to that observed on flat (plain) silicon wafers without any nanostructures, as reported in Chapter 5. The heat flux increases with increase in subcooling for both nucleate and film boiling regime, for each nanofin height. There is a marginal enhancement in the heat flux values with increase in subcooling for the film boiling regime for the range of subcooling explored in this study.

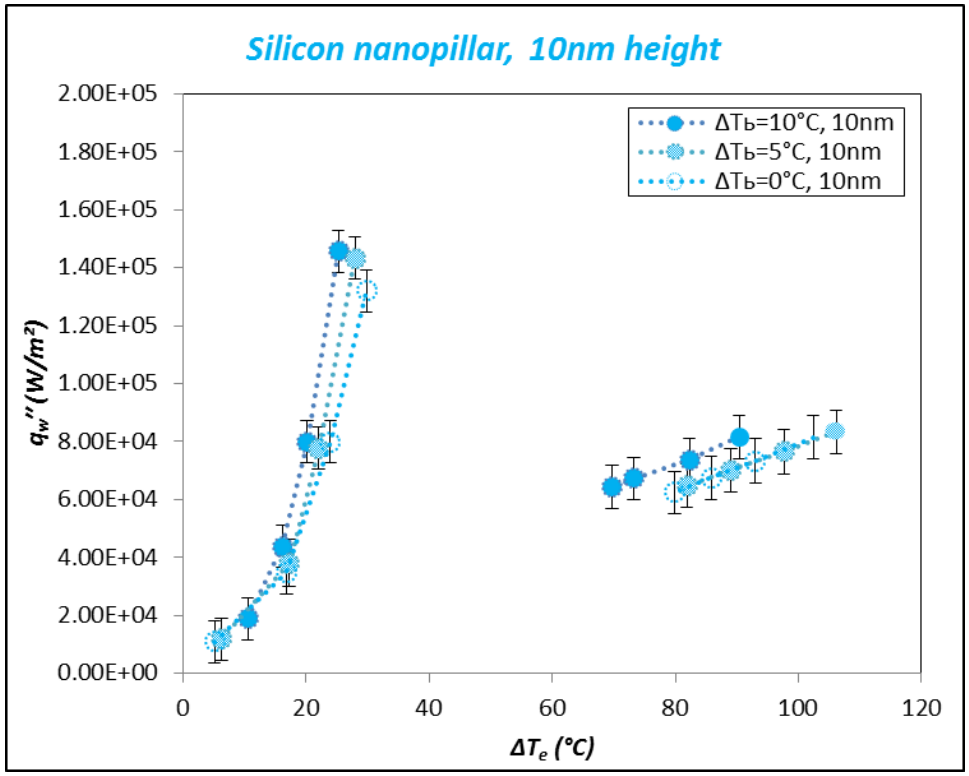

Figure 6-1 Pool boiling curve for rectangular heater with a silicon surface containing surface nanostructures (nanopillars or nanofins). The nanofin height in these experiments is fixed at 10 nm, where circular shaped icons represent experimental data points on the graph: solid (filled) circles represent liquid subcooling of 10 ^{o}C, patterned (filled) circles represent liquid subcooling of 5 ^{o}C, and hollow circles represent liquid subcooling of 5 ^{o}C (saturation boiling experiments). Thin Film Thermocouples (TFT) were used for the measurement of surface temperature of the heater.

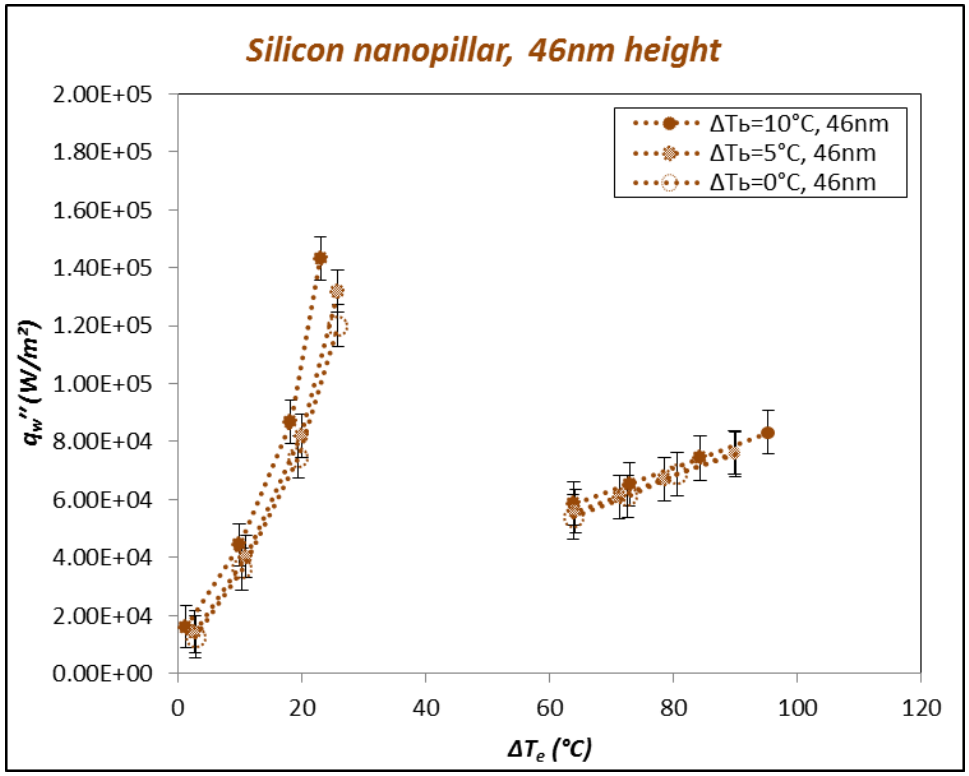

Figure 6-2 Pool boiling curve for rectangular heater with a silicon surface containing surface nanostructures (nanopillars or nanofins). The nanofin height in these experiments is fixed at 46 nm, where circular shaped icons represent experimental data points on the graph: solid (filled) circles represent liquid subcooling of 10 ^{o}C, patterned (filled) circles represent liquid subcooling of 5 ^{o}C, and hollow circles represent liquid subcooling of 5 ^{o}C (saturation boiling experiments). Thin Film Thermocouples (TFT) were used for the measurement of surface temperature of the heater.

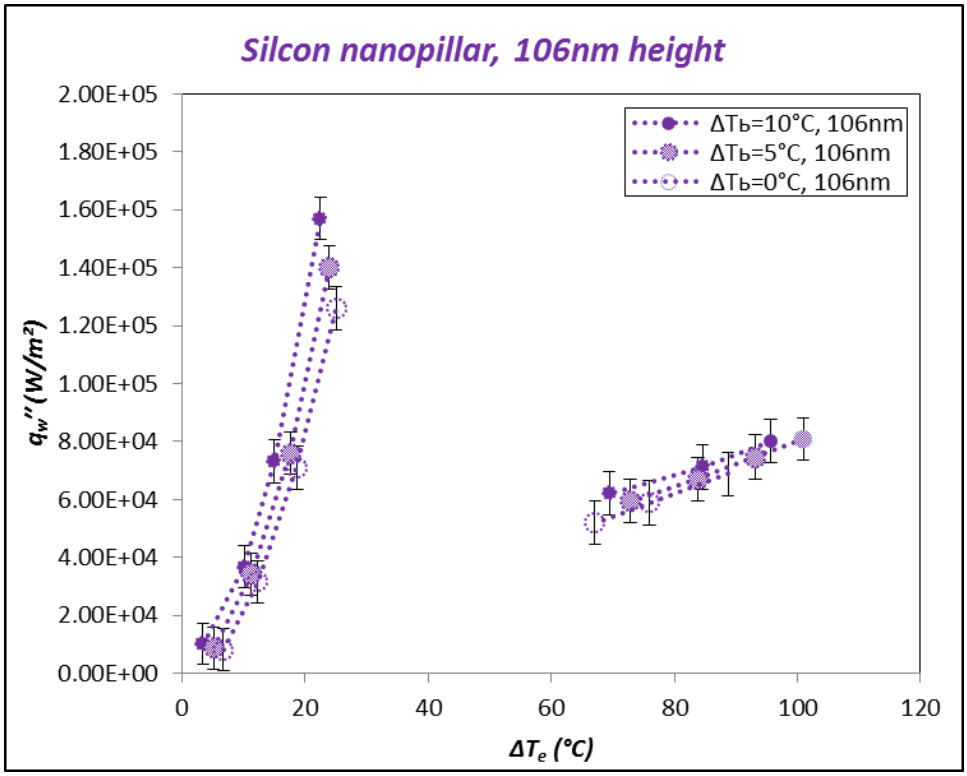

Figure 6-3 Pool boiling curve for rectangular heater with a silicon surface containing surface nanostructures (nanopillars or nanofins). The nanofin height in these experiments is fixed at 106 nm, where circular shaped icons represent experimental data points on the graph: solid (filled) circles represent liquid subcooling of 10 ^{o}C, patterned (filled) circles represent liquid subcooling of 5 ^{o}C, and hollow circles represent liquid subcooling of 5 ^{o}C (saturation boiling experiments). Thin Film Thermocouples (TFT) were used for the measurement of surface temperature of the heater.

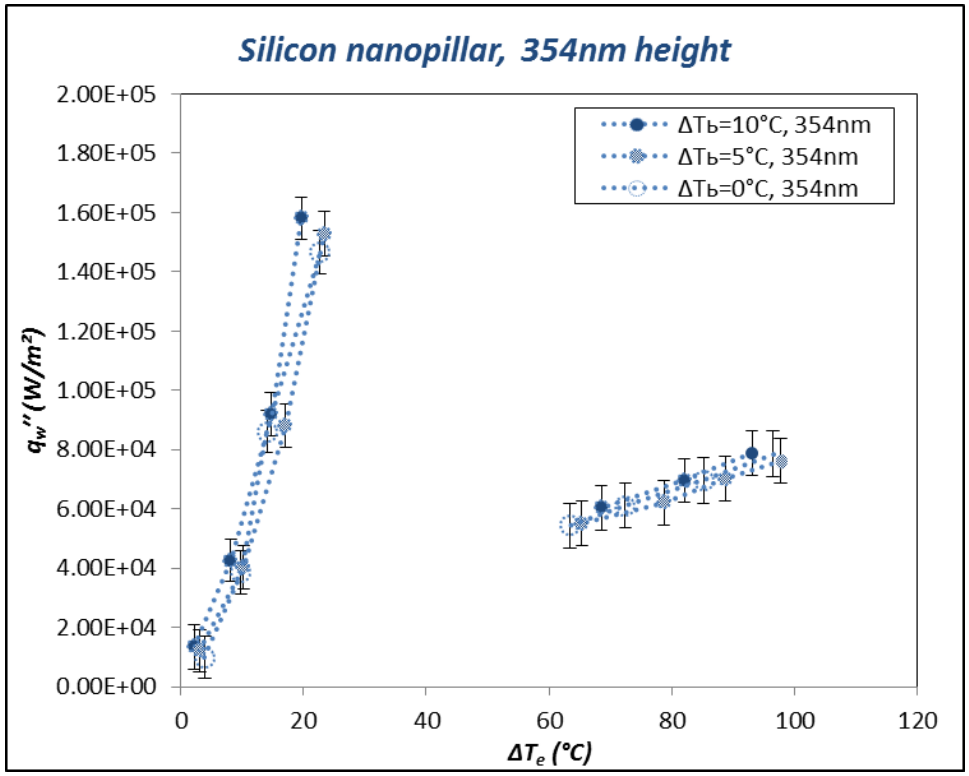

Figure 6-4 Pool boiling curve for rectangular heater with a silicon surface containing surface nanostructures (nanopillars or nanofins). The nanofin height in these experiments is fixed at 354 nm, where circular shaped icons represent experimental data points on the graph: solid (filled) circles represent liquid subcooling of 10 ^{o}C, patterned (filled) circles represent liquid subcooling of 5 ^{o}C, and hollow circles represent liquid subcooling of 5 ^{o}C (saturation boiling experiments). Thin Film Thermocouples (TFT) were used for the measurement of surface temperature of the heater.

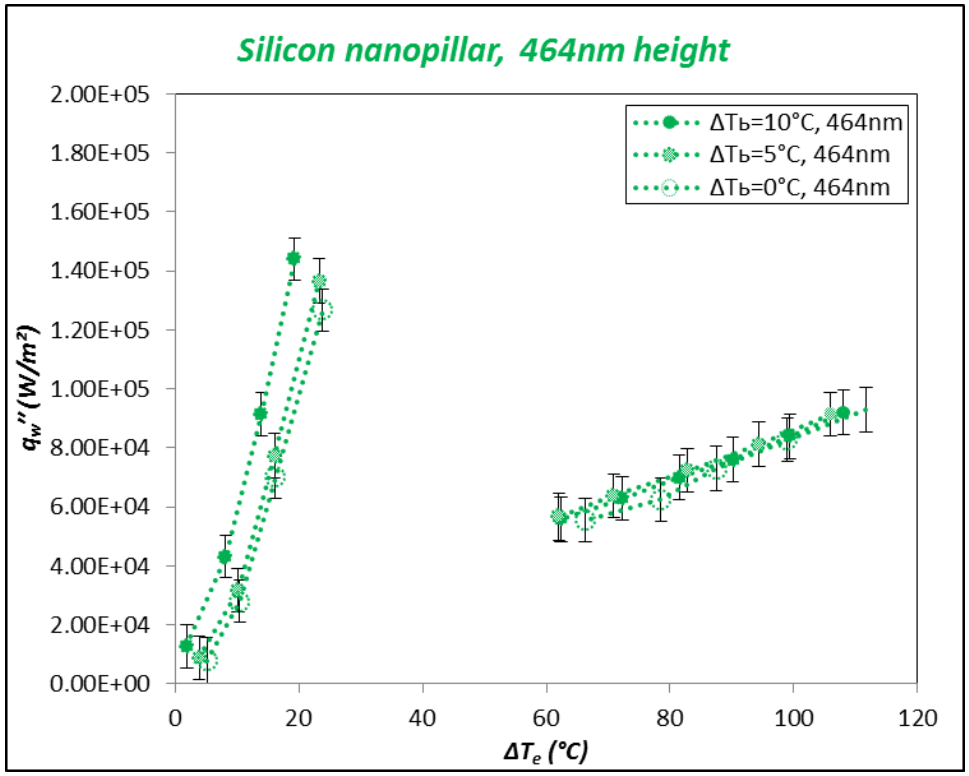

Figure 6-5 Pool boiling curve for rectangular heater with a silicon surface containing surface nanostructures (nanopillars or nanofins). The nanofin height in these experiments is fixed at 464 nm, where circular shaped icons represent experimental data points on the graph: solid (filled) circles represent liquid subcooling of 10 ^{o}C, patterned (filled) circles represent liquid subcooling of 5 ^{o}C, and hollow circles represent liquid subcooling of 5 ^{o}C (saturation boiling experiments). Wire-bead thermocouples were used for the measurement of surface temperature of the heater surface.

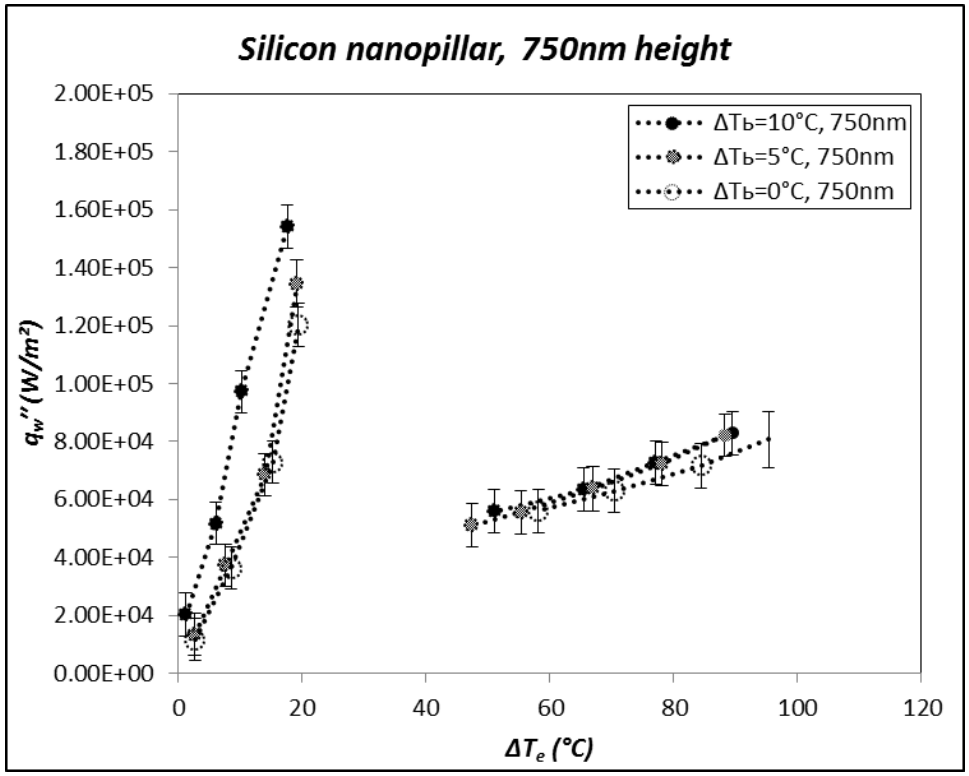

Figure 6-6 Pool boiling curve for rectangular heater with a silicon surface containing surface nanostructures (nanopillars or nanofins). The nanofin height in these experiments is fixed at 750 nm, where circular shaped icons represent experimental data points on the graph: solid (filled) circles represent liquid subcooling of 10 ^{o}C, patterned (filled) circles represent liquid subcooling of 5 ^{o}C, and hollow circles represent liquid subcooling of 5 ^{o}C (saturation boiling experiments). Thin Film Thermocouples (TFT) were used for the measurement of surface temperature of the heater.

6.2. Data Analysis

6.2.1. Total Heat Flux, q_w"

The details of the fabrication process for obtaining nanofins of different heights on the silicon wafer substrates were described in Chapter 2. The diced wafer substrate (41.5 mm × 69.5 mm) was mounted on the experimental setup using a stainless clamp

with a rectangular aperture (aperture size was 31.8 mm × 58.7 mm) for performing the pool boiling experiments. The schematic diagram in Figure 6-7 shows the test surface - starting from the silicon wafer (of 114.3 mm diameter) to the final diced silicon heater surface with the square patterns containing the surface nanostructures and the exposed area of the heater on which pool boiling was obtained after mounting the diced wafer on the calorimeter apparatus (copper block).

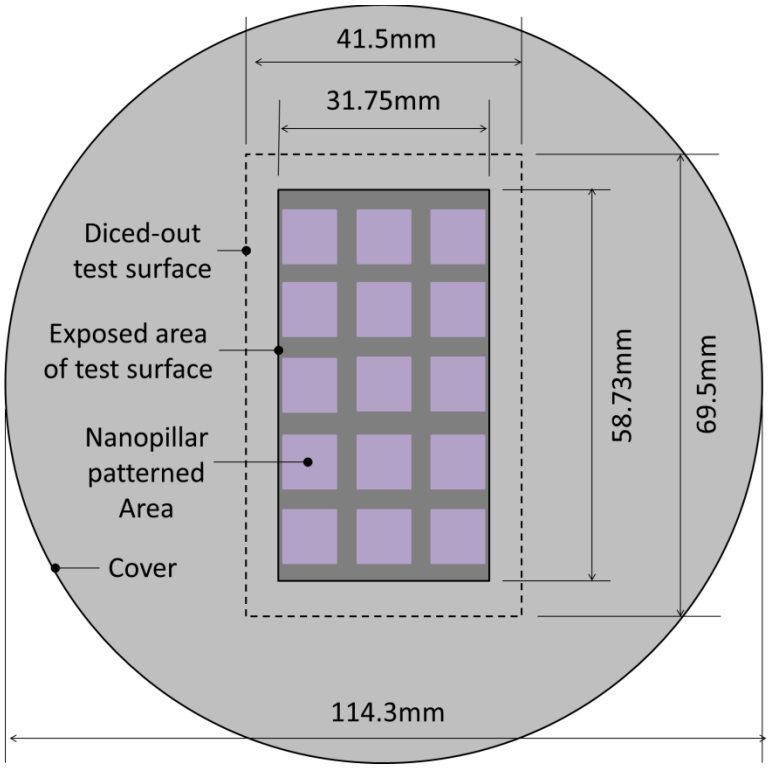

Figure 6-7 Schematic showing the starting point of the fabrication (single sided polished silicon wafer with a diameter of 114.3 mm) to the final diced wafer containing surface nanostructures or nanofins (square shaped patterned area) with the area exposed to pool boiling after mounting on the calorimeter apparatus (copper block) using a steel clamp with a rectangular aperture (aperture size of 31.8 mm × 58.7 mm).

The pool boiling heat flux values for the different test surfaces are plotted in Figure 6-8 ~ Figure 6-10 for each value of liquid subcooling, and selected values are also listed in Table 6-1 (Uncertainty values are available in Appendix D). A consistent trend was observed in these figures for each value of liquid subcooling. For any given value of liquid subcooling, it was observed that in the nucleate boiling regime, the pool boiling heat flux increased with increase in the height of the nanofins. However, within the bounds of the measurement uncertainty, no enhancement in film boiling heat flux was observed with increase in the height of the nanofins. The minimum heat flux or "MHF" (i.e., the Leidenfrost point) is observed to decrease with increase in the height of the nanofins with a concomitant decrease in the value of the wall superheat at which Leidenfrost point is achieved. Hence, it is observed that the boiling curve progressively shifts to the left as the height of the nanofins is increased, for both nucleate and film boiling regime. For example, the test surface with 750 nm pillar height the CHF and MHF conditions are achieved at lower values of wall superheat than that of the flat surface or that of the heater surfaces containing nanofins of intermediate heights.

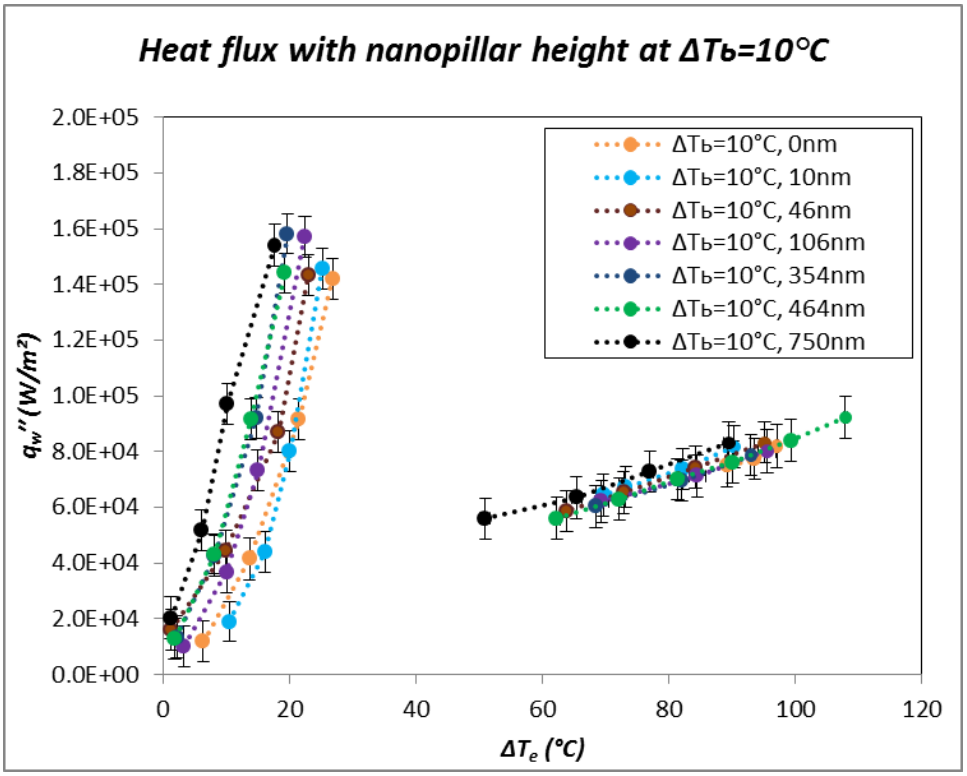

Figure 6-8 Pool boiling curve for rectangular heater with a silicon surface containing surface nanostructures (nanopillars or nanofins). The subcooling in these experiments is fixed at 10 ^{o}C, where circular shaped icons represent experimental data points on the graph with different height of nanofins: black circles - 750 nm, green circles - 464 nm, blue circles - 354 nm, purple circles - 106 nm, brown circles - 46 nm, sky blue circles – 10 nm, and yellow circles – 0 nm (plain surface without any nanopillars). Thin Film Thermocouples (TFT) were used for the measurement of surface temperature of the heater except for the 464 nm data (which was obtained using wire-bead thermocouple).

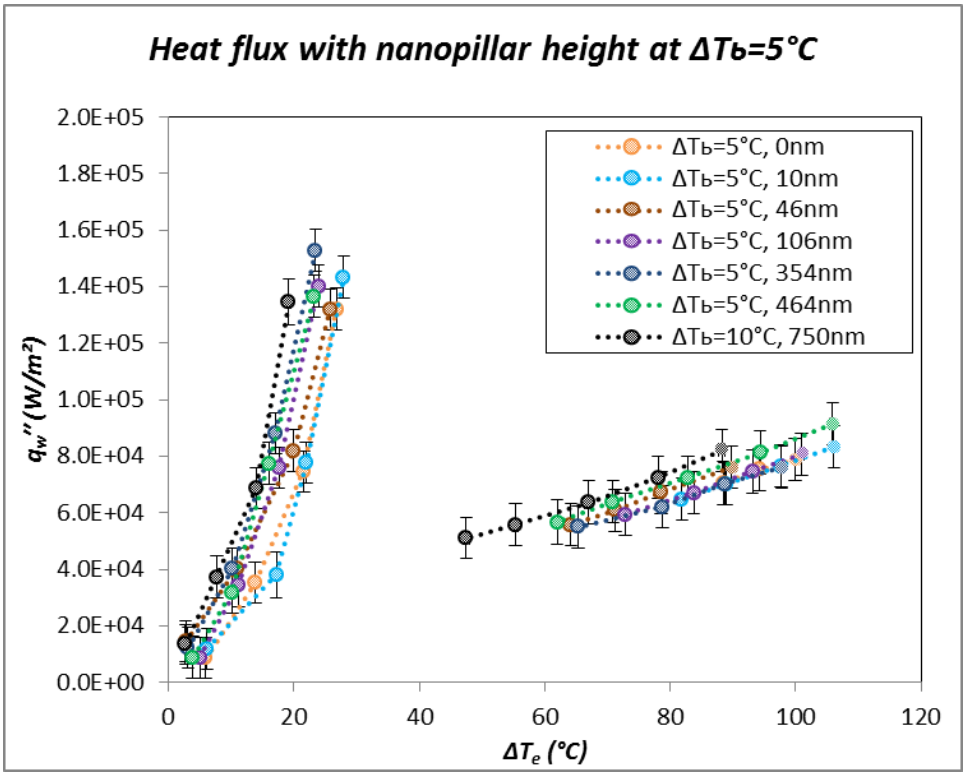

Figure 6-9 Pool boiling curve for rectangular heater with a silicon surface containing surface nanostructures (nanopillars or nanofins). The subcooling in these experiments is fixed at 5 ^{o}C, where circular shaped icons represent experimental data points on the graph with different height of nanofins: black circles - 750 nm, green circles - 464 nm, blue circles - 354 nm, purple circles - 106 nm, brown circles - 46 nm, sky blue circles – 10 nm, and yellow circles – 0 nm (plain surface without any nanopillars). Thin Film Thermocouples (TFT) were used for the measurement of surface temperature of the heater except for the 464 nm data (which was obtained using wire-bead thermocouple).

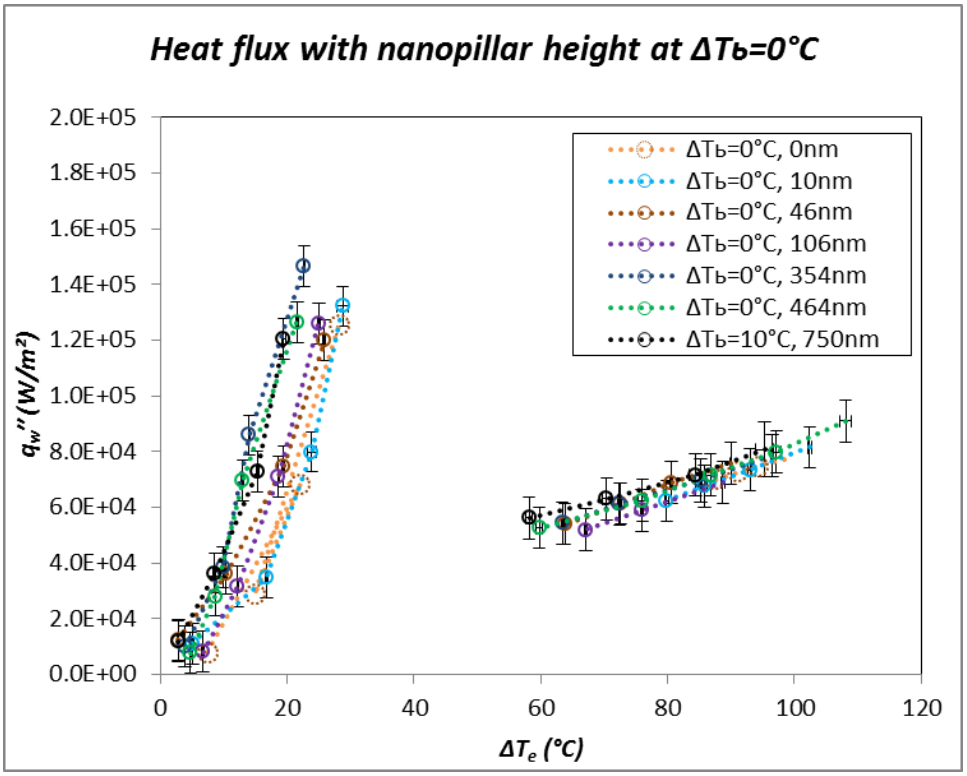

Figure 6-10 Pool boiling curve for rectangular heater with a silicon surface containing surface nanostructures (nanopillars or nanofins). The subcooling in these experiments is fixed at 0 ^{o}C (saturated pool boiling condition), where circular shaped icons represent experimental data points on the graph with different height of nanofins: black circles - 750 nm, green circles - 464 nm, blue circles - 354 nm, purple circles - 106 nm, brown circles - 46 nm, sky blue circles – 10 nm, and yellow circles – 0 nm (plain surface without any nanopillars). Thin Film Thermocouples (TFT) were used for the measurement of surface temperature of the heater except for the 46 nm data (which was obtained using wire-bead thermocouple).

Table 6-1 Summary of heat flux values (CHF and MHF) on the heater surface (q_w") with silicon nanofins at liquid subcooling values of 10 ^oC, 5 ^oC and 0 ^oC (saturated pool boiling experiments)

Subcooling 10°C	Critical heat flux		Minimum heat flux	
Height of nanopillar	Wall superheat, °C	Heat flux, W/m²	Wall superheat, °C	Heat flux, W/m²
0	26.8	1.42E+05	89.3	7.49E+04
10.1	25.2	1.46E+05	69.7	6.44E+04
46.1	23.0	1.43E+05	63.9	5.86E+04
105.6	22.4	1.57E+05	69.4	6.21E+04
351	19.7	1.58E+05	68.6	6.03E+04
464	19.3	1.44E+05	62.4	5.59E+04
750	17.7	1.54E+05	51.0	5.60E+04
Subcooling 5°C	Critical heat flux		Minimum heat flux	
Height of nanopillar	Wall superheat, °C	Heat flux, W/m²	Wall superheat, °C	Heat flux, W/m²
0	26.8	1.32E+05	88.4	7.05E+04
10.1	27.9	1.43E+05	81.9	6.48E+04
46.1	25.8	1.32E+05	64.1	5.58E+04
105.6	23.9	1.40E+05	72.8	5.94E+04
351	23.5	1.53E+05	65.3	5.50E+04
464	23.3	1.37E+05	62.0	5.67E+04
750	19.2	1.35E+05	47.5	5.11E+04
Saturated	Critical heat flux		Minimum heat flux	
Height of nanopillar	Wall superheat, °C	Heat flux, W/m²	Wall superheat, °C	Heat flux, W/m²
0	28.2	1.25E+05	87.5	7.00E+04
10.1	29.8	1.32E+05	79.9	6.24E+04
46.1	25.9	1.20E+05	63.8	5.40E+04
105.6	25.0	1.26E+05	67.1	5.19E+04
351	22.7	1.47E+05	63.4	5.43E+04
464	21.6	1.26E+05	59.8	5.26E+04
750	19.5	1.20E+05	58.2	5.61E+04

6.2.2. Heat Flux Through the Heater Projected Area Containing Nanofins (q_n")

The fabrication process (SFIL) for obtaining the nanofins includes a stepping operation where in each step an area of 1 cm × 1 cm is covered for performing nanolithography in order to be patterned with nanofins. Out of this area covered in each step, an area of 0.8 cm × 0.8 cm is covered with nanostructures. Also, a gap is

maintained between each step in which no patterns are obtained. In addition, in some of the nanolithography steps nanofins were not obtained due to process issues resulting in nanolithography not being successful (e.g., due to dust particles settling in the target zone from the ambient of the clean room environment). Therefore meta-data needs to be generated based on the experimental data. Two types of meta-data were generated based on the raw experimental data for wall heat flux (q_w"):

1. Heat flux through the projected area on the wafer containing the nanofins (q_n"), which is obtained by subtracting the heat flux through the unpatterned area of the wafer (q_b") weighted by the area of the unpatterned region - from - the total heat flux through the wafer weighted by the total projected area of the heater surface exposed to the boiling liquid.
2. Heat flux through the total surface area containing the nanofins (q_{nc}"), which is obtained from meta-data for the projected area (q_n") adjusted for the total surface area of the surface nanostructures.

The two sets of meta-data for pool boiling heat flux, as mentioned above, are obtained by following the procedures mentioned next. The heat flux on the test surface (q_w") can be expressed the summation of the heat flux on the nanofin patterned surface (q_n") and the heat flux on the non-patterned surface (q_b"). Each of these values (q_w" and q_b") can be obtained from the experimental data presented in Chapter 5 and Chapter 6. By the law of conservation of energy the heat flux relation can be expressed as follows:

$$q_w^{"}A_w = q_b^{"}A_b + q_n^{"}A_n \text{ or } q_n^{"} = \frac{q_w^{"}A_w - q_b^{"}A_b}{A_n} \tag{6-1}$$

Where, A_n is the projected area of the diced wafer containing the nanostructured surface, A_b is the area of the diced wafer without any nanostructures and A_w is the total projected area of the test surface area in contact with the boiling liquid (which is the same as the aperture of the stainless steel clamp). The relation between the different projected areas can be expressed as follows:

$$A_w = A_b + A_n \; ; \; A_n = (L_m)^2 N \tag{6-2}$$

Where, L_m is the length of the each side of the square patterns containing the surface nanostructures (in this study this value is 0.8 mm) and N is the number of squares which contain the surface nanostructures (in other words, N is the number of times the stepper operation was successful for performing nanolithography in the SFIL process on each diced wafer). This calculation procedure is illustrated in the schematic shown in Figure 6-11.

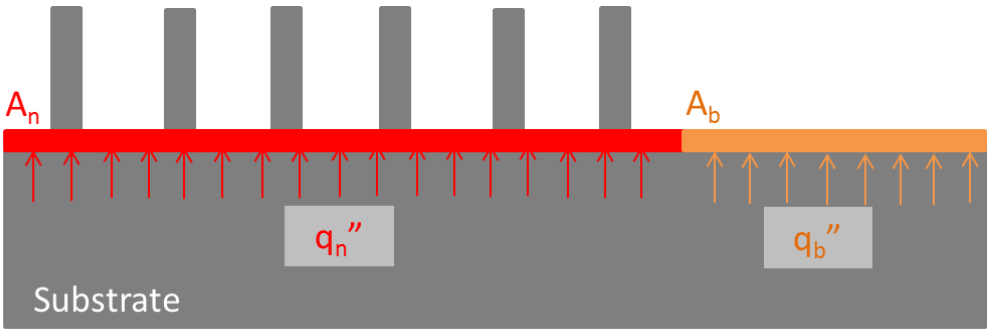

Figure 6-11 Schematic diagram for calculation of the heat flux values (meta-data) through the projected area of the heater containing patterned nanofins (q_n"). (Note: figure is not to scale).

The heat flux on the non-patterned silicon surface at given wall superheat temperature was estimated by using the heat flux data obtained from experiments performed on the flat silicon surface (without any patterned surface nanostructure) that were discussed in Chapter 5. A best fit curve (using exponential fit) was calculated for the experimental data for heat flux as a function of wall superheat for each value of liquid subcooling. The best fit curve predicted the heat flux as a function of wall superheat for a plain silicon heater (without any nanostructures) for each value of liquid subcooling and the plots are shown in Figure 6-12. The plots show fairly good fit for the curves with R^2 values exceeding 0.94 (for liquid subcooling of 10 ^oC) and 0.97 (for saturation condition and liquid subcooling of 5 ^oC) in the nucleate boiling, as well as, with R^2 values exceeding 0.94 (for liquid subcooling of 10 ^oC) and 0.98 (for saturation condition and liquid subcooling of 5 ^oC) in the film boiling regime.

After obtaining the best-fit curves for the raw experimental data for the heat flux values on the plain silicon heater (without any nanostructures), the meta-data for the heat flux values for the projected area of the patterned silicon surface (i.e., the portion of the diced wafer containing nanofins) is calculated for liquid subcooling of 10 ^oC, 5 ^oC and 0 ^oC (saturation condition). These values are then plotted in Figure 6-13 ~ Figure 6-15 and selected values are also listed in Table 6-2. The meta-data for the values of heat flux (based on the projected area of the heater surface containing nanofins) show a significant contrast as the height of the nanofins is increased, for all values of liquid subcooling explored in this study.

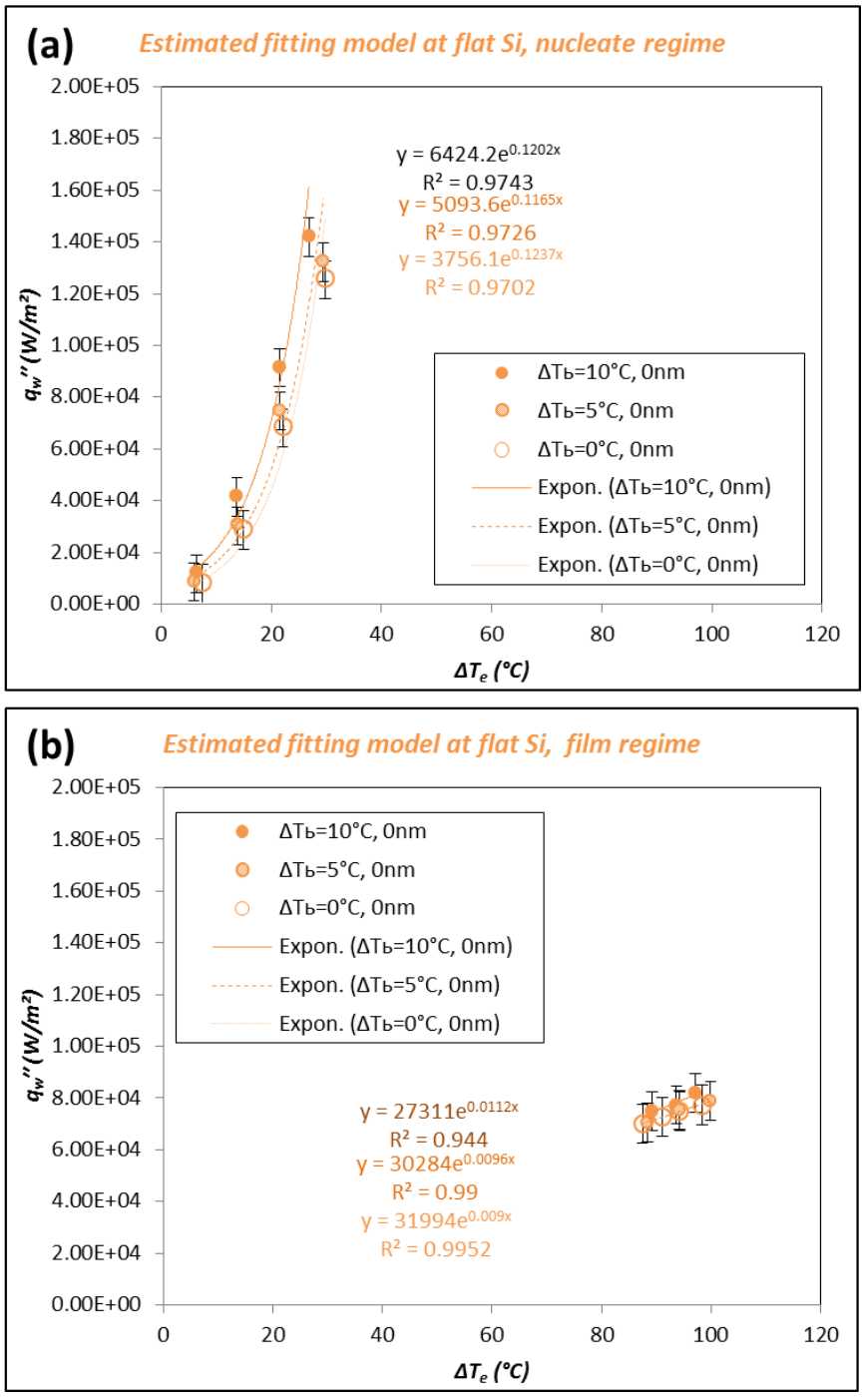

Figure 6-12 Best fit curves (with exponential fit) obtained for experimental data on flat silicon heater with plain surface (without any patterned nanostructures) for liquid subcooling of 10°C and 5°C as well as saturated pool boiling experiments for the: (a) Nucleate boiling regime; and (b) Film boiling regime.

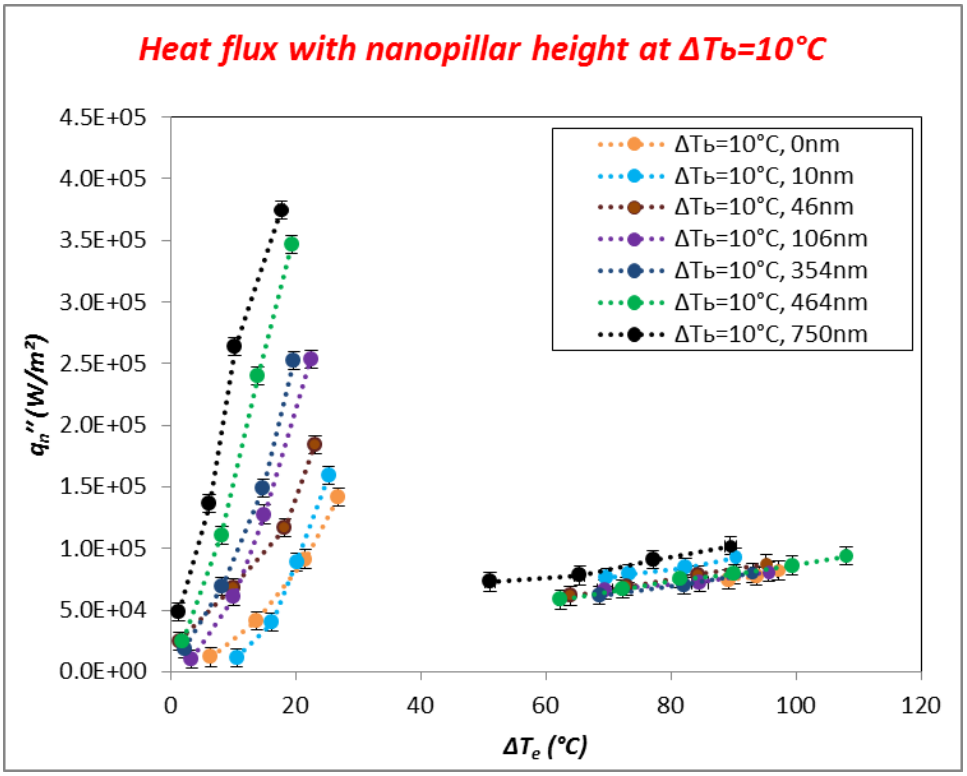

Figure 6-13 Pool boiling curve for rectangular heater with a silicon surface containing surface nanostructures (nanopillars or nanofins). The heat flux values are based on projected area occupied by the nanofins (q_n"). The subcooling in these experiments is fixed at 10 ^{o}C, where circular shaped icons represent experimental data points on the graph with different height of nanofins: black circles - 750 nm, green circles - 464 nm, blue circles - 354 nm, purple circles - 106 nm, brown circles - 46 nm, sky blue circles – 10 nm, and yellow circles – 0 nm (plain surface without any nanopillars). Thin Film Thermocouples (TFT) were used for the measurement of surface temperature of the heaters except for the data for nanofins with 464 nm height (which was obtained using wire-bead thermocouple).

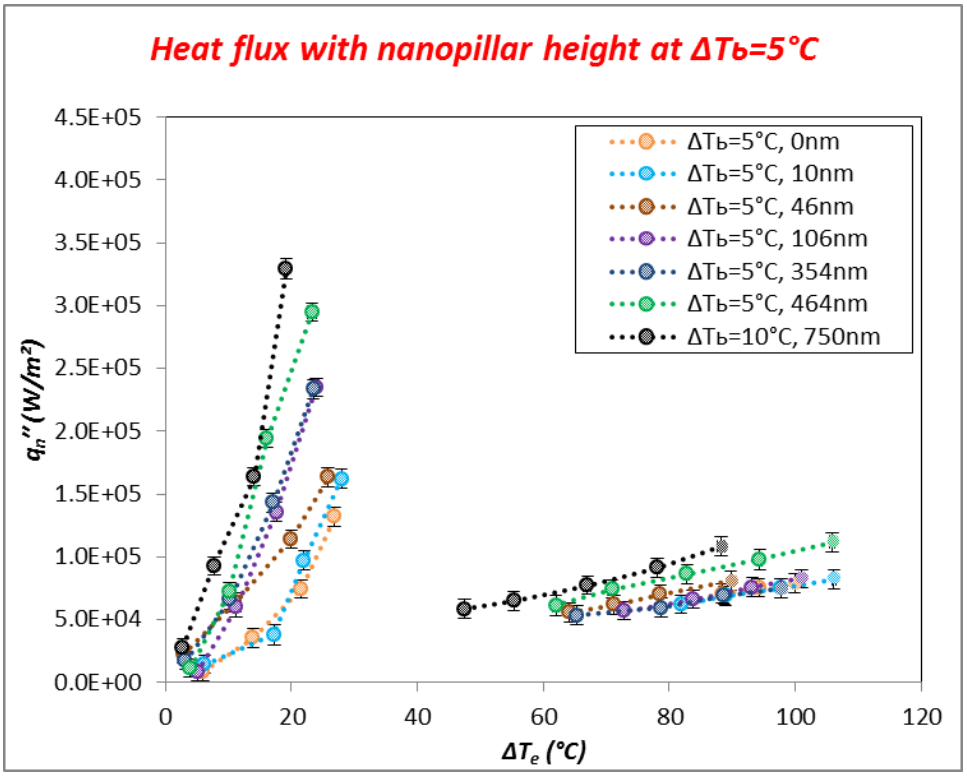

Figure 6-14 Pool boiling curve for rectangular heater with a silicon surface containing surface nanostructures (nanopillars or nanofins). The heat flux values are based on projected area occupied by the nanofins (q_n"). The subcooling in these experiments is fixed at 5 ^{o}C, where circular shaped icons represent experimental data points on the graph with different height of nanofins: black circles - 750 nm, green circles - 464 nm, blue circles - 354 nm, purple circles - 106 nm, brown circles - 46 nm, sky blue circles – 10 nm, and yellow circles – 0 nm (plain surface without any nanopillars). Thin Film Thermocouples (TFT) were used for the measurement of surface temperature of the heaters except for the data for nanofins with 464 nm height (which was obtained using wire-bead thermocouple).

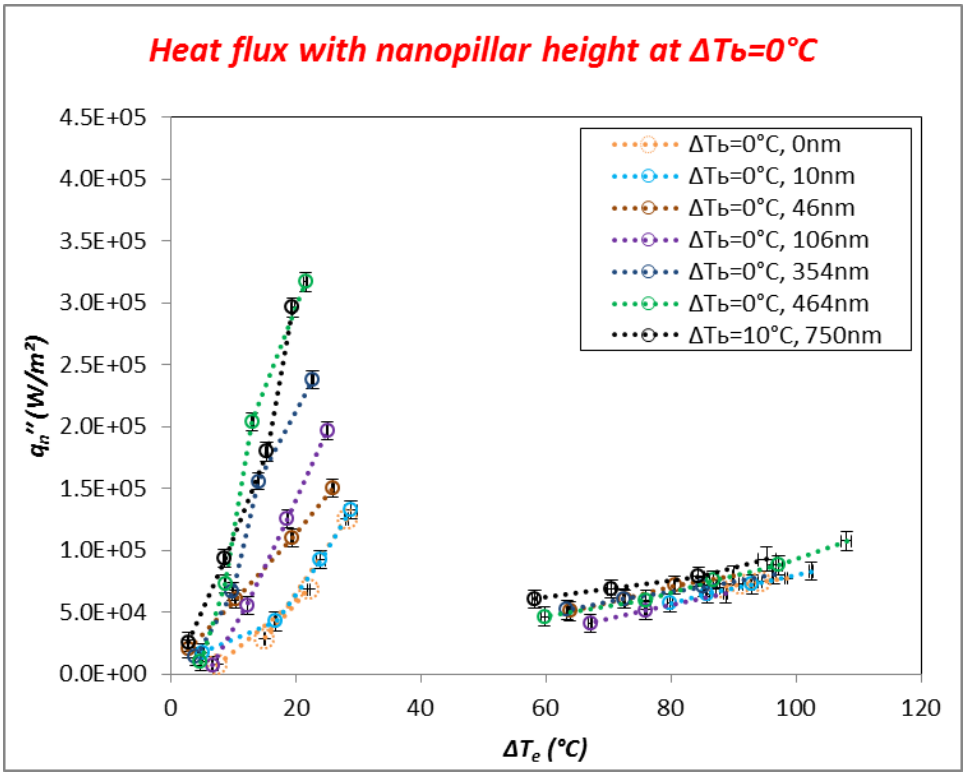

Figure 6-15 Pool boiling curve for rectangular heater with a silicon surface containing surface nanostructures (nanopillars or nanofins). The heat flux values are based on projected area occupied by the nanofins (q_n"). The subcooling in these experiments is fixed at 0 ^{o}C (saturated pool boiling condition), where circular shaped icons represent experimental data points on the graph with different height of nanofins: black circles - 750 nm, green circles - 464 nm, blue circles - 354 nm, purple circles - 106 nm, brown circles - 46 nm, sky blue circles – 10 nm, and yellow circles – 0 nm (plain surface without any nanopillars). Thin Film Thermocouples (TFT) were used for the measurement of surface temperature of the heaters except for the data for nanofins with 46 nm height (which was obtained using wire-bead thermocouple).

Table 6-2 Summary of heat flux values (CHF and MHF) through the projected area of the heater surface (q_n") with silicon nanofins at liquid subcooling values of 10 °C, 5 °C and 0 °C (saturated pool boiling experiments)

Subcooling 10°C	Critical heat flux		Minimum heat flux	
Height of nanopillar	Wall superheat, °C	Heat flux, W/m²	Wall superheat, °C	Heat flux, W/m²
0	26.8	1.42E+05	89.3	7.49E+04
10.1	25.2	1.59E+05	69.7	7.63E+04
46.1	23.0	1.84E+05	63.9	6.16E+04
105.6	22.4	2.54E+05	69.4	6.64E+04
351	19.7	2.53E+05	68.6	6.19E+04
464	19.3	3.47E+05	62.4	5.84E+04
750	17.7	3.75E+05	51.0	7.29E+04
Subcooling 5°C	Critical heat flux		Minimum heat flux	
Height of nanopillar	Wall superheat, °C	Heat flux, W/m²	Wall superheat, °C	Heat flux, W/m²
0	26.8	1.32E+05	88.4	7.05E+04
10.1	27.9	1.62E+05	81.9	6.20E+04
46.1	25.8	1.63E+05	64.1	5.56E+04
105.6	23.9	2.35E+05	72.8	5.69E+04
351	23.5	2.33E+05	65.3	5.32E+04
464	23.3	2.95E+05	62.0	6.13E+04
750	19.2	3.29E+05	47.5	5.85E+04
Saturated	Critical heat flux		Minimum heat flux	
Height of nanopillar	Wall superheat, °C	Heat flux, W/m²	Wall superheat, °C	Heat flux, W/m²
0	28.2	1.25E+05	87.5	7.00E+04
10.1	29.8	1.32E+05	79.9	5.71E+04
46.1	25.9	1.50E+05	63.8	5.09E+04
105.6	25.0	1.97E+05	67.1	4.11E+04
351	22.7	2.38E+05	63.4	5.19E+04
464	21.6	3.17E+05	59.8	4.66E+04
750	19.5	2.96E+05	58.2	6.08E+04

The figures show that within the bounds of the measurement uncertainty - for saturated pool boiling - no significant enhancement in CHF (based on projected area of the nanofin surface, q_n") is observed for nanofins with 10 nm height when compared to that of plain heaters (with no nanostructures). Marginal enhancement (10 ~ 20%) in CHF (based on projected area of the nanofin surface, q_n") is observed for nanofins with 46 nm

height in the case of saturated pool boiling when compared to that of plain heaters (with no nanostructures). Significant enhancement (20~50%) in CHF (based on projected area of the nanofin surface, q_n'') is observed for nanofins with height of 10 nm and 46 nm for liquid subcooling of 5 ^oC and 10 ^oC, when compared to that of plain heaters (with no nanostructures).

In contrast, CHF (based on projected area of the nanofin surface, q_n'') is enhanced by more than 100% (i.e., 100% ~ 300%) for nanofin heights exceeding 100 nm (i.e., for nanofin heights of 106 nm – 750 nm, respectively) for all of the experiments performed in this study (i.e., for saturated pool boiling as well as liquid subcooling of 5 ^oC and 10 ^oC), when compared to that of plain heaters (with no nanostructures). For a given value of liquid subcooling (i.e., 0 ^oC, 5 ^oC or 10 ^oC) the level of enhancement in CHF (based on projected area of the nanofin surface, q_n'') increases progressively with the height of the nanofin. The largest enhancement in CHF (based on projected area of the nanofin surface, q_n'') is observed for the pool boiling experiments with liquid subcooling of 10 ^oC for nanofin height of 750 nm.

No significant or consistent trend in enhancement or degradation in the value of minimum heat flux or "MHF" (based on projected area of the nanofin surface, q_n'') is observed in these experiments as the height of the nanofins are increased progressively from 10 nm to 750 nm for a given value of liquid subcooling. For the saturated pool boiling experiments the value of MHF is enhanced marginally (or virtually remains the same accounting for the measurement uncertainty) when comparing the data for 10 nm to that of 750 nm height. On the other hand, for the subcooled pool boiling experiments

the value of MHF is decreased marginally (or virtually remains the same accounting for the measurement uncertainty) when comparing the data for 10 nm to that of 750 nm height. It is interesting to observe that the value of MHF decreases sharply (by 10~20%) when the height of the nanofins is increased from 0 nm (plain heater surface with no nanostructures) to 10 nm for experiments performed under saturation condition or for liquid subcooling of 5 ^{o}C. On the other hand, for liquid subcooling of 10 ^{o}C the value of MHF is decreased marginally (or virtually remains the same accounting for the measurement uncertainty) when comparing the data for 10 nm to that of plain silicon heater (without any patterned nanostructures/ nanofins).

The value of wall superheat in the vicinity of the CHF condition (based on projected area of the nanofin surface, q_n'') is also observed to decrease by 7.5 ^{o}C ~ 10 ^{o}C with increase in height of the nanofins from 10 nm to 750 nm. The value of wall superheat in the vicinity of the CHF condition (based on projected area of the nanofin surface, q_n'') is observed to decrease marginally (or remain the same within the bounds of the measurement uncertainty) with the increase in the degree of liquid subcooling for a given height of the nanofins (or for the plain surface without any patterned nanofins). Considering the bounds of the measurement uncertainty, there is virtually no change in the value of wall superheat in the vicinity of the CHF condition (based on projected area of the nanofin surface, q_n'') for the heater with nanofins of height 10 nm when compared to that of the plain surface without any patterned nanofins. On the other hand - the value of wall superheat in the vicinity of the CHF condition (based on projected area of the nanofin surface, q_n'') is decreased by approximately 3 ^{o}C ~ 10 ^{o}C for the heaters with

nanofins of height exceeding 100 nm - when compared to that of the plain surface without any patterned nanofins.

The value of minimum heat flux or "MHF" (based on projected area of the nanofin surface, q_n'') is observed to be enhanced by approximately 30% in these experiments with increase in liquid subcooling (from 0 C to 10 C), for a given value of nanofin height. For a fixed value of liquid subcooling, no significant or consistent trend in the enhancement or degradation in the values of MHF are observed, since the MHF values are observed to both increase and decrease with increase in height of the nanofins.

For the film boiling data it is observed that the Leidenfrost point occurs at significantly lower values of wall superheat as the height of the nanofins is increased progressively from 106 nm to 750 nm, for any given value of liquid subcooling. Hence the wall superheat for the achieving the Leidenfrost condition is more sensitive to the variation in the height of the nanofins than the degree of liquid subcooling explored in this study. For nanofin heights of 10 nm, 46 nm and 106 nm – a peculiar behavior is observed. The wall superheat values (in the vicinity of the Leidenfrost point) are found to decrease when the nanofin height is increased from 10 nm to 46 nm, and then increase when the nanofin height increases to 106 nm. This is probably due to high levels of measurement uncertainty for the surface temperature measurements for the silicon heater with nanofins of 46 nm height – since a wire bead thermocouple was used for these experiments. Wire-bead thermocouples have larger values of measurement uncertainty than that of thin film thermocouples (TFT). The boiling curves (based on projected area of the nanofin surface, q_n'') shift to the left as the height of the nanofins are increased or

for higher values of liquid subcooling (except for the anomalous behavior observed for silicon heaters with nanofins of 46 nm height – due to higher levels of measurement uncertainty in the measurement of surface temperature values using wire-bead thermocouples, as mentioned above).

6.2.3. Heat Flux Through Nanofin (q_{nc}")

The heat flux through the total surface area of the heater with the patterned nanofins (q_{nc}") is also calculated based on the law of conservation of energy, and is expressed as follows:

$$q''_{nc} A_{nc} = q''_n A_n \; ; \; q''_{nc} = q''_n \frac{A_n}{A_{nc}} \tag{6-3}$$

Where A_{nc} is the total surface area of the section of the heater with nanofins (i.e., adding the surface area of the nanofins to A_n). A_n and A_{nc} values for each nanofin heaters are available in Appendix D. This calculation procedure is illustrated in Figure 6-16.

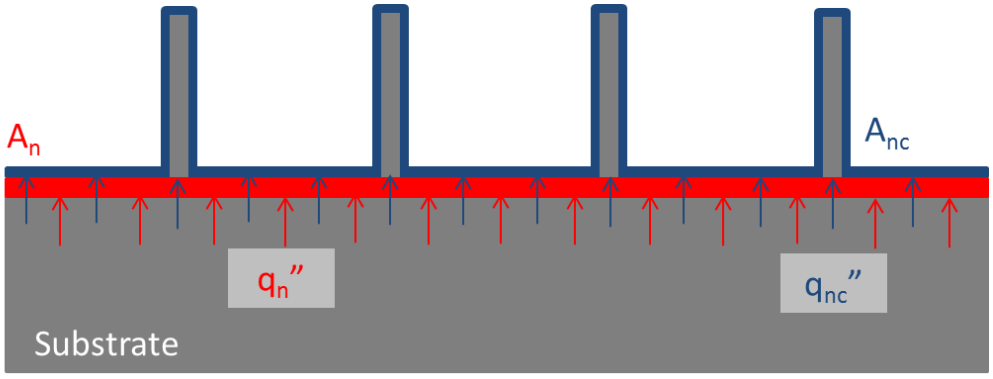

Figure 6-16 Schematic diagram for calculation of heat flux (meta-data) through the total surface area for the segment of the heater contatining nanofins (q_{nc}"). (Note: Figure is not to scale).

The heat flux values considering the total surface area for the segment of the heater containing nanofins (q_{nc}") are plotted in Figure 6-17 for liquid subcooling of 10°C, Figure 6-18 for liquid subcooling of 5°C and Figure 6-19 for saturated condition. In addition, selected values are available in Appendix D.

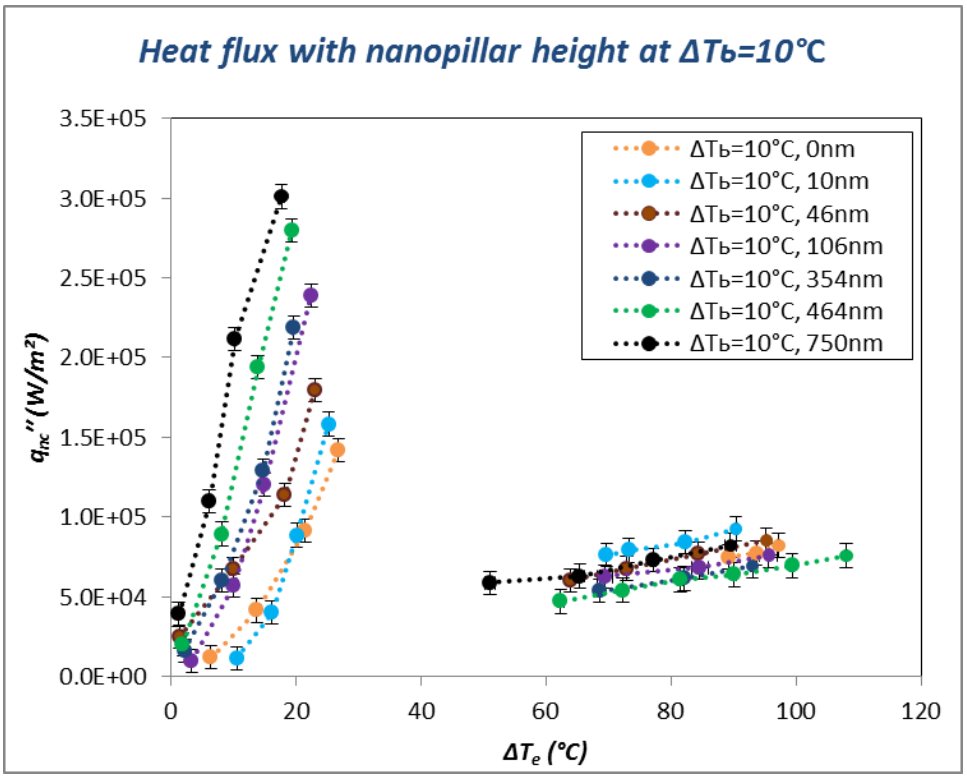

Figure 6-17 Pool boiling curve for rectangular heater with a silicon surface containing surface nanostructures (nanopillars or nanofins). The heat flux values are based on the total surface area occupied by the nanofins (q_{nc}"). The subcooling in these experiments is fixed at 10 °C, where circular shaped icons represent experimental data points on the graph with different height of nanopillars: black circles - 750 nm, green circles - 464 nm, blue circles - 354 nm, purple circles - 106 nm, brown circles - 46 nm, sky blue circles – 10 nm, and yellow circles – 0 nm (plain surface without any nanopillars). Thin Film Thermocouples (TFT) were used for the measurement of surface temperature of the heater except for the data for nanofins with 464 nm height (which were obtained using wire-bead thermocouple).

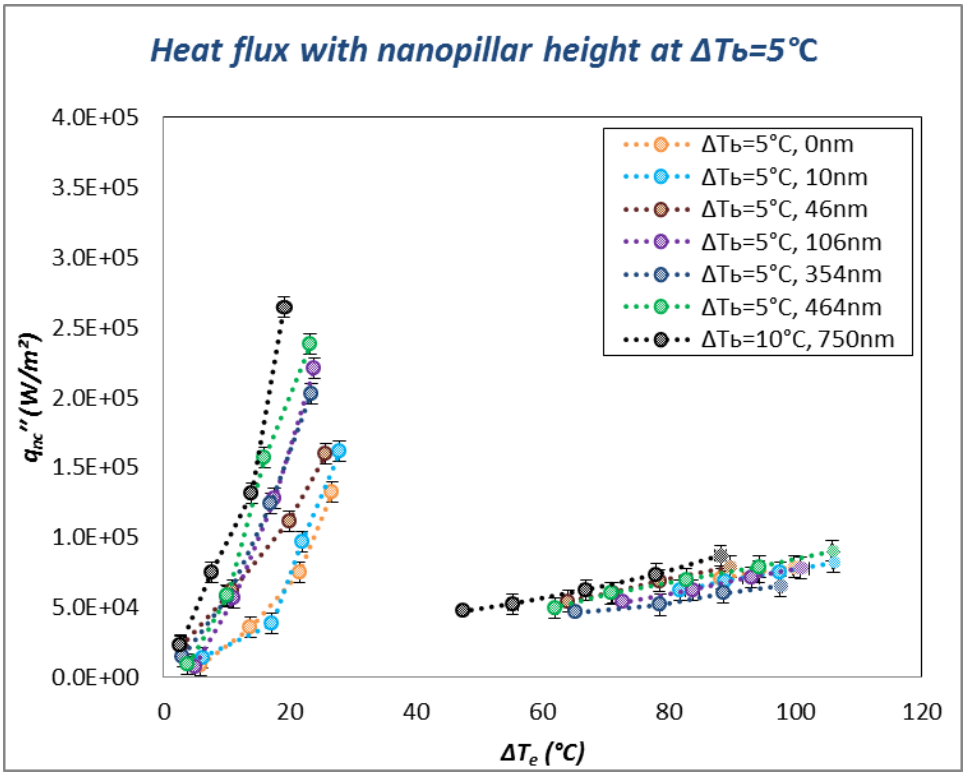

Figure 6-18 Pool boiling curve for rectangular heater with a silicon surface containing surface nanostructures (nanopillars or nanofins). The heat flux values are based on the total surface area occupied by the nanofins (q_{nc}"). The subcooling in these experiments is fixed at 5 ^{o}C, where circular shaped icons represent experimental data points on the graph with different height of nanopillars: black circles - 750 nm, green circles - 464 nm, blue circles - 354 nm, purple circles - 106 nm, brown circles - 46 nm, sky blue circles – 10 nm, and yellow circles – 0 nm (plain surface without any nanopillars). Thin Film Thermocouples (TFT) were used for the measurement of surface temperature of the heater except for the data for nanofins with 464 nm height (which were obtained using wire-bead thermocouple).

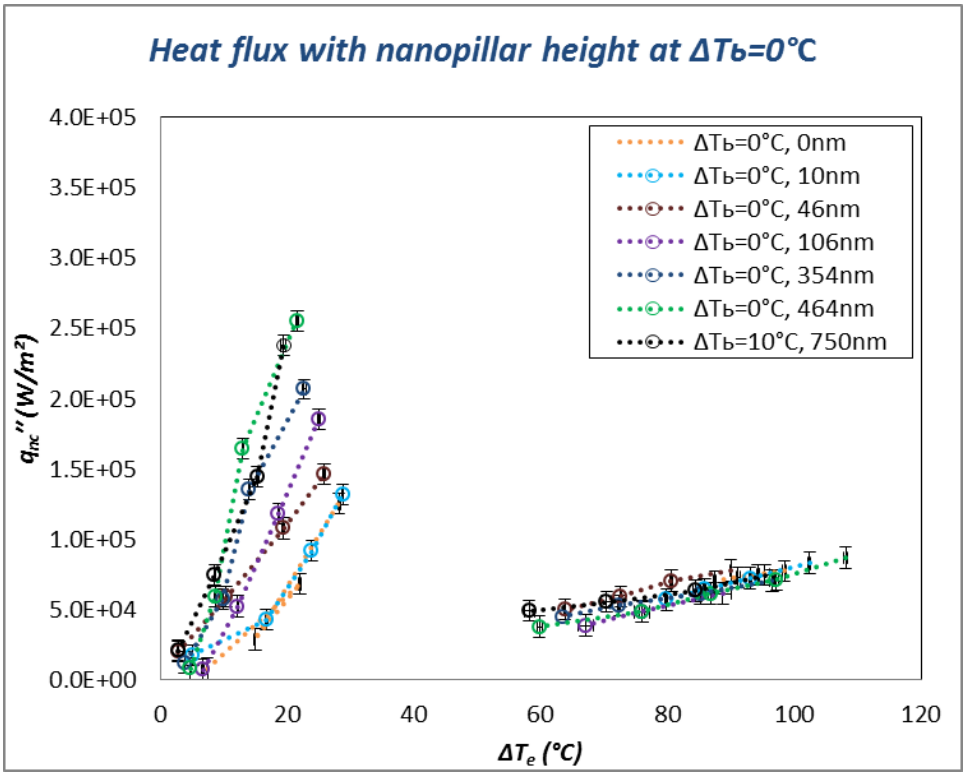

Figure 6-19 Pool boiling curve for rectangular heater with a silicon surface containing surface nanostructures (nanopillars or nanofins). The heat flux values are based on the total surface area occupied by the nanofins (q_{nc}"). The subcooling in these experiments is fixed at 0 ^{o}C (saturated pool boiling condition), where circular shaped icons represent experimental data points on the graph with different height of nanopillars: black circles - 750 nm, green circles - 464 nm, blue circles - 354 nm, purple circles - 106 nm, brown circles - 46 nm, sky blue circles – 10 nm, and yellow circles – 0 nm (plain surface without any nanopillars). Thin Film Thermocouples (TFT) were used for the measurement of surface temperature of the heater except for the data for nanofins with 464 nm height (which were obtained using wire-bead thermocouple).

6.3. Analysis of Wall Superheat Variation for Nanofins

The variation of wall superheat for CHF and MHF conditions as a function of the height of the nanofins is plotted in Figure 6-20. The wall superheat value at CHF (based heat flux through the total surface area of heater segment containing nanofins) decreases

with increase in the height of the nanofins, as shown in the value of Figure 6-20(a). Similarly the wall superheat value at MHF (based heat flux through the total surface area of heater segment containing nanofins) decreases with increase in the height of the nanofins, as shown in the value of Figure 6-20(b). These trends are observed for all values of liquid subcooling explored in this study.

Since both T_{CHF} and T_{MHF} are observed to decrease with increase in the height of the nanofins - this indicates that the pool boiling curve is shifting to the left with increase in height of the nanofins. Hence, as expected, the pool boiling heat flux is enhanced with increase in the height of the nanofins.

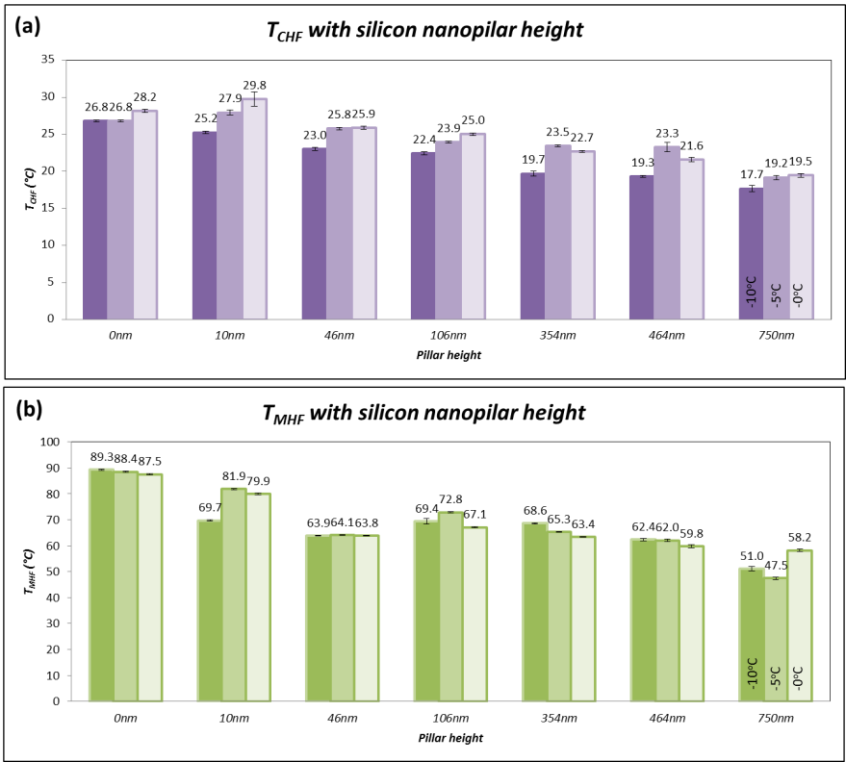

Figure 6-20 Variation of wall superheat with the height of the nanofins (a) at CHF; and (b) MHF.

The temperature interval between T_{CHF} and T_{MHF}, was plotted in Figure 6-21, to establish the temperature range for transition boiling regime. At liquid subcooling of 10°C, the temperature interval for the heater with flat surface is 62.4°C, and the temperature interval for the heater with 750nm nanofin is 33.4°C. Similarly for the saturated pool boiling experiments, the temperature interval for the heater with flat surface is 59.3°C, and the temperature interval for the heater with 750nm nanofin is 38.7°C. These results show that the temperature interval for the transition boiling regime on the horizontal heater surface decreases with increase in the height of the nanofins for all values of liquid subcooling explored in this study. These results also imply that the temperature range of the transition boiling regime can be manipulated by varying the height of the nanofins.

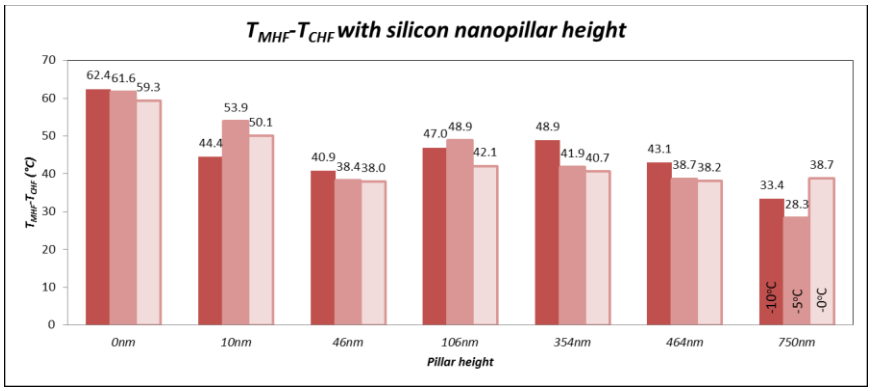

Figure 6-21 Temperature difference between T_{MHF} and T_{CHF} for liquid subcooling of 10 °C, 5 °C and 0 °C (saturated pool boiling condition) for differernt height of the nanofins.

As mentioned before, the minimum heat flux point is also known as the "Leidenfrost point", and typically the value of T_{MHF} can also be interpreted to be T_{LP}. The Leidenfrost point can be measured by dispensing liquid droplets on a heater with fairly uniform temperature where the temperature is varied parametrically over a range of temperatures. This technique can be used to determine the wall superheat at which Leidenfrost condition is achieved without requiring a pool boiling experiment to be performed [96]. Reports in the literature have shown that higher values of surface roughness increase the temperature for attaining the Leidenfrost point condition [97]. The protrusions from the surface roughness have a propensity for disrupting the vapor film supporting the liquid droplet (or liquid pool), compared to that of a smooth heater surface. Hence, surfaces with higher surface roughness have higher propensity for interrupting the vapor film and therefore reducing the stability of the vapor film for the same value of wall superheat. As a result, higher values of micro-scale surface roughness can lead to higher values of wall superheat at which the film boiling can collapse. However the effect of microstructure on the Leidenfrost point is quite ambiguous. Kim et al. showed that surface microstructures (i.e., a flat surface with engineered array of micro-pillars) can increase the Leidenfrost temperature [98]. Kruse et al. reported that the Leidenfrost temperature is enhanced on a micro/nanostructured surface when compared to that of a smooth (polished) surface [99]. In contrast, Cerro et al. reported that the Leidenfrost temperature decreased for a microstructured surface when compared to a relatively smooth surface [100]. Banerjee and Dhir reported that the thickness of the vapor film in the film boiling regime is over 15μm for a copper surface, and over 8μm

for a steel surface [77]. The contradictory results from Kim, Correy and Cerro might be explained by accounting for the vapor film thickness, which is expected to be in the same size range for the smooth surface as with that of the microstructured surface. Hence, depending on the height of the microstructure, it may interrupt the stability of vapor film while accounting for the geometry of the surface microstructures and the resulting vapor film thickness.

The effect of nanostructured surfaces on Leidenfrost temperature has not been explored in the literature as extensively. As shown in Figure 6-20(b), the T_{MHF} for heaters with nanofins is smaller than that on a flat (smooth) surface. The experimental results also showed that the value of T_{MHF} is decreased with the increase in height of nanofins as discussed earlier.

In contrast with microstructured surfaces, nanostructured surfaces cannot interrupt the vapor film stability, because the height of the nanofins is much smaller than the minimum thickness of the vapor film. Moreover the surface with nanofins causes lower values of MHF to be achieved as the height of the nanofins is increased, as shown in Figure 6-22.

This conundrum can be resolved by considering that the heat transfer from the nanofins to the vapor film is primarily by conduction (plausibly in a non-continuum flow regime). Therefore the enhanced surface area caused by the presence of the nanofins with higher height – results in more heat to be conducted into the vapor film for a given value of wall superheat. As a result, more vapor is produced in the liquid-vapor interface during film boiling causing the vapor film to be more stable. This implies that the vapor

film is more stable at lower values of wall superheat and the vapor film survives at lower values of wall superheat as the height of the nanofins is increased.

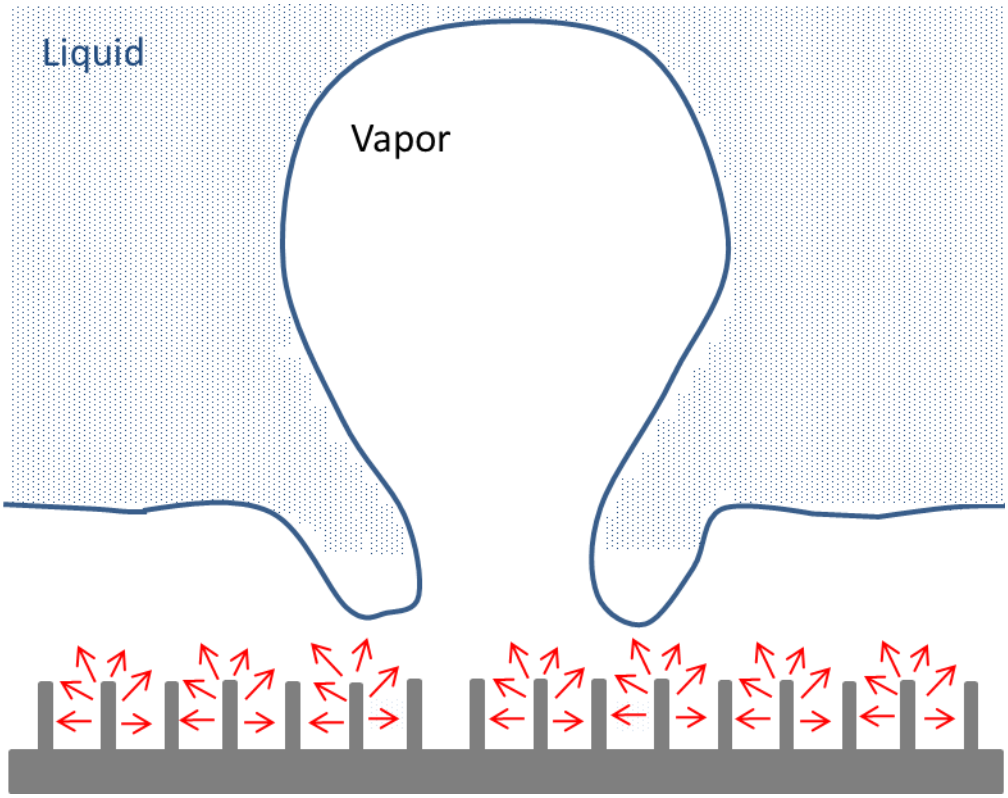

Figure 6-22 Schematic of film boiling on a heater with patterned arrays of nanofins. (Note: figure is not to scale)

6.4. Analysis of Wall Heat Flux Variation for Silicon Nanofins

6.4.1. Heat Flux Through Projected Area of Nanofins (q_n")

The values of heat flux through the projected area of a surface with nanofins (q_n") are plotted in Figure 6-23 for CHF and MHF conditions. The results show that

CHF increases with increase in height of the nanofins, while MHF is decreased with increase in height of the nanofins, for all values of liquid subcooling explored in this study.

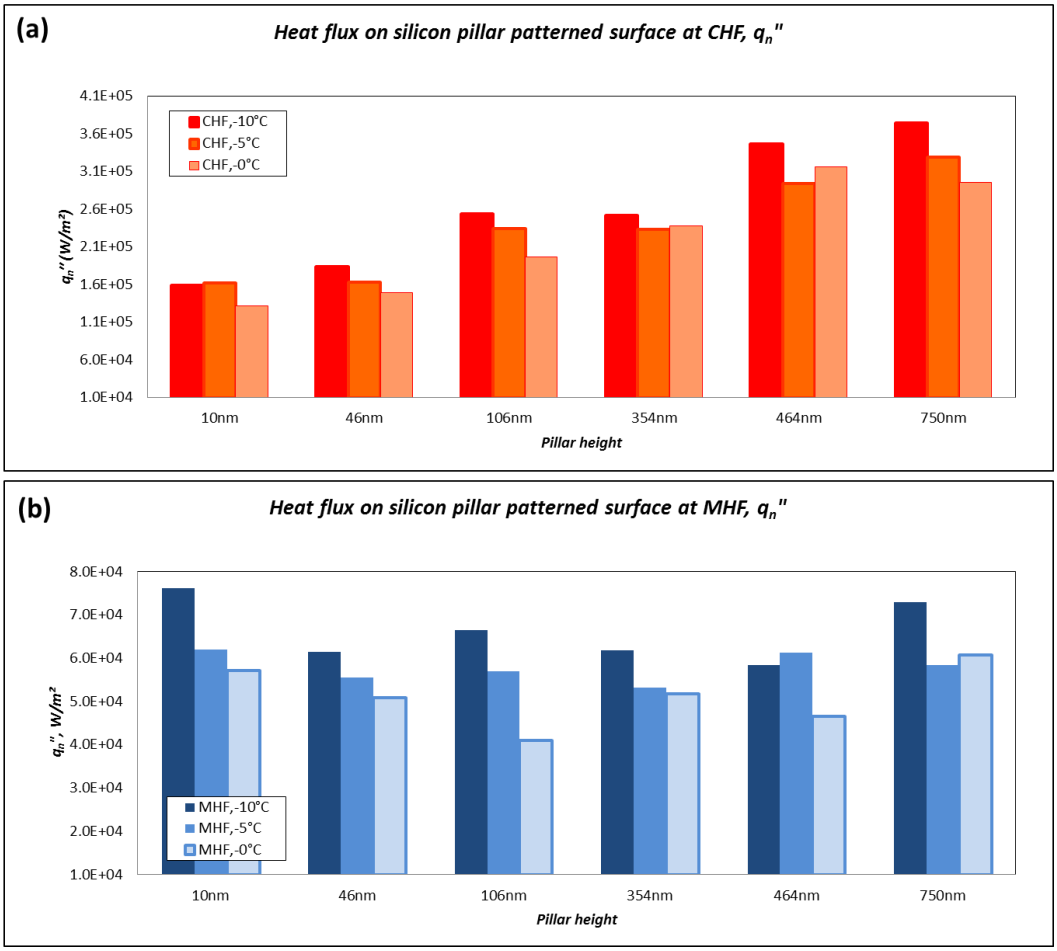

Figure 6-23 Heat flux through projected area for surface with nanofins (qn") as a function of the height of the nanofins for (a) CHF; and (b) for MHF.

The heat flux values plotted in the previous figure were normalized with that of a flat surface (without nanofins) and plotted in Figure 6-24. In this plot, the dark bar

represents liquid subcooling of 10^{o}C, the bright bar represents liquid subcooling of 5^{o}C and the hollow bar represents liquid subcooling of 0 ^{o}C (saturated pool boiling condition).

The plots show that for liquid subcooling of 10^{o}C the CHF values for the nanofinned surfaces are enhanced (compared to that of the smooth heater) by 12% for nanofin height of 10 nm (which is within the bounds of measurement uncertainty based on results shown in the Appendix), by 29% for nanofin height of 46 nm (which is within the bounds of measurement uncertainty based on results shown in the Appendix), by 79% for nanofin height of 106 nm, by 78% for nanofin height of 354 nm, by 144% for nanofin height of 464 nm and 164% for nanofin height of 750 nm. The maximum enhancement of critical heat flux was observed for the nanofins with a height of 750 nm. The figure shows that for the nanofins with a height of 750 nm the CHF values are enhanced (compared to that of a flat or smooth silicon heater surface) by 164% at liquid subcooling of 10 ^{o}C, by 149% at liquid subcooling of 5 ^{o}C, and by 136% at liquid subcooling of 0 ^{o}C (i.e., for saturated pool boiling experiments). It is expected that the surfaces with nanofins will enhance the pool boiling heat flux because of the higher surface area with increase in height of the nanofins for these patterned surfaces. It is not clear if the heat flux values obtained for the projected values of the heater surface area (with nanofins) would scale as the increase in surface area of the surface with nanofins.

In contrast for the heat flux values based on the projected area of the heater surface with nanofins, the change in MHF values is not as significantly large as that of the CHF values, but on the contrary the MHF values decrease marginally as the height of

the nanofins is increased. . For example, the value of MHF for a heater with nanofins of 750nm height (compared to that of a flat smooth surface) is decreased by: 3% for liquid subcooling of 10°C, by 17% for liquid subcooling of 5°C, and by 13% for saturated pool boiling experiments nm (which are within the bounds of measurement uncertainty based on results shown in the Appendix, hence can be concluded they remain unchanged).

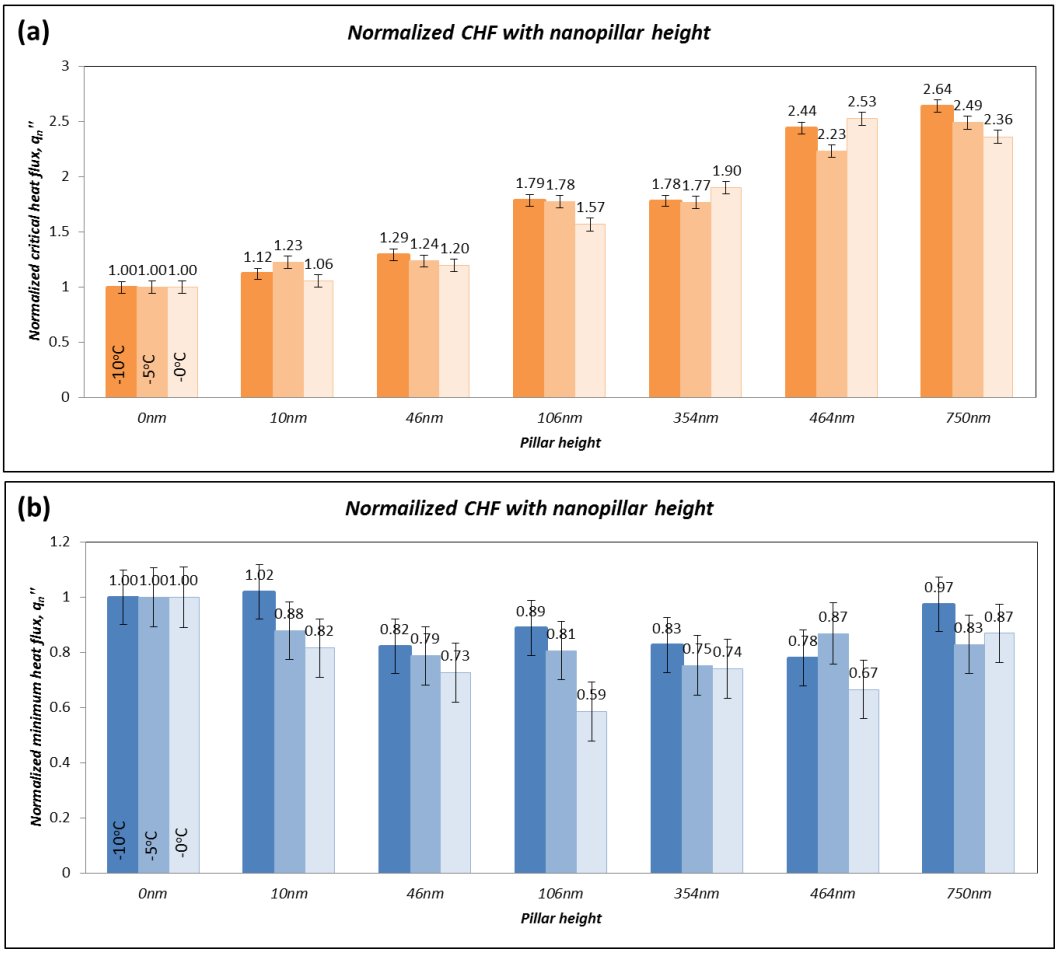

Figure 6-24 Normalized values for heat flux (q_n") through the projected area on the surface of the heater with nanofins for: (a) CHF; and (b) MHF conditions; at liquid subcooling of 10°C and 5°C as well as saturated pool boiling experiments. The heat flux values are normalized with that of a flat smooth heater surface.

Since the Leidenfrost point occurs at lower values of wall superheat (as it is expected that the vapor film is more stable with increase in height of the nanofins) there is lower magnitudes of heat transfer by conduction from the heater surface to the vapor film due to lower values of the temperature difference (even though the surface area is increased), leading to lower values of MHF.

6.4.2. Heat Flux Through the Total Surface Area of Heater Segment Containing Nanofins (q_{nc}")

The heat flux through the total surface area of heater segment with nanofins (q_{nc}") is plotted in Figure 6-25 for both CHF and MHF conditions. As expected, the CHF values are observed to increase with increase in height of the nanofins, as shown in Figure 6-25(a). In contrast, the MHF values are observed to decrease with decrease in the height of the nanofins, as shown in Figure 6-25(b), respectively.

These results show that even after accounting for the surface area enhancement the CHF values are enhanced at a higher rate than the rate of increase of the surface area of the heaters with the nanofins. In other words, the CHF values are enhanced at a higher rate than the rate of increase of surface area, as the height of the nanofins is increased. It is expected that the bubble departure size for nanostructured surfaces is decreased (typically by a factor of 2-4) resulting in higher bubble nucleation density, lower bubble departure volume and higher bubble departure frequency. In addition, the nanofins can enhance the transient heat transfer during liquid-solid interactions that occurs with the departure of each vapor bubble. A cumulative effect of these transient heat transfer

phenomena is higher impact on the heat transfer enhancement due to the rate at which surface area is enhanced with the increase in height of the nanofins.

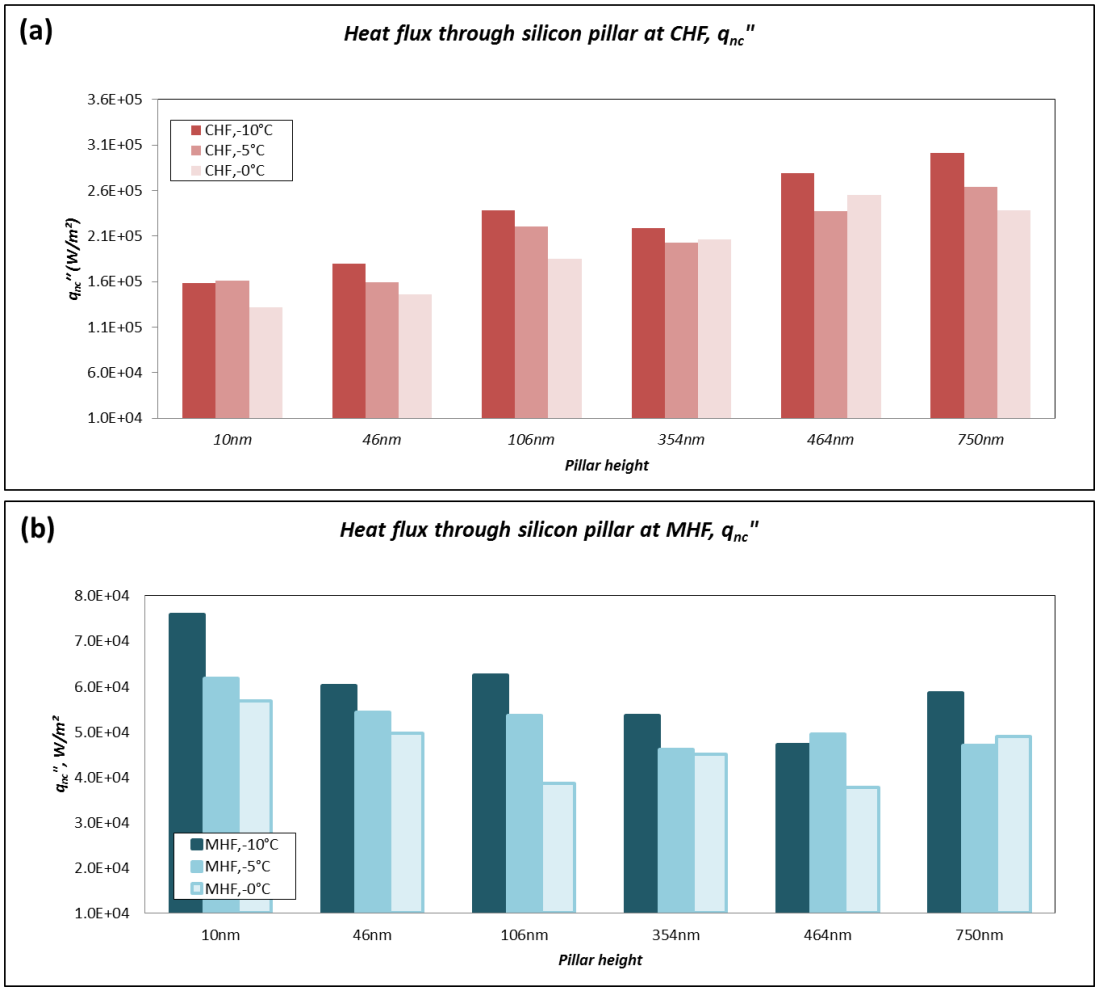

Figure 6-25 Heat flux through the total surface area of heater segment containing nanofins (qnc") for: (a) CHF; and (b) MHF conditions (as a function of the height of the nanofins).

6.5. Contact Angle

The contact angle of PF-5060 on the diced silicon wafers with the nanofins of different heights was measured, both before and after conducting the pool boiling experiments. The contact angle measurements obtained after performing the pool boiling experiments are shown in Figure 6-26. Contact angles were measured 3 times for each substrate and the details of the measurement procedure were described in Chapter 5. Contact angle was measured for nanofins with different heights, both before and after the pool boiling experiments and are shown in Figure 6-27.

The contact angle values for the silicon heaters with nanofins for different height of the nanofins are listed in Table 6-3, for both before and after conducting the pool boiling experiments.

The heat flux values for liquid subcooling of 10 °C were normalized with that of the flat smooth silicon heater and are plotted in Figure 6-28 for both CHF and MHF conditions as a function of the height of the nanofins along with the values of contact angle of PF-5060 (both before and after the experiments). The figure shows that the contact angle decreases as the height of the nanofins is increased (both of before and after the pool boiling experiments) with a concomitant increase in the values of CHF as well as concomitant decrease in the values of MHF.

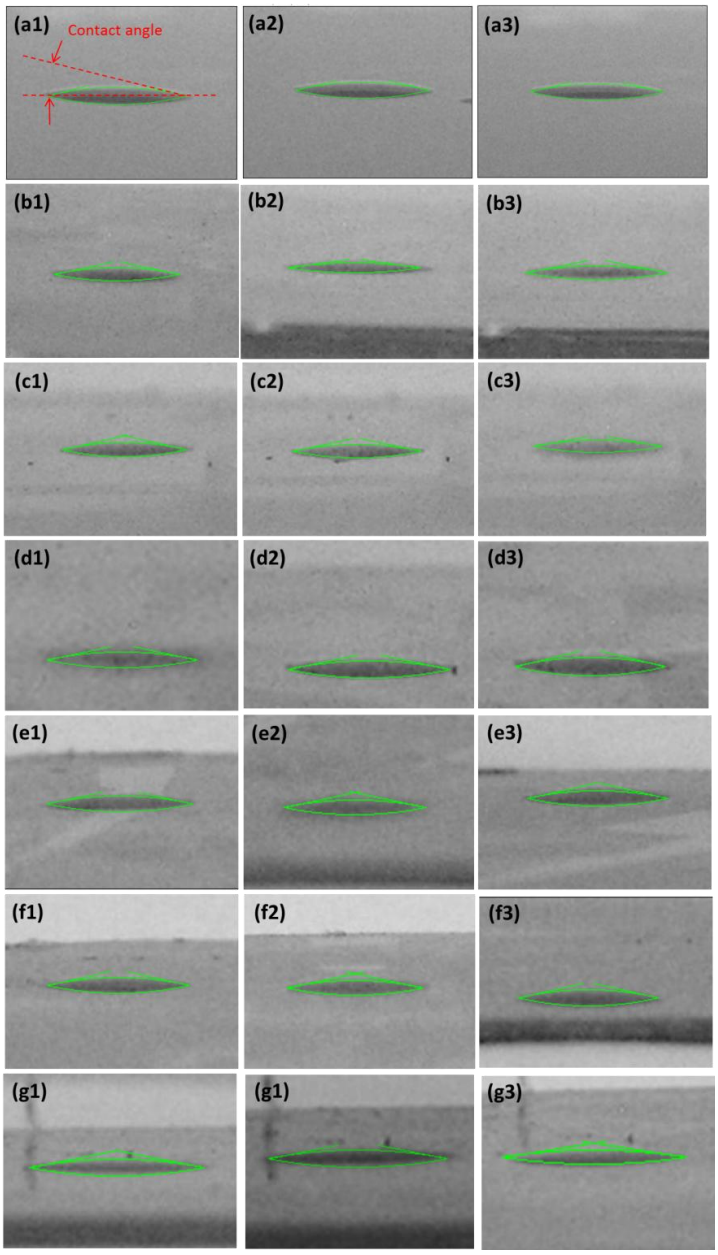

Figure 6-26 Contact angle measurement for PF-5060 after performing boiling experiment as function of the height of the nanofins: (a) 0 nm (flat smooth surface), (b) 10 nm, (c) 46 nm, (d) 106 nm, (e) 354 nm, (f)464 nm, and (g) 750 nm. Contact angles were measured 3 times for each surface. For example on flat silicon surface, (a1) 14.070°, (a2) 13.604°, and (a3) 13.590°: yields and average contact angle of 13.8° and standard deviation of 0.22°. Contact angle was measured by using freeware tool called "Image J".

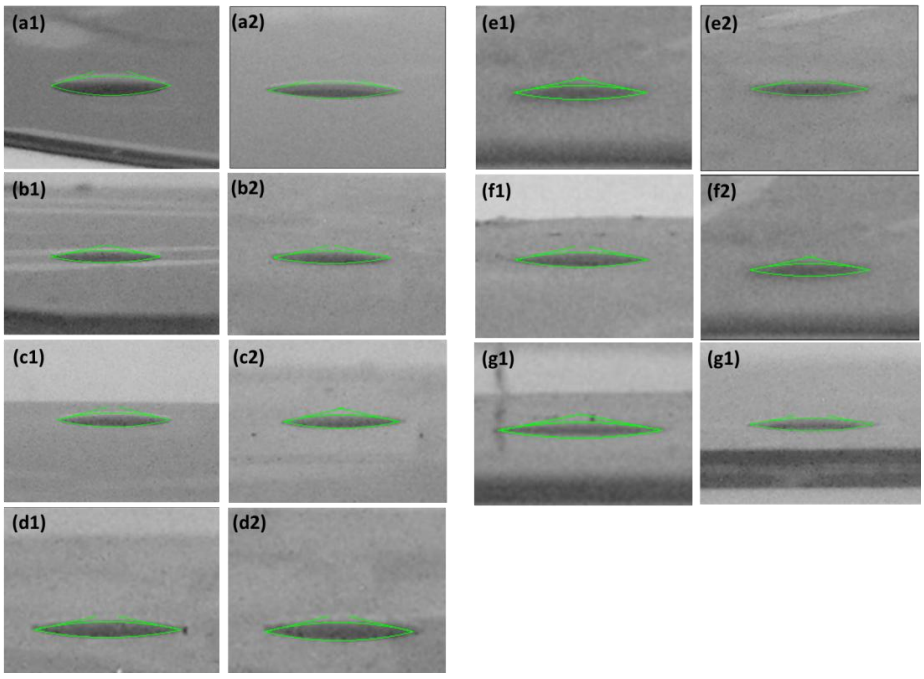

Figure 6-27 Contact angle measurement for PF-5060 for (1) before, and (2) after performing boiling experiments. The measurements are reported as a function of the height of the nanofins for silicon heater: (a) 0nm(flat), (b) 10nm, (c) 46nm, (d) 106nm, (e) 354nm, (f)464nm and (g) 750nm. For example, contact angle of flat silicon surface is shown in (a1) for results obtained before performing the pool boiling experiments and in (a2) for results obtained after performing the pool boiling experiments.

Table 6-3 Contact angle measurements for silicon heaters with nanofins of different height, both before and after performing the pool boiling experiments

Height of silicon nanopillar	Before pool boiling		After pool boiling	
	Average, °	STD	Average, °	STD
Flat	17.8	0.75	13.8	0.22
10nm	11.4	0.54	10.4	1.43
46nm	14.7	1.32	12.1	0.70
106nm	13.2	0.79	12.4	0.84
354nm	12.2	1.00	11.1	0.28
464nm	12.7	0.67	12.6	0.36
750nm	11.7	0.26	10.1	1.11

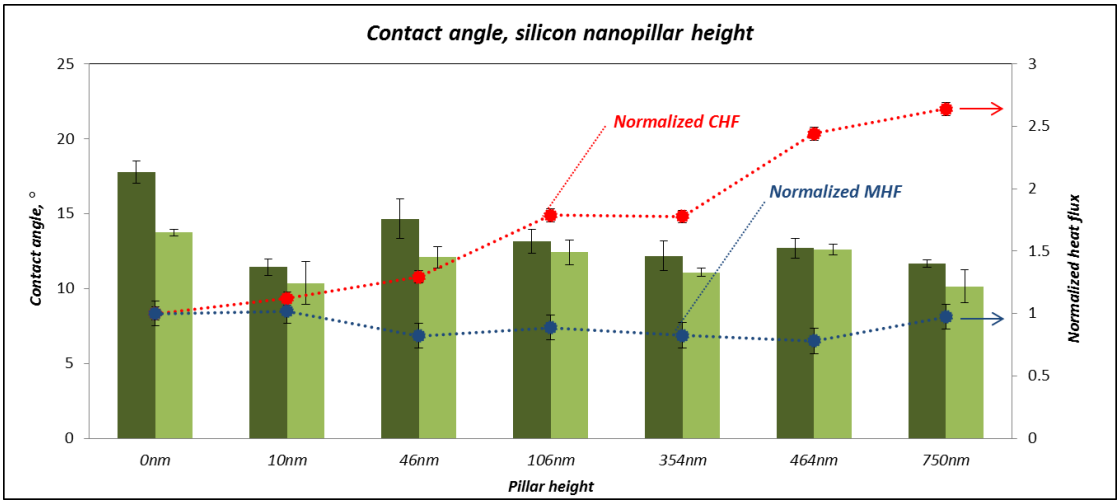

Figure 6-28 Plot of contact angle values (dark: before; and light: after conducting the pool boiling experiments) as a function of height of the silicon nanofins. The values of heat flux normalized with that of a plain smooth silicon wafer for liquid subcooling of 10 °C are also plotted for both CHF and MHF conditions.

6.6. Summary

In this chapter, the pool boiling phenomena was explored for a flat silicon heater with surface nanostructures (nanopillars or nanofins) of different height. Pool boiling curves were plotted for these heaters with nanofins of different heights for different values of liquid subcooling. The results show that wall superheat for CHF and MHF conditions decreases with increase in the height of the nanofins. This indicates that the pool boiling curve progressively shifts to the left with increase in height of the nanofins. In addition, the temperature difference between T_{CHF} and $T_{MHF,}$ also decreases with increase in the height of the nanofins. This implies that the temperature interval of the transition boiling regime decreases with increase in the height of the nanofins. The

contact angle values (both for before and after performing the pool boiling experiments) are observed to decrease with the increase in the height of the nanofins.

7. POOL BOILING EXPERIMENTS ON HORIZONTAL FLAT HEATERS WITH SILICA NANOFINS

In this chapter, the effect of variation of material properties of surface nanostructures (i.e., nanopillars or nanofins) on pool boiling phenomena will be studied. The silicon dioxide (i.e., silica) nanofins were fabricated using nanolithography techniques on a silicon wafer along with dry etching followed by oxidation of the nanofins. Thin Film Thermocouple arrays were then fabricated on the silica nanostructures for measuring the surface temperature fluctuations of the silica nanofins during pool boiling of PF-5060 on the heater surface. The objective of the experiments described in this chapter is to explore the effect of variation in material properties of heater surface with nanofins on the pool boiling curve.

7.1. Experimental Results

The silicon wafer surface with different height of nanofins was prepared using fabrication techniques described in Chapter 2 followed by oxidation of the nanofins to obtain a heater surface with silica nanostructures. The height of silica nanofins were 108 nm and 210 nm. The details of the silica nanofin geometric dimensions were described in Chapter 2 and listed in Appendix A. The wafer with the silica nanofins was mounted on the calorimeter apparatus (copper block) using a stainless steel clamp with a rectangular aperture. Pool boiling experiments were performed using the rectangular heater configuration for different values of liquid subcooling (10 ^{o}C, 5 ^{o}C and 0 ^{o}C) and

each experiment was performed twice to ensure repeatability of the experiments. The experimental data were used to plot the pool boiling curves which were used for further analyses.

The pool boiling curves for silica nanofins are shown in Figure 7-1 for nanofins with a height of 108 nm and in Figure 7-2 for nanofins with a height of 210 nm. In these plots, icons with solid (filled) circle represents experimental data for liquid subcooling of 10 ^{o}C, patterned circle represents experimental data for liquid subcooling of 5 ^{o}C, and hollow circle represents experimental data for liquid subcooling of 0 ^{o}C (saturated pool boiling experiments). The individual boiling curves obtained from Run 1 and Run 2 of each experiment are plotted in Appendix E. The plots show that for nucleate boiling the pool boiling curves shift to the left with increasing values of liquid subcooling. On the other hand, for film boiling, the pool boiling curves shift to the right with increasing values of liquid subcooling.

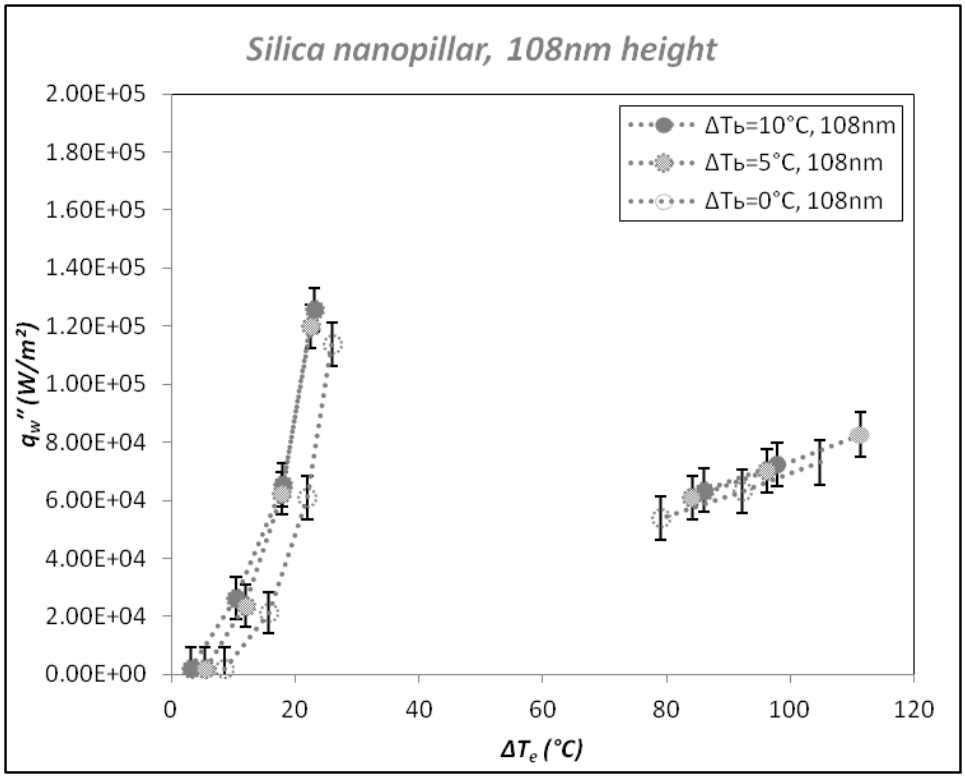

Figure 7-1 Pool boiling curves on rectangular silica heater surface with nanofins of 108 nm height for liquid subcooling of 10 °C, 5 °C and 0 °C (saturated pool boiling experiments). Thin Film Thermocouples (TFT) were used for surface temperature measurement.

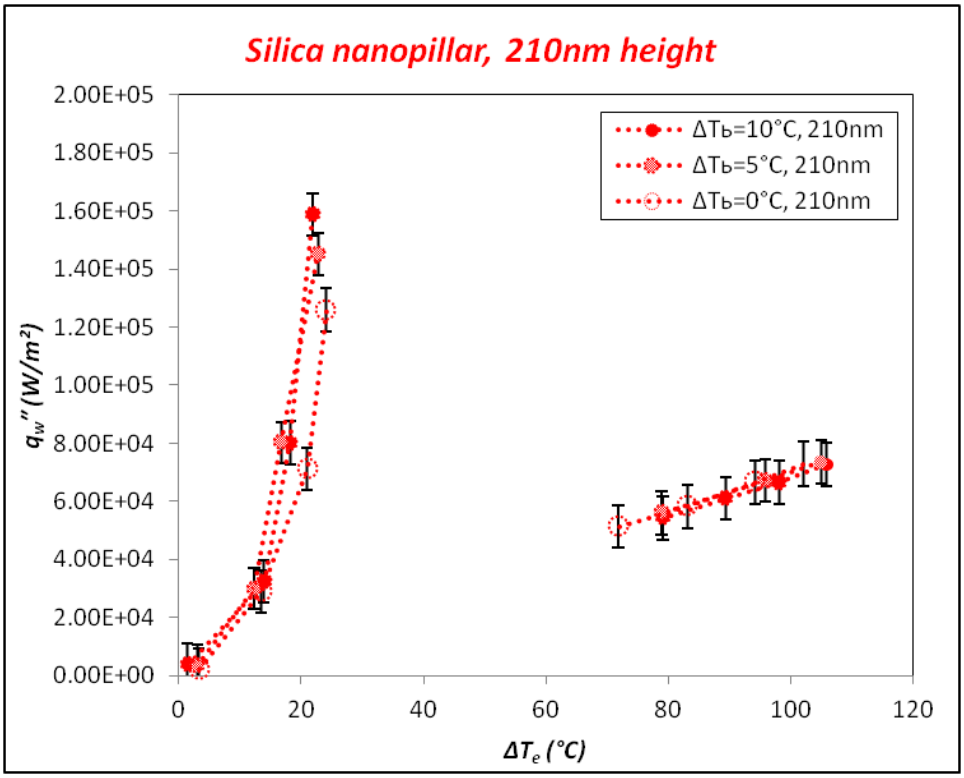

Figure 7-2 Pool boiling curves on rectangular silica heater surface with nanofins of 210 nm height for liquid subcooling of 10 °C, 5 °C and 0 °C (saturated pool boiling experiments). Thin Film Thermocouples (TFT) were used for surface temperature measurement.

7.2. Data Analysis for Heat Flux on Silica Nanofins

The wall heat flux values for rectangular heater with silica nanofins are compiled and plotted in Figure 7-3. Moreover selected values are also listed in Table 7-1 (Uncertainty values are listed in Appendix E). The figure shows that for the nucleate boiling regime the boiling curves progressively shift to the left with increase in height of the nanofins and with increase in liquid subcooling. In addition, the CHF values for the silica heater surface increases with the height of the nanofins. The pool boiling

experimental results for silica nanofins has similar trends to that of silicon nanofins for the nucleate boiling regime.

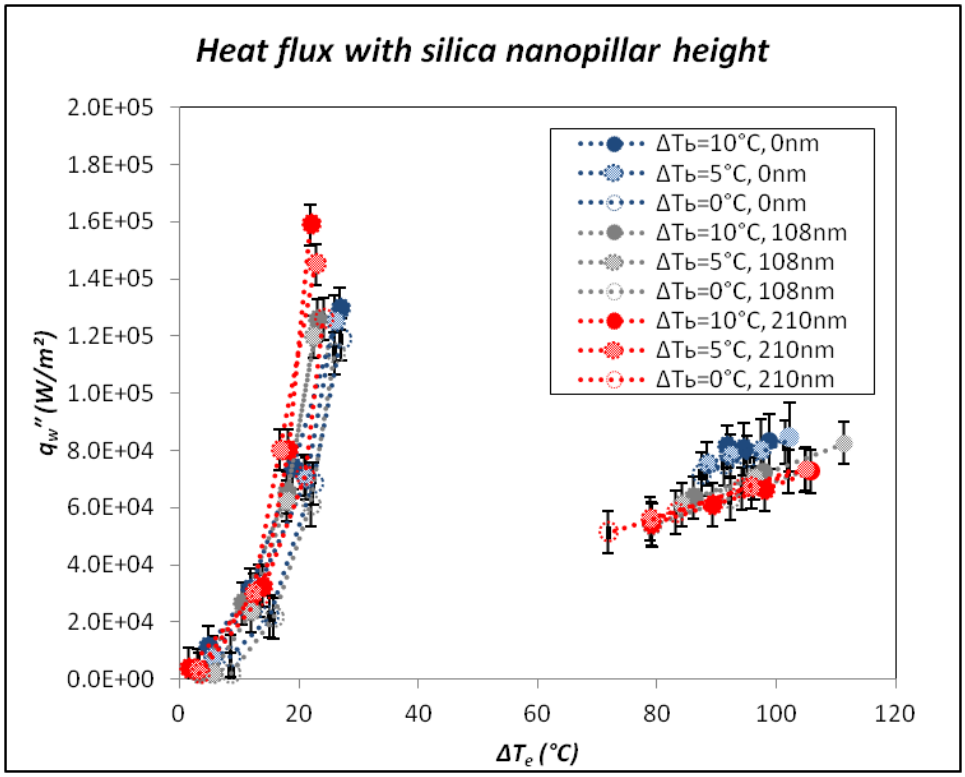

Figure 7-3 Pool boiling curves on rectangular silica heater surface with smooth surface as well as nanofins of 108 nm and 210 nm height, for liquid subcooling of 10 °C, 5 °C and 0 °C (saturated pool boiling experiments). Thin Film Thermocouples (TFT) were used for surface temperature measurement.

Table 7-1 Summary of heat flux values (CHF and MHF) on the heater surface (q_w") with silica nanofins at liquid subcooling values of 10 ^oC, 5 ^oC and 0 ^oC (saturated pool boiling experiments)

Subcooling 10°C	Critical heat flux		Minimum heat flux	
Height of nanopillar	Wall superheat, °C	Heat flux, W/m²	Wall superheat, °C	Heat flux, W/m²
0	26.8	1.30E+05	91.7	8.13E+04
108.3	23.1	1.26E+05	86.1	6.34E+04
210.4	21.9	1.59E+05	79.1	5.44E+04
Subcooling 5°C	Critical heat flux		Minimum heat flux	
Height of nanopillar	Wall superheat, °C	Heat flux, W/m²	Wall superheat, °C	Heat flux, W/m²
0	26.0	1.25E+05	88.4	7.53E+04
108.3	22.5	1.20E+05	84.2	6.10E+04
210.4	22.8	1.45E+05	78.9	5.61E+04
Saturated	Critical heat flux		Minimum heat flux	
Height of nanopillar	Wall superheat, °C	Heat flux, W/m²	Wall superheat, °C	Heat flux, W/m²
0	27.1	1.19E+05	87.5	7.16E+04
108.3	26.0	1.14E+05	79.1	5.38E+04
210.4	24.1	1.26E+05	71.8	5.12E+04

Best fit curves (exponential fit) were generated for the pool boiling curves in the nucleate boiling regime for heater with plain silica surface. This procedure is similar to that performed for silicon nanofins. The heat flux values on the non-patterned area of the silica surface was estimated using the best fit curve generated in this exercise, as shown in Figure 7-4.

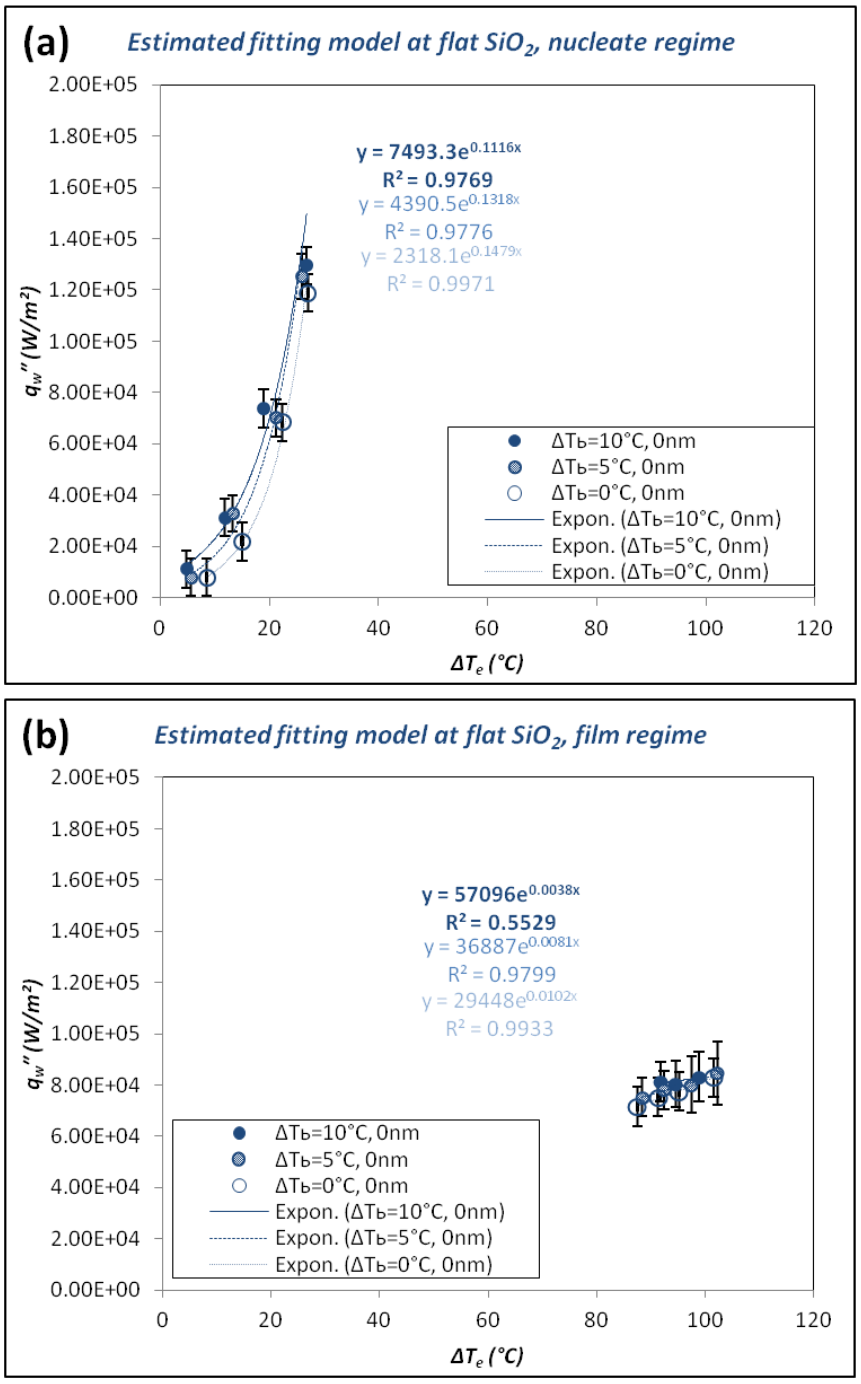

Figure 7-4 Best fit curves (with exponential fit) obtained for experimental data on flat silica heater with plain surface (without any patterned nanostructures) for liquid subcooling of 10^{o}C and 5^{o}C as well as saturated pool boiling experiments for the: (a) nucleate boiling regime; and (b) film boiling regime.

The best fit curves are then used to estimate the heat flux through the projected area of the heater with the silica nanofins and is plotted in Figure 7-5 and selected values are also listed in Table 7-2. The figure shows significant enhancement in the pool boiling heat flux values with increase in height of the nanofins, for all values of liquid subcooling used in this study.

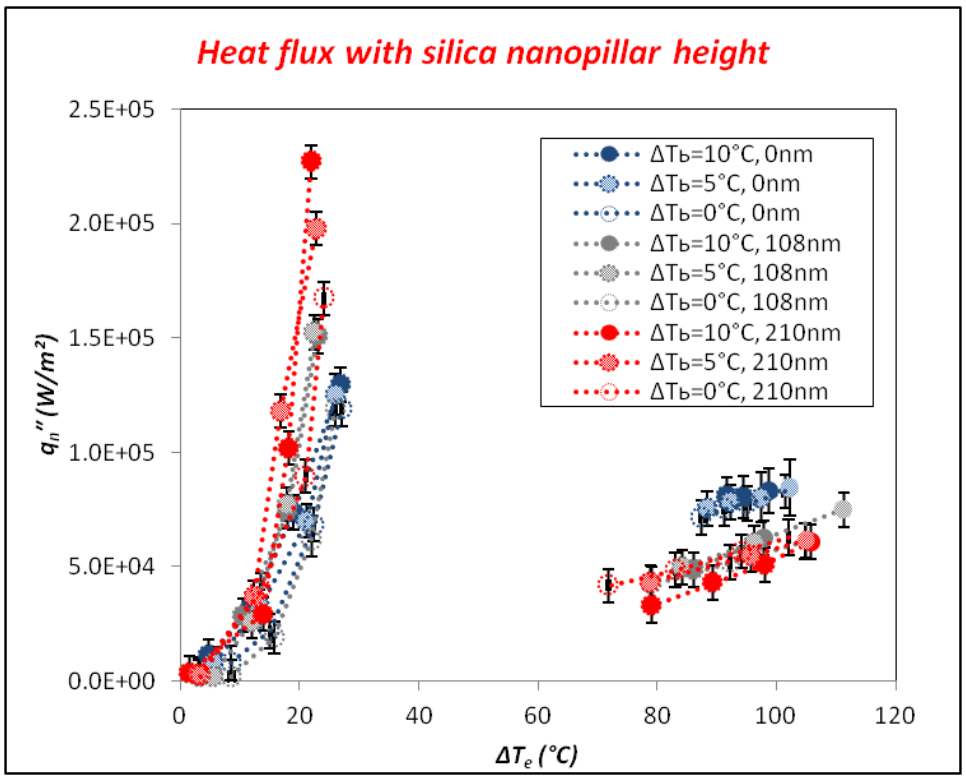

Figure 7-5 Pool boiling curve for rectangular heater with a silica surface containing surface nanostructures (nanofins). The heat flux values are based on the projected area occupied by the nanofins (q_n"). The liquid subcooling in these experiments were 10 °C, 5 °C and 0 °C.

Table 7-2 Summary of heat flux values (CHF and MHF) through the projected area of the heater surface (q_n") with silica nanofins at liquid subcooling values of 10 ^oC, 5 ^oC and 0 ^oC (saturated pool boiling experiments)

Subcooling 10°C	Critical heat flux		Minimum heat flux	
Height of nanopillar	Wall superheat, °C	Heat flux, W/m²	Wall superheat, °C	Heat flux, W/m²
0	26.8	1.30E+05	91.7	8.13E+04
108.3	23.1	1.51E+05	86.1	4.85E+04
210.4	21.9	2.27E+05	79.1	3.29E+04
Subcooling 5°C	Critical heat flux		Minimum heat flux	
Height of nanopillar	Wall superheat, °C	Heat flux, W/m²	Wall superheat, °C	Heat flux, W/m²
0	26.0	1.25E+05	88.4	7.53E+04
108.3	22.5	1.53E+05	84.2	4.97E+04
210.4	22.8	1.98E+05	78.9	4.30E+04
Saturated	Critical heat flux		Minimum heat flux	
Height of nanopillar	Wall superheat, °C	Heat flux, W/m²	Wall superheat, °C	Heat flux, W/m²
0	27.1	1.19E+05	87.5	7.16E+04
108.3	26.0	1.19E+05	79.1	4.23E+04
210.4	24.1	1.67E+05	71.8	4.18E+04

Based on the heat flux values calculated through the projected area occupied by the nanofins (q_n") the heat flux values through the total area of the fins on the heater surface (q_{nc}") were calculated. The heat flux through the silica nanofin patterned surface (q_{nc}") for liquid subcooling of 10^{o}C and 5^{o}C as well as saturated pool boiling condition are plotted in Figure 7-6 (Selected values are available in Appendix E). The results show significant enhancement in the heat flux values for the nucleate boiling regime with increase in height of the silica nanofins.

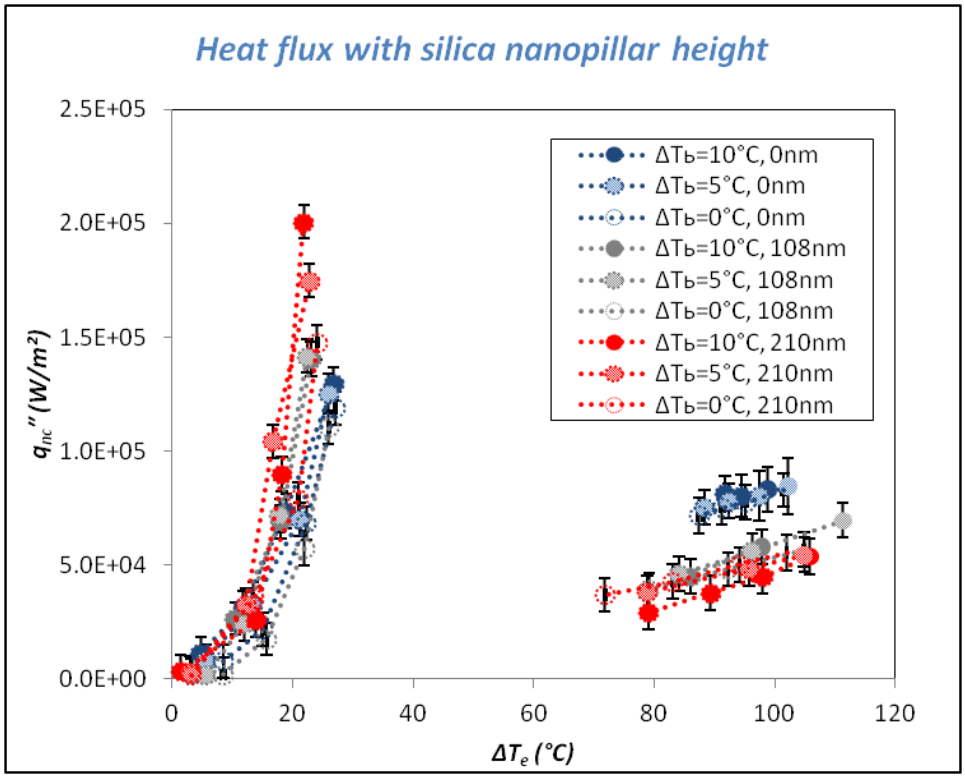

Figure 7-6 Pool boiling curve for rectangular heater with a silica surface containing surface nanostructures (nanofins). The heat flux values are based on the total surface area occupied by the nanofins (q_{nc}"). The liquid subcooling in these experiments were 10 °C, 5 °C and 0 °C.

7.3. Analysis of Wall Superheat Variation for Nanofins

The variation of wall superheat for CHF and MHF conditions as a function of the height of the nanofins is plotted in Figure 7-7. The wall superheat values for CHF and MHF are plotted in Figure 7-7(a) and Figure 7-7(b). The figures show that the CHF values are enhanced and MHF values are degraded with increase in height of the nanofins as well as increase in liquid subcooling. This indicates that the boiling curves progressively shift to the left with increase in height of the nanofins as well as increase in liquid subcooling.

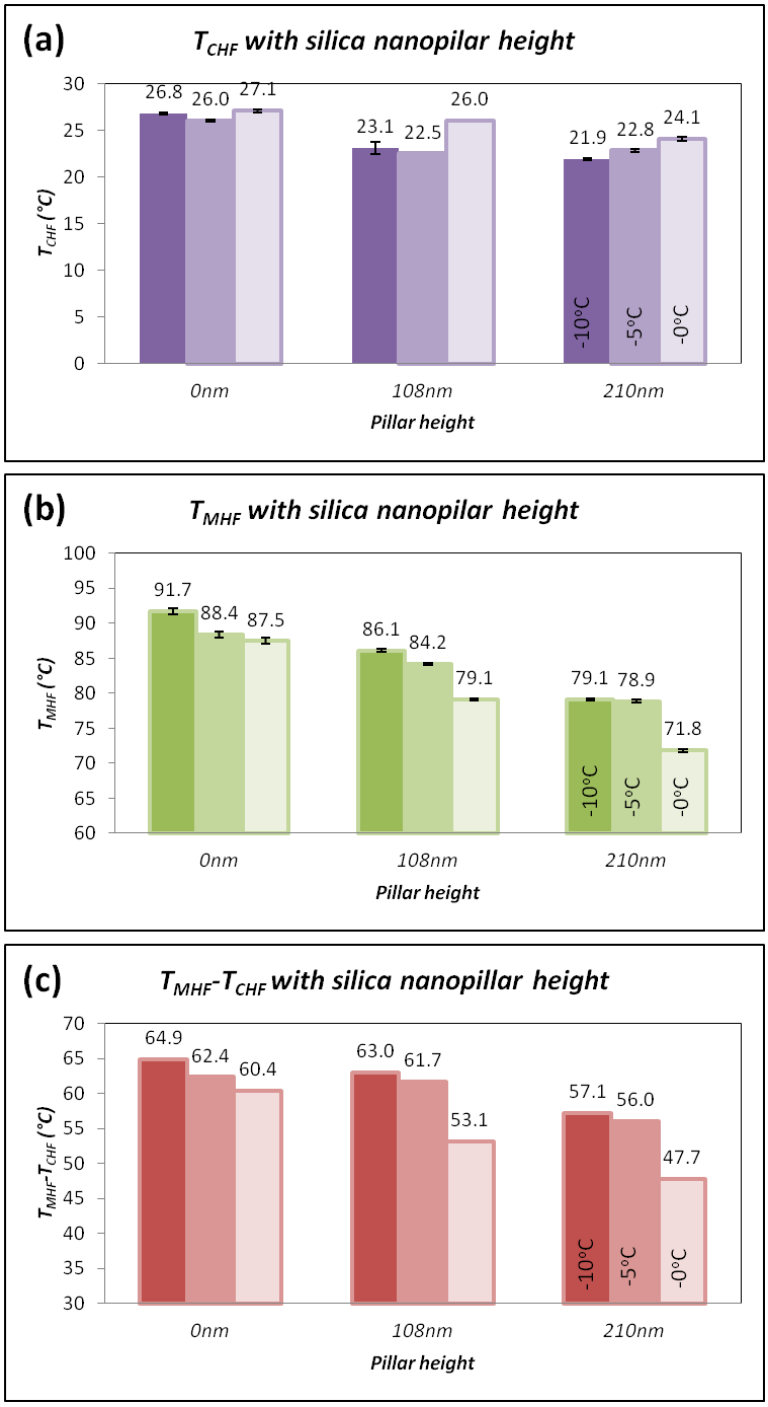

Figure 7-7 Variation of wall superheat with the height of the silica nanofins at (a) CHF; and (b) MHF. (c) Temperature difference between T_{MHF} and T_{CHF} for differernt height of the nanofins

The temperature difference between T_{CHF} and T_{MHF} is plotted in Figure 7-7(c). The result shows that range of wall superheat for transition boiling decreases with increase in height of the nanofins.

7.4. Analysis of Wall Heat Flux Variation for Silica Nanofins

7.4.1. Heat Flux Through Projected Area of Silica Nanofins (q_n")

The values of heat flux through the projected area of heater surface with silica nanofins (q_n") are plotted in Figure 7-8 for CHF and MHF conditions. The results show that CHF increases with increase in height of the nanofins, while MHF is decreased with increase in height of the nanofins, for all values of liquid subcooling explored in this study. These results are similar to that of the silicon nanofins, which indicates that nanofins enhance pool boiling heat flux regardless of the material composition of the nanofins.

The heat flux values plotted in the previous figure were normalized with that of a flat surface (without nanofins) and plotted in Figure 7-9. In this plot, the dark bar represents liquid subcooling of 10^{o}C, the bright bar represents liquid subcooling of 5^{o}C and the hollow bar represents liquid subcooling of 0 ^{o}C (saturated pool boiling condition). The plots show that for liquid subcooling of 10^{o}C the CHF values for the nanofinned surfaces are enhanced (compared to that of the smooth heater) by 16% for nanofin height of 108 nm (which is within the bounds of the measurement uncertainty), and by 75% for nanofin height of 210 nm. The CHF values are observed to increase with height of the nanofins for all values of liquid subcooling. In contrast the MHF values

decrease as the height of the nanofins is increased. For example, at liquid subcooling of 10 ^{o}C the value of MHF for a heater with nanofins (compared to that of a flat smooth surface) is decreased by: 36% for height of 108 nm and by 56% for height of 210 nm. Similar trends are observed for the saturated pool boiling experiments and for liquid subcooling of 5 ^{o}C.

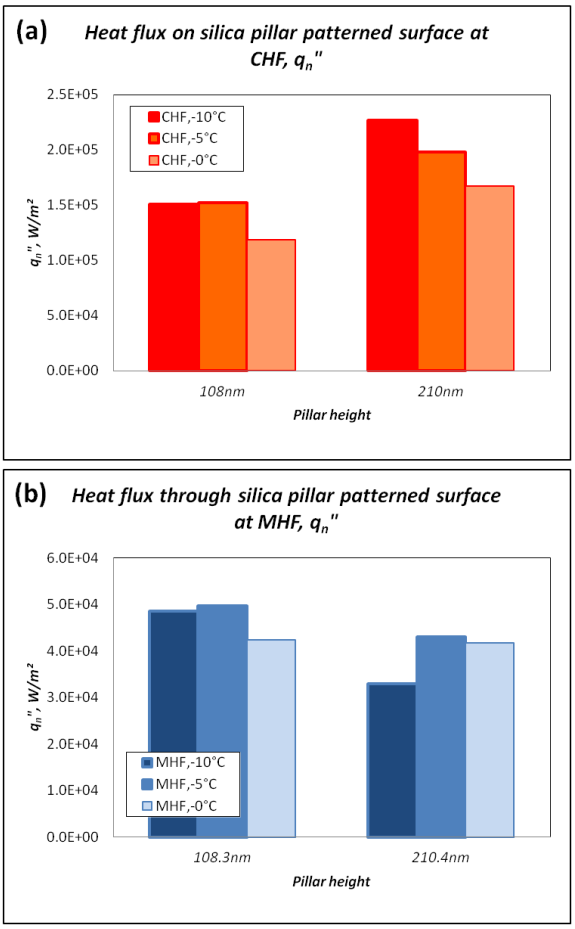

Figure 7-8 Heat flux through projected area for surface with nanofins (q_n") as a function of the height of the nanofins for (a) CHF; and (b) MHF.

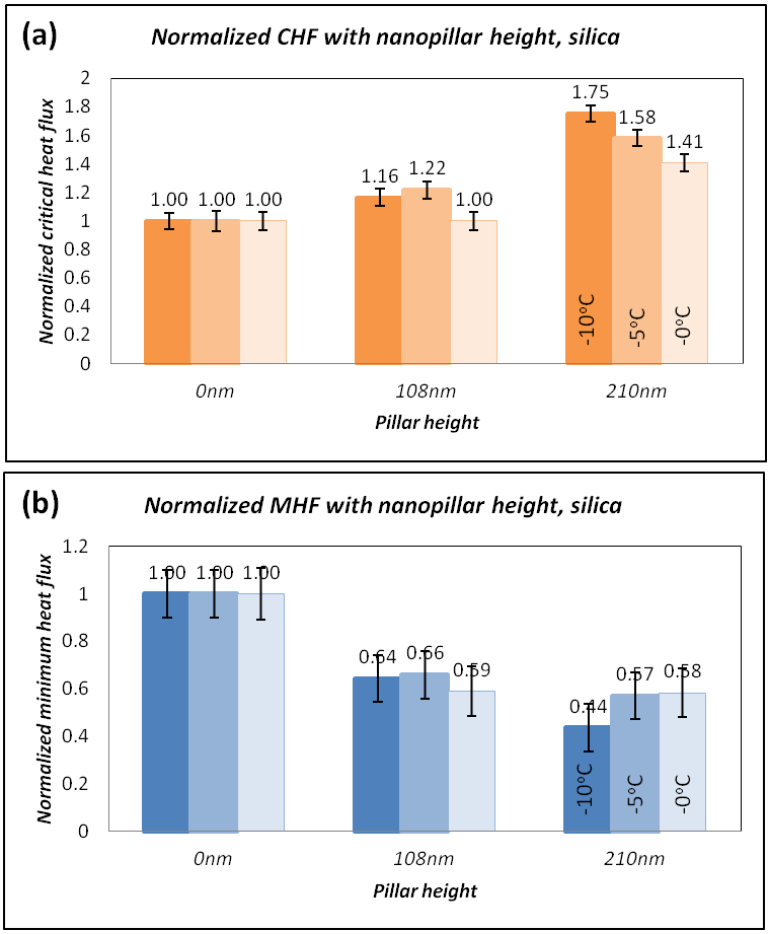

Figure 7-9 Normalized values for heat flux (q_n") through the projected area on the surface of the heater with nanofins for: (a) CHF; and (b) MHF conditions; at liquid subcooling of 10°C and 5°C as well as saturated pool boiling experiments. The heat flux values are normalized with that of a flat smooth heater surface.

7.4.2. Heat Flux Through the Total Surface Area of Heater Segment Containing Nanofins (q_{nc}")

The heat flux through the total surface area of heater segment with nanofins (q_{nc}") is plotted in Figure 7-10. As expected, the CHF values are observed to increase with increase in height of the nanofins. These trends are similar to that of silicon nanofins. This indicates that the heat flux through nanofin is enhanced by nanofins, regardless of

the material composition of the nanofins.Hence the pool boiling heat flux enhancement is a function of nanofin geometry as well as material composition of the nanofins.

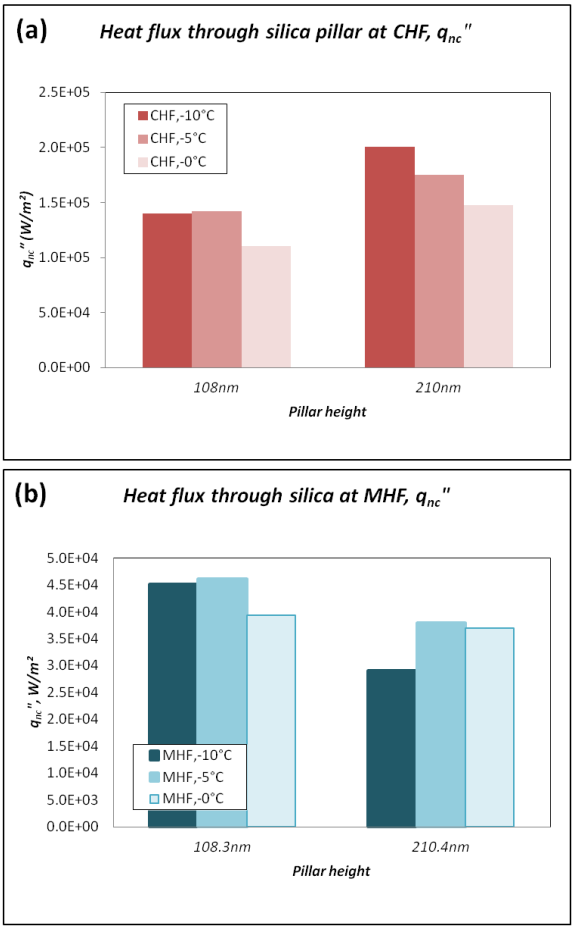

Figure 7-10 Heat flux through the total surface area of heater segment containing silica nanofins (q_{nc}") for: (a) CHF; and (b) MHF conditions (as a function of the height of the nanofins).

7.5. Contact Angle with Height

The contact angle of PF-5060 on the diced silicon wafers with the silica nanofins of different heights were measured, both before and after conducting the pool boiling

experiments. The contact angle measurements obtained after performing the pool boiling experiments are shown in Figure 7-11 along with the heat flux values normalized with that of the flat smooth silica heaters (without any patterned nanofins) for the CHF and MHF conditions.

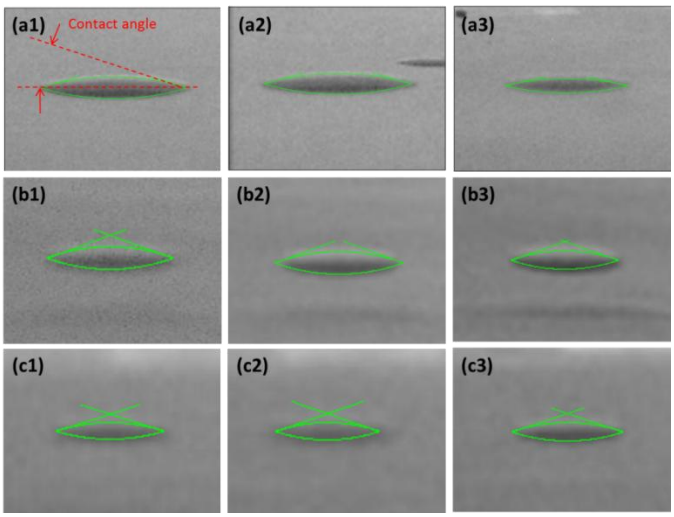

Figure 7-11 Contact angle measurements for PF-5060 on silica heater surface after boiling experiment for different nanofin heights of: (a) 0nm (flat) (b) 108nm (c) 210nm. Contact angle values were measured 3 times for each surface. For example, flat silica surface (a1) 20.703° (a2) 19.846° (a3) 17.094°: hence the average contact angle is 19.2° and the standard deviation is 1.54°. Contact angle was measured by freeware tool called "Image J".

Contact angle measurements for silica heater surfaces with nanofins of different heights (both before and after the pool boiling experiments) are shown in Figure 7-12.

The contact angle values for PF-5060 on silica heaters with nanofins of different height are listed in Table 7-3, for both before and after performing the pool boiling experiments.

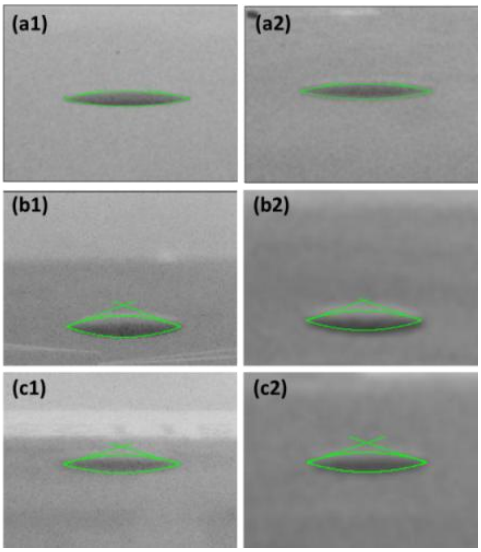

Figure 7-12 Contact angle measurements for PF-5060 on silica heaters with nanofins of different heights: 0nm(flat) surface (a1) before boiling, and (a2) after boiling; 108 nm (b1) before boiling, and (b2) after boiling; 210 nm (c1) before boiling, and (c2) after boiling.

Table 7-3 Contact angle measurements for silica heater with nanofins

Height of silica nanopillar	Before pool boiling		After pool boiling	
	Average, °	STD	Average, °	STD
Flat	17.5	0.18	19.2	1.54
108nm	17.5	2.63	19.6	0.42
210nm	15.9	1.71	18.1	0.73

The contact angle values were plotted along with heat flux values (normalized with that of flat smooth silica heater) for CHF and MHF conditions at liquid subcooling of 10°C in Figure 7-13. The figures show that the contact angle decreases with increase in height of the nanofins. The figure shows that the CHF increases and MHF decreases with increase in height of the nanofins. . These trends are similar to that of silicon nanofins. This indicates that the CHF enhancement (and degradation of MHF) is function of both geometrical sizes of the nanofins as well as the material composition of the nanofins.

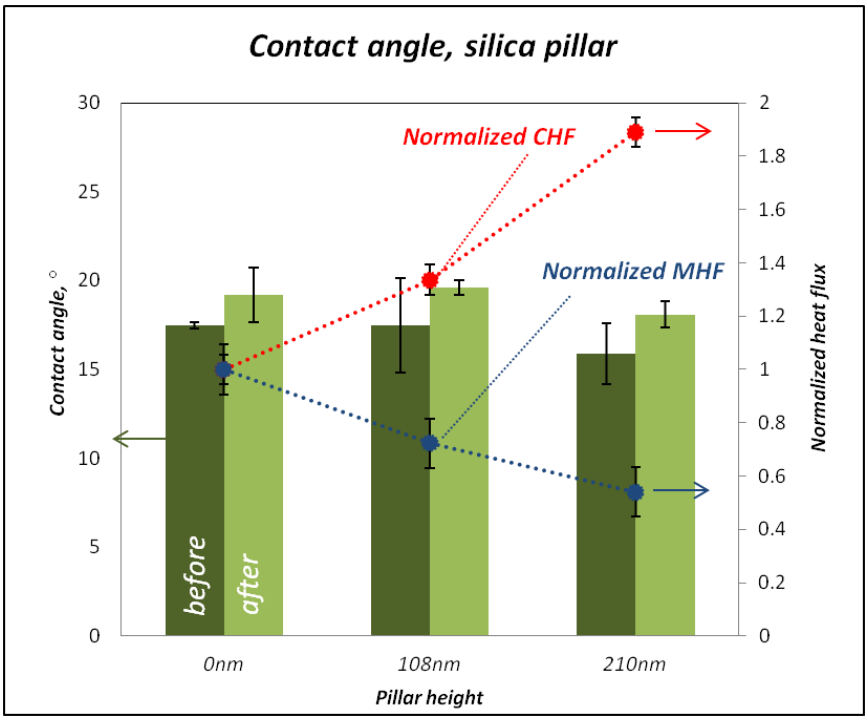

Figure 7-13 Variation of contact angle with height of silica nanofins, before and after performing the pool boiling experiments. The heat flux values are normalized with that of a flat smooth heater surface. Normalized values of CHF and MHF are plotted as a function of height of the silica nanofins.

7.6. Summary

In this chapter, the results from pool boiling experiments performed on rectangular heaters with silica nanofins were presented. The wall superheat values were measured using an array of thin film thermocouples (TFT). The results for silica nanofins show similar trend to that of silicon nanofins. The results show that the wall superheat for CHF and MHF condition decreases with increase in height of silica nanofins. In addition, the pool boiling heat flux values for the nucleate pool boiling regime are observed to increase with increase in height of the nanofins. The contact angle is observed to decrease with increase in height of the silica nanofins.

8. POOL BOILING EXPERIMENTS ON HORIZONTAL FLAT HEATERS WITH METAL NANOFINS

In this chapter, the results from pool boiling experiments are reported for a horizontal flat heater with metal nanostructures patterned on a silicon wafer substrate. The nanostructures consist of an array of cylindrical protrusions (nanofins) with a diameter of 100 nm ~ 200 nm and pitch of 800 nm ~ 900 nm. The height of the metal nanofins was ~90 nm. An array of thin film thermocouples (TFT) was fabricated to measure the surface temperature fluctuations on the heater surface with the metal nanofins. The objective of the experiments performed in this study is to investigate the effect of metal nanofins on the pool boiling curve.

8.1. Experimental Results

Diced silicon wafers with Nickel thin films (flat smooth wafer without any patterned nanofins) and diced wafers with silicon nanofins that were coated with Nickel thin films (Nickel nanofins) were fabricated for this study. These heater substrates were used for performing pool boiling experiments and the boiling curves were generated from the experimental data.

8.1.1. Nickel Flat Surface

Pool boiling curves for flat smooth rectangular nickel heater surface (without any nanofins) are plotted in Figure 8-1. As expected, the pool boiling curve shows similar

trends to that of flat smooth rectangular heaters with silicon and silica surfaces (without any nanofins). The individual boiling curves obtained from Run 1 and Run 2 of each experiment is plotted in Appendix E. The plots show that for nucleate boiling the pool boiling curves shift to the left with increasing values of liquid subcooling. On the other hand, for film boiling, the pool boiling curves shift marginally to the right (i.e., within the bounds of the measurement uncertainty the curves remain unchanged) with increasing values of liquid subcooling.

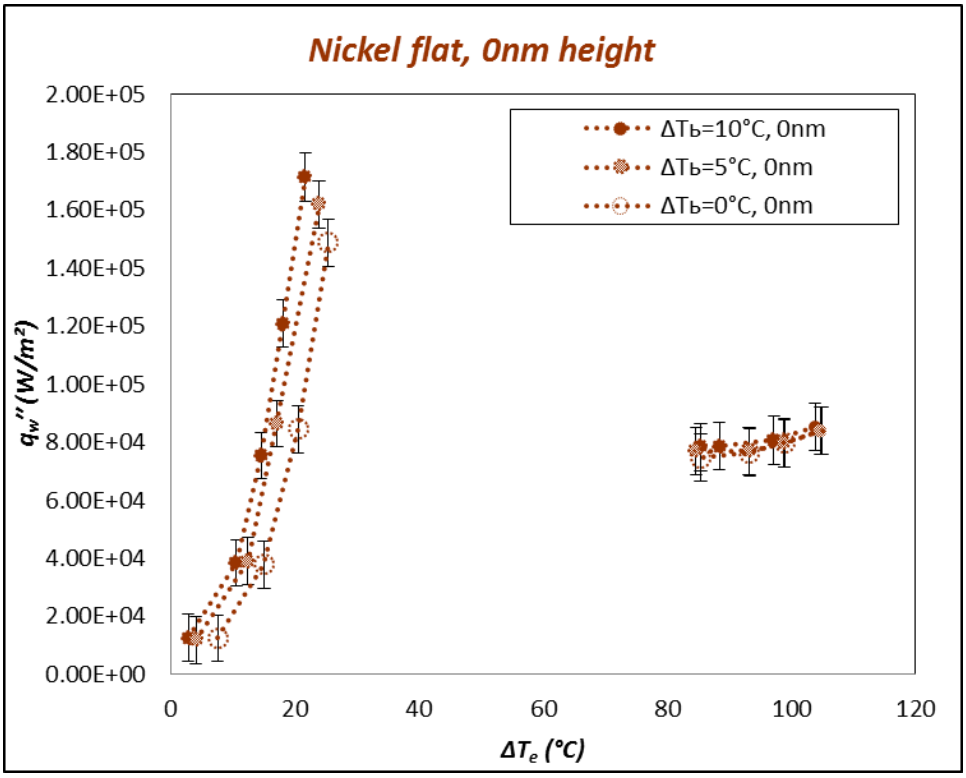

Figure 8-1 Pool boiling curves on smooth flat rectangular Nickel heater surface (without any patterned nanofins) for liquid subcooling of 10 °C, 5 °C and 0 °C (saturated pool boiling experiments). Thin Film Thermocouples (TFT) were used for surface temperature measurement.

8.1.2. Nickel Nanofin Surface

Pool boiling curves for flat rectangular heater surface with Nickel nanofins with a height of 93 nm are plotted in Figure 8-2. The individual boiling curves obtained from Run 1 and Run 2 of each experiment is plotted in Appendix E. The plots show that for nucleate boiling the pool boiling curves shift to the left with increasing values of liquid subcooling. On the other hand, for film boiling, the pool boiling curves shift to the right with increasing values of liquid subcooling.

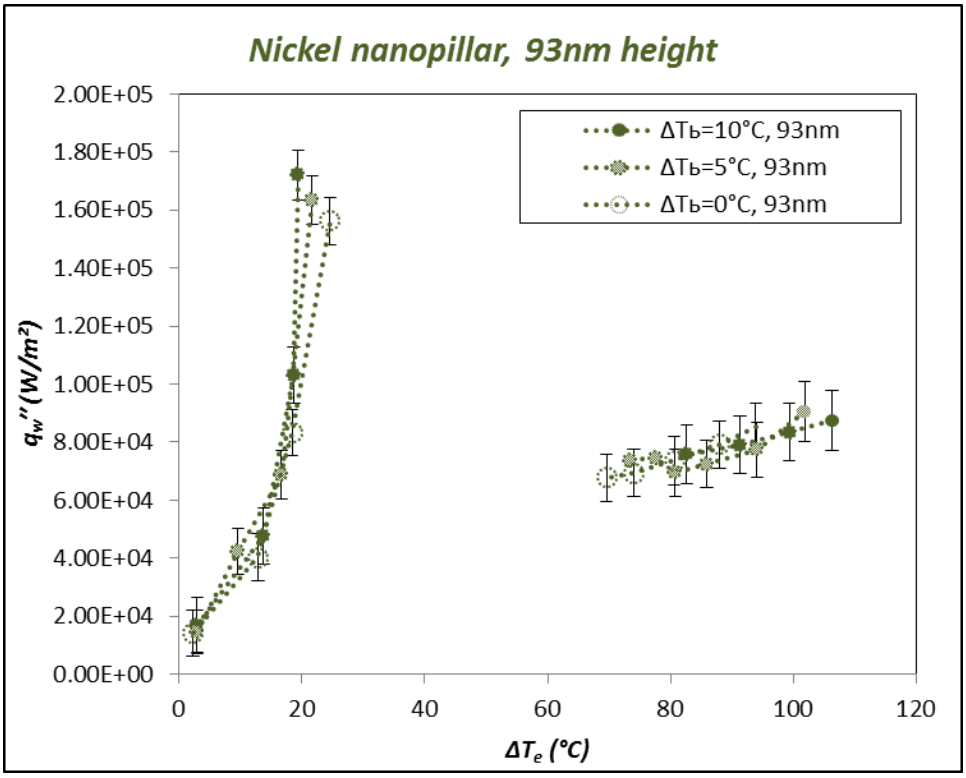

Figure 8-2 Pool boiling curves on rectangular Nickel heater surface with nanofins of 93 nm height for liquid subcooling of 10 °C, 5 °C and 0 °C (saturated pool boiling experiments). Thin Film Thermocouples (TFT) were used for surface temperature measurement.

8.2. Data Analysis for Heat Flux on Nickel Nanofins

The wall heat flux values for rectangular heater with smooth Nickel surface and Nickel nanofins (with height of 93 nm) are plotted in Figure 8-3. Moreover selected values are also listed in Table 8-1 (Uncertainty values are available in Appendix E). The figure shows that for the nucleate boiling regime the boiling curve shifts to the left with the introduction of nanofins and with increase in liquid subcooling.

In addition, the CHF values for the Nickel heater surface increases marginally with the introduction of the nanofins. The pool boiling experimental results for Nickel nanofins has similar trends to that of silicon and silica nanofins for the nucleate boiling regime.

Table 8-1 Summary of heat flux values (CHF and MHF) on the heater surface (q_w") with nickel nanofins at liquid subcooling values of 10 °C, 5 °C and 0 °C (saturated pool boiling experiments)

Subcooling 10°C	Critical heat flux		Minimum heat flux	
Height of nanopillar	Wall superheat, °C	Heat flux, W/m²	Wall superheat, °C	Heat flux, W/m²
0	21.7	1.71E+05	85.4	7.83E+04
93	19.4	1.72E+05	82.6	7.57E+04
Subcooling 5°C	Critical heat flux		Minimum heat flux	
Height of nanopillar	Wall superheat, °C	Heat flux, W/m²	Wall superheat, °C	Heat flux, W/m²
0	23.9	1.62E+05	84.6	7.70E+04
93	21.7	1.64E+05	73.4	7.37E+04
Saturated	Critical heat flux		Minimum heat flux	
Height of nanopillar	Wall superheat, °C	Heat flux, W/m²	Wall superheat, °C	Heat flux, W/m²
0	25.4	1.49E+05	85.4	7.46E+04
93	24.6	1.56E+05	69.6	6.78E+04

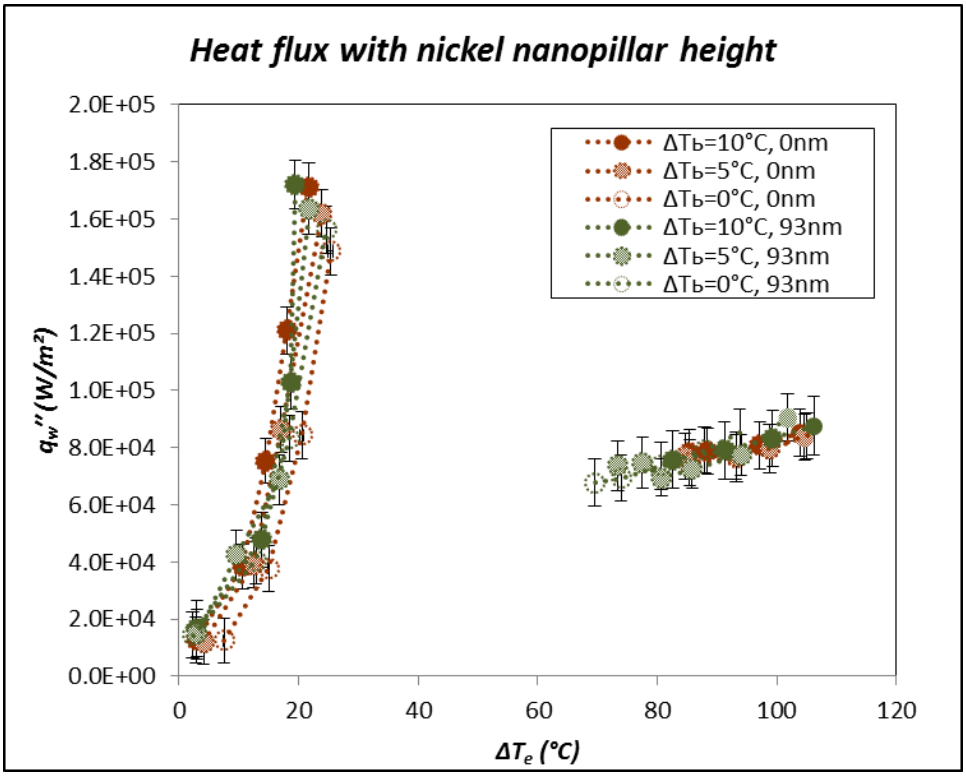

Figure 8-3 Pool boiling curves on rectangular Nickel heater surface with smooth surface as well as nanofins of 93 nm height, for liquid subcooling of 10 °C, 5 °C and 0 °C (saturated pool boiling experiments). Thin Film Thermocouples (TFT) were used for surface temperature measurement.

Best fit curves (exponential fit) were generated for the pool boiling curves in the nucleate boiling regime for heater with plain Nickel surface (without any patterned nanofins). This procedure is similar to that performed for silicon and silica heaters. The heat flux values on the non-patterned area of the silica surface was estimated using the best fit curve generated in this exercise, as shown in Figure 8-4.

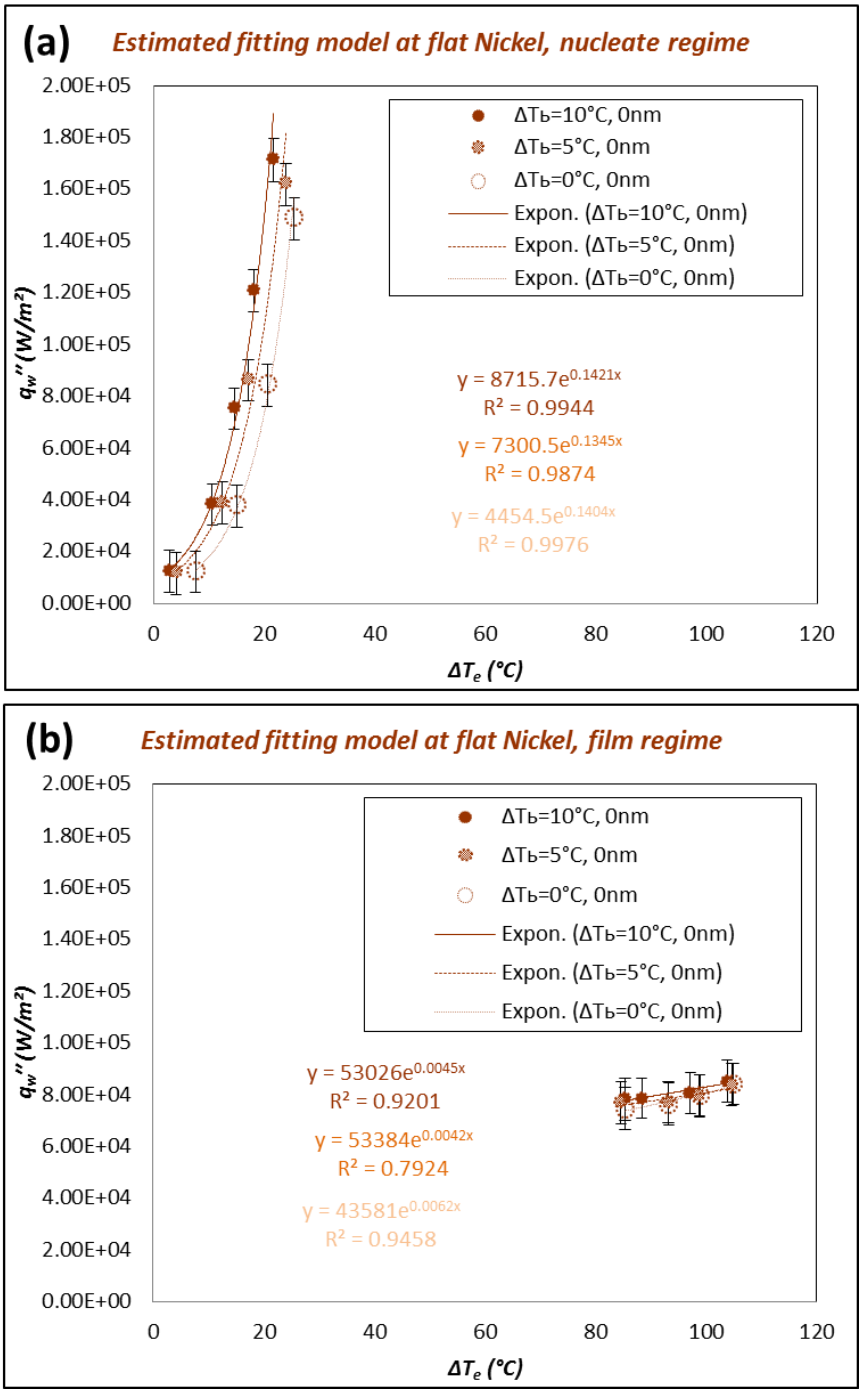

Figure 8-4 Best fit curves (with exponential fit) obtained for experimental data on flat Nickel heater with plain surface (without any patterned nanostructures) for liquid subcooling of 10^{o}C and 5^{o}C as well as saturated pool boiling experiments for the: (a) nucleate boiling regime; and (b) film boiling regime.

The best fit curves are then used to estimate the heat flux through the projected area of the heater with the nickel nanofins and is plotted in Figure 8-5. In addition, selected values are also listed in Table 8-2. The figure shows significant enhancement in the pool boiling heat flux values with the introduction of the nanofins, for all values of liquid subcooling used in this study.

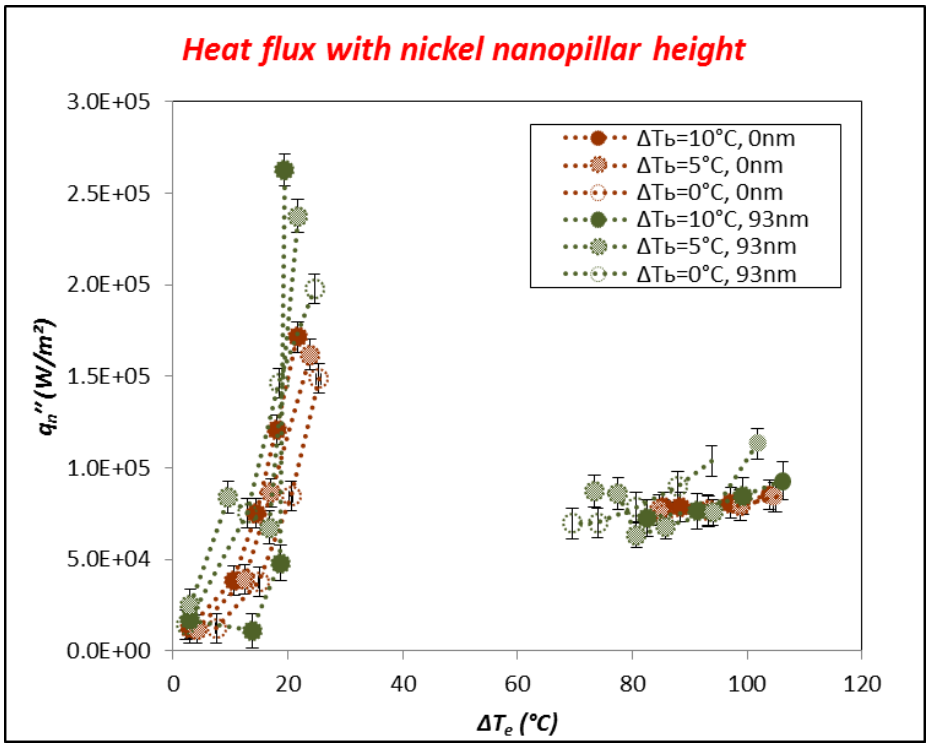

Figure 8-5 Pool boiling curve for rectangular heater with a Nickel surface containing surface nanostructures (patterned nanofins of 93 nm height) and for smooth heater (without patterned nanofins). The heat flux values are based on the projected area occupied by the nanofins (q_n"). The liquid subcooling in these experiments were 10 °C, 5 °C and 0 °C.

Based on the heat flux values calculated through the projected area occupied by the nanofins (q_n") the heat flux values through the total area of the fins on the heater surface (q_{nc}") were calculated. The heat flux through the silica nanofin patterned surface (q_{nc}") for liquid subcooling of 10°C and 5°C as well as saturated pool boiling condition are plotted in Figure 8-6 (Selected values are available in Appendix E).

Table 8-2 Summary of heat flux values (CHF and MHF) through the projected area of the heater surface (q_n") with Nickel nanofins at liquid subcooling values of 10 °C, 5 °C and 0 °C (saturated pool boiling experiments)

Subcooling 10°C	Critical heat flux		Minimum heat flux	
Height of nanopillar	Wall superheat, °C	Heat flux, W/m²	Wall superheat, °C	Heat flux, W/m²
0	21.7	1.71E+05	85.4	7.83E+04
93	19.4	2.63E+05	82.6	7.26E+04
Subcooling 5°C	Critical heat flux		Minimum heat flux	
Height of nanopillar	Wall superheat, °C	Heat flux, W/m²	Wall superheat, °C	Heat flux, W/m²
0	23.9	1.62E+05	84.6	7.70E+04
93	21.7	2.38E+05	73.4	8.70E+04
Saturated	Critical heat flux		Minimum heat flux	
Height of nanopillar	Wall superheat, °C	Heat flux, W/m²	Wall superheat, °C	Heat flux, W/m²
0	25.4	1.49E+05	85.4	7.46E+04
93	24.6	1.98E+05	69.6	6.96E+04

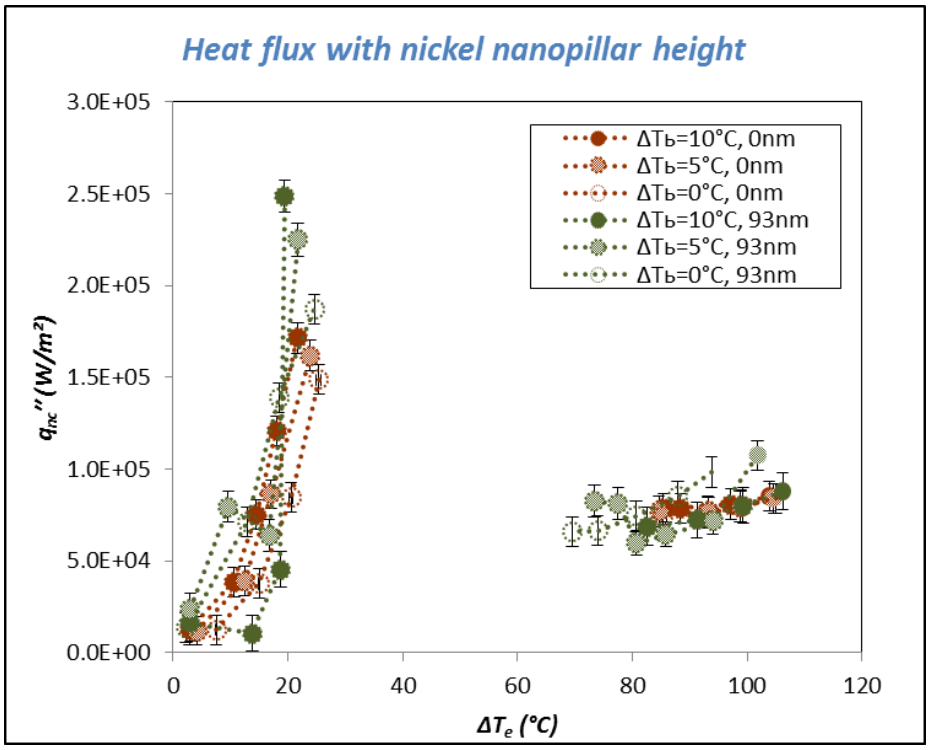

Figure 8-6 Pool boiling curve for rectangular heater with a Nickel surface containing surface nanostructures (patterned nanofins of 93 nm height) and for smooth heater (without patterned nanofins). The heat flux values are based on the total surface area occupied by the nanofins (q_{nc}"). The liquid subcooling in these experiments were 10 ^{o}C, 5 ^{o}C and 0 ^{o}C.

8.3. Analysis of Wall Superheat Variation for Nanofins

The variation of wall superheat for CHF and MHF conditions as a function of the height of the nanofins is plotted in Figure 8-7. The figures show that the CHF values are enhanced and MHF values are degraded with the introduction of the nanofins as well as increase in liquid subcooling. This indicates that the boiling curves progressively shift to the left with the introduction of the nanofins as well as increase in liquid subcooling. The temperature difference between T_{CHF} and T_{MHF} is plotted in Figure 8-7(c). The result

shows that range of wall superheat for transition boiling decreases with the introduction of the nanofins.

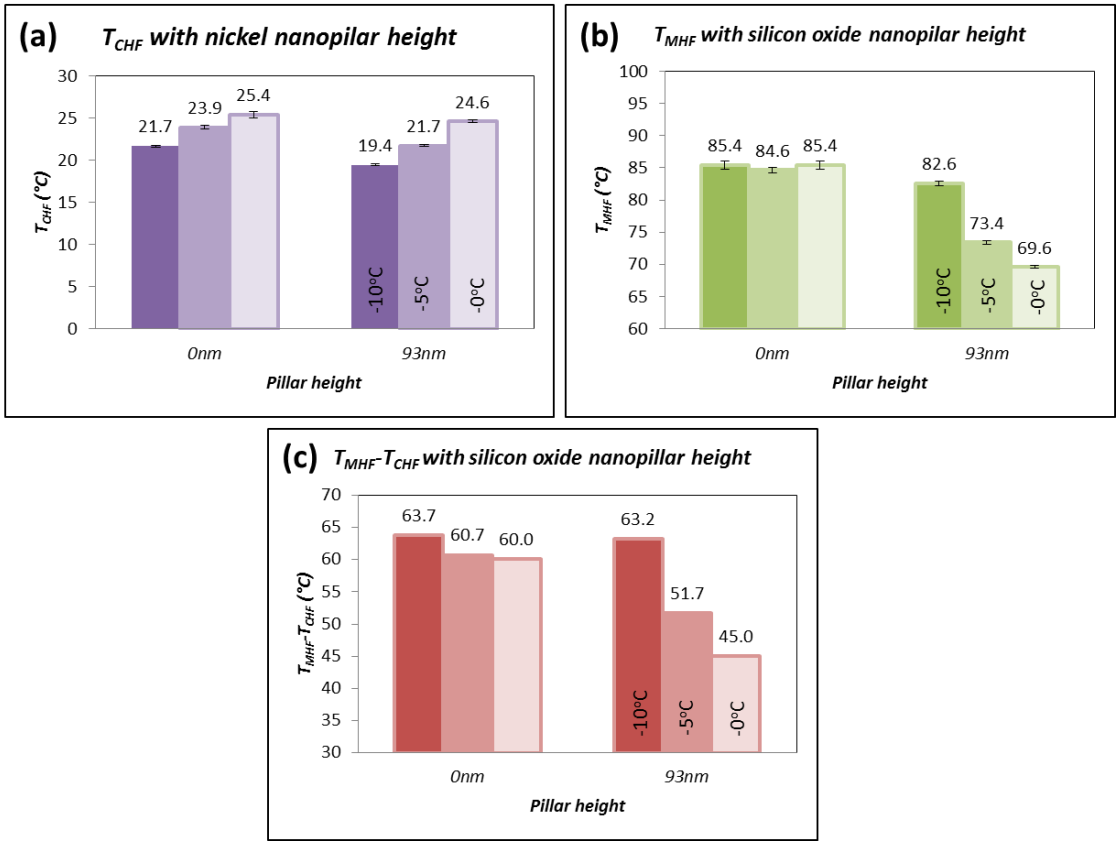

Figure 8-7 Variation of wall superheat with the introduction of the Nickel nanofins at (a) CHF; and (b) MHF. (c) Temperature difference between T_{MHF} and T_{CHF} for the Nickel nanofins

8.4. Analysis of Wall Heat Flux Variation for Nickel Nanofins

The values of heat flux through the projected area of heater surface with Nickel nanofins (q_n") were calculated. The heat flux values plotted in the previous figures were normalized with that of a flat surface (without nanofins) and plotted in Figure 8-8 for

CHF and MHF conditions. In this plot, the dark bar represents liquid subcooling of 10°C, the bright bar represents liquid subcooling of 5°C and the hollow bar represents liquid subcooling of 0 °C (saturated pool boiling condition).

The results show that CHF increases with the introduction of the nanofins, while MHF is decreased marginally with the introduction of the nanofins, for all values of liquid subcooling explored in this study. These results are similar to that of the silicon and silica nanofins, which indicates that nanofins enhance pool boiling heat flux regardless of the material composition of the nanofins.

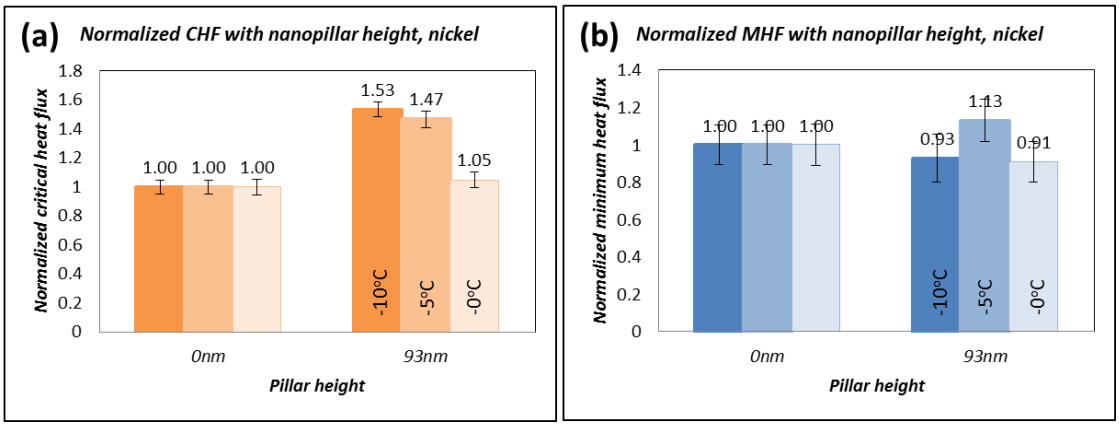

Figure 8-8 (a) Normalized CHF and (b) normalized MHF at subcool 10°C, 5°C and saturation condition for nickel nanofin patterned surface

8.5. Contact Angle Measurements

The contact angle of PF-5060 on the diced silicon wafers with the Nickel nanofins of different heights were measured, both before and after conducting the pool boiling experiments. The contact angle measurements obtained after performing the pool

boiling experiments are shown in Figure 8-9, and these measurements were compared to that of a flat smooth Nickel heater surface (without patterned nanofins) in Figure 8-10.

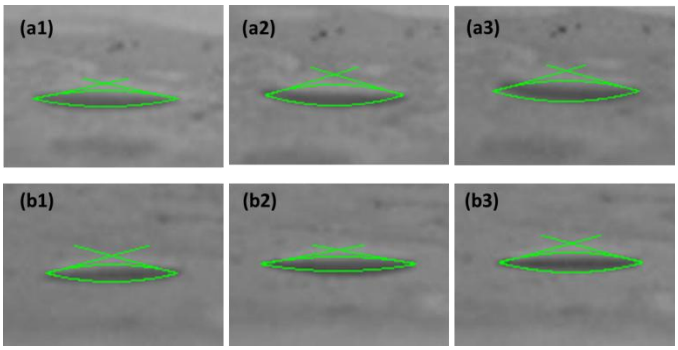

Figure 8-9 Contact angle measurement for PF-5060 on Nickel heater surface after boiling experiment for: 0 nm (smooth heater surface) and heaters with patterned nanofins (height of 93 nm). Contact angle values were measured 3 times for each surface. For example, flat Nickel surface (a1) 12.215° (a2) 17.051° (a3) 15.904°: hence the average contact angle is 14.8° and standard deviation is 1.99°. Contact angle was measured by freeware tool called "Image J".

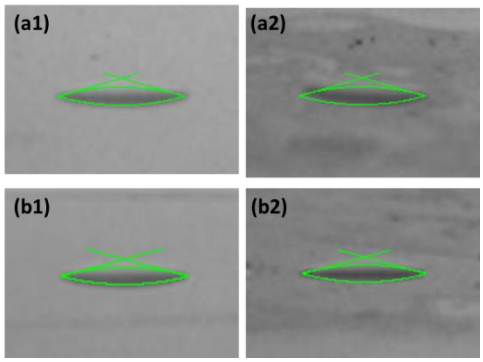

Figure 8-10 Contact angle measurements for PF-5060 on Nickel heater patterned with nanofins and plain (without patterned nanofins) Nickel heater surface. The images show: 0 nm (plain) surface: (a1) before boiling, and (a2) after boiling; patterned nanofin surface with height of 93 nm: (b1) before boiling, and (b2) after boiling

The contact angle values for PF-5060 on silica heaters with nanofins of different height are listed in Figure 8-11, for both before and after performing the pool boiling experiments. The contact angle values were plotted along with heat flux values (normalized with that of flat smooth Nickel heater) for CHF and MHF conditions at liquid subcooling of 10°C in Figure 8-11. The results show that within the bounds of the measurement uncertainty the value of contact angle and the MHF values remain unchanged, with the introduction of the nanofins. However, there is a significant enhancement in the value of CHF (based on the values of q_n").

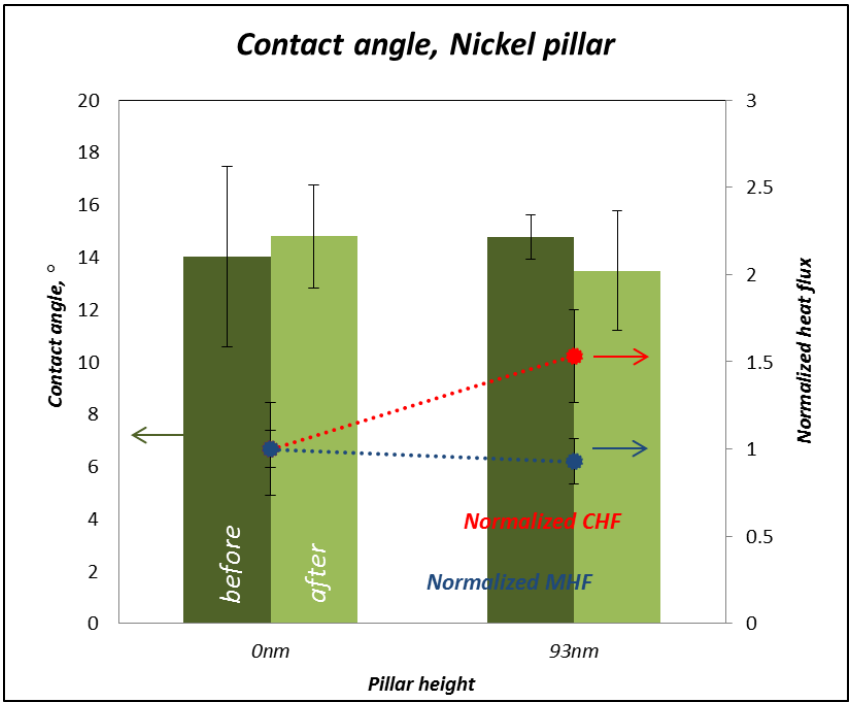

Figure 8-11 Variation of contact angle with the introduction of Nickel nanofins (of 93 nm height), both before and after the pool boiling experiments. The heat flux values are normalized with that of a flat smooth heater surface (q_n"). Normalized values of CHF and MHF are plotted as a function of heater surface configuration: with and without Nickel nanofins.

Table 8-3 Contact angle measurements for Nickel heaters

Height of Nickel nanopillar	Before pool boiling		After pool boiling	
	Average, °	STD	Average, °	STD
Flat	14.0	3.43	14.8	1.99
93nm	14.8	0.84	13.5	2.27

8.6. Summary

In this chapter, the results from pool boiling experiments performed on rectangular Nickel heaters with and without patterned Nickel nanofins were presented. The wall superheat values were measured using an array of thin film thermocouples (TFT). The results for Nickel nanofins show similar trend to that of silicon and silica nanofins. The results show that the wall superheat for CHF and MHF condition decreases with increase in height of silica nanofins. In addition, the pool boiling heat flux values for the nucleate pool boiling regime are observed to increase with the introduction of the nanofins. The contact angle is observed to be unchanged (within the bounds of the measurement uncertainty) with the introduction of the Nickel nanofins.

9. EFFECT OF MATERIAL COMPOSITION OF NANOFINS ON POOL BOILING

In this chatper the results from pool boiling experiments are compiled for a horizontal flat heater with patterned nanofins of different material composition (silicon, silica and Nickel). The nanofins are of similar height (~ 100 nm): 108 nm for silicon, 106 nm for silica, and 93 nm for nickel.

9.1. Comparison of Experimental Results

The pool boiling curves for the nanofins of different material composition are plotted in Figure 9-1. The figure shows that the pool boiling heat flux in the nucleate boiling regime is highest for Nickel nanofins and lowest for silica nanfins. Even though the height of is the nanofins are approximately the same, the pool boiling curve is progressively shifted to the left starting from silica nanofins to silicon nanofins to metal nanofins.

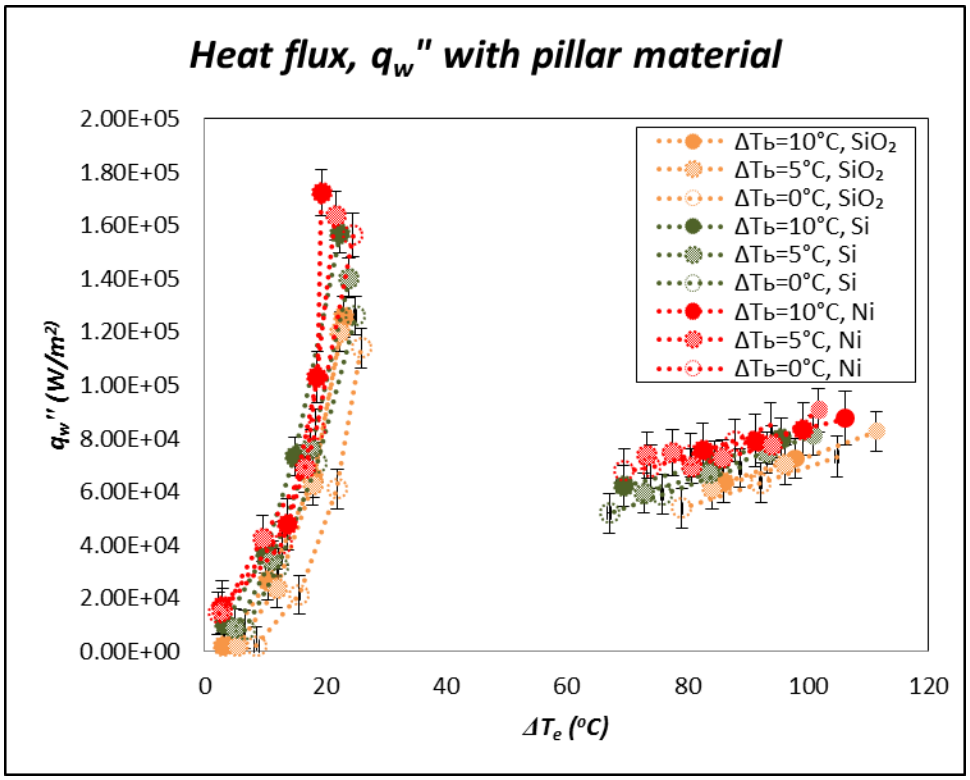

Figure 9-1 Pool boiling curve for nanofins of approximately the same height but different material composition: silicon nanofin of 106 nm height, silica nanofin of 108 nm height, and Nickel nanofin of 93 nm height.

9.2. Analysis of Wall Superheat Temperature with Materials at CHF/MHF

The values of T_{CHF} and T_{MHF} as well the difference between T_{CHF} and T_{MHF} for silicon, silica, and nickel nanofins is shown in Figure 9-2. T_{CHF} and T_{MHF} for silica is supposed to be slightly highest regardless of degree of liquid subcooling. Hence the temperature difference: ΔT (T_{MHF}-T_{CHF}) for silica is highest for nanofinheight of ~100nm. This means that the interval in the wall superheat values for the transition boiling regime for silica is higher than that of silicon and nickel.

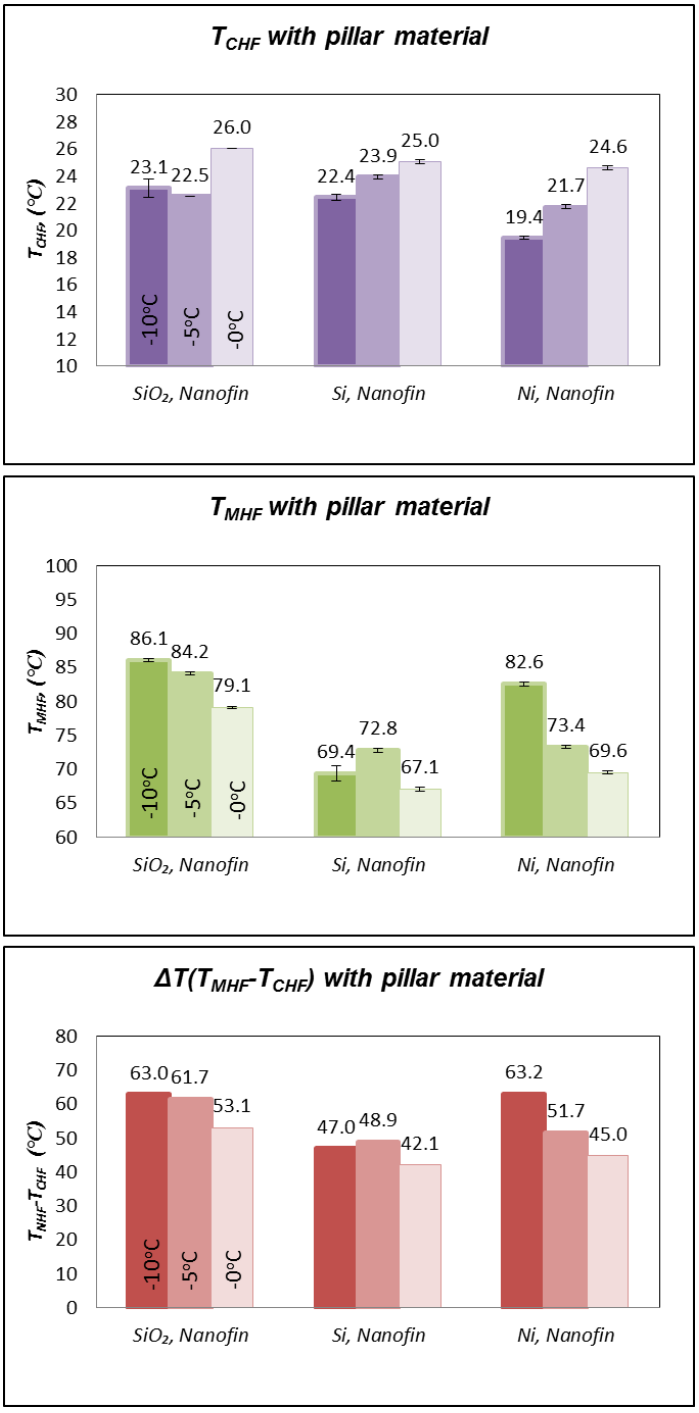

Figure 9-2 Wall superheatvalues for different nanofin compositions at: (a) CHF, and (b) MHF point. (c) Temperature difference between T_{MHF} and T_{CHF}.

9.3. Analysis of Meta-data for Heat Flux Values (q_n" and q_{nc}")

The meta-data for the heat flux values on the nanofins: q_n" and q_{nc}" are shown in Figure 9-3 for nanofins of different material composition. The heat flux values (both q_n" and q_{nc}") of the patterned nickel nanofins are higher than that of silica and silicon for both nucleate and film boiling regimes (as well as for the CHF and MHF values) regardless of the degree of liquid subcooling.

The values of CHF and MHF through the projected area of heater surface with silica/silicon/nickel nanofins (q_n") were calculated. The heat flux values plotted in the previous figures were normalized with that of silica nanofins and plotted in Figure 9-4. The results show that CHF of nickel nanofins surface is higher than CHF of silica nanofins surface by 74% at subcooling of 10^{o}C, by 56% at subcooling of 5^{o}C, and by 66% at saturation condition (these levels of enhancement are substantially higher than the measurement uncertainty values).

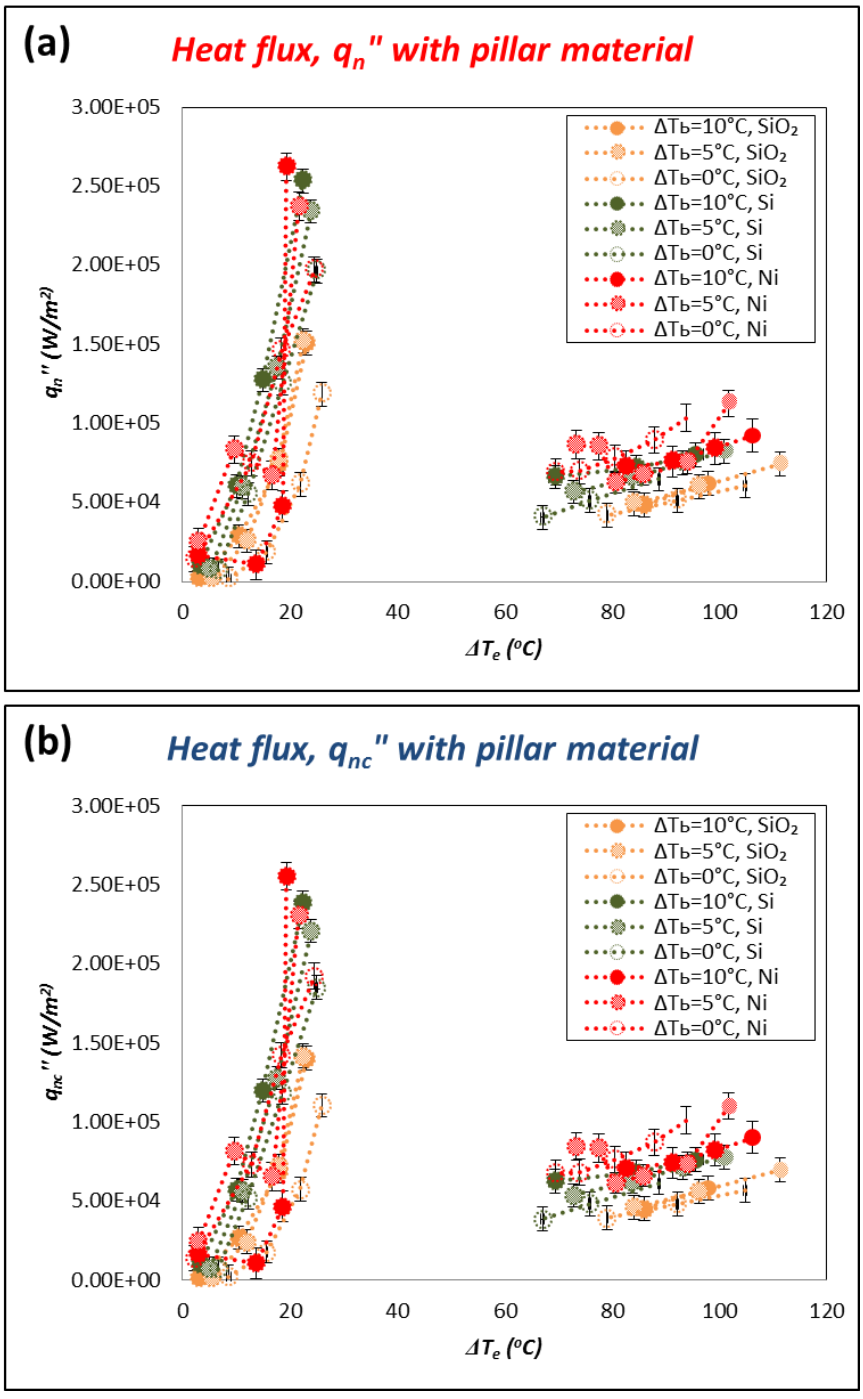

Figure 9-3 Plot of meta-data for heat flux values for nanofins of the same height (~ 100 nm) with different material composition, for: (a) q_n", and (b) q_{nc}".

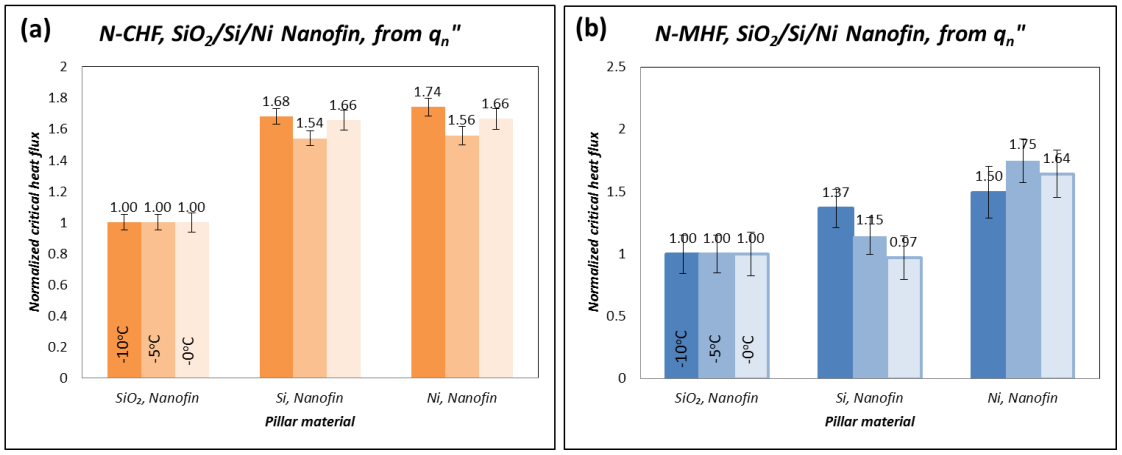

Figure 9-4 Plots showing (q_n"): (a) normalized values of CHF, and (b) normalized values of MHF. The results are for silica, silicon, and nickel nanofins with height ~100nm; for saturation condition as well as liquid subcooling of 10 ^{o}C and 5 ^{o}C.

9.4. Contact Angle Measurements

The contact angles for nanofins of approximately the same height (~ 100 nm) and different material compositions are shown in Figure 9-5 (these measurements were performed after conducting the pool boiling experiments on these surfaces).

The contact angle measurements for nanofins of approximately the same height (~ 100 nm) and different material compositions are shown in Figure 9-6 (these measurements were performed both before and after conducting the pool boiling experiments on these surfaces).

The contact angle measurements for nanofins of approximately the same height (~ 100 nm) and different material compositions are listed in Table 9-1, (these measurements were performed both before and after conducting the pool boiling experiments on these surfaces).

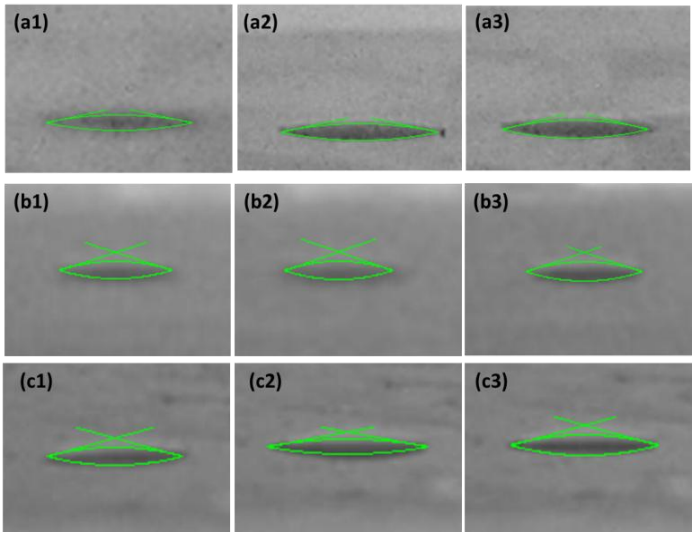

Figure 9-5 Contact angle measurement for PF-5060 (after performing pool boiling experiments on these surfaces) on: (a) silicon nanofins of height 106nm, (b) silica nanofins of height 108nm, and (c) nickel nanofins of height 93 nm. For example on silicon nanofins of height 106 nmthe contact angle measurements were: (a1) 11.798° (a2) 11.868° (a3) 13.612°: average contact angle is 12.4° and standard deviation is 0.84°. Contact angle was measured by using freeware tool "Image J".

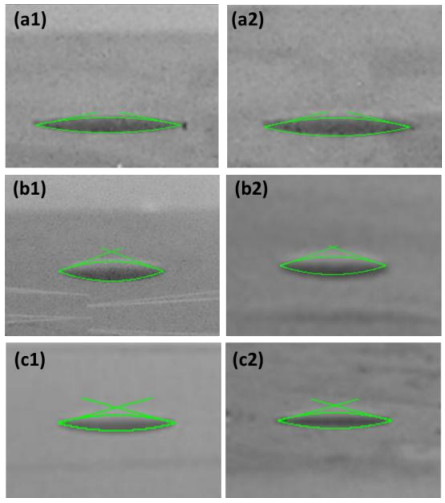

Figure 9-6 Contact angle measurement for PF-5060 (for both before and after performing pool boiling experiments on these surfaces) on: (a) silicon nanofins with a height of 106 nm , (b) silica nanofins with a height of 108nm, (c) nickel nanofins with a height of 93 nm. Numeral 1 indicates before and numeral 2 indicates after performing the pool boiling experiments.

Table 9-1 Contact angle measurements for different nanofins

Pillar material (Pillar height)	Before pool boiling		After pool boiling	
	Average, °	STD	Average, °	STD
Silica (108nm)	17.5	2.63	19.6	0.42
Silicon (106nm)	13.2	0.79	12.4	0.84
Nickel (93nm)	14.8	0.84	13.5	2.27

The critical heat flux (q_n") and minimum heat flux (q_n") of the patterned nanofin surfaces (silicon, silica and Nickel) for liquid subcooling of 10°C, are plotted along with the measured values of the contact angle in Figure 9-7. Within the bounds of the measurement uncertainty, for nanofins of the approximately the same height - both nickel nanofins and silicon nanofins have similar values of contact angle whereas silica nanofins have higher values of contact angle. The patterned nanofins of metal (Nickel) have higher value of CHF than ceramic (silica) nanofins and semiconductor (silicon) nanofins. However, in this case the CHF values increase progressively while the contact angle decreases and then remains approximately unchanged (i.e., remains within the bounds of the measurement uncertainty).

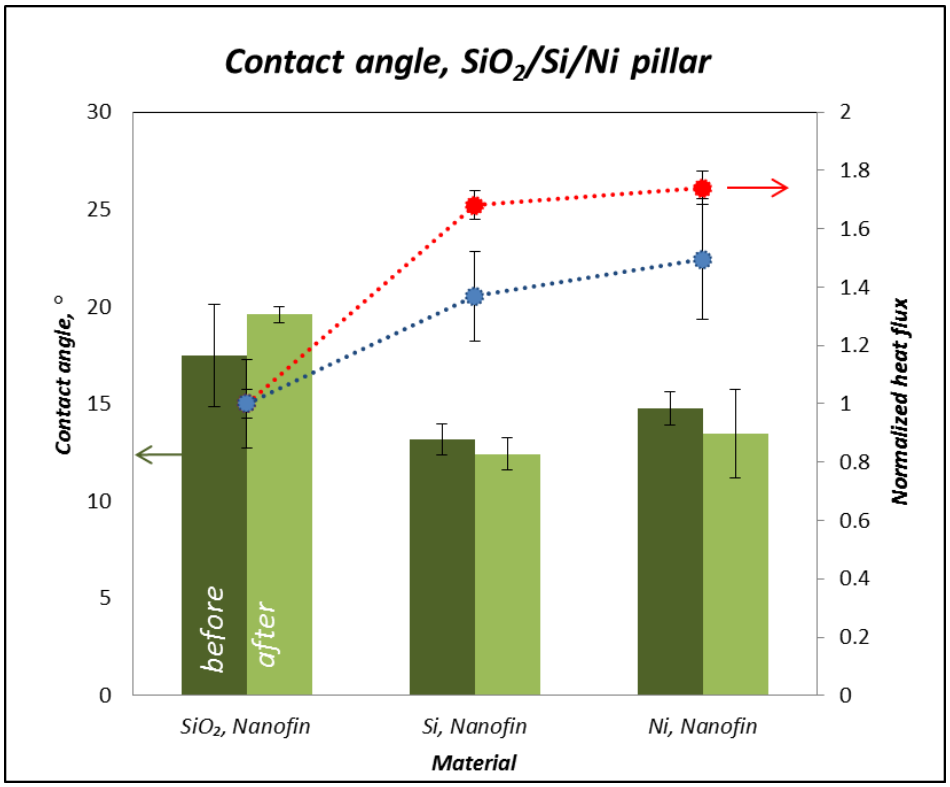

Figure 9-7 Contact angle for nanofins of different material composition but approximately same height (~ 100 nm) for both before and after the pool boiling experiments. The heat flux values are normalized with that of a flat smooth heater surface (q_n"). Normalized values of CHF and MHF are plotted for nanofins with different material composition.

9.5. Summary

In this chapter, the effect of nanofins with approximately the same height (~ 100 nm) yet different material composition (silicon, silica and Nickel) on the pool boiling curve are explored. The results show that the materials composition of the nanofins can significantly impact the pool boiling heat flux values for nucleate, film and transition boiling. The wall superheat values for the CHF and MHF condition are also affected by the material composition of the nanofins.

10. INTERFACIAL THERMAL RESISTANCE

In this chapter, the values for the interfacial thermal resistance (also known as the Kapitza Resistance, or "R_k") between the ensemble of molecules of the working fluid (PF-5060) and the surface atoms of the nanofins were explored by Molecular Dynamics (MD) simulations. The simulations were performed by varying the material composition and the material properties of the nanofins. MD techniques were chosen in this study to explore the effect of thermo-physical properties of the nanofins and the molecules of the working fluid on the interfacial transport phenomena between the solid and liquid materials. MD techniques are amenable to incorporation of molecular scale interactions such as Van der Waals forces and ionic/ Coulomb force interactions based on Newtonian model for force interactions. The interfacial thermal resistance between the solid surface of nanoparticles and the liquid was estimated using these inter-molecular force interactions in the MD simulations.

The motivation for this study is described as follows. The thermal conductivity of different material classes used in the experimental study of pool boiling: ceramic (SiO_2), semiconductor (Si) and metal (Ni) were plotted to explore if the critical heat flux (such as shown in Figure 10-1) scales with increase in the thermal conductivity (k) of the nanofins. The figure shows that there is no scaling relationship between the thermal conductivity of the nanofins and the CHF values observed in the pool boiling experiments performed in this study. As mentioned before, this is consistent with the prior reports in the literature, where it was observed that the pool boiling heat flux is not significantly sensitive to the thermal conductivity (or the thermal conduction resistance

within) the nanostructures or nanofins. For example, the critical heat flux during pool boiling on silicon is smaller than that of Nickel, even though the thermal conductivity of silicon is higher than that of Nickel. Hence, it is expected that in pool boiling the interfacial thermal resistance plays a more dominant role in the thermal resistance network (than the thermal resistance within the heater material). Hence, the total value of the thermal resistance (in the thermal resistance network) is expected to be dominated by the value of the Kapitza resistance.

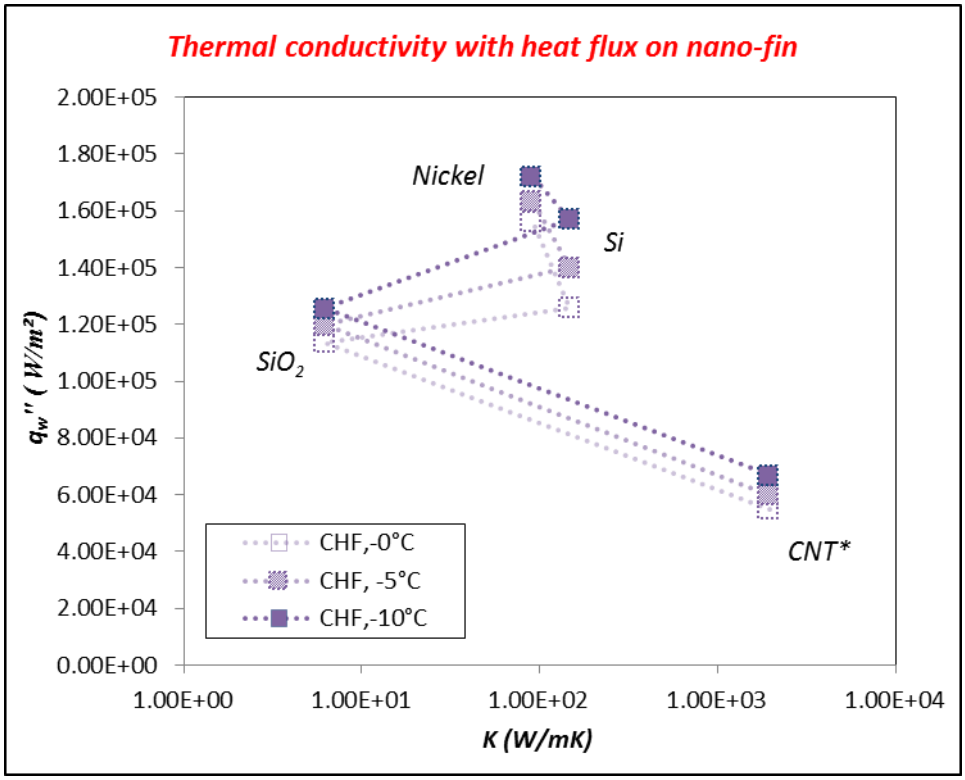

Figure 10-1 Plot of critical heat flux (CHF) as a function of the thermal conductivity of the nanofins for pool boiling experiments performed in this study, heat flux on CNT surface was obtained from literature data [8]**.**

Estimation of the Kapitza resistance values for different solid-liquid material combinations is not easily amenable for experimental measurements. Therefore, in this study the interfacial thermal resistance values between the solid surface and liquid molecules were estimated by using molecular dynamic (MD) simulations. The simulations were limited to the materials used in the experiments that are reported in the previous chapters, i.e., silicon, silica and Nickel.

10.1. Molecular Dynamic Simulations

10.1.1. Simulation Setup

PF-5060 which is used as the test fluid in the pool boiling experiments is chosen as the solvent liquid material for the simulation runs in this study. Moreover three different materials silicon dioxide (ceramic material), silicon (semiconductor material) and nickel (metal) were selected for the material properties of the solid nanoparticle. The nanoparticle is assumed to be of cylindrical shape to be consistent with the shape of the nanofins used in the experiments (i.e., cylindrical nano-pillars). The simulation domain (also called as "simulation box") for molecular dynamic simulation was implemented using a commercial tool (Material Studio 5.0, Accelrys Inc.). The length of the cylindrical nanoparticle was selected to fit the length of the simulation box (50Å, 350 EA).The cylindrical shaped nanoparticle is 49.12Å in length and 6.78Å in diameter. Each nanoparticle was created by importing standard features available from the commercial toolbox (i.e., from the Material Studio library). The simulation box and the lattice configuration of each nanoparticle are shown in Figure 10-2.

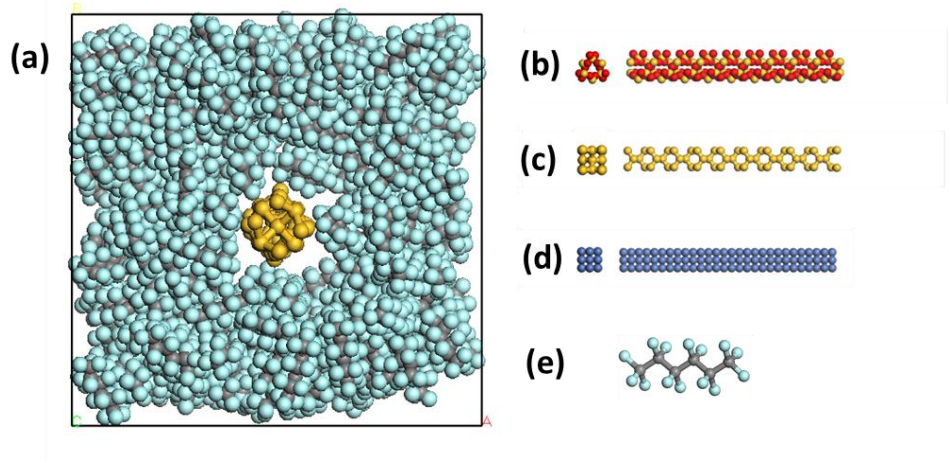

Figure 10-2 (a) Example of simulation domain: silicon nanoparticle surrounded by molecules of PF-5060. The lattice configuration of each nanoparticle is shown in : (b) silicon dioxide, SiO_2 ; (c) silicon, Si; and (d) nickel, Ni. (e) The structure of an individual molecule of PF-5060 is shown here.

The interactions between any two atoms can be expressed by Lennard-Jones (LJ) potential along with Coulomb force interactions for non-bonded atoms are shown in Equation (9-1).

$$E(r) = \frac{q_i \cdot q_j}{r} + 4\varepsilon\left[\left(\frac{\sigma}{r}\right)^{12} - \left(\frac{\sigma}{r}\right)^{6}\right] \qquad (9\text{-}1)$$

Where, r is the center-of-mass distance between any two atoms. The parameters for LJ potential with Coulomb force for interactions were obtained from Material Studio library (using the CVFF force field). The cutoff radius of 12 Å was employed for the simulations. This is based on, literature reports that demonstrate that the intermolecular

interactions are not influenced significantly beyond the cutoff length, i.e., for intermolecular distances exceeding a certain value [53, 101, 102].

For calculation of interaction potentials between atoms of different chemical species, the parameters for calculation were obtained by using the arithmetic mean as shown in Equation (9-2). In addition, the bond stretching, bond bending and torsion effects were also considered as shown in Equation (9-3).

$$\varepsilon_{ij} = \sqrt{\varepsilon_i \cdot \varepsilon_j}\ ,\ \sigma_{ij} = \frac{\left(\sigma_i + \sigma_j\right)}{2} \tag{9-2}$$

$$E = K_s(r - R_0)^2 + K_b(\theta - \theta_0) + K_t(1 + d \cdot \cos(n\phi)) \tag{9-3}$$

The parameters for MD simulation for each atom are summarized in Table 10-1.

Table 10-1 Parameters used for the molecular dynamics simulations

Material	LJ potential parameter			
	Interaction	Atomic weight	ε (kcal/mol)	σ (Å)
Silicon dioxide	Si-Si	28.0860	0.0400	4.0534
	O-O	15.9994	0.2280	2.8598
Silicon	Si-Si	28.0860	0.0400	4.0534
Nickel	Ni-Ni	58.7100	11.9830	4.0534
PF5060	C-C	12.0112	0.1600	3.4745
	F-F	18.9984	0.0688	3.2777

Material	Stretching		Bonding		Torsion		
	K_s	r_o	K_b	θ_o	Kt	d	n
Silicon dioxide	322.72	1.526	46.6	110.50	0.300	1	3
Silicon	480.00	1.340	5.0	109.47	12.370	-1	2
PF5060	496.00	1.363	46.6	110.50	0.158	1	3

10.1.2. Simulation Procedure

Molecular dynamics program, LAMMPS (Large-scale Atomic/Molecular Massively Parallel Simulator, Sandia National Laboratories) was used in this study. Each nanoparticle (SiO_2, Si, or Ni) was placed at the center of simulation box, and then solvent molecules (PF-5060) were randomly distributed inside the simulation box initially. This initial configuration is not physically accurate for performing the desired MD simulation, because some of molecules may overlap and may be placed at distances shorter than the equilibrium distance (or equilibrium configuration between two molecules), which can lead to computational instability. Therefore energy minimization step was performed to redistribute the atoms from the initial configuration - in order to ensure computational stability. The computational instabilities may be induced by the physically inaccurate values for the high velocity of the atoms in the initial configuration. After the completion of the energy minimization step, the physical state in the simulation box is expected to be more realistic and/ or physically representative of the molecular distribution within the simulation box. Hence, the atoms in the simulation box are rearranged that corresponds to an equilibrium state at 0 K. After minimization step, relaxation step is performed by micro canonical ensemble (NVE). This enables readjusting the value of the temperature within the simulation domain to room temperature by using isothermal-isobaric ensemble (NPT) technique. Subsequently the temperature of the nanoparticle was raised instantaneously to 800 K. Finally NVE ensemble is performed once again for the nanoparticle temperature to decay with time in order to reach the thermodynamic equilibrium state. In this process, heat transfer occurs

from the nanoparticle (at a higher temperature) to the surrounding solvent molecules (after ensuring that there is no significant rise in the bulk average temperate of these solvent molecules).

10.2. Interfacial Thermal Resistance

10.2.1. Interfacial Thermal Resistance Calculation

The interfacial thermal resistance was obtained by monitoring the temperature difference between the nanoparticle and the solvent, based on the lumped capacitance method [52]. The interfacial thermal resistance between the solid nanoparticle and the solvent are determined by using the following equation (9-4) [52, 62, 76].

$$R_k = \frac{\tau A}{C} = \frac{\tau A}{(\rho V C_p)} \tag{9-4}$$

Where R_k is the interfacial thermal resistance (Kapitza resistance), A is the surface area of the nanoparticle, V is the volume of the nanoparticle, C_p is the specific heat capacity of the nanoparticle, ρ is the density of the nanoparticle and τ is the rate of temperature decay with time of the nanoparticle (which is akin to the time constant of the nanoparticle-fluid system).

The time constant can be obtained by using a best-fit curve for the transient temperature profile (or the transient temperature difference profile for the temperature difference between the nanoparticle and the solvent) in time domain, as shown in Figure 10-3. The specific heat capacity is 0.721 J/gK for silicon, 0.745 J/gK for silica, and 0.444 J/gK for Nickel [4]. The time constant, which is obtained in this study, was

calculated for nanoparticle temperature exceeding 400K. In other words, the temperature between 800K (input temperature) and 400K (cutoff temperature), is used for the calculation of the time constant.

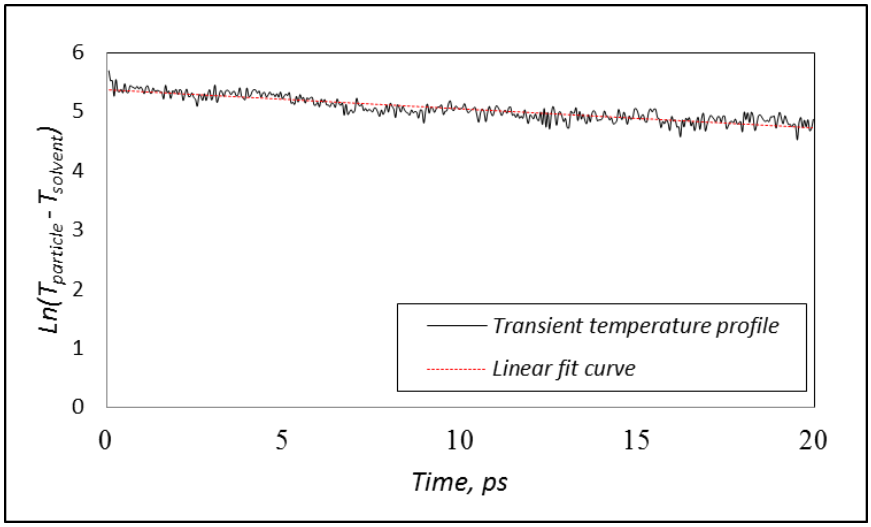

Figure 10-3 Transient temperature profiles of PF-5060 in contact with heated silicon nanofin.

10.2.2. Interfacial Thermal Resistance for Nanofins with Different Material Properties

The interfacial thermal resistance between fluid molecules (PF-5060) and solid nanofins (silicon, silica and Nickel), are plotted along with the values of CHF obtained from the experimental data – and are shown in Figure 10-4. Figure 10-4(b) shows the dependence of CHF (critical heat flux) on the Kapitza resistance for a flat rectangular heater surface (without patterned nanofins). The interfacial thermal resistance for silica is highest, and concomitantly it has the lowest CHF. The interfacial thermal resistance for the metal surface is lowest, while it also has the highest CHF. Therefore among the

three materials explored in this study, the materials which have lower interfacial thermal resistance, have a higher critical heat flux.

In addition, Figure 10-4(a) shows the plot of CHF for the heaters with nanofins as a function of interfacial thermal resistance (with the critical heat flux based on the wall heat flux q_w"). The critical heat flux for nickel nanofins is the highest while it also has the lowest Kapitza resistance (among the htree types of nanofins considered in this study, i.e., Si, SiO_2, and Ni) as well as CNT (Carbon Nanotubes) – which were explored in prior reports in the literature. The values of CHF (for q_n" and q_{nc}") are plotted as a function of R_k in Appendix F.

10.2.3. Contact Angle

Contact angle is an indicator for the surface energy of any substrate (i.e., if the surface is wetting or non-wetting). If a surface is wetting, it is expected to have a lower value of interfacial thermal resistance between the chosen solid and liquid due to higher inter-molecular forces or affinity between the solid and the liquid material). On the other hand, for a non-wetting surface, the value of interfacial thermal resistance is expected to be higher due to lower affinity between the molecules of the solid and the liquid material.

The contact angle of PF-5060 droplet on the heater surface was measured and plotted along with the interfacial thermal resistance as shown in Figure 10-5. The contact angle is 19.2° for silica (SiO_2), 13.6° for silicon (Si) and 10.3° for nickel (Metal). Hence, materials with higher values of interfacial thermal resistance also have high contact angles (i.e., less wetting).

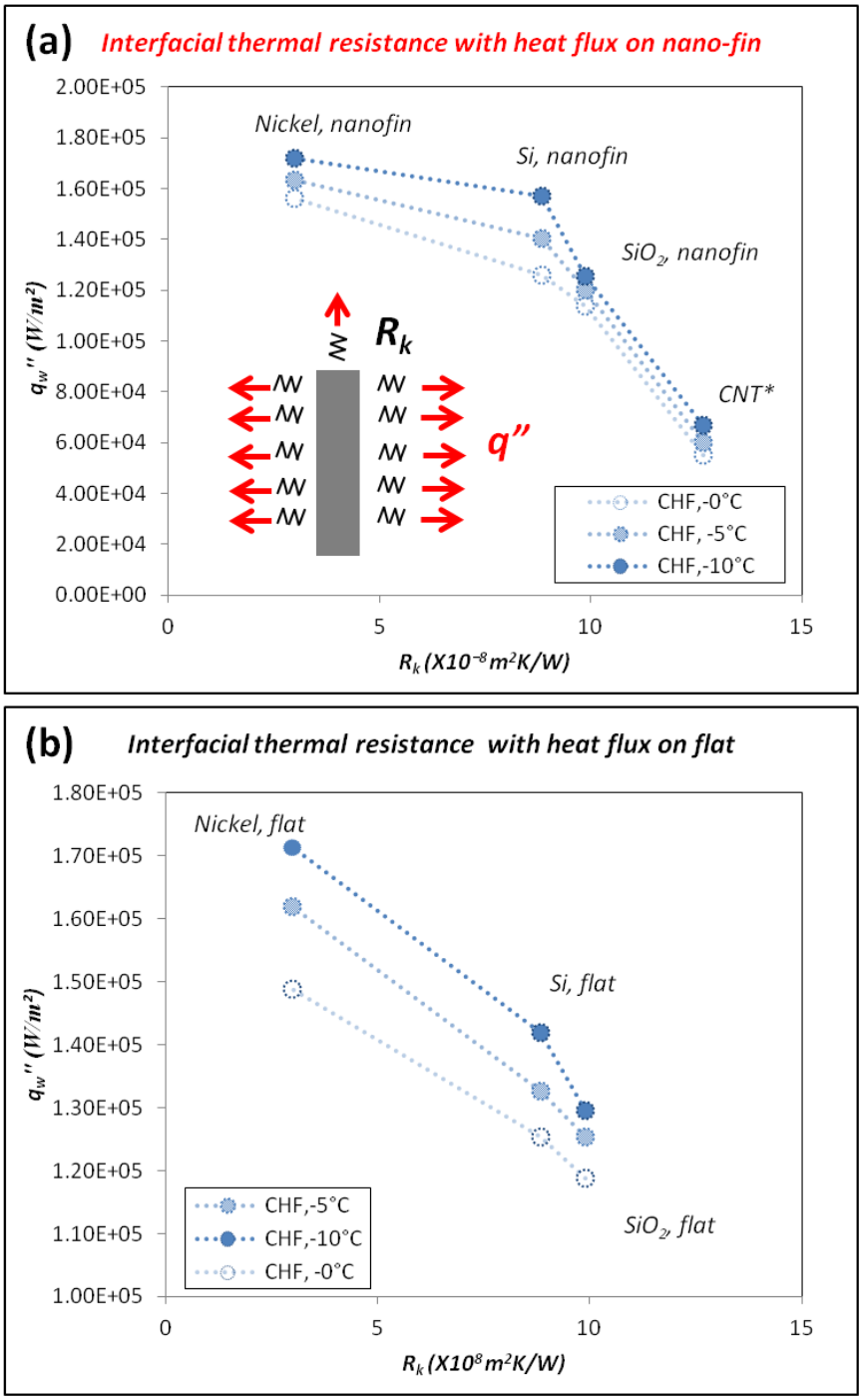

Figure 10-4 Plot of wall (q_w") critical heat flux (CHF) as a function of interfacial thermal resistance (R_k) between PF-5060 and heater material for: (a) nanofin surface; and (b) flat surface. Heat flux on CNT surface was obtained from literature data [8].

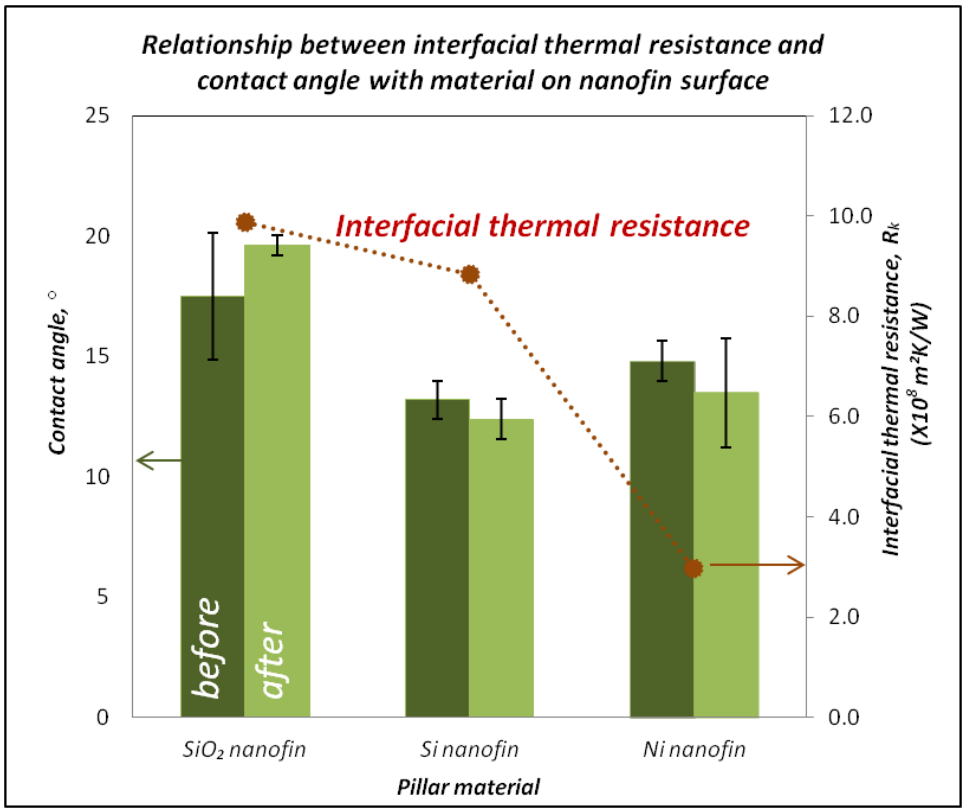

Figure 10-5 Plot of interfacial thermal resistance along with contact angle for silica, silicon, and nickel surface (before and after the pool boiling)

10.3. Summary

In this chapter, the interfacial thermal resistance values were estimated for nanofins with different materials composition. The nanofins were in contact with the working fluid used in this study (PF-5060) for performing the pool boiling experiments. The interfacial thermal resistance was calculated by using molecular dynamics (MD) simulations. The predictions from the numerical simulations were found to be consistent with the experimental data for pool boiling heat flux values (critical heat flux/ CHF) and contact angle measurements. The results show that CHF scales inversely as the

interfacial thermal resistance (i.e., CHF decreases as R_k increases). Similarly the value of static contact angle are found to scale with R_k (i.e., contact angle increases as R_k increases).

11. THERMAL CAPACITANCE AND DIODE

The interfacial thermal resistance for nanofin materials was discussed in the previous chapter. In this chapter, thermal capacitance and diode effect (which arise from the esistence of surface adsorbed layer of fluid molecules on the nanofin – also termed as the "compressed layer") will be discussed based on results obtained from the molecular dynamics (MD) simulations.

The inter-molecular interactions between solid and fluid phases can manifest in several ways. These can be cateogirized into three different manifestations that arise from the complex interactions between the several transport mechanisms. The first is the interfacial thermal resistance (which was discussed in the previous chapter, which is shown to be a more dominant parameter than the conduction thermal resistance for heat transfer within the solid nanofin). The second is the thermal capacitance arising from the existence of the compressed layer of fluid molecules (which has a higher density, and may be comparable to the thermal capacitance of the solid nanofin). The third manifestation of these transport mechanisms is the bias in heat transfer values based on direction of temperature drop (or diode effect), which is driven by the concentration gradient of fluid molecules from the solid nanofin surface to the bulk fluid (that can aid or oppose the heat transfer between the nanofin and the fluid molecules). Schematic diagram depicting the thermophysical interactions between the solid nanofin and fluid molecules is shown in Figure 11-1.

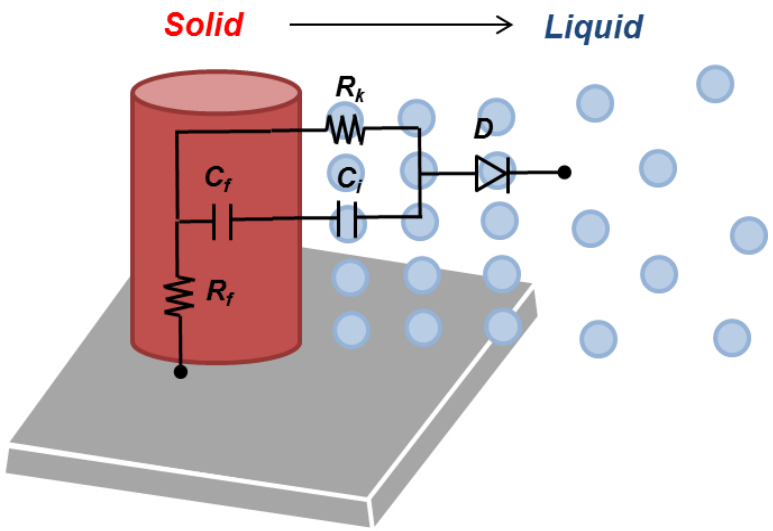

Figure 11-1 Schematic diagram of thermophyscial interactions between solid nanofin and liquid molecules. R_k: interfacial thermal resistance, R_f: conduction thermal resistance within the solid nanoparticle, C_i: thermal capacitance of compressed layer, C_f: thermal capacitance of solid nanofin, and D: thermal bias of the compressed layer (diode effect)

11.1. Total Thermal Resistance

First of all, conduction thermal resistance for heat transfer within each nanofin can be estimated using the Fourier's law. For comparison, the length of the nanofin was selected as 100 nm for SiO_2/Si/Ni, 25μm for CNT (to be consistent with the CHF values that were reported by Ahn [8, 9, 103]). Moreover the thermal conductivity was obtained from the literature [4] as, 6.21 W/m-K for SiO_2, 148 W/m-K for Si, 90.9 W/m-K for Ni, and 1950 W/m-K for CNT (graphite). Total thermal resistance (R_t) can be obtained by the summing the interfacial thermal resistance (R_k) and the thermal conduction resistance (R_f). The thermal resistance values for different nanofin materials are summarized in Table 11-1. The table shows that the values of interfacial thermal resistance are 10~100

times higher than the values of thermal conduction resistance for all of the cases considered in this study. Hence the interfacial thermal resistance is observed to be the most dominant factor during heat transfer between the solid nanofin and the fluid molecules.

The critical heat flux values obtained from the experiments were plotted as a function of the total thermal resistance values (estimated by summing thermal conduction resistance and interfacial thermal resistance), and are shown in Figure 11-2. Critical heat flux on CNT coated Si surface was also plotted together for comparison [8, 9, 103]. The plot shows that the values of CHF for heaters with surface nanostructures (nanofins) decrease with increase in the values of total thermal resistance (regardless of the degree of liquid subcooling) as shown in Figure 11-2 (a). In addition, the values of CHF on the plain heaters (i.e., without any engineered nanostructures) also decrease with total thermal resistance as shown in Figure 11-2 (b). Hence we can conclude that the critical heat flux in pool boiling is inversely proportional to the total thermal resistance for the heater surface.

Table 11-1 Values of thermal resistance ($\times 10^8$ m^2K/W)

Material	R_k	R_f	R_t
*CNT**	*12.7*	*1.28*	*13.9*
SiO_2	*10.4*	*1.61*	*12.1*
Si	*9.9*	*0.07*	*9.9*
Ni	*3.0*	*0.11*	*3.1*

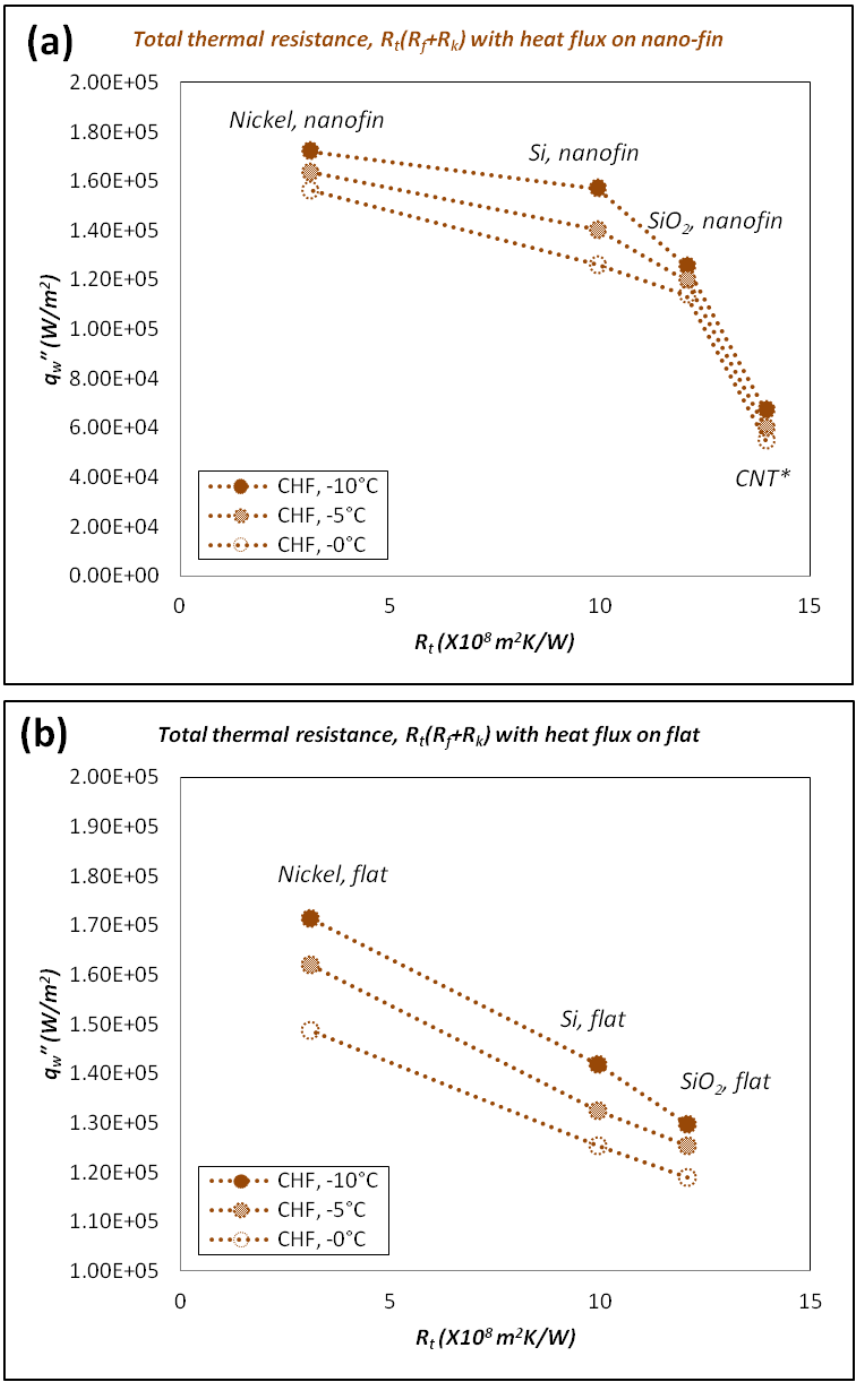

Figure 11-2 Variation of critical heat flux with total thermal resistance for heaters with: (a) engineered surface nanostructures (nanofins), and (b) plain surface (without any engineered surface nanostructures). Heat flux values for heaters with CNT coatings were obtained from literature data [8]**.**

11.2. Thermal Capacitance

The inter-molecular interactions between solid and fluid molecules (also called the solvent molecules) can cause oscillations in the local value of density (number of molecules per unit volume) in the vicinity of the solid-liquid interface. Molecular dynamics (MD) simulations show that the solvent molecules are attracted to the surface of the solid phase – thus forming a layer of molecules that have a different density (number of molecules per unit volume) than in the bulk of the fluid phase. Thus a layer of solvent molecules are formed on the solid surface with a different density (typically higher density) than in the bulk of the solvent. This layer of solvent molecules (also termed as the "compressed layer") can be considered to have a higher chemical potential (i.e., concentration) than in the bulk phase of the solvent. Similarly, the compressed layer, owing to the higher values of density and chemical concentration, can also have a different value of specific heat capacity and thermal conductivity – than that of the bulk of the solvent phase (i.e., if the solid surface was not present). Thus the difference in the specific heat capacity values between the bulk phase and the compressed layer (or "compressed phase") can act as a mechanism for thermal energy storage – and therefore serve as the electrical network equivalent of a thermal capacitor. The thermal capacitance values of this compressed phase can modulate the transient heat transfer during the inter-molecular interactions between the solid nanofin and the fluid phase. It is expected that the layer of fluid molecules adsorbed on the surface of the solid nanofin (compressed layer) has a higher thermal capacitance, because the MD simulations show that it has a higher density than the bulk fluid phase. By estimating the thermal

capacitance of the nanofin as well as the compressed phase, the total thermal capacitance arising from the insertion of a nanoparticle in a fluid (or the insertion of a nanofin on a heater surface) can be estimated. This is the motivation for this study – i.e., to estimate the total thermal capacitance of a nanoparticle (or nanofin) and the compressed phase that is formed at the solid-fluid interface.

11.2.1. Density Profile of Compressed Liquid

The formation of the compressed layer occurs due to the adhesive inter-molecular forces between the molecules of the solid and fluid phases. If the adhesive forces are higher than the cohesive forces (i.e., the inter-molecular forces between molecules of the same species) - it can lead to wetting of the fluid on the surface of the solid. The values for the thickness of the compressed layer were obtained from results for the MD simulations performed in this study. The values obtained for the thickness of the compressed layer in these simulations are consistent with the reports in the literature. For example, the thickness of the compressed phase for argon on a copper nanoparticle was predicted to be ~1 nm [104]. Also computational study for density oscillations of water molecules on a gold surface was predicted to be ~1 nm [105]. In addition, experimental measurements performed using HR-TEM show that the thickness of the ordered liquid aluminum (compressed phase) at the interface with sapphire (solid) is ~1 nm [106].

Figure 11-3 shows the plot of density profile for molecules of PF-5060 surrounding nanofins of different material composition (SiO_2/ Si/ Ni). The origin of the

plot is the center of each cylindrical nanofin. The density oscillations are observed to be different for each nanofin (depending on the material property of the nanofin) while the material property of the fluid molecules is unchanged in each simulation. The variation in the density oscillations arises from the variability in the inter-molecular interactions between the solid and fluid phase. The first peak in the density oscillations of the fluid phase was observed at a radial location of ~7 Å, and the density oscillations subsided after a radial distance of ~17 Å (thus reaching the free stream value or the bulk phase value). For all three simulations the bulk value of density is attained after a radial distance of ~17 Å regardless of the material property of solid (nanofin). Hence thickness of the compressed layer is expected to be ~1 nm which is consistent with previous reports in the literature (based on both experimental measurements and numerical predictions). However the density profile for nickel fluctuates more than that on silicon and silica, which indicates that there is significant variation in the density of compressed layer for each nanoparticle (or nanofin).

The value of bulk fluid density, which is the value of average density far away from the solid surface (15 Å to 20 Å), was obtained to contrast this value with that of the compressed phase (i.e., in the vicinity of the solid surface). The simulation results show that the compressed phase has significantly higher value of density than the average density of the bulk phase of the fluid molecules. The contrast in the density values is used to distinguish the effective boundary of the compressed phase. Figure 11-3 shows the average liquid density (dashed line) and compressed phase (red color) for nanoparticles (or nanofins) of different materials composition.

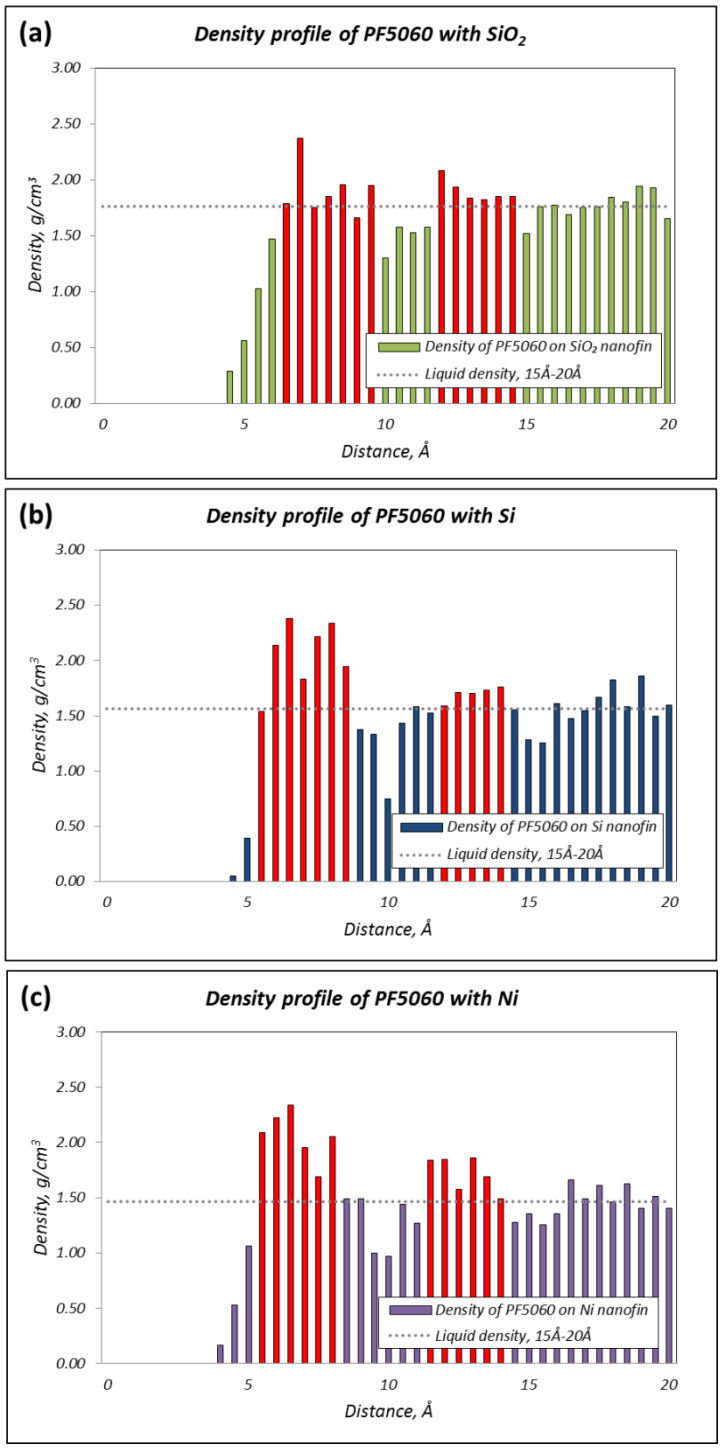

Figure 11-3 Density profile of fluid (solvent) phase in contact with nanoparticle (or nanofin) surface with different material composition. The figure shows the different regions (marked in red) of compressed phase for the following nanofin materials: (a) SiO_2, (b) Si, and (c) Ni.

11.2.2. Thermal Capacitance Calculation

Figure 11-4 (a) shows the schematic diagram for the different components for calculating the total thermal capacitance (C_t): the thermal capacitance of solid nanofin (C_f), and the thermal capacitance of 1st ordered layer of fluid molecules (C_i). In addition, the peak density of 1st ordered layer for different nanofin materials are also shown in Figure 11-4 (b).

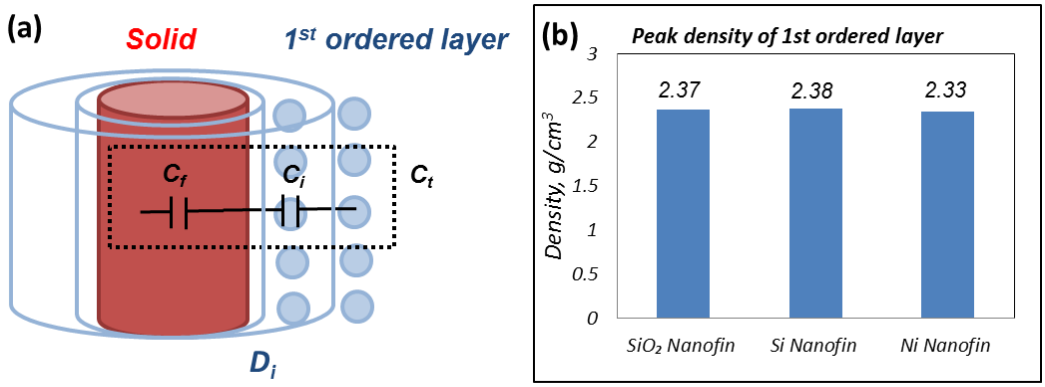

Figure 11-4 (a) Schematic showing the thermal capacitance of solid nanofin (C_f), the thermal capacitance of the compressed phase (C_i), and the total thermal capacitance (C_t). D_i represents the extent of the compressed phase in the vicinity of the nanoparticle (or nanofin) which corresponds to the first peak of the density oscillation. (b) Value for the first density peak obtained from MD simulations for different nanofin materials.

Thermal capacitance (C) and thermal capacitance per unit area (C') can be calculated from the following equation (11-1):

$$C = \rho V C_p \; ; \; C' = \frac{\rho V C_p}{A_s} \qquad (11\text{-}1)$$

Where ρ is the density, V is the volume, C_p is the heat capacity, and A_s is the surface area. The total thermal capacitance per unit area (C'_t) can be calculated from the following equation (11-2):

$$\frac{1}{C'_t} = \frac{1}{C'_f} + \frac{1}{C'_i} \tag{11-2}$$

Where C'_f is the thermal capacitance per unit area of the solid material (i.e., nanoparticle or nanofin), C'_i is thermal capacitance per unit area of the compressed phase (which corresponds to the first peak of the density profile of the solvent phase).

The thermal capacitance per unit area for both the solid phase and the compressed phase (corresponding to the first peak in the density profile obtained from the MD simulations) are listed in Table 11-2. Based on the results from the MD simulations the thermal capacitance per unit area of the compressed phase (C'_i), is estimated to be 4.60×10^{-4} J/m^2·K for SiO_2, 4.78×10^{-4} J/m^2·K for Si, and 3.77×10^{-4} J/m^2·K for Ni. These results show that the thermal capacitance per unit area of the compressed phase varies as the material composition of the nanofin (or nanoparticle) is changed. In addition, the ratio of thermal capacitance per unit area between the compressed phase (corresponding to the first density peak) and nanofin (C'_i/C'_f), is 1.64 for SiO_2, 1.68 for Si, and 0.56 for Ni. In case of silica nanofin (or nanoparticle), the thermal capacitance per unit area of the compressed phase (corresponding to the first density peak of the fluid or solvent phase) is of higher value than that of the silica nanofin itself.

In addition, the ratio of thermal capacitance per unit area with the peak density and the average density of 1st ordered layer was summarized at Appendix F.

Table 11-2 Thermal capacitance per unit area for nanofins with different material composition

Material	C'_f, J/m²K	C'_i, J/m²K	C'_t, J/m²K	C'_i/C'_f
SiO_2	2.80E-04	4.60E-04	1.74E-04	**1.64**
Si	2.85E-04	4.78E-04	1.78E-04	**1.68**
Ni	6.70E-04	3.77E-04	2.41E-04	**0.56**

** Capacitiance per unit area for the compressed phase on the surface of the solid phase (corresponding to the first density peak of the fluid)*

** D_i : 6.5 Å for SiO_2, 5.5Å for Si, 5.5Å for Ni*

11.3. Diode Effect

Heat transfer in a fluid medium can be mediated by several transport mechanisms – such as:

(a) due to conduction or temperature gradient (i.e., thermal potential gradient) which is modeled by Fourier's Law,

(b) due to mass transfer or diffusion that is governed by chemical concentration gradient (i.e., chemical potential gradient) which is modeled by Fick's Law (also termed as "Sorret effect"), or

(c) due to a combination thereof (e.g., also termed as "Duffour effect").

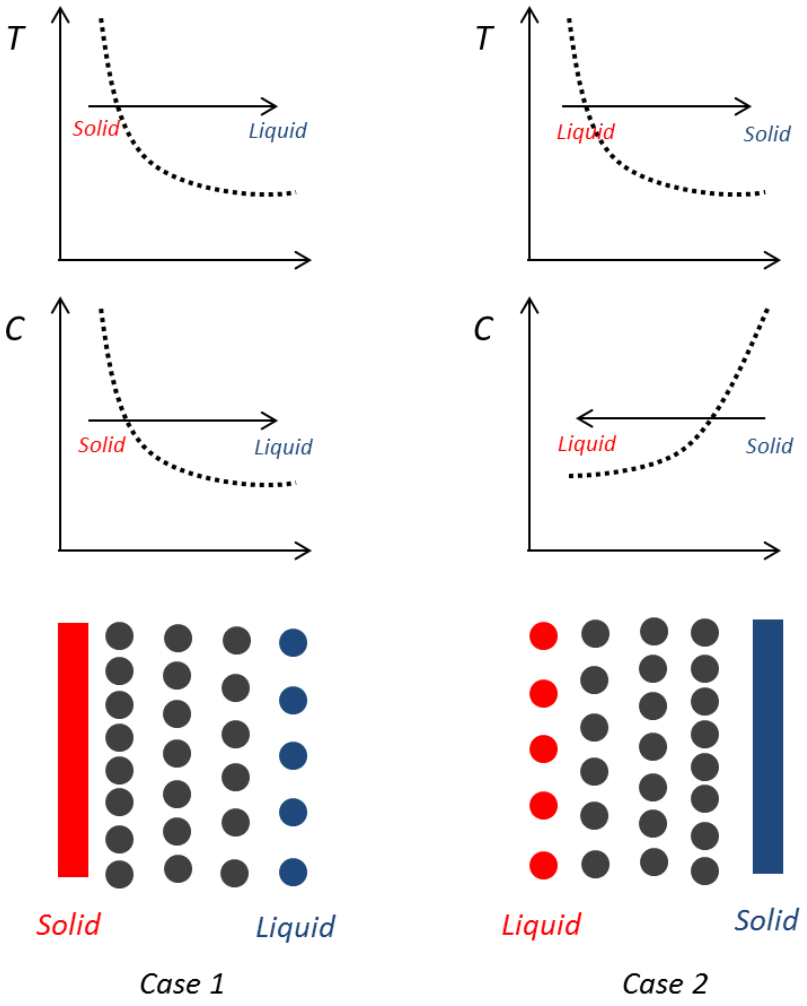

Figure 11-5 Schematic showing heat transfer mediated by temperature gradient (conduction heat transfer) and concentration gradient (heat transfer due to mass diffusion) at the interface between solid and l fluid phases. The dark circles represent molecules in the compressed phase formed by the inter-molecular interactions at the interface between the solid and fluid phase.

The schematic diagram in Figure 11-5 shows a 1-D (one-dimensional) configuration for the two situations where:

(a) the temperature gradient and concentration gradient are in the same direction (therefore contribute to heat flux in the same direction); or

(b) the temperature gradient and concentration gradients are in opposite direction (therefore each mechanism causes heat transfer in opposite directions – the result of the two mechanisms results in net heat transfer in either direction depending on the magnitude of the dominant mechanism).

The following two scenarios are discussed next:

Case 1: For heat transfer from hot solid (e.g., nanoparticle or nanofin) to cold liquid, temperature and concentration values decay with distance away from the surface of the hot solid. This means the heat transfer due to conduction (temperature gradient) and mass transfer (concentration gradient) are in the same direction.

Case 2: However, for heat transfer from hot liquid to cold solid (e.g., nanoparticle or nanofin), temperature gradient (conduction heat transfer) and concentration gradient (heat transfer mediated by mass diffusion) are in opposite direction. Temperature gradient rallies with distance away from the surface of the solid phase (thus heat transfer by conduction is from liquid to solid). In contrast, the concentration gradient decays from the solid side because of the adsorbed layer of fluid with higher chemical potential (compressed phase).

Therefore the heat transfer cannot be same for both Case 1 and Case 2. In other words, the heat transfer from the hot solid to liquid (Case 1) is expected to be higher than the heat transfer from hot liquid to solid (Case 2). Hence there is a bias in the magnitude of heat transfer depending on the direction of the temperature drop (i.e., the

electrical network analogy of a thermal diode). Hence for heat transfer between solid and fluid phases at "small" length scales, for the same temperature difference, the heat flux can be significantly different depending on the directionality of heat transfer – thus in effect realizing a thermal diode. The primary cause of this bias (or diode like behavior) is driven by the directionality of the concentration gradient of the fluid molecules on the solid surface (i.e., the formation of the compressed phase by the solvent molecules).

11.3.1. Dimensionless Analysis for Diode Effect

Due to the different profiles for the spatial distribution of density values at the interface between fluid and solid phase (i.e., nanoparticle or nanofin) with different material composition (i.e. SiO_2, Si, and Ni), the concentration gradient at the solid-fluid interface is expected to be different for each configuration. Hence, dimensionless analysis is performed to provide a relative estimate for the bias in heat transfer between solid and fluid phases (i.e., the magnitude of diode effect for the different nanofin configurations).

The mass flux as a function of chemical potential (concentration) and thermal potential (temperature) can be expressed using the following equation (11-3) [107].

$$J_x = -\rho D \nabla C - \rho D_T C_o (1 - C_o) \nabla T \tag{11-3}$$

The first term in this equation is termed as Fick's law of diffusion, and second term in this equation is termed as the Soret effect. Where J_x is the value of mass flux, ρ is density, D is diffusion coefficient, D_T is the thermo-diffusion coefficient, and C_o is

mass fraction. The total energy flux can be expressed using the following equation, which is obtained as a sum of the Dufour effect and Fouier's law [108].

$$q" = \sum h_i J_i - K\nabla T = \bar{h} J_x - K\nabla T \tag{11-4}$$

Where *q"* is heat flux, h is the partial enthalpy, $\bar{h}$ is the overall enthalpy, K is thermal conductivity, and J_i is the partial mass flux. By substitutting equation (11-3) into (11-4), the overall heat flux is estimated to be:

$$q" = -\rho D \bar{h} \nabla C - [\rho \bar{h} D_T C_o (1 - C_o) + K] \nabla T \tag{11-5}$$

Equation (11-3) can by non-dimensionalized using the following scaling parameters as shown below:

$$q_o" = -K \frac{(T_s - T_\infty)}{L_{C.T}},\ Nu = \frac{h_T L_{C.T}}{K} = \frac{(q"/\Delta T) L_{C.T}}{K} = \frac{q"}{q_o"} \ \text{ or } \ q" = q_o" Nu \tag{11-6}$$

$$\theta = \frac{T - T_\infty}{T_s - T_\infty},\ C^* = \frac{C - C_\infty}{C_s - C_\infty},\ \nabla C = \nabla C^* \frac{(C_s - C_\infty)}{L_{C.C}},\ \nabla T = \nabla \theta \frac{(T_s - T_\infty)}{L_{C.T}} \tag{11-7}$$

Where , q_o is the scaling factor for heat flux by conduction, K is the thermal conductivity of the fluid phase in the vicinity of the solid surface (i.e., the thermal conductivity of the compressed phase), T_s is the surface temperature of the solid phase, T_∞ is the bulk temperature of the fluid phase (far away from the surface of the solid phase), $L_{C,T}$ is the characteristic length scale for temperature gradient (estimated to be the size of the simulation box), Nu is the Nusselt number, h_T is the equivalent heat transfer coefficient, θ is the non-dimensional temperature, C^* is the non-dimensional concentration, C_s is the concentration of the fluid molecules on the surface of the solid (first density peak of the compressed phase), C_∞ is the bulk concentration of the fluid

molecules, and $L_{C,C}$ is the characteristic length scale for concentration gradient. Hence equation (11-5) can be simplified as follows:

$$-K\frac{(T_s-T_\infty)}{L_{C.T}}Nu=-\rho\bar{h}D\frac{(C_s-C_\infty)}{L_{C.C}}\nabla C^*-[\rho\bar{h}D_T\,C_o(1-C_o)+K]\frac{(T_s-T_\infty)}{L_{C.T}}\nabla\theta \quad (11\text{-}8)$$

Therefore, the Nu number can be expressed as follows:

$$Nu=\frac{\rho\bar{h}D}{K}\frac{(C_s-C_\infty)}{(T_s-T_\infty)}\frac{L_{C.T}}{L_{C.C}}\nabla C^*+[\frac{\rho\bar{h}D_T}{K}C_o(1-C_o)+1]\,\nabla\theta \quad (11\text{-}9)$$

$Nu._f$ represents Case 1 (as mentioned above) where the heat transfer is from hot solid to cold fluid, while $Nu._b$ represents Case 2 (mentioned above) where the heat transfer is from hot liquid to cold solid. As mentioned before, for Case 1 - the concentration and temperature gradient are in the same direction, while for Case 2 the concentration and temperature gradient are in the opposite directions. Therefore, Equation (11-9) can be expressed as follows:

$$Nu._f=\frac{\rho\bar{h}D}{K}\frac{(C_s-C_\infty)}{(T_s-T_\infty)}\frac{L_{C.T}}{L_{C.C}}\nabla C^*+[\frac{\rho\bar{h}D_T}{K}C_o(1-C_o)+1]\nabla\theta \quad (11\text{-}10)$$

$$Nu._b=-\frac{\rho\bar{h}D}{K}\frac{(C_s-C_\infty)}{(T_s-T_\infty)}\frac{L_{C.T}}{L_{C.C}}\nabla C^*+[\frac{\rho\bar{h}D_T}{K}C_o(1-C_o)+1]\nabla\theta \quad (11\text{-}11)$$

So the bias in the non-dimensional value of heat flux (i.e., 'diode effect', $Nu._D$) can be expressed as the follows:

$$Nu._D=Nu._f-Nu._b=2\frac{\rho\bar{h}D}{K}\frac{(C_s-C_\infty)}{(T_s-T_\infty)}\frac{L_{C.T}}{L_{C.C}}\nabla C^* \quad (11\text{-}12)$$

Equation (11-12) implies that there exists a diodicity to heat transfer depending on the directionality of temperature gradient at the solid-fluid interface (which is driven

by the directionality of concentration gradient), even though the magnitude of the temperature gradient remains same.

Many of the material property values required (e.g., mass diffusivity or diffusion coefficient) for PF-5060 to estimate the thermal diodicity are not readily available in the literature. Hence, the values of the diffusion coefficient are estimated from the following equations culled from the literature [109] [110]:

$$D = 7.4\times10^{-8} T \frac{(\phi M)^{0.5}}{\mu V^{0.6}} \tag{11-13}$$

Where, D is the diffusion coefficient, M is the molecular weight of the solvent, V is molar volume of solute, T is the absolute temperature, μ is the viscosity of the solvent, and ϕ is the association factor in Wilke-Chang correlation [110]. Details of the calculation procedure are described in Appendix F. The thermo diffusion coefficient can be obtained from the following equation [111].

$$D_T = \frac{\overline{D}_T}{C_1 C_2}, \overline{D_T} = k(x_1)(M_1 - M_2)\frac{\alpha}{\mu}, \; k(x_1) = (5.34x_1 - 7.00x_1^2 + 1.65x_1^3)10^{-11} \tag{11-14}$$

Where, M is the molar mass, α is the thermal expansion coefficient, and μ is the viscosity of the lighter component.

11.3.2. Diode Effect Calculation

11.3.2.1. $L_{C.T}$=$L_{C.C}$

The density values (and the gradients) in the compressed phase obtained from the MD simulations are plotted in Figure 11-6. The density of the compressed surrounding

the Ni nanofin, decays more sharply compared with that of Si or SiO_2. This means that the compressed phase of the PF-5060 fluid molecules on the Ni surface (solid surface) are packed in a tighter configuration (i.e., are more ordered) than in the case of Si or SiO_2. This implies that Nickel has more affinity for PF-5060 than silicon or silicon dioxide. This is also consistent with the previous experiment results for contact angle, where Ni heaters (plain and with nanofins) had a lower contact angle than that of Si or SiO_2.

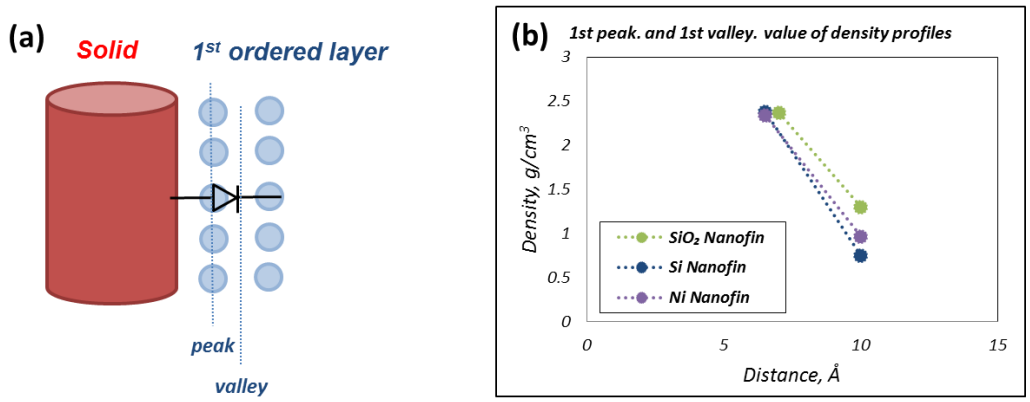

Figure 11-6 (a) Schematic showing bias in heat transfer (thermal diode effect) between solid surface to fluid; (b) Linear fit for density profile between the first peak and first valley of the compressed layer.

The values of $Nu._f$, $Nu._b$ and $Nu._D$ for the different nanfin configurations (Si, SiO_2, and Ni) are listed in Table 11-3. When $L_{C.T}$ is assumed to be the same as $L_{C.C}$, $L_{C.T}/L_{C.C}$ term is canceled out at equation (11-10), (11-11), and (11-12). The parameters used for calculating the values for the diode effect are listed in Table F2, and the details of the

calculation procedure are listed in Table F3. The values of D and D_T for Si are higher than that of Ni or SiO_2. The results show that the diodicity ($Nu._D$) is approximately 0.5% for SiO_2, 1.3% for Si and 0.9% for Ni, respectively.

As discussed before, since the energy flux terms that are driven by the values of concentration gradient, where the direction of the concentration gradient is oriented from the bulk fluid phase to the solid surface (i.e., the concentration is higher on the solid surface and lower in the bulk fluid phase). When the concentration gradient and temperature gradients are in the same direction (i.e., the magnitdues are higher on the solid surface than in the bulk fluid phase), the energy flux has higher magnitude than in the case where the respective gradients are in opposite directions. In other words, when the concentration and temperature gradients are in the opposite direction, the magnitude of the energy flux is lower.

Table 11-3 Values of D and D_T as well as Nu for various materials by assuming $L_{C.T} = L_{C.C}$

Material	D, m²/s	D_T, m²/sK	$Nu._f$	$Nu._b$	$Nu._D$	$Nu._D/Nu._f$ X 100, %
SiO_2	9.82E-10	1.74E-10	1.2296	1.2231	0.0065	0.5
Si	1.63E-09	3.35E-10	1.3032	1.2868	0.0164	1.3
Ni	1.32E-09	2.47E-10	1.2669	1.2557	0.0112	0.9

In estimation of diode effect, the local temperature of 1st peak layer was assumed as 800K and the local temperature of 1st valley layer is 300K. However local temperature

and local density vary with time in the MD simulations that were performed for calculating the interfacial thermal resistance. Therefore in future work (for obtaining better accuracy in the calculations), it is recommended that the local values of temperature and local values of density be used in the calculations at the "cutoff -time" for calculating the interfacial thermal resistance.

11.3.2.2. $L_{C.T} \neq L_{C.C}$

Under assumption that $L_{C.T}$ is not the same magnitude as $L_{C.C}$, the values of *Nu* ($Nu._f$ $Nu._b$, and $Nu._D$) can be calculated using the following procedure. $L_{C.T}$ is estimated to be equal to half of the width of the simulation box used in the Molecular Dynamics (MD) simulations.

11.3.2.2.1. $L_{C.C} = V/A_s$

Characteristic length for concentration ($L_{C.C}$) is estimated using the following equation:

$$L_{C.C} = \frac{V}{A_s} = \frac{D}{4} \tag{11-15}$$

Where V is volume of nanofin, A_s is surface area of nanofin, and D is diameter of the nanofin (6.78Å). The values of Nu ($Nu._f$, $Nu._b$ and $Nu._D$) for the nanofins ($Si/SiO_2/Ni$) obtained in these simulations are summarized in Table 11-4.

Table 11-4 Values of *Nu* when $L_{C.C} = V/A_s$

$L_{C.C} = V/A_s$				
Material	***Nu.f***	***Nu.b***	***Nu.D***	***Nu.D/Nu.f X 100, %***
SiO_2	*1.2733*	*1.1794*	*0.0940*	*7.4*
Si	*1.4142*	*1.1757*	*0.2385*	*16.9*
Ni	*1.3425*	*1.1800*	*0.1625*	*12.1*

** $L_{C.T}$: 24.595Å, half of MD box*
** $L_{C.C}$: 1.695Å, V/As*

11.3.2.2.2. $L_{C.C} = R_m$

Characteristic length for concentration ($L_{C.C}$) can also be estimated from the Lennard-Jones (LJ) potential as shown in the following equation [112].

$$E(R) = 4\varepsilon\left[\left(\frac{\sigma}{R}\right)^{12} - \left(\frac{\sigma}{R}\right)^{6}\right] \tag{11-16}$$

Where E is LJ potential, R is the distance between two molecules, σ is the finite distance at which inter-particle potential is zero, and ε is the depth of the potential well.

The distance when the potential is minimum (R_m), is expressed in the following equation:

$$R_m = 2\sigma^{\frac{1}{6}} \tag{11-17}$$

The values of σ and R_m are listed in Table 11-5 for each nanofin configuration. Average values of R_m were used for the estimation of *Nu* values. The values of *Nu* ($Nu._f$, $Nu._b$ and $Nu._D$) for different nanofin configuration (Si, SiO_2, and Ni) are summarized in Table 11-6. All of these estimates show that Si nanofins are expected to display higher

values of thermal diodicity than Ni (which is approximately 20-30% lower than that of Si) while silica has the lowest value of thermal diodicity (which is approximately 50% lower than that of Si) among the three cases considered in this study.

Table 11-5 Values of R_m for different nanofins (Si, SiO_2 andNi)

SiO_2 nanofin	σij	R_m, Å	Si nanofin	σij	R_m, Å	Ni nanofin	σij	R_m, Å
Si-C	3.753	1.251	Si-C	3.753	1.251	Ni-C	3.753	1.251
Si-F	3.645	1.215						
O-C	3.152	1.051	Si-F	3.645	1.215	Ni-F	3.645	1.215
O-F	3.062	1.021						
Average	3.403	1.134	Average	3.699	1.233	Average	3.699	1.233

Table 11-6 Values of Nu ($Nu._f$, $Nu._b$, and $Nu._D$) for nanofins (Si, SiO_2 and Ni) when $L_{C.C} = R_m$

$L_{C.C} = R_m$				
Material	Nu.f	Nu.b	Nu.D	Nu.D/Nu.f X 100, %
SiO_2	1.2965	1.1561	0.1404	10.8
Si	1.4589	1.1310	0.3279	22.5
Ni	1.3729	1.1496	0.2233	16.3

* $L_{C.T}$: 24.595Å, half of MD box
* $L_{C.C}$: R_m, from LJ potential

11.4. Summary

In this chapter, based on the results obtained from the molecular dynamics (MD) simulation, the thermal capacitance of the compressed layer and the associated diode effect was explored. Dimensional analysis was performed to estimate the relative magnitudes of the different transport mechanisms.

12. CONCLUSION

In this study, nano-scale transport phenomena was explored for pool boiling of a fluorocarbon refrigerant on various heater configurations (shape, size and materials as well as with surface nanostructures) using nano-scale temperature metrology techniques by using Thin Film Thermocouples (TFT). The nanopillars (which acted as nanofins) were engineered to be on a specific pitch, height and diameter on a flat heater surface using nano/microfabrication techniques involving Step and Flash Imprint Lithography (SFIL) and conventional Nano/Micro Electro Mechanical Systems (NEMS/MEMS) techniques such as surface micromachining, Physical Vapor Deposition (PVD) and "lift-off" process. The surface temperature fluctuations during pool boiling were recorded using a high speed data acquisition system connected to an array of Thin Film Thermocouples (TFT) that were fabricated in-situ on the heater surface containing surface nanostructures/ nanofins (or for plain atomically smooth silicon wafers). Hence, this enabled the measurement of surface temperature fluctuations during pool boiling with minimal spatial perturbation of the transport mechanisms involved on the heater surface during pool boiling. Numerical and analytical models were also developed in this study to explore the effect of heater size as well as the effect of material properties (e.g., thermal conduction resistance and interfacial thermal resistance) on the pool boiling heat flux.

The analysis for vapor-bubble "jet" configuration at critical heat flux condition on the horizontal flat surface was conducted. The maximum jet number and formation were estimated for different heater shapes. Investigation for jet configuration was

performed for rectangular and circular shaped heaters. The result shows that the dimensionless critical heat flux varies with non-dimensional value of the heater width (length-scales were scaled using the "most dangerous" Taylor instability wavelength) regardless of the heater shape. The analytical model for dimensionless heat flux on square heater can be successfully applied for rectangular and circular shaped heaters in horizontal configuration during pool boiling. The predictions from the analytical model are observed to be consistent with the experimental measurements for pool boiling heat flux.

The effect of the material composition of the heater (for both atomically smooth and engineered nanostructures/ nanopillars which act as nanofins) on the pool boiling heat flux for a horizontal flat surface was also explored in this study. Silicon, silica and Ni-based thin films (e.g., chromel - a Ni alloy and Ni thin films) were chosen as the candidate materials that represent the class of materials corresponding to: semiconductor material, ceramic material, and metals, respectively. The experiments were performed with the purpose of investigating the effect of each class of materials on pool boiling for the chosen working fluid (PF-5060). The result shows that the pool boiling curve is strongly influenced by the material property, size and shape of the heater as well as the morphology of the engineered surface nanostructures, i.e., the nanopillars (which act as nanofins). In particular both the critical heat flux (CHF) and minimum heat flux (MHF) vary with the variation of the material property, size and shape of the heater as well as the morphology of the of the engineered surface nanostructures, i.e., the nanopillars (which act as nanofins). It was observed that the temperature at which the CHF and

MHF conditions are achieved also vary with the variation in these experimental parameters (i.e., the material composition and material property of the heater, size and shape of the heater as well as the morphology of the engineered surface nanostructures, i.e., the nanofins) thus causing a variation in the extent of the transition boiling regime on the pool boiling curve for these materials and heater configurations.

The contact angle between a PF-5060 droplet and each of the heater substrates was also measured. Since metallic surface demonstrated the highest value of critical heat flux it was also observed to have the lowest contact angle. In contrast the ceramic surface demonstrated the lowest value of critical heat flux and correspondingly the highest value of the measurements for the static contact angle (among the materials considered in this study).

Pool boiling phenomena on nanostructured surfaces were also studied experimentally. The silicon nanofin arrays were fabricated with various heights and pool boiling phenomena was investigated experimentally for silicon heaters with these engineered surface nanostructures. Significant enhancement in the CHF values were measured in the pool boiling experiments where the CHF was observed to increase with increase in height of the nanofins. In contrast the minimum heat flux (MHF) values were observed to decrease marginally with increase in the height of the nanofins. In addition, the values of the wall superheat for both CHF and MHF were found to decrease with increase in the height of the nanofins. Thus the pool boiling curve is observed to shift in these experiments (compared to the boiling curve obtained for a plain atomically smooth silicon wafer surface). In addition, the extent of the transition boiling regime is also

found to shrink for the boiling curves in these experiments as the height of the nanofins is increased. The static contact angle is also observed to decrease with increase in height of the nanofins (i.e., surface is observed to become increasingly wetting to PF-5060).

The pool boiling phenomena for heater surfaces (silicon wafer substrates) composed of ceramic nanofins were also investigated. Even though the material composition of the heater surface and the morphology of the surface nanostructures were changed from silicon to silica, the observed trends in the experiments (as mentioned in the previous paragraph) were similar. As the height of the nanofins is increased the CHF values were enhanced significantly, while the MHF values were degraded marginally and the wall superheat (the heater surface temperature) at which CHF and MHF conditions were achieved were also found to decrease (more significantly for MHF than CHF) – resulting in reduction in the extent of the transition boiling regime.

When comparing the effect of the material composition and property as well as the morphology of the nanofins on the heater surface for pool boiling phenomena (e.g., pool boiling heat flux, wall superheat, CHF, MHF, etc.) the experimental results show that the silicon nanofins contribute more to enhancing the pool boiling heat transfer than that of the silica nanofins, while Ni nanofins show the highest level of enhancement of CHF values.

The interfacial thermal resistance (Kapitza resistance, R_k) values for the different nanofin materials were estimated by employing molecular dynamic (MD) simulations. The numerical predictions were compared with the trends in the experimental data. The results show that critical heat flux (CHF) increases with decrease in the values of

interfacial thermal resistance, while minimum heat flux (MHF) decreases with decrease in the values of the interfacial thermal resistance.

The MD simulations also show the formation of a surface adsorbed layer of the fluid molecules on the nanofins – which typically have a higher density than in the bulk phase (this is termed as the "compressed phase"). The manifestation of the different transport mechanisms at the molecular scale is termed as the "nanofin effect". Three different manifestations of the nanofin effect were explored in this study:

(1) Interfacial thermal resistance (Kapitza resistance) arising as a barrier to energy transfer from the nanofin to the bulk fluid phase (due to impedance mismatch arising from different values of vibration frequency of the molecules in the solid and fluid phases);

(2) Thermal capacitance arising from the higher density of the compressed phase in the vicinity of the nanofin surface than in the bulk fluid phase; and

(3) Thermal diode effect where the heat flux can be marginally higher or lower by as much as 25% depending on the direction of the temperature drop between the nanofin surface and the bulk fluid phase (this arises from the directionality of the concentration gradient either aiding or opposing the temperature gradient, resulting in mass transfer mediated thermal energy transport that either aids or opposes the thermal energy transport due to temperature gradients).

The nanofin effect (and particularly the thermal diode effect) explored in this study - can be leveraged for various nanotechnology and engineering applications involving transport phenomena at the molecular scale.

13. FUTURE DIRECTION

It is recommended that the effect of surface roughness on the pool boiling curve be explored to properly characterize the transport phenomena in heterogeneous phase change heat transfer [113]. The surface characteristics before and after boiling experiments, should be analyzed by using microscopy techniques, such as: SEM (Scanning Electron Microscopy), AFM (Atomic Force Microscopy), and EDX (Energy Dispersive X-Ray Spectroscopy). Results show that boiling processes are modulated by progressive fouling of the heater surfaces. In addition, the metrology techniques developed in this study using temperature nanosensors such as - Thin Film Thermocouples (TFT) – can be adapted for the study of fouling and the effect of fouling on pool boiling. Some of the feasibility studies are presented here as a prelude for these topics that are suggested for future exploration.

13.1. Analysis of Residue on Boiling Surface

In previous studies reported in the literature on pool boiling experiments involving nanofluids, nanoparticle residues (precipitates) were observed on the boiling surface after the experiments [114]. Hence, it is recommended in pool boiling studies that the boiling surface be characterized for residues both before and after the experiments. In this study, the residues (precipitates and contaminants) were also detected on the heater surface after conducting the pool boiling experiments, when surface characterization was performed both before and after the boiling experiments. Figure 13-1 shows the optical microscopy image of silicon heater surfaces (flat surfaces

without patterned nanofins) before and after performing the boiling experiments. From the images of the heater surface obtained after performing the pool boiling experiments, it is observed that residues are formed on the whole silicon wafer surface.

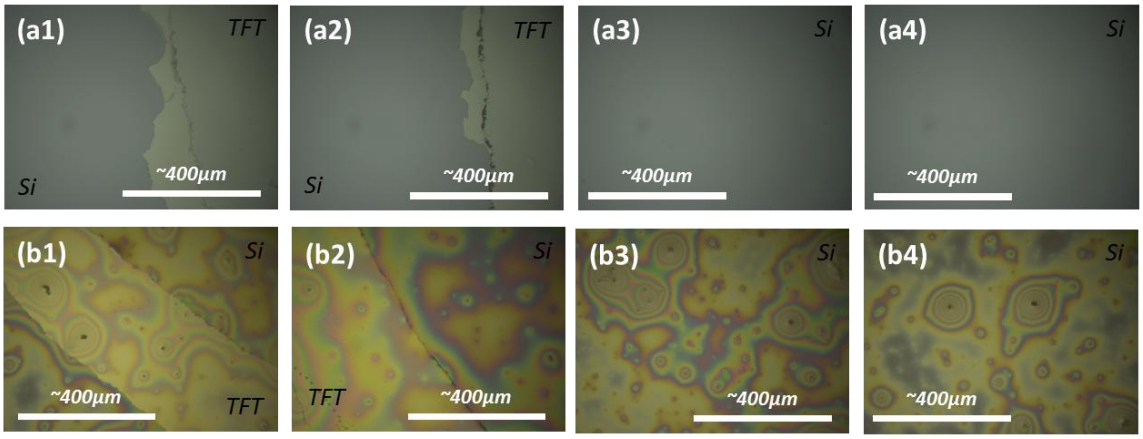

Figure 13-1 Optical microscopy images of the silicon heater surfaces (without patterned nanofin surfaces) : (a) before boiling experiments, and (b) after boiling experiments.

Figure 13-2 shows Scanning Electron Microscopy (SEM) images of the flat silicon heater surfaces for both before and after the boiling experiments. The images show that residues were formed on the boiling surface all over the heater surface that was in contact with the test fluid (PF-5060).

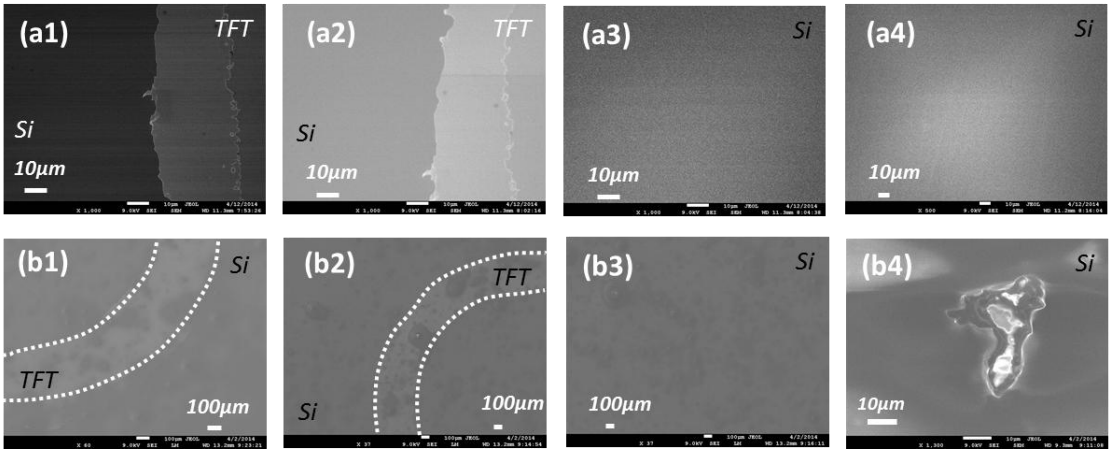

Figure 13-2 SEM (Scanning Electron Microscopy) images of the silicon heater surfaces (without patterned nanofin surfaces): (a) before boiling experiments, and (b) after boiling experiments.

Atomic Force Microscopy (AFM) was used to estimate the change in surface roughness of the heater surface (silicon wafer without patterned nanofins) for both before and after the boiling experiments. The images obtained from the AFM experiments are shown in Figure 13-3.

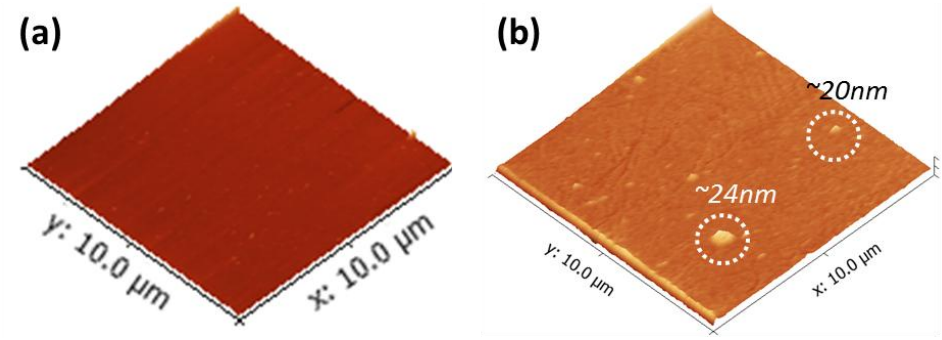

Figure 13-3 Images obtained from AFM (Atomic Force Microscopy) of flat silicon heaters without any patterned nanofins, for: (a) before boiling experiment and (b) after boiling experiment

In addition, from the AFM data, root mean square roughness (R_q) can be obtained by using the following equation:

$$R_q = \sqrt{\frac{1}{N}\sum_{j=1}^{N} r_j^2} \tag{12-1}$$

The root mean square roughness (R_q) of the heaters with plain surface (without engineered nanofins) for different material compositions (Si, SiO_2, Ni, and Chromel), was plotted for before and after pool boiling experiments in Figure 13-4(a). The images show that the root mean square roughness (R_q) of the heater surfaces increased after performing the pool boiling experiments. This shows that residues (contaminants) are deposited on the plain heater surface (without patterned nanofins) during the pool boiling experiments. Figure 13-4(b) shows the root mean square roughness (R_q) of heater surfaces with patterned nanofins for different material composition (Si, SiO_2, and Ni). The images show that the root mean square roughness (R_q) also increases after pool boiling on the heater surfaces with nanofins. The images show that the increase in surface roughness is significantly higher for silica heaters with patterned nanofins than that of the plain silica heater surfaces (without patterned nanofins). Similarly, the images show that the increase in surface roughness is significantly higher for Ni heaters with patterned nanofins than that of the plain Ni heater surfaces (without patterned nanofins). In contrast, the images show that for the heaters with patterned nanofins - the increase in surface roughness is marginally higher for silicon heaters than that of silica or Nickel. Similarly, the images show that for the plain heaters (without patterned nanofins) the increase in surface roughness is marginally higher for silicon heaters than that of silica

or Nickel. This is probably due to lower surface affinity of the contaminants/ residues for Si than for silica or Ni.

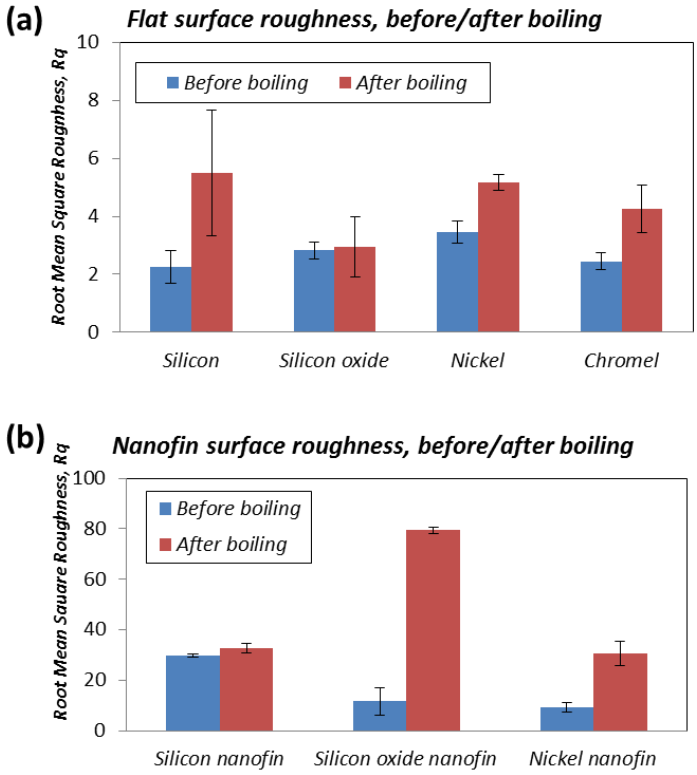

Figure 13-4 Surface Roughness (R_q) measurements for: (a) flat heater surface, and (b) heater surface with patterned nanofins.

Energy Dispersive X-ray Spectroscopy (EDX) was performed to analyze the material composition of the residues, and are shown in Figure 13-5. EDX results for the heater surface before boiling show that no unexpected contaminants were detected in the elemental composition of the heater surface. However EDX results for the heater

surfaces obtained after boiling show that carbon and oxygen were detected (which are not expected to be detected except those arising from residues on the surface).

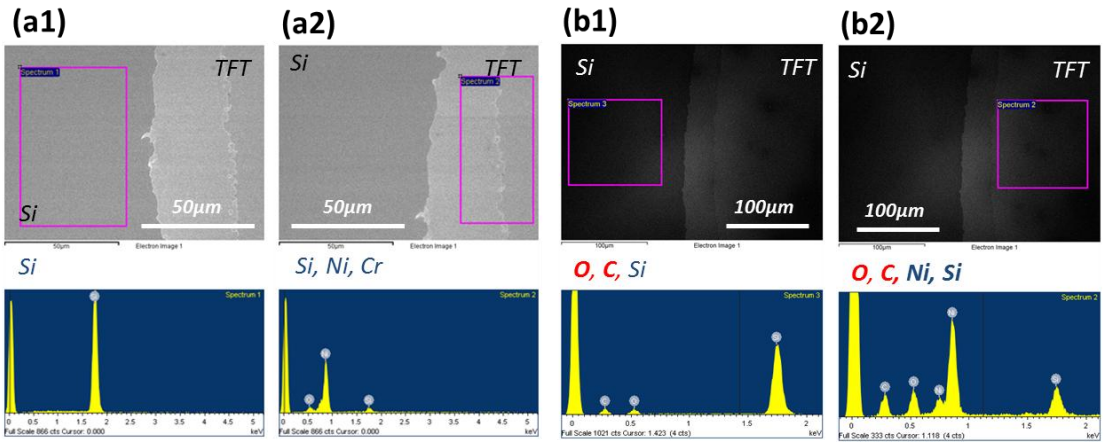

Figure 13-5 EDX (Energy Dispersive X-ray spectroscopy) analysis of flat plain (without patterned nanofins) silicon heater surface: (a) before, and (b) after boiling experiments.

EDX analysis of the residues (as observed in the SEM images) enables more clear identification that the residue on the plain silicon heater surface is an organic residue, as shown in Figure 13-6. The carbon and oxygen peaks are clearly observable in these images. (Silicon peak observed in the EDX results is expected to be from the silicon substrate.)

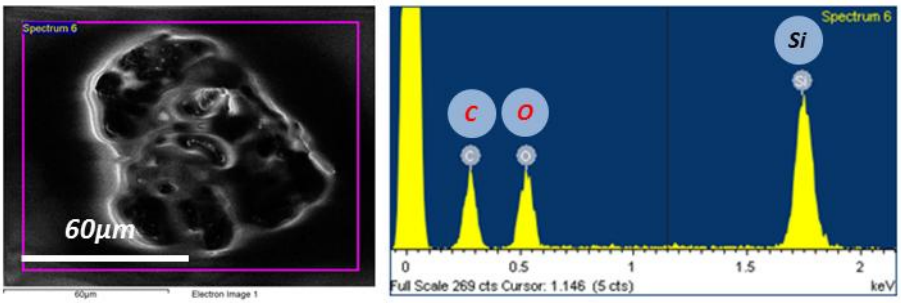

Figure 13-6 EDX analysis of residue that was formed on a plain flat silicon heater surface during boiling experiments.

In this study, the working fluid (PF-5060) for pool boiling is organic fluid, which also contains dissolved oxygen. Therefore the likely origin of the organic residue that is formed on the boiling surface is from PF-5060 (or contaminants in the test chamber that were dissolved in the test fluid and then precipitated on the heater surface). It is likely that the high temperature of the heater surface can also lead to chemical fouling of the heater surface. Similar results were obtained when the residues formed on heaters with patterned nanofins were analyzed using EDX (the results from EDX analyses as well as microscopy images obtained from SEM and AFM are listed in Appendix G). Moreover similar analyses were performed for silica/nickel/chromel heaters as shown in Appendix G.

13.2. Effect of Fouling of Heater Surface on Pool Boiling

The surface characterization of the heater surfaces (both before and after boiling) show that formation of residues during boiling (i.e., fouling of the heater surface) can

affect the pool boiling heat transfer. Hence properly designed experiments are needed to analyze the effect of fouling on pool boiling – in order to delineate the role of the nanofins in boiling heat transfer enhancement. This is the motivation for the suggesting fouling as a future topic of study for pool boiling investigations involving heaters with patterned surfaces. Fouling of the heater surface is expcted to reduce the magnitudes of pool boiling heat flux – though counterintuitive results can occur dpending in the regime of pool boiling (e.g., fouling can stabilize film boiling or enhance nucleate boiling depending on the morphology of the precipitates, such as when isolated precipitates form "nanofins"). A preliminary literature review of fouling will be explored in the next section.

13.2.1. Literature Review of Fouling

Fouling is the primary reason for wastage of energy and also the increase in operational cost of various heat exchangers. As fouling builds up progressively with longer durations of operation of heat exchangers - the performance of the heat exchanger continues to degenerate, since the added thermal resistance from fouling causes reduction in heat transfer while the flow area (cross-section) continues to shrink which drives up pressure drops in the heat exchangers (this in turn increases the pump work and therefore the operational cost). The fouling mechanisms are complicated and there are various parameters to consider, which can be segmented into physical and chemical parameters. These parameters are coupled strongly, which makes the fouling phenomena difficult to characterize and model [115].

Watkinson provides a comprehensive review for chemical reaction fouling [116]. The factors affecting fouling rate and chemical reaction mechanisms for fouling involving organic fluids were thoroughly discussed in this review. Recent investigations have focused on autoxidation as plausible mechanism that accelerates fouling. These reviews have been performed by characterizing fouling rate as a function of test fluid, operational temperature, mass flow rate, and analysis methods. In addition, a comprehensive discussion on the effect of surface properties and chemical kinetics models were also reported on the behavior of chemical reaction fouling [117].

The initial fouling rate increases with temperature (this was established by Crittenden [118]). Numerical models for the initial fouling rate are often expressed as a function of temperature and mass flow rates. The predictions from the numerical models are found to be consistent with the experimental data.

The initial fouling rate was observed to be dominated by the isokinetic temperature [119]. For a clean surface (which serves as an initial condition) when the temperature is higher than the isokinetic temperature, the initial fouling rate increases with increasing velocity. Similarly the initial fouling rate decreases with velocity, when the temperature falls below the isokinetic temperature threshold. In addition, the initial and final fouling rates were also found to scale with the Reynolds number of the flow [120]. The final fouling rate increases marginally with velocity, while the initial fouling rate decreases with velocity. The authors argued that this implies that the fouling mechanism was not controlled by bulk mass transfer rates or mass averaged values of velocity.

The effect of system pressure on the fouling rate was investigated along with surface temperature in hydrocarbon based heat exchangers [121]. At high operating pressures, the heat flux decreased with increasing pressure (potentially due to higher rates of fouling). In general, a linear relationship was reported between initial fouling rate and system pressure, whereas a significant correlation between initial fouling rate and surface temperature was not observed in this study.

Comprehensive discussion on the relationship between corrosion and fouling were also reported [122]. Corrosion increases the wall roughness. Hence corrosion results in generation of more nucleation sites that promote various transport mechanisms responsible for fouling. The corrosion induced fouling rate is affected by fluid composition, operational temperature and mass flow rate.

The fouling phenomena were investigated experimentally using kerosene mixtures that were mixed with different olefin species [123]. Six different olefins were tested such as: indene, hexadencene-1, 4-vinyl-1-cyclohexene, decene-1, di-cyclopentadience, and hexadencene-1. The results show that the fouling resistance is strongly dependent on the material properties (and the chemical composition) of the olefin species.

The fouling resistance along the length of a heat exchanger was investigated and the authors reported that fouling was observed both before and after the heating zone [124]. The results from this interesting investigation also showed that fouling rates are not uniformly distributed within the heating zone. Depending on the position and at certain times during operation, the rate of buildup of fouling resistance has a slight

negative value. This indicates that the morphology and composition of the deposit (such as the formation of insoluble gums on the walls) affect the profile of the thermal boundary layer and can occasionally drive heat transfer enhancement. Moreover the fouling resistance has a strong relationship with gum concentration [125]. This gum concentration was consistent with the observation of the decomposition of primary oxidation products that were observed in this study. The effect of finned surfaces on fouling was studied using aqueous solution of $CaSO_4$ [126]. The results showed that grooved surfaces are less sensitive to fouling than smooth surfaces.

The preliminary literature review on fouling shows that it is a complex interaction of material properties and chemical kinetics. In addition, it was observed that patterned surfaces (with micro-scale features) have lower rates of fouling and therefore demonstrate better performance in pool boiling than a plain heater surface (without any patterned micro-structures). Prior studies demonstrate that the fouling phenomena are more sensitive to the local effects (such as temperature and surface patterning) than the global parameters (such as flow rate). This forms the basis for the suggested topics for future direction. Temperature nano-sensor arrays, such as Thin Film Thermocouples (TFT) are adept at making local measurements while causing minimal disruptions to the surface topology and therefore the local transport mechanisms. Hence pool boiling studies can be performed with TFT arrays for monitoring local values of fouling rates in real time as the experiments are performed. TFT measurements in conjunction with surface characterization can enable additional insights in the initial rates of fouling during pool boiling experiments. Hence, preliminary experiments were performed to

explore the feasibility of utilizing TFT arrays for measuring the effect of fouling on pool boiling.

13.2.2. Schematic for Fouling Analysis

Figure 13-7(a) shows the schematic diagram for the experimental apparatus that was used for performing the fouling experiments. In these experiments SU-8 (negative type photoresist, Manufacturer: Microchem Corp.) was deposited to form a barrier layer to heat transfer during pool boiling. The deposited SU-8 film represents the initial fouling layer (i.e., a uniform coating of organic residue formed on the boiling surface). A TFT array was fabricated on the wafer surface prior to deposition of the SU-8 film - for the purpose of measuring the surface temperature transients during pool boiling after an initial fouling film has been established on the heater surface. The merit of this particular choice of photoresist (which represents the fouling film), is that the thickness of photoresist can be controlled easily by modulating the spin speed during the coating operation in a spin-coater. In prior literature reports - the fouling resistance values were reported to change from 0.015 to 0.75 m^2K/kW [123]. Using the property values of SU-8 this would correspond to change in thickness of SU-8 layer from 5μm to 225μm. For estimation of the thickness of the SU-8 layer, thermal conductivity of 0.3 W/mK is used based on the manufacturer data sheet. Figure 13-7 (b) shows the SU-8 thickness that can be obtained as a function of spin speed for the spin-coater. The figure shows that, the SU-8 thickness can be changed from sub-micron thickness to several microns (to up to several hundreds of microns). After the photoresist (SU-8) was deposited on a wafer

with TFT (which were fabricated in prior steps, as described in Chapter 2) – photographic images were obtained. The images are shown in Figure 13-7 (c) after spin coating, and as shown in Figure 13-7 (d) after packaging of the TFT. This is followed by mounting of the silicon wafer with the packaged TFT arrays on a calorimeter apparatus (copper block) prior to performing the pool boiling experiments.

It is well known that the heat flux values are degraded with increase in fouling layer thickness. Therefore it is expected that critical heat flux (CHF) values can degrade with imcrease in the thickness of SU-8, as shown in the schematic of Figure 13-8 (a). Incidentally (as mentioned before), M. Esawy et al. reported that a finned surface was less susceptible to fouling during pool boiling [126]. To verify this experimental result – finned structures can be formed by photoligraphic patterning of SU-8 films (either in a single layer deposition or by deposition of multiple layers). The morphology of these surface structures fabricated from photoresists such as SU-8 can be controlled effectively by conventional photolithography. Moreover these micro-structures of SU-8 can be fabricated and their thickness can be controlled with high precision - as shown in Figure 13-8 (b). Hence the rate of degradation of CHF with increase in the thickness of SU-8 on the heater surfaces with engineered micro-structures (ΔCHF2) is expected to be smaller than the rate of degradation of CHF on a flat surface (ΔCHF1), even though the net increase in thickness is the same for both cases.

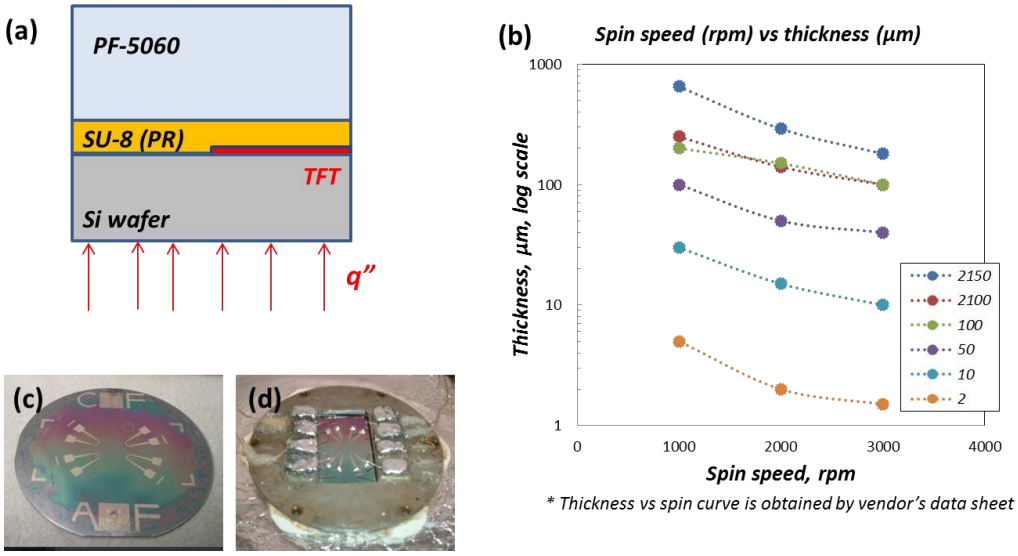

Figure 13-7 (a) Schematic diagram for fouling experiment, (b) Graph of SU-8 thickness with spin speed, (c) Image of flat silicon wafer surface with TFT (fabricated apriori) after photoresist coating (SU-8, 5μm thickness), and (d) After packaging of the TFT arrays.

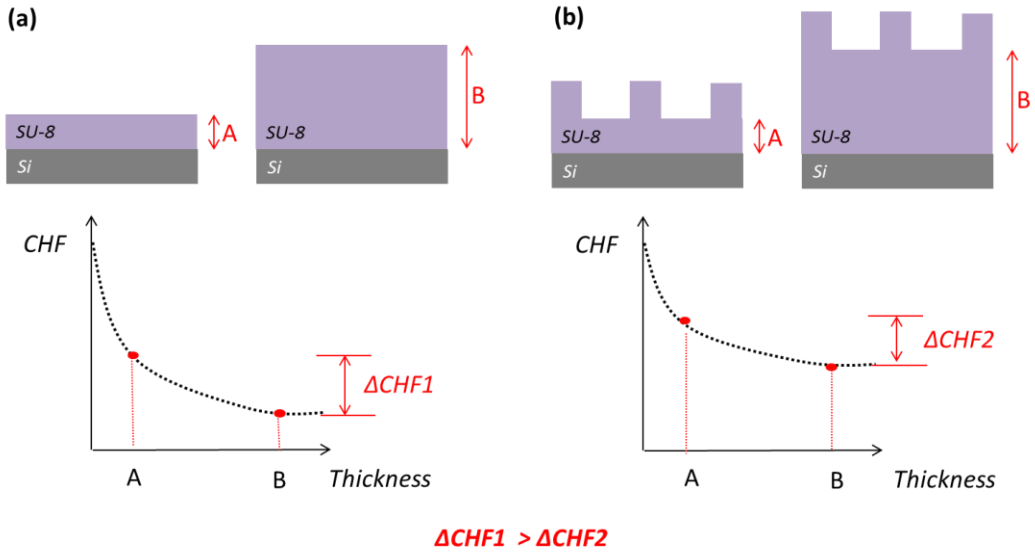

Figure 13-8 Expected data for rate of change of CHF with SU-8 for a (a) Flat surface, and (b) Micro-structured surface.

13.2.3. Preliminary Experimental Result

SU-8 layers were deposited on two different silicon wafers (with TFT arrays fabricated apriori) with a thickness of 5μm and 20.5μm. Pool boiling experiments were performed using these wafers. The surface temperature of the SU-8 coating was calculated by using Fourier's law as follows (13-1).

$$T_w = T_{TFT} - \frac{q'' L}{K} \tag{13-1}$$

Where T_s is the surface temperature, T_{TFT} is the temperature value recorded by TFT under steady state conditions, *q"* is the value of heat flux obtained from the calorimeter apparatus under steady state conditions, *L* is the thickness of SU-8, and K is thermal conductivity of SU-8 obtained from manufacturer's data sheet (0.3 W/mK).

The pool boiling curve for SU-8 (with a thickness of 5μm) is shown in Figure 13-9. In addition, the heat flux plot with (T_{TFT}-T_{sat}) is available in Appendix G. CHF of SU-8 5μm (or 20.5μm) thickness surface has higher value than the CHF value of flat silicon surface. This is because that the surface roughness of the SU-8 coating is significantly higher than the silicon wafer (which is a single crystal with a crystal plane exposed – so has atomic scale roughness of the order of 1 ~ 10 Å). Owing to the higher roughness values, SU-8 coatings are expected to have significantly higher values of bubble nucleation site density (which in turn could also affect the bubble growth rates, bubble departure diameter and bubble departure frequency values). Hence it is expected that SU-8 coatings can result in higher values of heat flux than that of the bare silicon wafers.

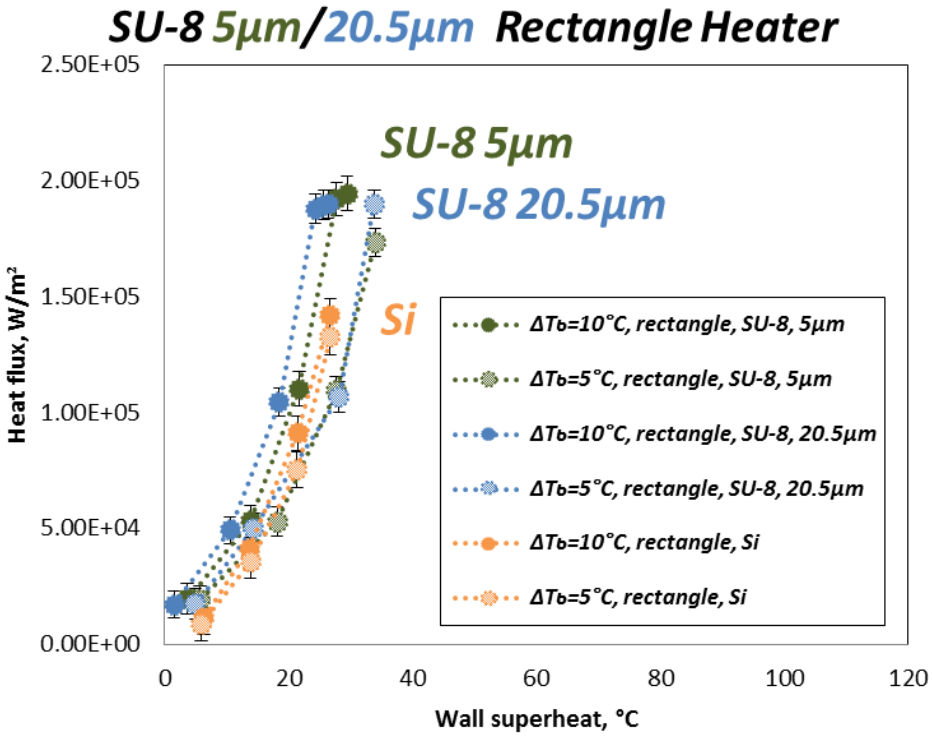

Figure 13-9 Pool boiling curve of photoresist coated surface

Pool boiling curves as well as critical heat flux (CHF) values were obtained as a function of SU-8 thickness and are plotted in Figure 13-10. (CHF and uncertainty values are also available in Appendix G). CHF marginally decreases with photoresist thickness at liquid subcooling of 10 ^{o}C (Figure 13-10 (a)), however CHF increases with PR thickness at liquid subcooling of 5 ^{o}C (Figure 13-10 (b)). For further exploration experimental validation of heater surfaces with larger range of film thickness of the deposited SU-8 films are required. In other words, to verify critical heat flux degradation with increase in thickness of the fouling films, additional pool boiling experiments need

to be performed involving heaters coated with thicker layers of SU-8 films – in order to resolve this conundrum.

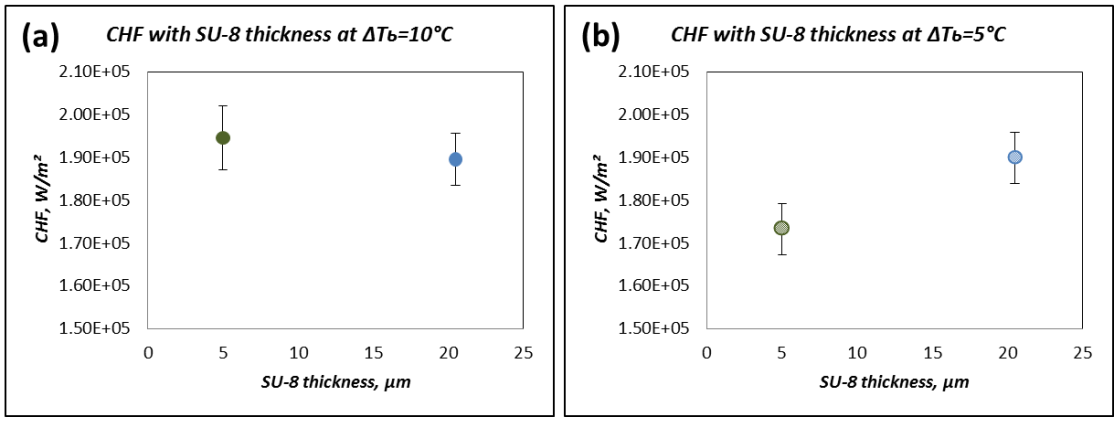

Figure 13-10 Plot of critical heat flux (CHF) values as a function of SU-8 thickness for: (a) ΔT_b = 10 ^{o}C and (b) ΔT_b = 5 ^{o}C.

13.3. Summary

In this chapter, the surface roughness values of heater surfaces (for before and after performing boiling experiments) were measured by performing surface characterization of the heater surface. It was observed that fouling was responsible for the observed increase in the surface roughness. Based on these results and a preliminary literature review of fouling phenomena it was suggested that the effect of fouling on pool boiling performance (for heater surfaces with patterned micro/nano-structures) be pursued as a topic for future investigations. Fouling can be simulated in experiments performed on silicon wafers (with TFT arrays fabricated apriori for measuring surface temperature transients) coated with photoresist films of various thicknesses. Feasibility experiments were performed and the results were reported to demonstrate feasibility of

this concept. The preliminary results demonstrate complex and non-intuitive interactions for the fouling films in pool boiling: since the experiments show that at lower subcooling the pool boiling heat flux values were enhanced with increase in fouling thickness while at higher subcooling the pool boiling heat flux values were degraded with increase in fouling thickness.

REFERENCES

[1] Dhir, V. K., 1998, "Boiling Heat Transfer," Annual Review of Fluid Mechanics, **30**, pp. 365-401.

[2] Leidenfrost, J.G., 1966, "A Tract about Some Qualities of Common Water," International Journal of Heat and Mass Transfer (translated by Carolyn Wares), **9**, pp. 1153-1166.

[3] Nukiyama, S., 1966, "The Maximum and Minimum Values of the Heat Q Transmitted from Metal to Boiling Water Under Atmospheric Pressure," International Journal of Heat and Mass Transfer, **9**(12), pp. 1419-1433.

[4] Bergman, T.L., Incropera, F.P., Lavine, A.S., 2011, "Fundamentals of Heat and Mass Transfer," John Wiley & Sons, Hoboken, New Jersey, USA.

[5] Banerjee, D., 1999, "Numerical and Experimental Investigation of Subcooled Film Boiling on a Horizontal Plate," Doctoral Dissertation, UCLA, California.

[6] Nukiyama, S., 1984, "The Maximum and Minimum Values of the Heat-Q Transmitted from Metal to Boiling Water Under Atmospheric-Pressure," International Journal of Heat and Mass Transfer, **27**(7), pp. 959-970.

[7] Chen, R., Lu, M., Srinivasan, V., 2009, "Nanowires for Enhanced Boiling Heat Transfer," Nano Letters, **9**(2), pp. 548-553.

[8] Ahn, H.S., 2003, "Heat Transfer Enhancement in Single-Phase Forced Convection with Blockages and in Two-Phase Pool Boiling with Nano-Structured Surfaces," Doctoral Dissertation, Texas A&M University, College Station, Texas.

[9] Ahn, H. S., Sathyamurthi, V., and Banerjee, D., 2009, "Pool Boiling Experiments on a Nano-Structured Surface," IEEE Transactions on Components and Packaging Technologies, **32**(1), pp. 156-165.

[10] Sathyamurthi, V., 2011, "Experimental & Numerical Investigation of Pool Boiling on Engineered Surfaces with Integrated Thin-Flim Temperature Sensors," Doctoral Dissertation, Texas A&M University, College Station, Texas.

[11] Taylor, R. A., and Phelan, P. E., 2009, "Pool Boiling of Nanofluids: Comprehensive Review of Existing Data and Limited New Data," International Journal of Heat and Mass Transfer, **52**(23-24), pp. 5339-5347.

[12] Bon, B., 2011, "The Role of Surface Microstructure and Topography in Pool Boiling Heat Transfer," Doctoral Dissertation, University of Florida, Gainesville, Florida.

[13] Lienhard, J.H., 1973, "Extended Hydrodynamic Theory of the Peak and Minimum Pool Boiling Heat Fluxes," National Aeronautics and Space Administration, NASA-CR-2270.

[14] Lienhard, J. H., Dhir, V. K., and Riherd, D. M., 1974, "Peak Pool Boiling Heat-Flux Measurements on Finite Horizontal Flat Plates," Mechanical Engineering, **96**(4), pp. 82-82.

[15] Lienhard, J. H., and Dhir, V. K., 1973, "Hydrodynamic Prediction of Peak Pool-Boiling Heat Fluxes from Finite Bodies," Journal of Heat Transfer-Transactions of the ASME, **95**(2), pp. 152-158.

[16] Chatpun, S., Watanabe, M., Shoji, M., 2004, "Experimental Study on Characteristics of Nucleate Pool Boiling by the Effects of Cavity Arrangement," Experimental Thermal and Fluid Science, **29**(1), pp. 33-40.

[17] Ramaswamy, C., Joshi, Y., Nakayama, W., 2003, "Effects of Varying Geometrical Parameters on Boiling from Microfabricated Enhanced Structures," Journal of Heat Transfer-Transactions of the ASME, **125**(1), pp. 103-109.

[18] Nakayama, W., Daikoku, T., Kuwahara, H., 1980, "Dynamic-Model of Enhanced Boiling Heat-Transfer on Porous Surfaces .1. Experimental Investigation," Journal of Heat Transfer-Transactions of the ASME, **102**(3), pp. 445-450.

[19] Nakayama, W., Daikoku, T., and Nakajima, T., 1982, "Effects of Pore Diameters and System Pressure on Saturated Pool Nucleate Boiling Heat-Transfer from Porous Surfaces," Journal of Heat Transfer-Transactions of the ASME, **104**(2), pp. 286-291.

[20] Chien, L. H., and Webb, R. L., 1998, "A Parametric Study of Nucleate Boiling on Structured Surfaces, Part II: Effect of Pore Diameter and Pore Pitch," Journal of Heat Transfer-Transactions of the ASME, **120**(4), pp. 1049-1054.

[21] Ujereh, S., Fisher, T., Mudawar, I., 2007, "Effects of Carbon Nanotube Arrays on Nucleate Pool Boiling," International Journal of Heat and Mass Transfer, **50**(19), pp. 4023-4038.

[22] Launay, S., Fedorov, A. G., Joshi, Y., 2006, "Hybrid Micro-Nano Structured Thermal Interfaces for Pool Boiling Heat Transfer Enhancement," Microelectronics Journal, **37**(11), pp. 1158-1164.

[23] El-Genk, M. S., and Parker, J. L., 2008, "Nucleate Boiling of FC-72 and HFE-7100 on Porous Graphite at Different Orientations and Liquid Subcooling," Energy Conversion and Management, **49**(4), pp. 733-750.

[24] Miller, W. J., Gebhart, B., and Wright, N. T., 1990, "Effects of Boiling History on a Microconfigured Surface in a Dielectric Liquid," International Communications in Heat and Mass Transfer, **17**(4), pp. 389-398.

[25] Chen, Y., Mo, D., Zhao, H., 2009, "Pool Boiling on the Superhydrophilic Surface with TiO_2 Nanotube Arrays," Science in China Series E: Technological Sciences, **52**(6), pp. 1596-1600.

[26] Banerjee, D., and Dhir, V. K., 2001, "Study of Subcooled Film Boiling on a Horizontal Disc: Part I - Analysis," Journal of Heat Transfer-Transactions of the ASME, **123**(2), pp. 271-284.

[27] Banerjee, D., and Dhir, V. K., 2001, "Study of Subcooled Film Boiling on a Horizontal Disc: Part 2 - Experiments," Journal of Heat Transfer-Transactions of the ASME, **123**(2), pp. 285-293.

[28] Sriraman, S. R., 2007, "Pool Boiling on Nano-Finned Surfaces," Master Thesis, Texas A&M University, College Station, Texas.

[29] Hendricks, T. J., Krishnan, S., Choi, C., 2010, "Enhancement of Pool-Boiling Heat Transfer using Nanostructured Surfaces on Aluminum and Copper," International Journal of Heat and Mass Transfer, **53**(15), pp. 3357-3365.

[30] Wu, W., Bostanci, H., Chow, L., 2010, "Nucleate Boiling Heat Transfer Enhancement for Water and FC-72 on Titanium Oxide and Silicon Oxide Surfaces," International Journal of Heat and Mass Transfer, **53**(9), pp. 1773-1777.

[31] Im, Y., Joshi, Y., Dietz, C., 2010, "Enhanced Boiling of a Dielectric Liquid on Copper Nanowire Surfaces," International Journal of Micro-Nano Scale Transport, **1**(1), pp. 79-96.

[32] Lu, M. C., Chen, R. K., Srinivasan, V., 2011, "Critical Heat Flux of Pool Boiling on Si Nanowire Array- Coated Surfaces," International Journal of Heat and Mass Transfer, **54**(25-26), pp. 5359-5367.

[33] Min, D., Hwang, G., Usta, Y., 2009, "2-D and 3-D Modulated Porous Coatings for Enhanced Pool Boiling," International Journal of Heat and Mass Transfer, **52**(11), pp. 2607-2613.

[34] Liter, S. G., and Kaviany, M., 2001, "Pool-Boiling CHF Enhancement by Modulated Porous-Layer Coating: Theory and Experiment," International Journal of Heat and Mass Transfer, **44**(22), pp. 4287-4311.

[35] Park, J. J., and Taya, M., 2005, "Design of Micro-Temperature Sensor Array with Thin Film Thermocouples," Journal of Electronic Packaging, **127**(3), pp. 286-289.

[36] Kreider, K. G., and Gillen, G., 2000, "High Temperature Materials for Thin-Film Thermocouples on Silicon Wafers," Thin Solid Films, **376**(1-2), pp. 32-37.

[37] Kreider, K. G., and DiMeo, F., 1998, "Platinum/palladium Thin-Film Thermocouples for Temperature Measurements on Silicon Wafers," Sensors and Actuators A-Physical, **69**(1), pp. 46-52.

[38] Yu, W., and Choi, S., 2003, "The Role of Interfacial Layers in the Enhanced Thermal Conductivity of Nanofluids: A Renovated Maxwell Model," Journal of Nanoparticle Research, **5**(1), pp. 167-171.

[39] Xie, H., Fujii, M., and Zhang, X., 2005, "Effect of Interfacial Nanolayer on the Effective Thermal Conductivity of Nanoparticle-Fluid Mixture," International Journal of Heat and Mass Transfer, **48**(14), pp. 2926-2932.

[40] Bhattacharya, P., Saha, S., Yadav, A., 2004, "Brownian Dynamics Simulation to Determine the Effective Thermal Conductivity of Nanofluids," Journal of Applied Physics, **95**(11), pp. 6492-6494.

[41] Jang, S. P., and Choi, S. U., 2004, "Role of Brownian Motion in the Enhanced Thermal Conductivity of Nanofluids," Applied Physics Letters, **84**(21), pp. 4316-4318.

[42] Evans, W., Prasher, R., Fish, J., 2008, "Effect of Aggregation and Interfacial Thermal Resistance on Thermal Conductivity of Nanocomposites and Colloidal Nanofluids," International Journal of Heat and Mass Transfer, **51**(5), pp. 1431-1438.

[43] Keblinski, P., Phillpot, S., Choi, S., 2002, "Mechanisms of Heat Flow in Suspensions of Nano-Sized Particles (Nanofluids)," International Journal of Heat and Mass Transfer, **45**(4), pp. 855-863.

[44] Keblinski, P., Prasher, R., and Eapen, J., 2008, "Thermal Conductance of Nanofluids: Is the Controversy Over?" Journal of Nanoparticle Research, **10**(7), pp. 1089-1097.

[45] Majumdar, A., and Mezic, I., 1999, "Instability of Ultra-Thin Water Films and the Mechanism of Droplet Formation on Hydrophilic Surfaces," Journal of Heat Transfer, **121**(4), pp. 964-971.

[46] Majumdar, A., and Mezic, I., 1998, "Stability Regimes of Thin Liquid Films," Microscale Thermophysical Engineering, **2**(3), pp. 203-213.

[47] Jo, B., 2012, "Numerical and Experimental Investigation of Organic Nanomaterials for Thermal Energy Storage and for Concentrating Solar Power Applications," Doctoral Dissertation, Texas A&M University, College Station, Texas.

[48] Unnikrishnan, V., Banerjee, D., and Reddy, J., 2008, "Atomistic-Mesoscale Interfacial Resistance Based Thermal Analysis of Carbon Nanotube Systems," International Journal of Thermal Sciences, **47**(12), pp. 1602-1609.

[49] Singh, N., Unnikrishnan, V., Banerjee, D., 2011, "Analysis of Thermal Interfacial Resistance between Nanofins and Various Coolants," International Journal for Computational Methods in Engineering Science and Mechanics, **12**(5), pp. 254-260.

[50] Singh, N., Banerjee, D., 2013, "Nanofins: Science and Applications," Springer, New York, N.Y,.

[51] Singh, N., Shin, D., and Banerjee, D., 2012, "Nanoscale Effects in Multiphase Flows and Heat Transfer," Microelectronics to Nanoelectronics: Materials, Devices & Manufacturability, pp. 309.

[52] Huxtable, S. T., Cahill, D. G., Shenogin, S., 2003, "Interfacial Heat Flow in Carbon Nanotube Suspensions," Nature Materials, **2**(11), pp. 731-734.

[53] Walther, J. H., Jaffe, R., Halicioglu, T., 2001, "Carbon Nanotubes in Water: Structural Characteristics and Energetics," The Journal of Physical Chemistry B, **105**(41), pp. 9980-9987.

[54] Hu, M., Goicochea, J. V., Michel, B., 2009, "Thermal Rectification at water/functionalized Silica Interfaces," Applied Physics Letters, **95**(15), pp. 151903-151903-3.

[55] Costa, M. F., 2008, "Molecular Dynamics of Molten Li_2CO_3–K_2CO_3," Journal of Molecular Liquids, **138**(1–3), pp. 61-68.

[56] Swiatla-Wojcik, D., Pabis, A., and Szala, J., 2008, "Density and Temperature Effect on Hydrogen-Bonded Clusters in Water-MD Simulation Study," Central European Journal of Chemistry, **6**(4), pp. 555-561.

[57] Shin, D., and Banerjee, D., 2011, "Effects of Silica Nanoparticles on Enhancing the Specific Heat Capacity of Carbonate Salt Eutectic," The International Journal of Structural Changes in Solids, **2**(2), pp. 25-31.

[58] Shin, D., and Banerjee, D., 2010, "Enhanced Thermal Properties of PCM Based Nanofluid for Solar Thermal Energy Storage," ASME 2010 4th International Conference on Energy Sustainability, pp. 841-845.

[59] Shin, D., and Banerjee, D., 2009, "Investigation of Nanofluids for Solar Thermal Storage Applications," ASME 2009 3rd International Conference on Energy Sustainability Collocated with the Heat Transfer and InterPACK09 Conferences, pp. 819-822.

[60] Shin, D., Jo, B., Kwak, H., 2010, "Investigation of High Temperature Nanofluids for Solar Thermal Power Conversion and Storage Applications," 14th International Heat Transfer Conference, pp. 583-591.

[61] Shin, D., 2011, "Molten Salt Nanomaterials for Thermal Energy Storage and Concentrated Solar Power Applications," Doctoral Dissertation, Texas A&M University, College Station, Texas.

[62] Jo, B., and Banerjee, D., 2011, "Interfacial Thermal Resistance Between a Carbon Nanoparticle and Molten Salt Eutectic: Effect of Material Properties, Particle Shapes and Sizes," ASME/JSME 8th Thermal Engineering Joint Conference, pp. T30084-T30084(7).

[63] Jo, B., and Banerjee, D., 2010, "Study of High Temperature Nanofluids using Carbon Nanotubes (CNT) for Solar Thermal Storage Applications," ASME 4th International Conference on Energy Sustainability, pp. 741-748.

[64] Shin, D., and Banerjee, D., 2011, "Enhanced Specific Heat of Silica Nanofluid," Journal of Heat Transfer, **133**(2), pp. 24501-24501(4).

[65] Shin, D., and Banerjee, D., 2011, "Enhancement of Specific Heat Capacity of High-Temperature Silica-Nanofluids Synthesized in Alkali Chloride Salt Eutectics

for Solar Thermal-Energy Storage Applications," International Journal of Heat and Mass Transfer, **54**(5), pp. 1064-1070.

[66] Shin, D., and Banerjee, D., 2011, "Experimental Investigation of Molten Salt Nanofluid for Solar Thermal Energy Application,"ASME/JSME 8th Thermal Engineering Joint Conference, pp. T30024-T30024(6).

[67] Singh, N., 2011, "Computational Analysis of Thermo-Fluidic Characteristics of a Carbon Nano-Fin," Doctoral Dissertation, Texas A&M University, College Station, Texas.

[68] Plimpton, S., 1995, "Fast Parallel Algorithms for Short-Range Molecular Dynamics," Journal of Computational Physics, **117**(1), pp. 1-19.

[69] Sriraman, S., Banerjee, D., 2008, "Subcooled and Saturated Pool Boiling on Nano-Finned Surfaces," Proceedings of ASME- Summer Heat Transfer Conference, HT2008-56393.

[70] Unnikrishnan, V. U., Reddy, J. N., Banerjee, D., and Rostam-Abadi, F., 2008, "Thermal Characteristics of Defective Carbon Nanotube-Polymer Nanocomposites," Interaction and Multiscale Mechanics, an International Journal, **1**(4), pp. 397-410.

[71] Singh, N., 2010, "Computational Analysis of Thermo-Fludic Performance of a Nano-Fin," Doctoral Dissertation, Texas A&M University, College Station, Texas.

[72] Sathyamurthi, V., Ahn, H., Banerjee, D., 2009, "Subcooled Pool Boiling Experiments on Horizontal Heaters Coated with Carbon Nanotubes," Journal of Heat Transfer, **131**(7), pp. 071501-071501.

[73] Sathyamurthi, V., 2006, "Pool Boiling Studies on Nanotextured Surfaces under Highly Subcooled Conditions," Master Thesis, Texas A&M University, College Station, Texas.

[74] Sathyamurthi, V., and Banerjee, D., 2009, "Non-Linear Dynamical Analyses of Transient Surface Temperature Fluctuations during Subcooled Pool Boiling on a Horizontal Disk," International Journal of Heat and Mass Transfer, **52**(23-24), pp. 5608-5623.

[75] Glenn, S. T., 2013, "Effects of Carbon Nanotube Coating on Bubble Departure Diameter and Frequency in Pool Boiling on a Flat, Horizontal Heater," Master Thesis, Texas A&M University, College Station, Texas.

[76] Jung, S., 2012, "Numerical and Experimental Investigation of Inorganic Nanomaterials for Thermal Energy Storage (TES) and Concentrated Solar Power (CSP) Applications," Doctoral Dissertation, Texas A&M University, College Station, Texas.

[77] Banerjee, D., Son, G., and Dhir, V., 1996, "Conjugate Thermal and Hydrodynamic Analyses of Saturated Film Boiling from a Horizontal Surface," ASME Heat Transfer Div Publ HTD, **334**(3), pp. 57-64.

[78] Chou, S. Y., Krauss, P. R., and Renstrom, P. J., 1996, "Nanoimprint Lithography," Journal of Vacuum Science & Technology B: Microelectronics and Nanometer Structures, **14**(6), pp. 4129-4133.

[79] Xu, F., Stacey, N. A., Watts, M., 2004, "Development of Imprint Materials for the Step and Flash Imprint Lithography Process," Microlithography 2004 - International Society for Optics and Photonics, pp. 232-241.

[80] Bailey, T., Johnson, S., Sreenivasan, S., 2002, "Step and Flash Imprint Lithography: An Efficient Nanoscale Printing Technology," Journal of Photopolymer Science and Technology, **15**(3), pp. 481-486.

[81] Colburn, M., Bailey, T., Choi, B., 2001, "Development and Advantages of Step-and-Flash Lithography," Solid State Technology, **44**(7), pp. 67-80.

[82] http://gwyddion.net.

[83] Sugawara, H., Ohkubo, T., Fukushima, T., 2003, "Emissivity Measurement of Silicon Semiconductor Wafer near Room Temperature," SICE Annual Conference, **2**, pp. 2201- 2204.

[84] Jeon, S. I., 2011, "Development of Micro/Nano-Scale Sensors for Investigation of Heat Transfer in Multi-Phase Flows," Doctoral Dissertation, Texas A&M University, College Station, Texas.

[85] Mills, A.F., and Mills, A., 1999, "Basic Heat and Mass Transfer," Englewood Cliffs, New Jersey: Prentice-Hall, USA.

[86] Rohsenow, W. M., 1951, "A Method of Correlating Heat Transfer Data for Surface Boiling of Liquids," Technical Report No.5 NP 3443, Division of Industrial Cooperation, Massachusetts Institute of Technology.

[87] Lienhard, J., 1980, "On the Prediction of the Minimum Pool Boiling Heat Flux," Transaction of ASME, **102**(3), pp. 457.

[88] Zuber, N., 1959, "Hydrodynamic Aspects of Boiling Heat Transfer," UCLA and Ramo-Wooldridge Corp., AECU-4439, LA, California.

[89] Lienhard, J. H, and Schrock, V. E., 1963, "The Effect of Pressure, Geometry, and the Equation of State upon the Peak and Minimum Boiling Heat Flux," Journal of Heat Transfer, **85**(3), pp. 261-268.

[90] Lienhard, J. H., Dhir, V. K., and Riherd, D. M., 1973, "Peak Pool Boiling Heat-Flux Measurements on Finite Horizontal Flat Plates," Journal of Heat Transfer-Transactions of the ASME, **95**(4), pp. 477-482.

[91] Dhir, V. K., and Lienhard, J. H., 1973, "Taylor Stability of Viscous Fluids with Application to Film Boiling," International Journal of Heat and Mass Transfer, **16**(11), pp. 2097-2109.

[92] Sernas, V., Lienhard, J. H., and Dhir, V. K., 1973, "The Taylor Wave Configuration during Boiling from a Flat Plate," International Journal of Heat and Mass Transfer, **16**(9), pp. 1820-1821.

[93] Kandlikar, S. G., 2001, "A Theoretical Model to Predict Pool Boiling CHF Incorporating Effects of Contact Angle and Orientation," Journal of Heat Transfer-Transactions of ASME, **123**(6) pp. 1071-1079.

[94] Liaw, S., and Dhir, V., 1986, "Effect of Surface Wettability on Transition Boiling Heat Transfer from a Vertical Surface," Proceeding of 8th Int. Heat Transfer Conference, **4**, pp. 2031-2036.

[95] Ramilison, J., and Lienhard, J., 1987, "Transition Boiling and the Correlation of Transition-Film Boiling," Journal of Heat Transfer, **109**, pp. 746-752.

[96] Baumeister, K., and Simon, F., 1973, "Leidenfrost Temperature-its Correlation for Liquid Metals, Cryogens, Hydrocarbons, and Water." Journal of Heat Transfer, **95**(2), pp. 166-173.

[97] Bernardin, J., and Mudawar, I., 1999, "The Leidenfrost Point: Experimental Study and Assessment of Existing Models," Journal of Heat Transfer-Transactions of the ASME, **121**, pp. 894-903.

[98] Kim, H., Truong, B., Buongiorno, J., 2011, "On the Effect of Surface Roughness Height, Wettability, and Nanoporosity on Leidenfrost Phenomena," Applied Physics Letters, **98**(8), pp. 083121-083121(3).

[99] Kruse, C., Anderson, T., Wilson, C., 2013, "Extraordinary Shifts of the Leidenfrost Temperature from Multiscale Micro/Nanostructured Surfaces," Langmuir, **29**(31), pp. 9798-9806.

[100] Arnaldo del Cerro, D., Mar n, A. G., Ro¨mer, G. R., 2012, "Leidenfrost Point Reduction on Micropatterned Metallic Surfaces," Langmuir, **28**(42), pp. 15106-15110.

[101] Li, L., Bedrov, D., and Smith, G. D., 2006, "Water-Induced Interactions between Carbon Nanoparticles," The Journal of Physical Chemistry B, **110**(21), pp. 10509-10513.

[102] Girifalco, L., Hodak, M., and Lee, R. S., 2000, "Carbon Nanotubes, Buckyballs, Ropes, and a Universal Graphitic Potential," Physical Review B, **62**(19), pp. 13104-13110.

[103] Ahn, H. S., Sinha, N., Zhang, M., 2006, "Pool Boiling Experiments on Multiwalled Carbon Nanotube (MWCNT) Forests," Journal of Heat Transfer, **128**(12), pp. 1335-1342.

[104] Li, L., Zhang, Y. W., Ma, H. B., 2010, "Molecular Dynamics Simulation of Effect of Liquid Layering Around the Nanoparticle on the Enhanced Thermal Conductivity of Nanofluids," Journal of Nanoparticle Research, **12**(3), pp. 811-821.

[105] Chang, C., Lee, W., Young, T., 2008, "Adsorption Mechanism of Water Molecules Surrounding Au Nanoparticles of Different Sizes," The Journal of Chemical Physics, **128**(15), pp. 154703-154703(8).

[106] Oh, S. H., Kauffmann, Y., Scheu, C., 2005, "Ordered Liquid Aluminum at the Interface with Sapphire," Science, **310**(5748), pp. 661-663.

[107] Platten, J. K., 2006, "The Soret Effect: A Review of Recent Experimental Results," Journal of Applied Mechanics, **73**(1), pp. 5-15.

[108] Probstein, R.F., 2005, "Physicochemical hydrodynamics: an introduction," John Wiley & Sons, Hoboken, New Jersey, USA.

[109] Clegg, G. T., and Tehrani, M. A., 1973, "Liquid-Phase Diffusion Coefficients for Dissolved Gases. Systems Chlorine-Carbon Tetrachloride and Hydrogen Chloride-Ethylene Glycol," Journal of Chemical and Engineering Data, **18**(1), pp. 59-60.

[110] Wilke, C., and Chang, P., 1955, "Correlation of Diffusion Coefficients in Dilute Solutions," AIChE Journal, **1**(2), pp. 264-270.

[111] Madariaga, J., Santamaria, C., Bou-Ali, M. M., 2010, "Measurement of Thermodiffusion Coefficient in n-Alkane Binary Mixtures: Composition Dependence," The Journal of Physical Chemistry B, **114**(20), pp. 6937-6942.

[112] Jones, J. E., 1924, "On the Determination of Molecular Fields II. from the Equation of State of a Gas," Proceedings of the Royal Society of London.Series A, **106**(738), pp. 463-477.

[113] Banerjee, D., 2013, "Guest Editorial for the Special Issue on Micro/Nanoscale Transport Phenomena," Journal of Nanotechnology in Engineering and Medicine, **3**(3), pp. 030301.

[114] Kim, H. D., and Kim, M. H., 2007, "Effect of Nanoparticle Deposition on Capillary Wicking that Influences the Critical Heat Flux in Nanofluids," Applied Physics Letters, **91**(1), pp. 014104-014104(3)

[115] Awad, M. M., El-Wahab, I. A., and Gad, H., 2007, "Effect of Surface Temperature on the Fouling of Heat Transfer Surfaces," Proceeding of 11th International Water Technology Conference, Egypt, pp. 283-298.

[116] Watkinson, A. P., and Wilson, D. I., 1997, "Chemical Reaction Fouling: A Review," Experimental Thermal and Fluid Science, **14**(4), pp. 361-374.

[117] Watkinson, A. P., 1992, "Chemical Reaction Fouling of Organic Fluids," Chemical Engineering and Technology, **15**(2), pp. 82-90.

[118] Crittenden, B. D., Hout, S. A., and Alderman, N. J., 1987, "Model Experiments of Reaction Fouling," Chemical Engineering Research and Design, **65**(2), pp. 165-170.

[119] Crittenden, B. D., Kolaczkowski, S. T., Takemoto, T., 2009, "Crude Oil Fouling in a Pilot-Scale Parallel Tube Apparatus," Heat Transfer Engineering, **30**(10-11), pp. 777-785.

[120] Wilson, D. I., Lai, R. C., and Watkinson, A. P., 1995, "Model Experiments of Autoxidation Reaction Fouling Part II: Effect of Flow Parameters and Antioxidants," Chemical Engineering Research and Design, **73**(1), pp. 69-77.

[121] Crittenden, B., and Khater, E., 1984, "Fouling in a Hydrocarbon Vaporizer," Proceeding of 1st National Conference on Heat Transfer, **86**, pp. 401-414.

[122] Crittenden, B., 1988, "Chemical Reaction Fouling of Heat Exchanger," Fouling Science and Technology, pp. 315-332.

[123] Asomaning, S., and Watkinson, A. P., 1992, "Heat- Exchanger Fouling by Olefin Kerosene Mixtures," Canadian Journal of Chemical Engineering, **70**(3), pp. 444-451.

[124] Wilson, D. I., and Watkinson, A. P., 1996, "A Study of Autoxidation Reaction Fouling in Heat Exchangers," The Canadian Journal of Chemical Engineering, **74**(2), pp. 236-246.

[125] Wilson, D. I., and Watkinson, A. P., 1995, "Model Experiments of Autoxidation Reaction Fouling 1: Mechanisms," Chemical Engineering Research & Design, **73**, pp. 59-68.

[126] Esawy, M., Malayeri, M. R., and Muller-Steinhagen, H., 2010, "Crystallization Fouling of Finned Tubes during Pool Boiling: Effect of Fin Density," Heat and Mass Transfer, **46**(10), pp. 1167-1176.

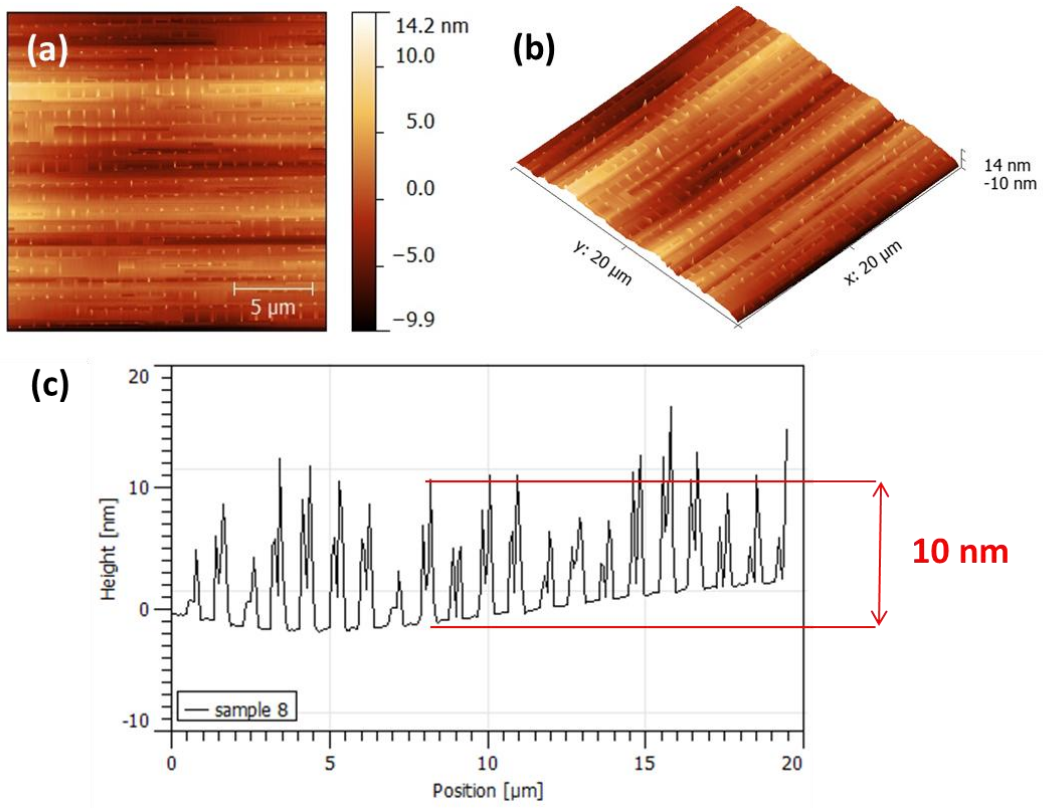

Figure A 1 Silicon pillar with height 10nm and diameter 164nm (a) AFM image (b) 3D image of AFM (c) profiles

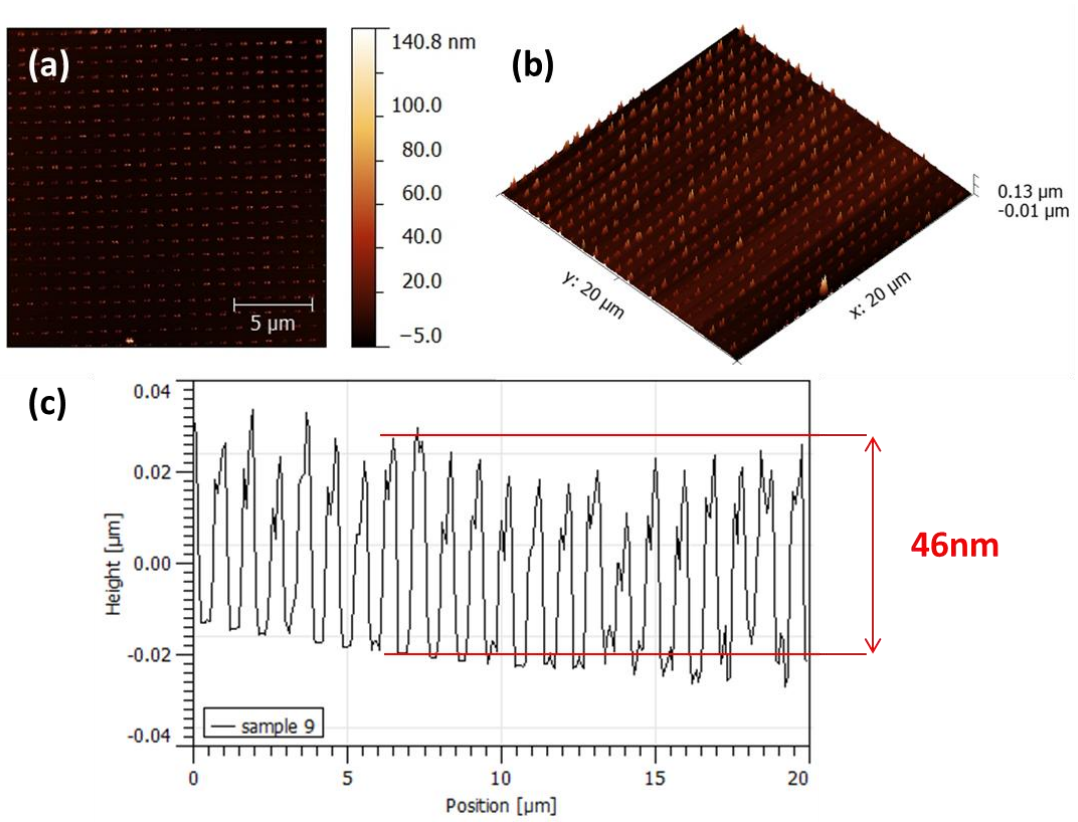

Figure A 2 Silicon pillar with height 46nm and diameter 173nm (a) AFM image (b) 3D image of AFM (c) Profiles

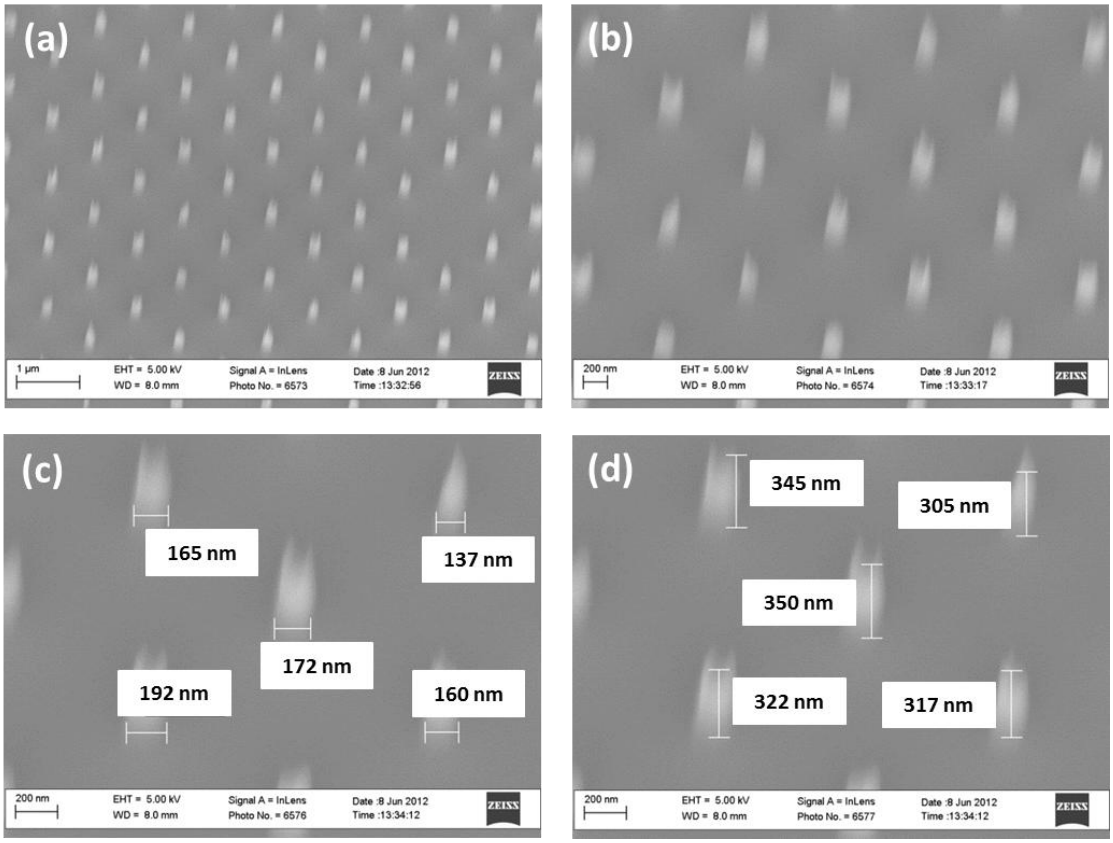

Figure A 3 Silicon pillar with height 464nm and diameter 165nm with 45^{o} tilted view (a) SEM image (b) Large view (c) Measurement of diameter (d) Measurement of height

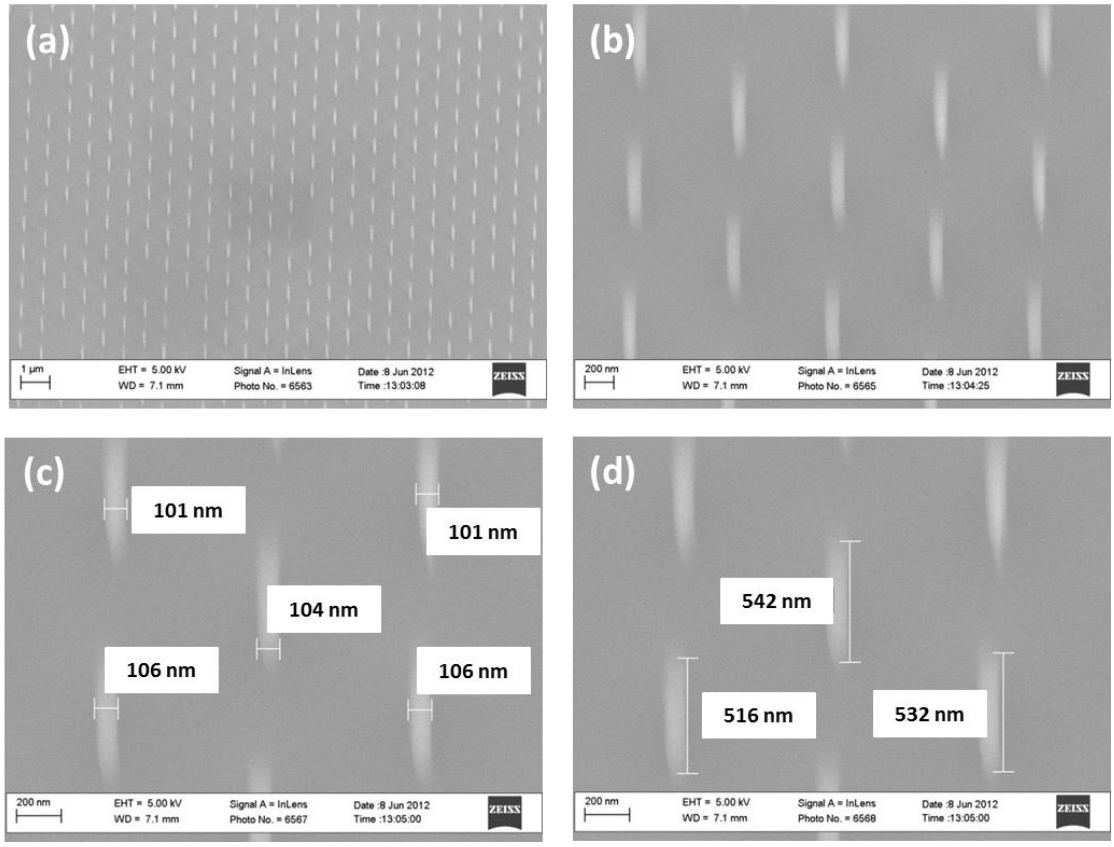

Figure A 4 Silicon pillar with height 750nm and diameter 104nm with 45^{o} tilted view (a) SEM image (b) Large view (c) Measurement of diameter (d) Measurement of height

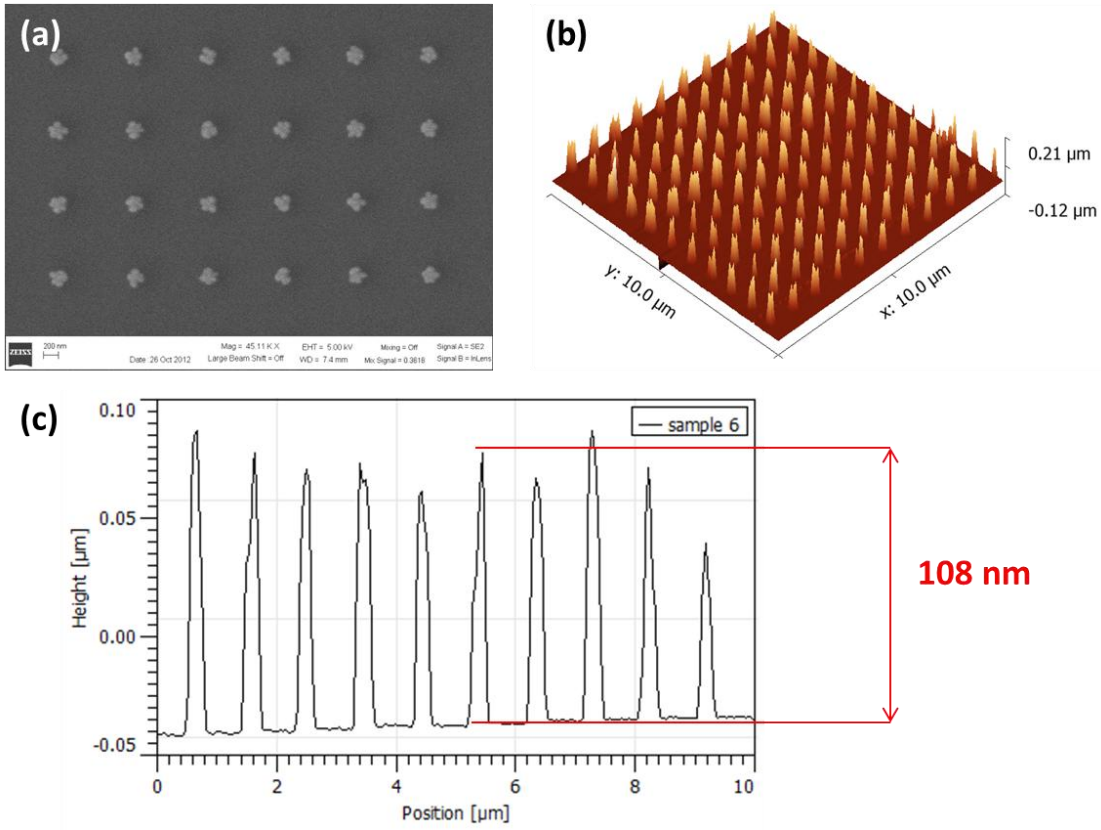

Figure A 5 Silicon dioxide pillar with height 108nm and diameter 225nm (a) SEM image (b) 3D image of AFM (c) Profiles

APPENDIX B

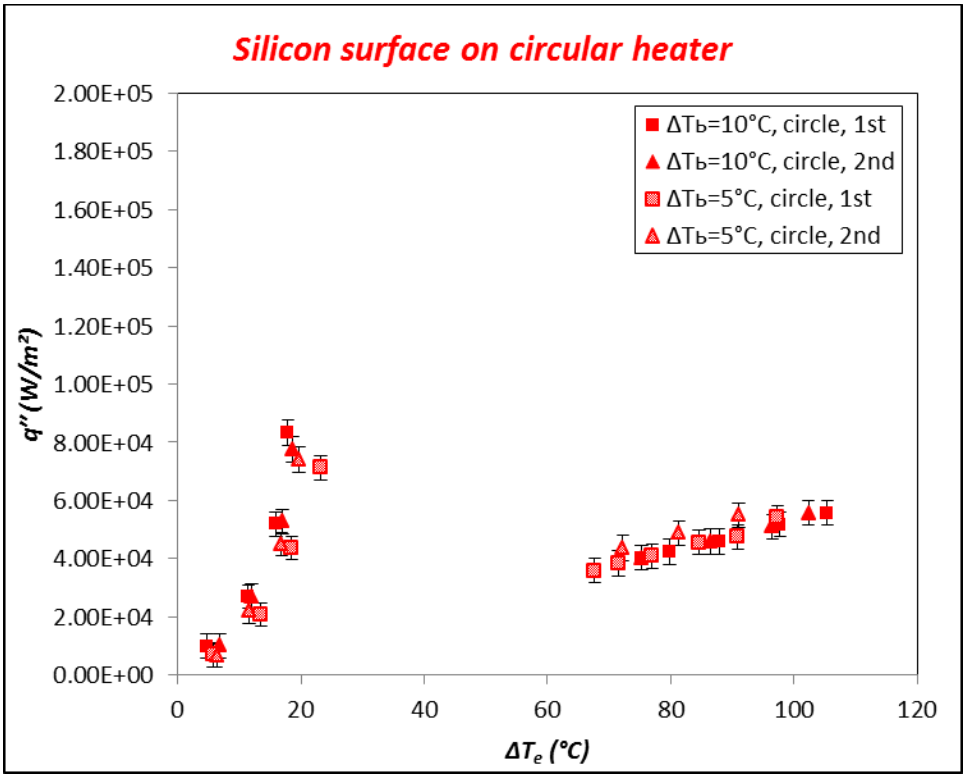

Figure B 1 Pool boiling curve on the silicon wafer at circular heater: square for 1st run, triangle is 2nd run: solid icons are for subcooling of 10 °C, patterned icons are for subcooling of 5°C. TFT is used.

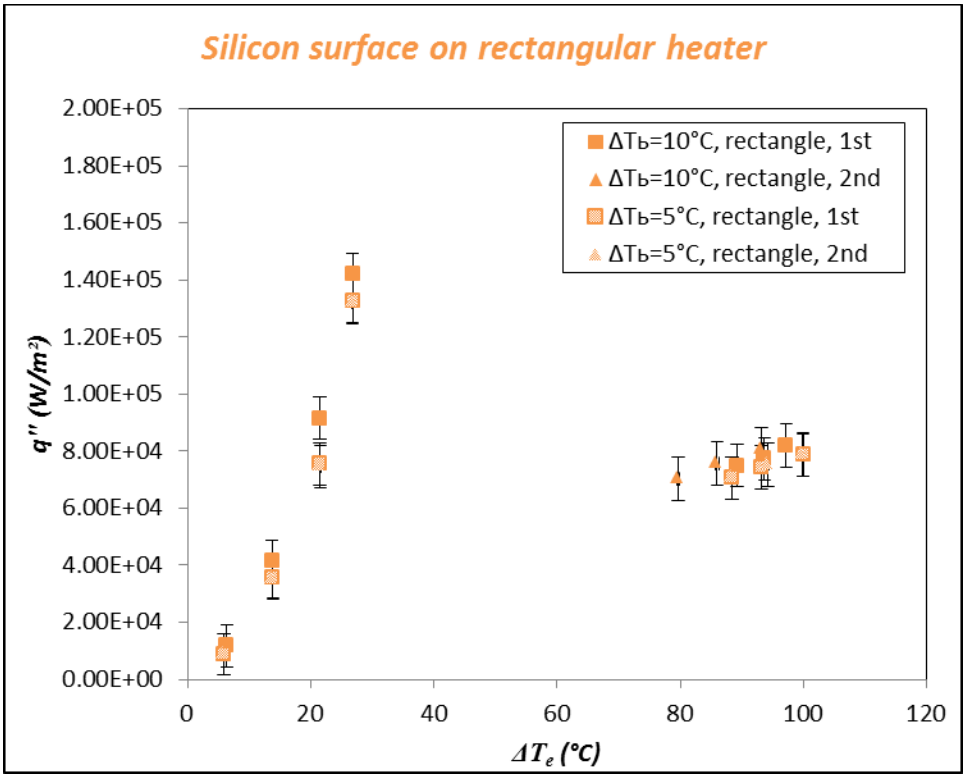

Figure B 2 Pool boiling curve on the silicon wafer at rectangular heater: square for 1st run, triangle is 2nd run: solid icons are for subcooling of 10 °C, patterned icons are for subcooling of 5°C. TFT is used.

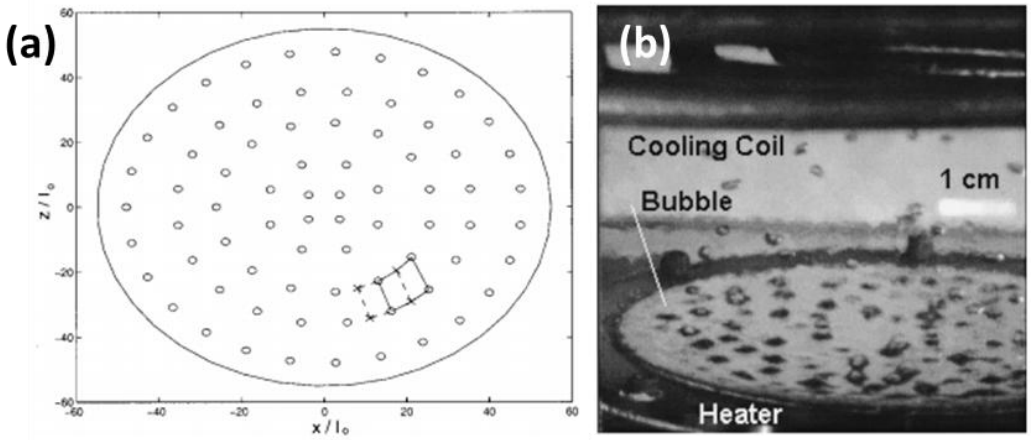

Figure B 3 (a) Plot of crests on horizontal circular heater for (m, n) values which is (4,1), (8,2), (15,3), (21,4), (27,5) and (b) Actual picture of crest on the horizontal circular heater

Note : (a) reprinted with permission from " Study of subcooled film boiling on a horizontal disc: part 1-analysis" by D. Banerjee, V. K. Dhir, Journal of Heat Transfer, 123(2), 271-284, 2000, Copyright 2000 by the American Society of Mechanical Engineers (ASME) (b) reprinted with permission from " Study of subcooled film boiling on a horizontal disc: part 2-experiments" by D. Banerjee, V. K. Dhir, Journal of Heat Transfer, 123(2), 285-293, 2000, Copyright 2000 by the American Society of Mechanical Engineers (ASME)

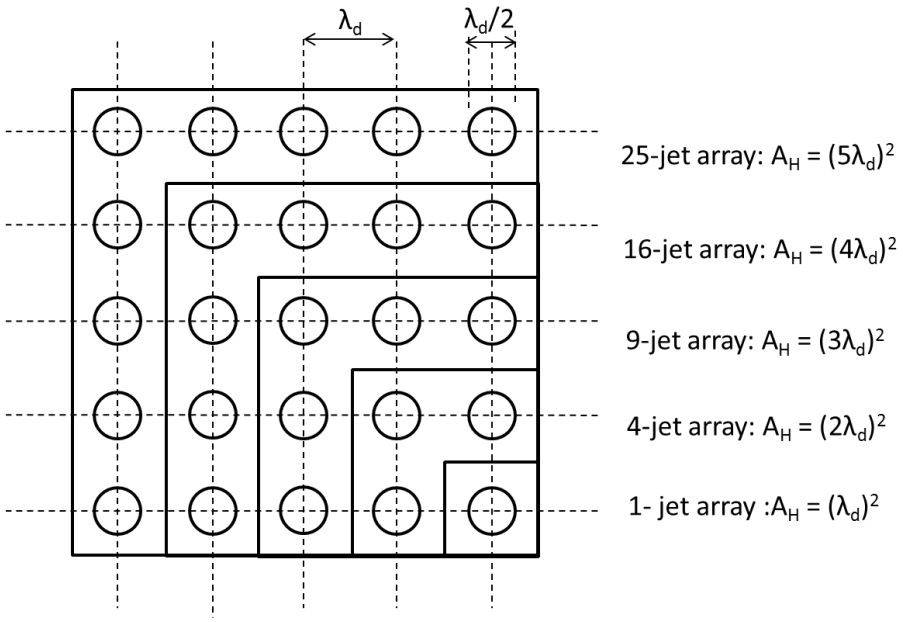

Figure B 4 Total available number of jet and jet configuration on a square heater

Note : reprinted with permission from " Peak pool boiling heat-flux measurements on finite horizontal flat plates" by J. H. Lienhard, V. K. Dhir, D. M. Riherd, Journal of Heat Transfer, 95(4), 477-482, 2001, Copyright 2001 by the American Society of Mechanical Engineers (ASME)

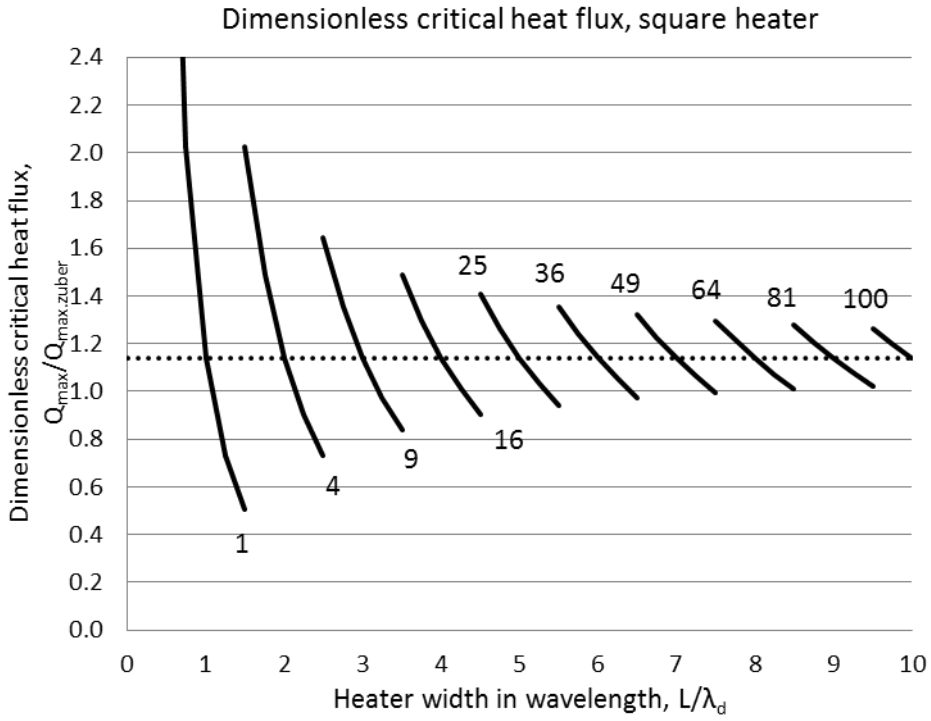

Figure B 5 Variation of dimensionless critical heat flux as a function of the heater width (non-dimensionalized as a multiple of the instability wavelength) for square heater. Numbers in the graph represent the total number of jets for each curve.

Note : reprinted with permission from " Peak pool boiling heat-flux measurements on finite horizontal flat plates" by J. H. Lienhard, V. K. Dhir, D. M. Riherd, Journal of Heat Transfer, 95(4), 477-482, 2001, Copyright 2001 by the American Society of Mechanical Engineers (ASME)

APPENDIX C

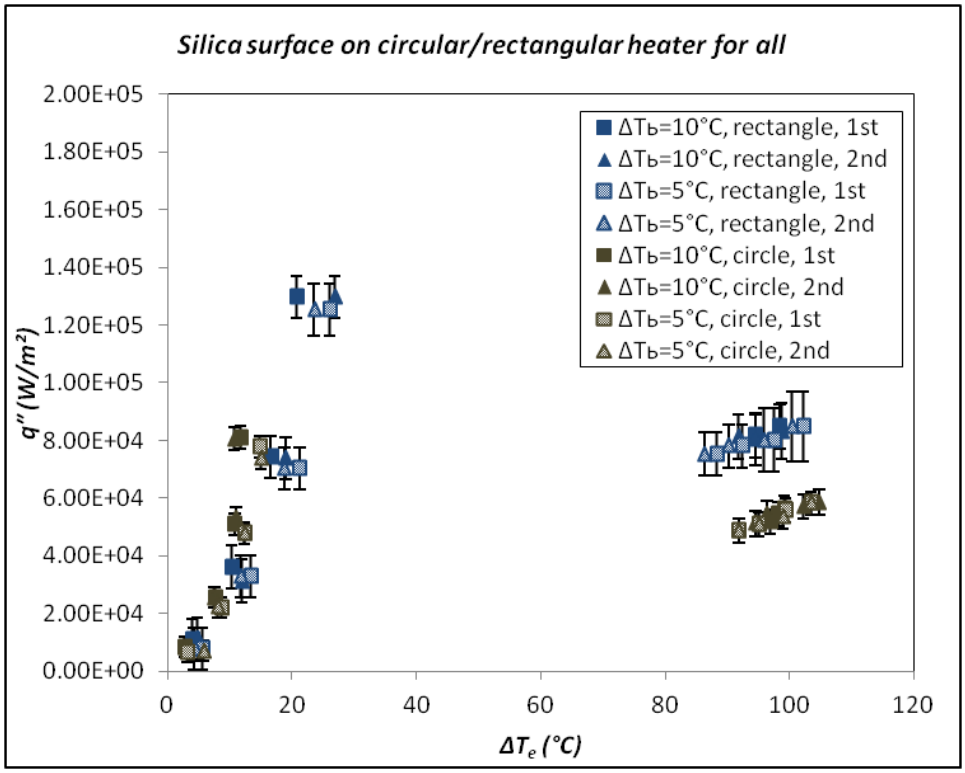

Figure C 1 pool boiling curve on rectangular and circular heater on the silica surface: square for 1st run, triangle is 2nd run: solid icons are for subcooling of 10 °C, patterned icons are for subcooling of 5 °C. TFT is used.

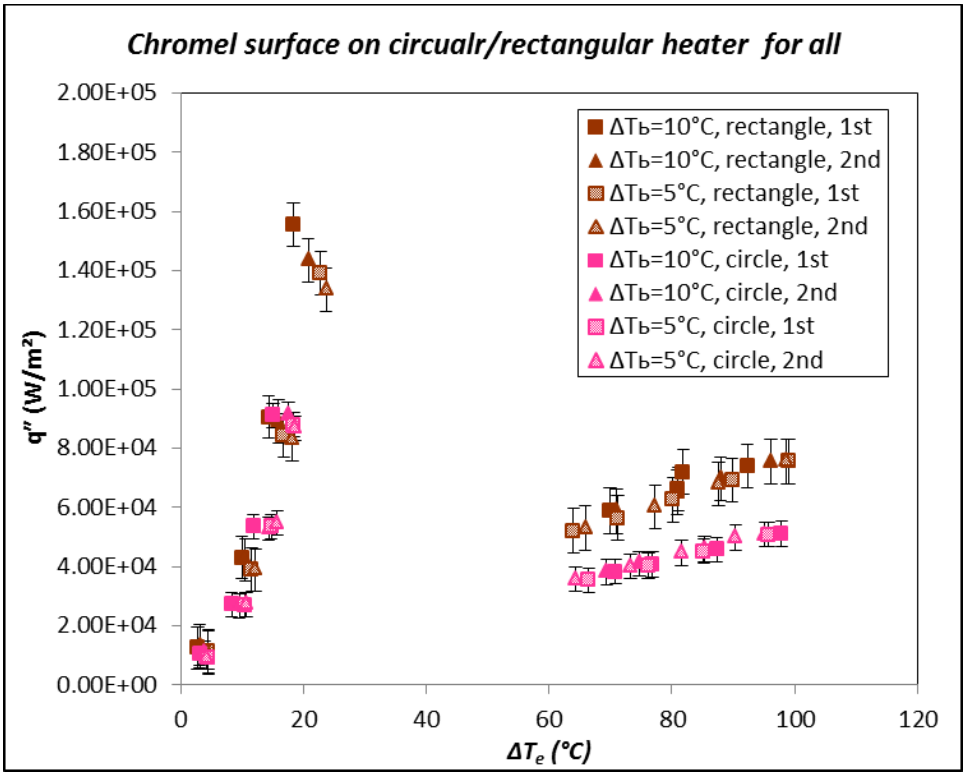

Figure C 2 pool boiling curve on rectangular and circular heater on the silica surface: square for 1st run, triangle is 2nd run: solid icons are for subcooling of 10 °C, patterned icons are for subcooling of 5 °C. TFT is used.

APPENDIX D

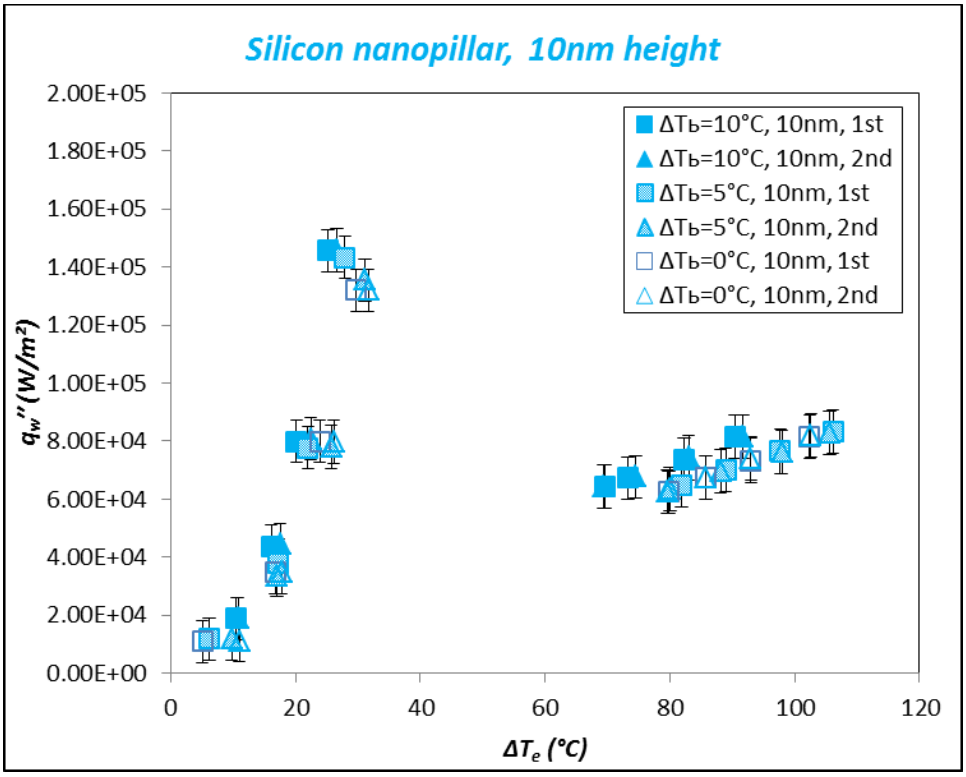

Figure D 1 Pool boiling curve on rectangular silicon surface with nanofin height 10nm: square for 1st run, triangle is 2nd run: solid icons are for subcooling of 10 °C, patterned icons are for subcooling of 5 °C, hollow icons are for saturation. TFT is used.

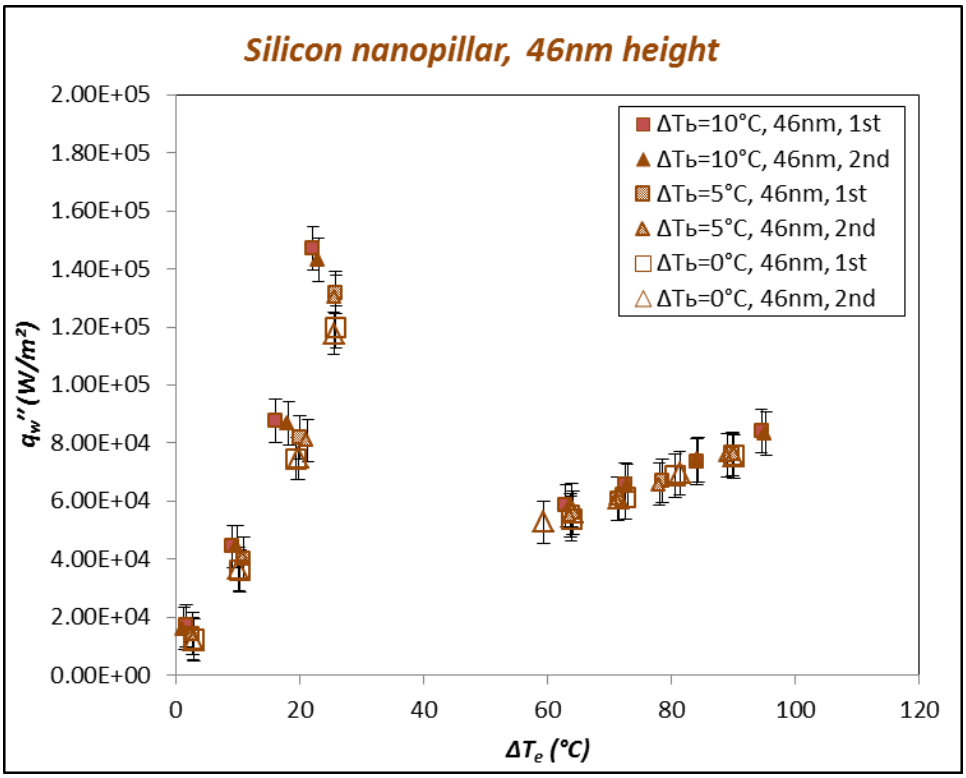

Figure D 2 Pool boiling curve on rectangular silicon surface with nanofin height 46nm: square for 1st run, triangle is 2nd run: solid icons are for subcooling of 10 °C, patterned icons are for subcooling of 5°C, hollow dot icons are for saturation. TFT is used.

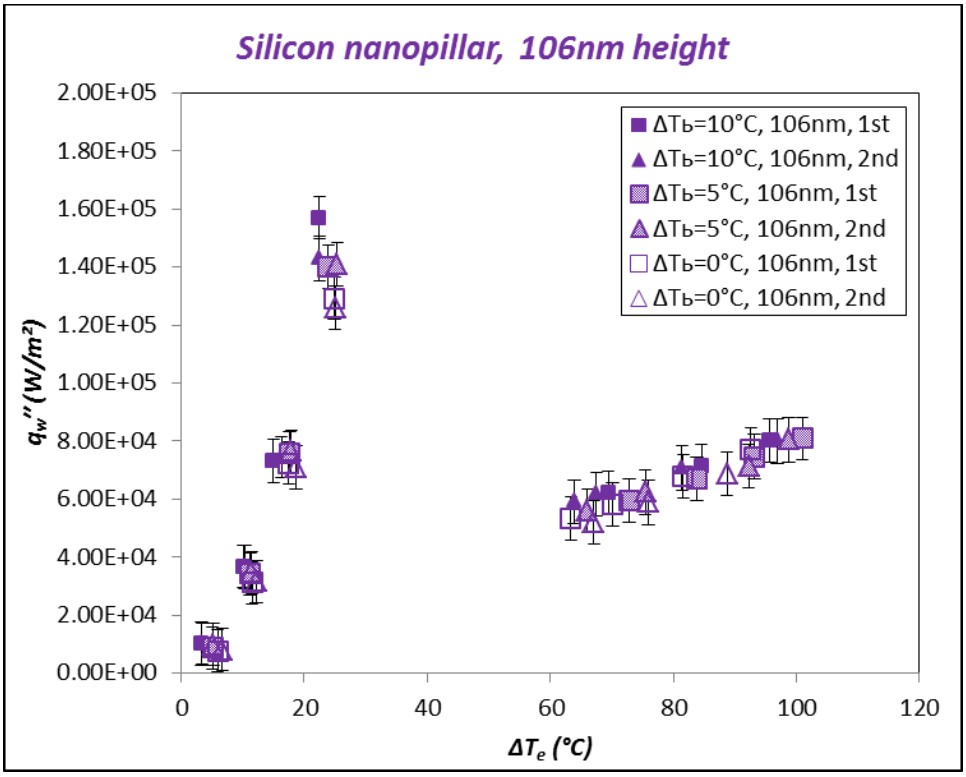

Figure D 3 Pool boiling curve on rectangular silicon surface with nanofin height 106nm: square for 1st run, triangle is 2nd run: solid icons are for subcooling of 10°C, patterned icons are for subcooling of 5°C, hollow icons are for saturation. TFT is used.

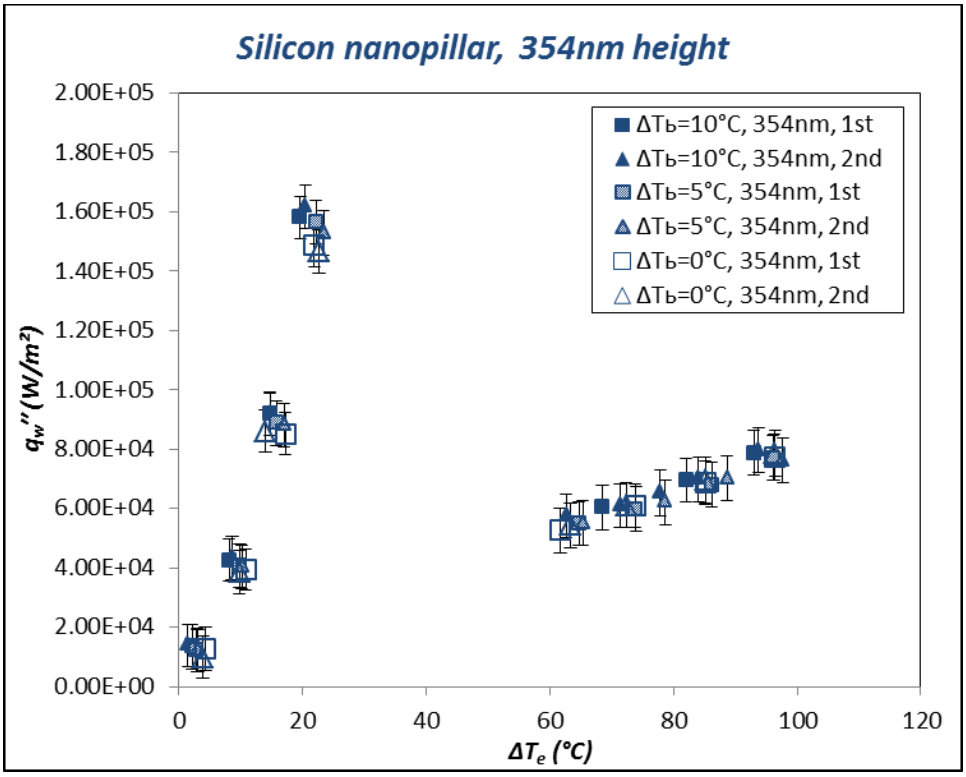

Figure D 4 Pool boiling curve on rectangular silicon surface with nanofin height 354nm: square for 1st run, triangle is 2nd run: solid dot is for subcool 10°C, patterned dot is for subcool 5°C, hollow dot is for saturation. TFT is used.

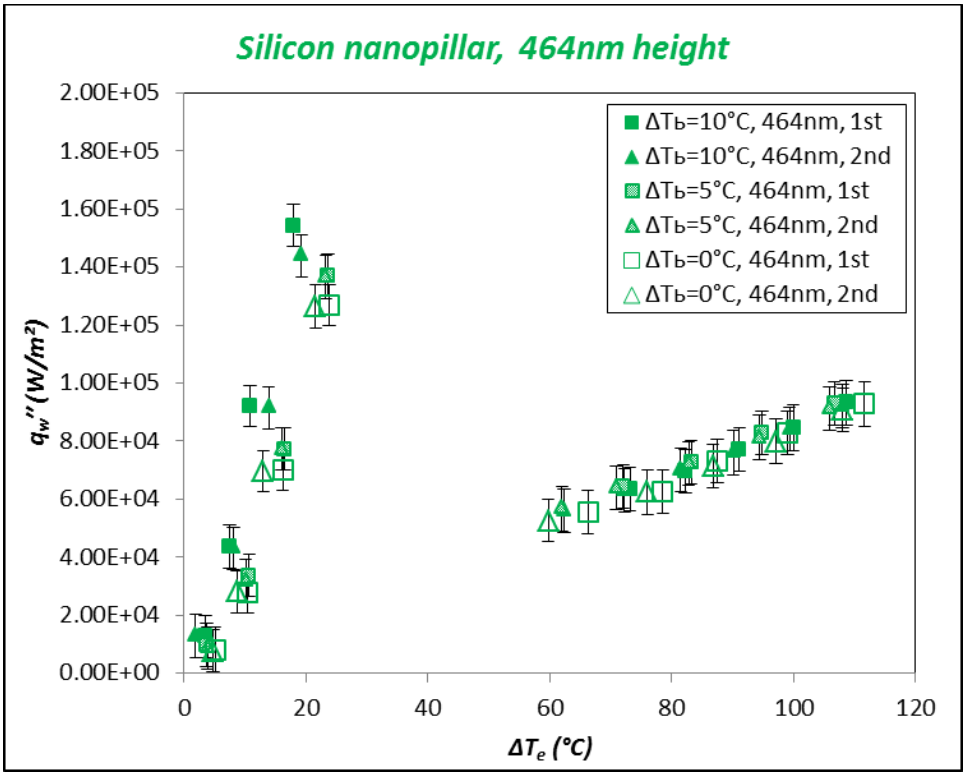

Figure D 5 Pool boiling curve on rectangular silicon surface with nanofin height 464nm: square for 1st run, triangle is 2nd run: solid dot is for subcool 10°C, patterned dot is for subcool 5°C, hollow dot is for saturation. Bead thermocouple is used.

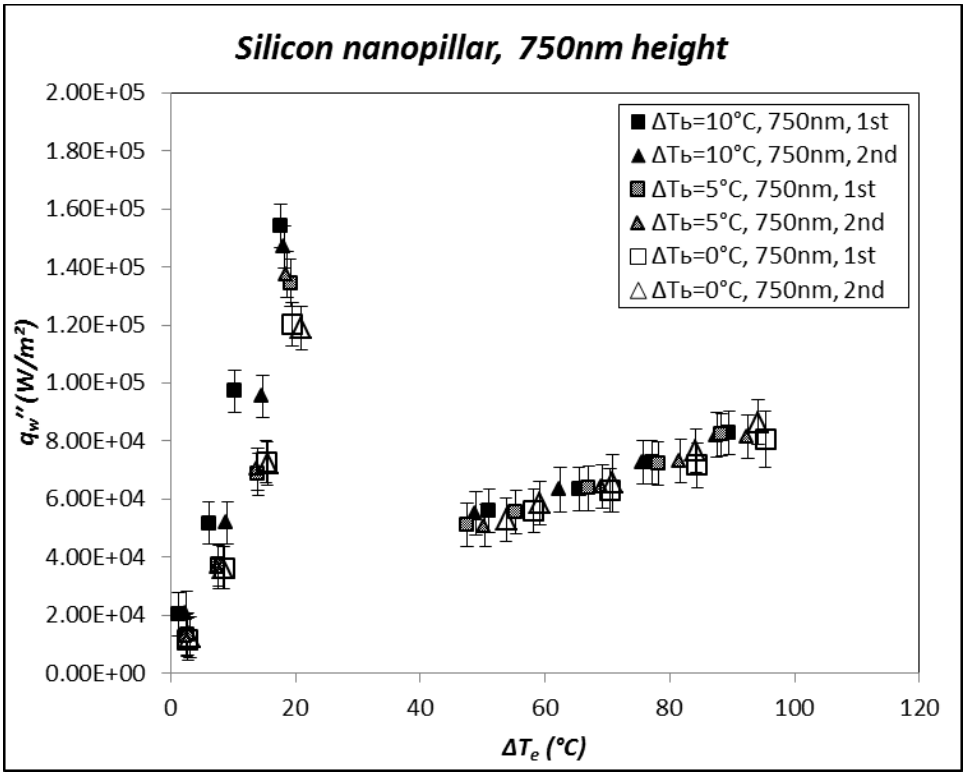

Figure D 6 Pool boiling curve on rectangular silicon surface with nanofin height 750nm: square for 1st run, triangle is 2nd run: solid dot is for subcool 10°C, patterned dot is for subcool 5°C, hollow dot is for saturation. TFT is used.

Table D 1 Summary of heat flux values (CHF and MHF) on the heater surface (q_w") with silicon nanofins at liquid subcooling values of 10 ^oC, 5 ^oC and 0 ^oC (saturated pool boiling experiments) with uncertainty values

Subcooling 10°C	Critical heat flux				Minimum heat flux			
Height of nanopillar	Wall superheat, °C	Uncertainty	Heat flux, W/m²	Uncertainty	Wall superheat, °C	Uncertainty	Heat flux, W/m²	Uncertainty
0	26.8	1.3E-01	1.42E+05	7.4E+03	89.3	2.2E-01	7.49E+04	7.4E+03
10.1	25.2	1.8E-01	1.46E+05	7.3E+03	69.7	2.1E-01	6.44E+04	7.4E+03
46.1	23.0	1.9E-01	1.43E+05	7.3E+03	63.9	1.1E-01	5.86E+04	7.4E+03
105.6	22.4	2.2E-01	1.57E+05	7.3E+03	69.4	1.2E+00	6.21E+04	7.5E+03
351	19.7	3.2E-01	1.58E+05	7.1E+03	68.6	2.3E-01	6.03E+04	7.5E+03
464	19.3	1.2E-01	1.44E+05	7.3E+03	62.4	4.8E-01	5.59E+04	7.5E+03
750	17.7	4.4E-01	1.54E+05	7.5E+03	51.0	8.3E-01	5.60E+04	7.4E+03
Subcooling 5°C	Critical heat flux				Minimum heat flux			
Height of nanopillar	Wall superheat, °C	Uncertainty	Heat flux, W/m²	Uncertainty	Wall superheat, °C	Uncertainty	Heat flux, W/m²	Uncertainty
0	26.8	1.3E-01	1.32E+05	7.5E+03	88.4	2.0E-01	7.05E+04	7.5E+03
10.1	27.9	3.3E-01	1.43E+05	7.3E+03	81.9	2.7E-01	6.48E+04	7.4E+03
46.1	25.8	1.6E-01	1.32E+05	7.3E+03	64.1	9.8E-02	5.58E+04	7.4E+03
105.6	23.9	1.4E-01	1.40E+05	7.3E+03	72.8	2.7E-01	5.94E+04	7.4E+03
351	23.5	1.4E-01	1.53E+05	7.4E+03	65.3	1.2E-01	5.50E+04	7.6E+03
464	23.3	6.5E-01	1.37E+05	7.5E+03	62.0	4.5E-01	5.67E+04	7.9E+03
750	19.2	2.9E-01	1.35E+05	8.1E+03	47.5	4.8E-01	5.11E+04	7.4E+03
Saturated	Critical heat flux				Minimum heat flux			
Height of nanopillar	Wall superheat, °C	Uncertainty	Heat flux, W/m²	Uncertainty	Wall superheat, °C	Uncertainty	Heat flux, W/m²	Uncertainty
0	28.2	2.1E-01	1.25E+05	7.4E+03	87.5	2.3E-01	7.00E+04	7.6E+03
10.1	29.8	9.7E-01	1.32E+05	7.3E+03	79.9	3.7E-01	6.24E+04	7.4E+03
46.1	25.9	2.3E-01	1.20E+05	7.2E+03	63.8	9.8E-02	5.40E+04	7.5E+03
105.6	25.0	1.6E-01	1.26E+05	7.4E+03	67.1	2.7E-01	5.19E+04	7.4E+03
351	22.7	1.4E-01	1.47E+05	7.3E+03	63.4	1.3E-01	5.43E+04	7.5E+03
464	21.6	2.8E-01	1.26E+05	7.3E+03	59.8	5.7E-01	5.26E+04	7.3E+03
750	19.5	2.8E-01	1.20E+05	7.3E+03	58.2	5.0E-01	5.61E+04	7.4E+03

Table D 2 Summary of heat flux values (CHF and MHF) through the total surface area of the heater with the patterned nanofins (q_{nc}") for silicon heater at liquid subcooling values of 10 ^{o}C, 5 ^{o}C and 0 ^{o}C (saturated pool boiling experiments)

Subcooling 10°C	Critical heat flux		Minimum heat flux	
Height of nanopillar	Wall superheat, °C	Heat flux, W/m²	Wall superheat, °C	Heat flux, W/m²
0	26.8	1.42E+05	89.3	7.49E+04
10.1	25.2	1.58E+05	69.7	7.59E+04
46.1	23.0	1.79E+05	63.9	6.01E+04
105.6	22.4	2.39E+05	69.4	6.25E+04
351	19.7	2.19E+05	68.6	5.36E+04
464	19.3	2.79E+05	62.4	4.71E+04
750	17.7	3.01E+05	51.0	5.86E+04
Subcooling 5°C	Critical heat flux		Minimum heat flux	
Height of nanopillar	Wall superheat, °C	Heat flux, W/m²	Wall superheat, °C	Heat flux, W/m²
0	26.8	1.32E+05	88.4	7.05E+04
10.1	27.9	1.61E+05	81.9	6.17E+04
46.1	25.8	1.59E+05	64.1	5.43E+04
105.6	23.9	2.21E+05	72.8	5.35E+04
351	23.5	2.02E+05	65.3	4.61E+04
464	23.3	2.38E+05	62.0	4.94E+04
750	19.2	2.64E+05	47.5	4.70E+04
Saturated	Critical heat flux		Minimum heat flux	
Height of nanopillar	Wall superheat, °C	Heat flux, W/m²	Wall superheat, °C	Heat flux, W/m²
0	28.2	1.25E+05	87.5	7.00E+04
10.1	29.8	1.32E+05	79.9	5.69E+04
46.1	25.9	1.46E+05	63.8	4.97E+04
105.6	25.0	1.85E+05	67.1	3.86E+04
351	22.7	2.07E+05	63.4	4.50E+04
464	21.6	2.55E+05	59.8	3.76E+04
750	19.5	2.38E+05	58.2	4.89E+04

Table D 3 Summary of A_n and A_{nc} on heater with nanofins of silicon, silica, and nickel.

Pillar Material	Height, nm	An, m²	Anc, m²
Silicon	10	7.04E-04	7.08E-04
	46	8.96E-04	9.18E-04
	106	7.04E-04	7.49E-04
	354	8.96E-04	1.03E-03
	464	5.12E-04	6.35E-04
	750	5.76E-04	7.17E-04
Silica	108	9.60E-04	1.03E-03
	210	9.60E-04	1.09E-03
Nikel	93	5.12E-04	5.41E-04

APPENDIX E

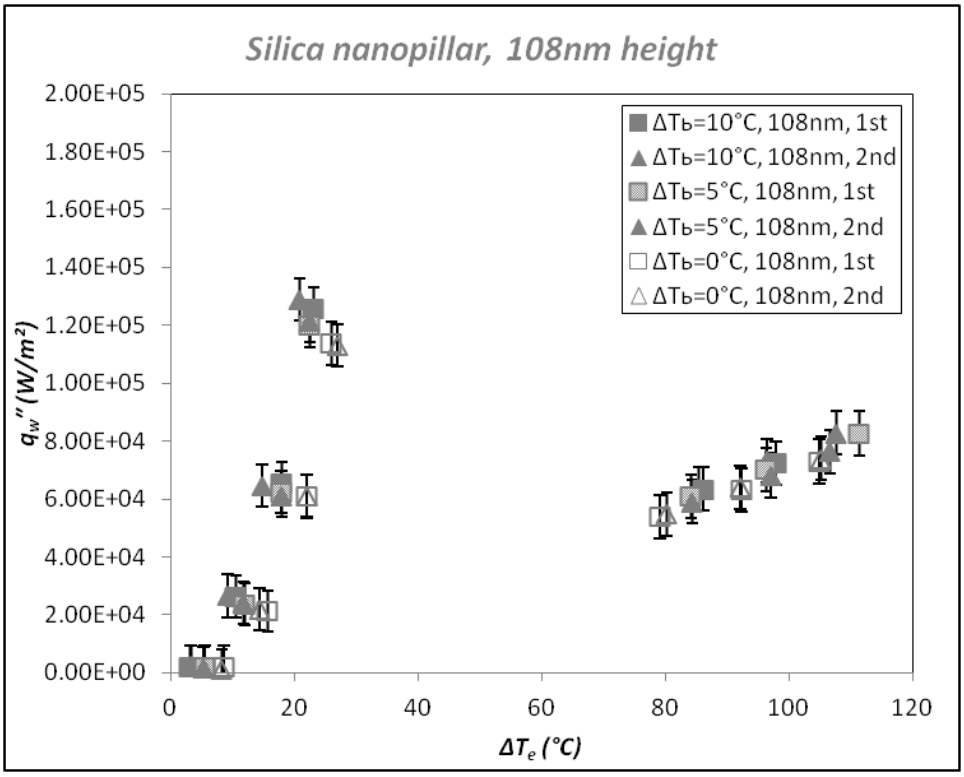

Figure E 1 Pool boiling curve on rectangular silica surface with nanofin height 108.3nm: square for 1st run, triangle is 2nd run: solid dot is for subcool 10°C, patterned dot is for subcool 5°C, hollow dot is for saturation. TFT is used.

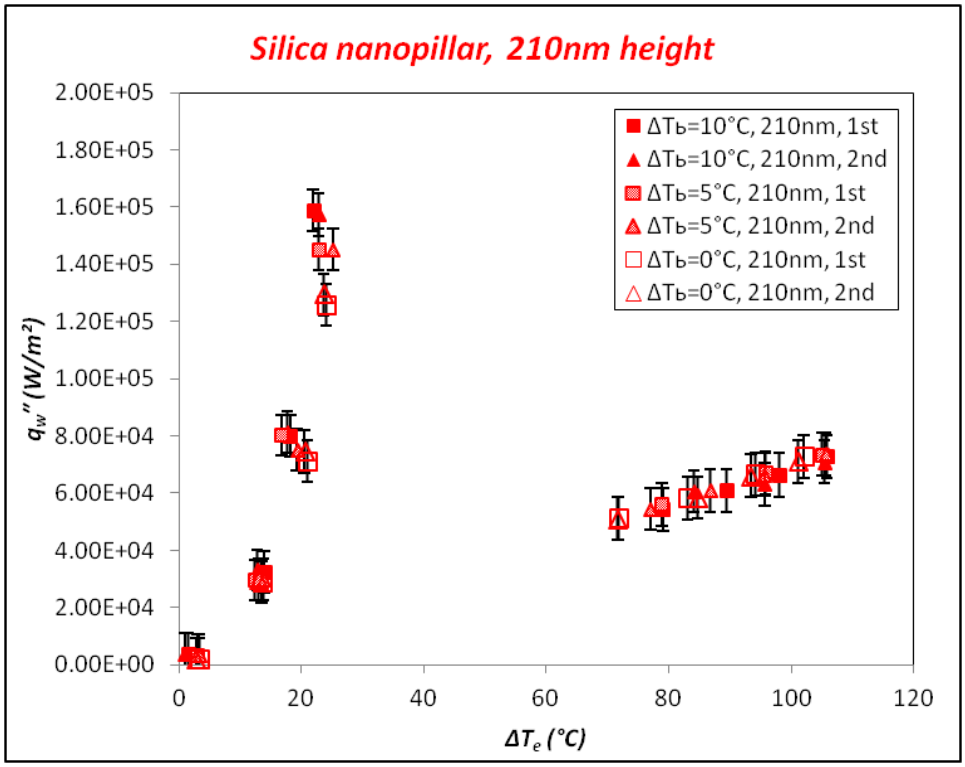

Figure E 2 Pool boiling curve on rectangular silica surface with nanofin height 210.4nm: square for 1st run, triangle is 2nd run: solid dot is for subcool 10°C, patterned dot is for subcool 5°C, hollow dot is for saturation. TFT is used.

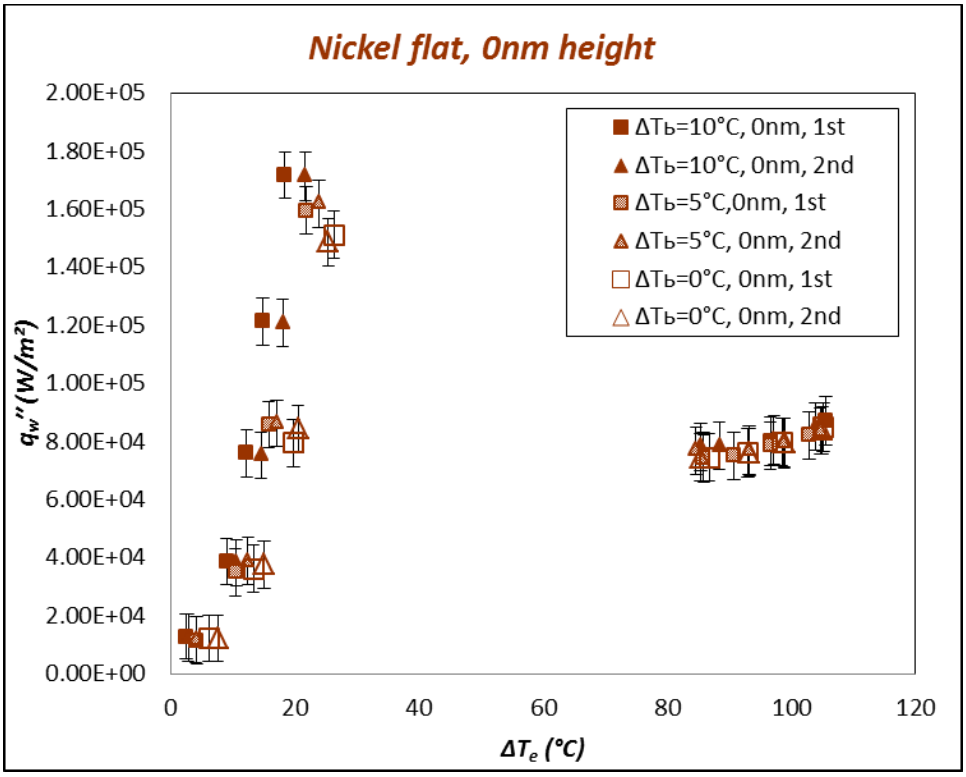

Figure E 3 Pool boiling curve on rectangular flat nickel surface: square for 1st run, triangle is 2nd run: solid dot is for subcool 10°C, patterned dot is for subcool 5°C, hollow dot is for saturation. TFT is used.

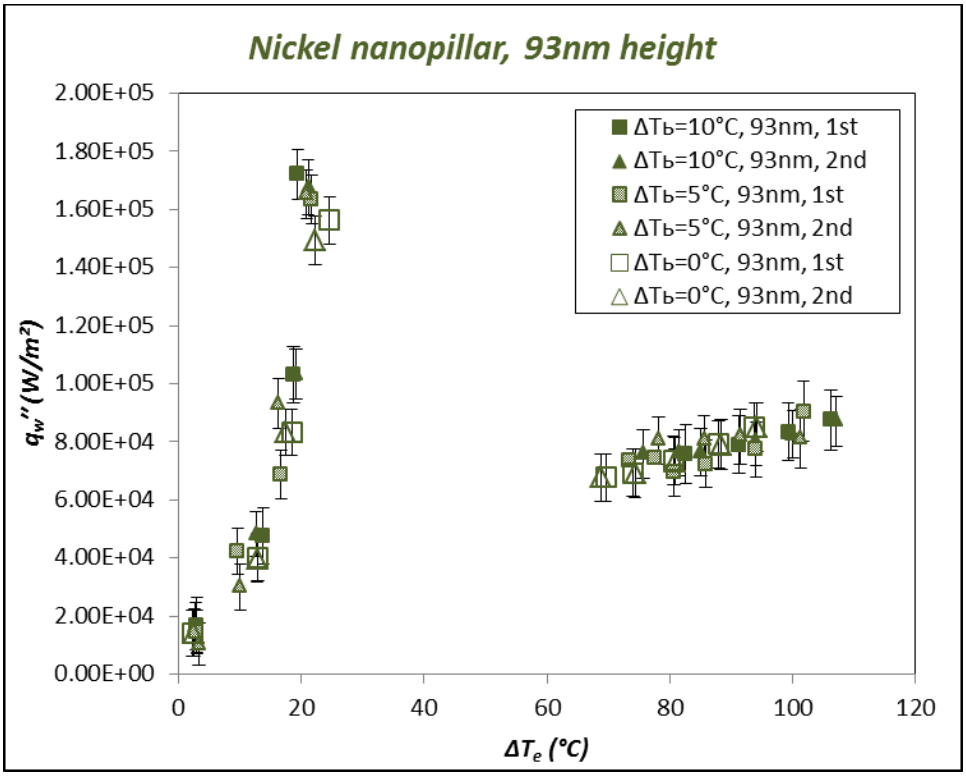

Figure E 4 Pool boiling curve on rectangular nickel surface with nanofin height 93nm: square for 1st run, triangle is 2nd run: solid dot is for subcool 10oC, patterned dot is for subcool 5oC, hollow dot is for saturation. TFT is used.

Table E 1 Summary of heat flux values (CHF and MHF) on the heater surface (q_w") with silica nanofins at liquid subcooling values of 10 ^oC, 5 ^oC and 0 ^oC (saturated pool boiling experiments) with uncertainty values

Subcooling 10°C	Critical heat flux				Minimum heat flux			
Height of nanopillar	Wall superheat, °C	Uncertainty	Heat flux, W/m²	Uncertainty	Wall superheat, °C	Uncertainty	Heat flux, W/m²	Uncertainty
0	26.8	1.1E-01	1.30E+05	7.3E+03	91.7	4.4E-01	8.13E+04	7.6E+03
108.3	23.1	6.6E-01	1.26E+05	7.5E+03	86.1	2.3E-01	6.34E+04	7.4E+03
210.4	21.9	1.1E-01	1.59E+05	7.3E+03	79.1	1.3E-01	5.44E+04	7.5E+03
Subcooling 5°C	Critical heat flux				Minimum heat flux			
Height of nanopillar	Wall superheat, °C	Uncertainty	Heat flux, W/m²	Uncertainty	Wall superheat, °C	Uncertainty	Heat flux, W/m²	Uncertainty
0	26.0	1.4E-01	1.25E+05	8.9E+03	88.4	4.0E-01	7.53E+04	7.5E+03
108.3	22.5	2.3E-01	1.20E+05	7.4E+03	84.2	1.7E-01	6.10E+04	7.6E+03
210.4	22.8	1.3E-01	1.45E+05	7.2E+03	78.9	2.0E-01	5.61E+04	7.4E+03
Saturated	Critical heat flux				Minimum heat flux			
Height of nanopillar	Wall superheat, °C	Uncertainty	Heat flux, W/m²	Uncertainty	Wall superheat, °C	Uncertainty	Heat flux, W/m²	Uncertainty
0	27.1	1.5E-01	1.19E+05	7.4E+03	87.5	4.3E-01	7.16E+04	7.7E+03
108.3	26.0	2.3E-01	1.14E+05	7.3E+03	79.1	1.3E-01	5.38E+04	7.4E+03
210.4	24.1	2.2E-01	1.26E+05	7.4E+03	71.8	2.4E-01	5.12E+04	7.3E+03

Table E 2 Summary of heat flux values (CHF and MHF) on the heater surface (q_w") with nickel nanofins at liquid subcooling values of 10 ^oC, 5 ^oC and 0 ^oC (saturated pool boiling experiments) with uncertainty values

Subcooling 10°C	Critical heat flux				Minimum heat flux			
Height of nanopillar	Wall superheat, °C	Uncertainty	Heat flux, W/m²	Uncertainty	Wall superheat, °C	Uncertainty	Heat flux, W/m²	Uncertainty
0	21.7	1.2E-01	1.71E+05	8.2E+03	85.4	5.9E-01	7.83E+04	8.2E+03
93	19.4	1.1E-01	1.72E+05	8.6E+03	82.6	3.4E-01	7.57E+04	1.0E+04
Subcooling 5°C	Critical heat flux				Minimum heat flux			
Height of nanopillar	Wall superheat, °C	Uncertainty	Heat flux, W/m²	Uncertainty	Wall superheat, °C	Uncertainty	Heat flux, W/m²	Uncertainty
0	23.9	1.8E-01	1.62E+05	8.1E+03	84.6	3.8E-01	7.70E+04	8.2E+03
93	21.7	1.4E-01	1.64E+05	8.9E+03	73.4	2.3E-01	7.37E+04	8.7E+03
Saturated	Critical heat flux				Minimum heat flux			
Height of nanopillar	Wall superheat, °C	Uncertainty	Heat flux, W/m²	Uncertainty	Wall superheat, °C	Uncertainty	Heat flux, W/m²	Uncertainty
0	25.4	3.8E-01	1.49E+05	8.2E+03	85.4	6.2E-01	7.46E+04	8.1E+03
93	24.6	1.6E-01	1.56E+05	8.2E+03	69.6	2.1E-01	6.78E+04	8.1E+03

Table E 3 Summary of heat flux values (CHF and MHF) through the total surface area of the heater with the patterned nanofins (q_{nc}") for silica heater at liquid subcooling values of 10 ^{o}C, 5 ^{o}C and 0 ^{o}C (saturated pool boiling experiments)

Subcooling 10°C	Critical heat flux		Minimum heat flux	
Height of nanopillar	Wall superheat, °C	Heat flux, W/m²	Wall superheat, °C	Heat flux, W/m²
0	26.8	1.30E+05	91.7	8.13E+04
108.3	23.1	1.40E+05	86.1	4.51E+04
210.4	21.9	2.00E+05	79.1	2.91E+04
Subcooling 5°C	Critical heat flux		Minimum heat flux	
Height of nanopillar	Wall superheat, °C	Heat flux, W/m²	Wall superheat, °C	Heat flux, W/m²
0	26.0	1.25E+05	88.4	7.53E+04
108.3	22.5	1.42E+05	84.2	4.61E+04
210.4	22.8	1.75E+05	78.9	3.80E+04
Saturated	Critical heat flux		Minimum heat flux	
Height of nanopillar	Wall superheat, °C	Heat flux, W/m²	Wall superheat, °C	Heat flux, W/m²
0	27.1	1.19E+05	87.5	7.16E+04
108.3	26.0	1.10E+05	79.1	3.93E+04
210.4	24.1	1.48E+05	71.8	3.69E+04

Table E 4 Summary of heat flux values (CHF and MHF) through the total surface area of the heater with the patterned nanofins (q_{nc}") for nickel heater at liquid subcooling values of 10 ^{o}C, 5 ^{o}C and 0 ^{o}C (saturated pool boiling experiments)

Subcooling 10°C	Critical heat flux		Minimum heat flux	
Height of nanopillar	Wall superheat, °C	Heat flux, W/m²	Wall superheat, °C	Heat flux, W/m²
0	21.7	1.71E+05	85.4	7.83E+04
93	19.4	2.49E+05	82.6	6.88E+04
Subcooling 5°C	Critical heat flux		Minimum heat flux	
Height of nanopillar	Wall superheat, °C	Heat flux, W/m²	Wall superheat, °C	Heat flux, W/m²
0	23.9	1.62E+05	84.6	7.70E+04
93	21.7	2.25E+05	73.4	8.24E+04
Saturated	Critical heat flux		Minimum heat flux	
Height of nanopillar	Wall superheat, °C	Heat flux, W/m²	Wall superheat, °C	Heat flux, W/m²
0	25.4	1.49E+05	85.4	7.46E+04
93	24.6	1.87E+05	69.6	6.59E+04

APPENDIX F

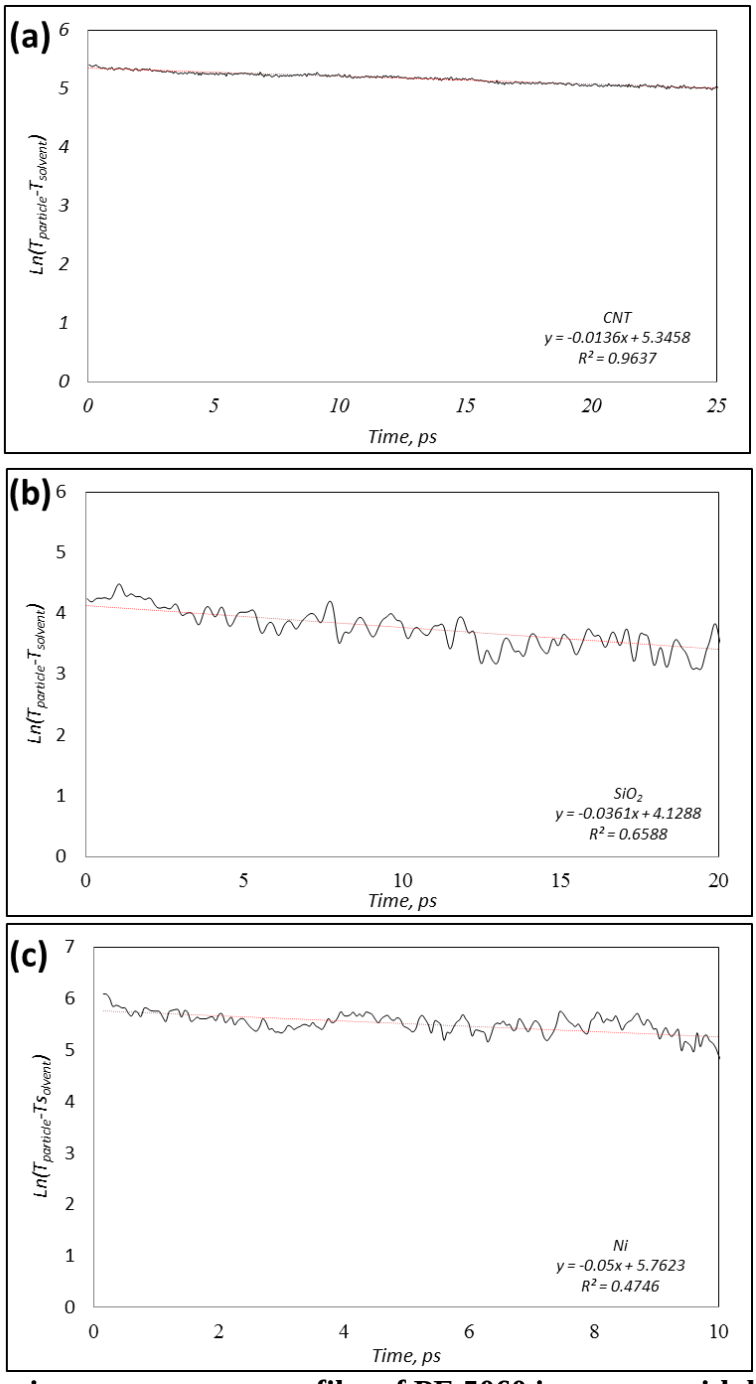

Figure F 1 Transient temperature profiles of PF-5060 in contact with heated nanofin; (a) CNT (b) Silica and (c) Nickel

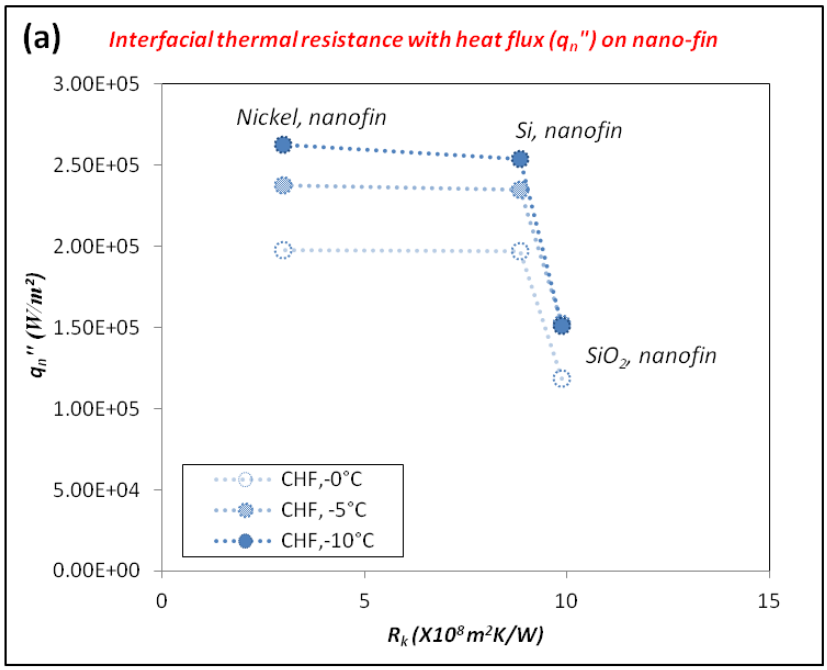

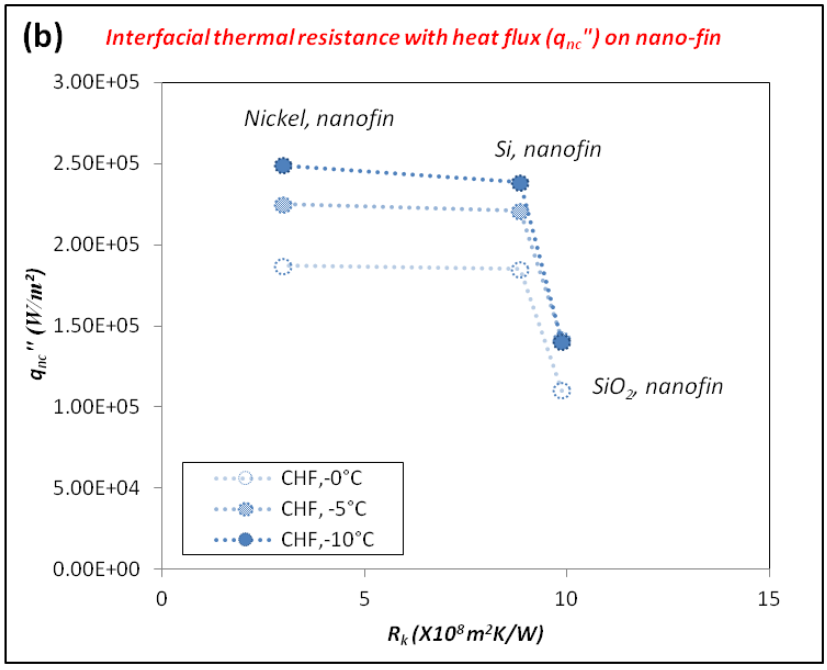

Figure F 2 Plot of critical heat flux (CHF) as a function of interfacial thermal resistance (R_k) between PF-5060 and heaters with nanofin surface; for (a) q_n", and (b) q_{nc}".

Table F 1 The ratio of thermal capacitance per unit area between nanofin and compressed phase (C'_i/C'_f): D_o corresponds to the outer extent of the first density peak, and D_{peak} means the distance for the first density peak of the fluid phase. ρ_{peak} is the magnitude of the first density peak and $\rho_{average}$ is the average density of the bulk phase of the fluid (at a large distance away from the surface of the solid phase)

SiO_2 nanofin	C'_i/C'_f	
	ρ_{peak} (2.37 g/cm³)	$\rho_{average}$ (1.91 g/cm³)
D_i (6.5Å)	1.64	1.32
D_{peak} (7.0Å)	1.52	1.22
D_o (9.5Å)	1.12	0.9
D_i+D_o	0.67	0.54

Si nanofin	C'_i/C'_f	
	ρ_{peak} (2.38 g/cm³)	$\rho_{average}$ (2.06 g/cm³)
D_i (5.5Å)	1.68	1.45
D_{peak} (6.5Å)	1.42	0.99
D_o (8.5Å)	1.09	0.94
D_i+D_o	0.66	0.57

Ni nanofin	C'_i/C'_f	
	ρ_{peak} (2.33 g/cm³)	$\rho_{average}$ (2.06 g/cm³)
D_i (5.5Å)	0.56	0.49
D_{peak} (6.5Å)	0.48	0.42
D_o (8.5Å)	0.39	0.34
D_i+D_o	0.23	0.2

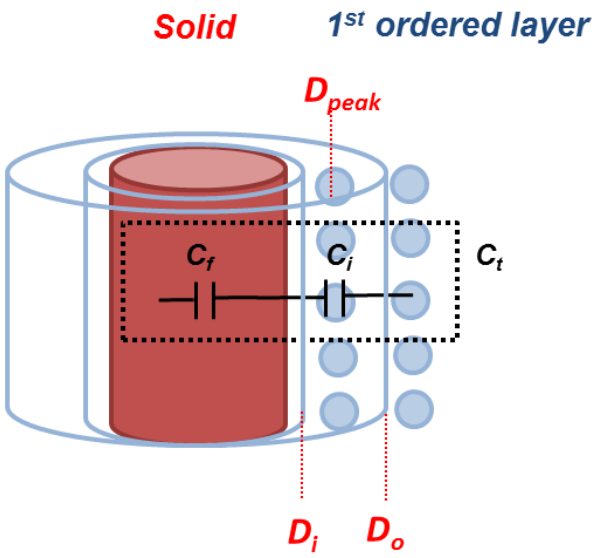

Figure F 3 Schematic for calculation of capacitance values of the solid phase (nanoparticle or nanofin) and compressed phase. KEY: D_i represents the starting location of the fluid phase molecules, D_o corresponds to the outer extent of the first density peak, and D_{peak} means the distance for the first density peak of the fluid phase.

Table F 2 **Parameters for diode effect calculation at 1st peak and 1st valley value.**

Material	*K, W/mK*	*$\bar{h}$, J/kg*	*ρ_p, density of peak, g/cm³*	*ρ_v, density of valley, g/cm³*	*Distance between 1st peak to 1st valley, Å*
SiO_2	*0.057*	*88000*	2.371	*1.303*	*3.00*
Si	*0.057*	*88000*	2.383	*0.751*	*3.50*
Ni	*0.057*	*88000*	2.338	*0.969*	*3.50*

** $\bar{h}$: latent heat of vapoization of PF-5060*

** K: thermal conductivity of PF-5060*

Table F 3 Detail calculation at 1st peak and 1st valley

Material	$\bar{\rho}$, average density of peak and valley kg/m³	LC.T, Å	LC.C, Å	Cs, Cpeak/(Cpeak+Cvalley)	C∞, Cvalley/(Cpeak+Cvalley)	(Cs-C∞)	Ts	T∞	(Ts-T∞)	Co(1-Co)
SiO_2	3.67E+03	1.695	1.695	6.45E-01	3.55E-01	2.91E-01	800	300	500	2.29E-01
Si	3.13E+03	1.695	1.695	7.60E-01	2.40E-01	5.21E-01	800	300	500	1.82E-01
Ni	3.31E+03	1.695	1.695	7.07E-01	2.93E-01	4.14E-01	800	300	500	2.07E-01

* $L_{C.T}$=$L_{C.C}$, 1.695 Å, V/As

Material	$\bar{\rho}\hbar D/K$	(Cs-C∞)/(Ts-T∞)	LC.T/LC.C	$\rho\hbar D/K$*(Cs-C∞)/(Ts-T∞)*LC.T/LC.C	$\bar{V}C$*	$\bar{\rho}\hbar DT/K$	$\bar{\rho}\hbar D_{T}/K$*Co(1-Co)+1	$\bar{V}\vartheta$
SiO_2	5.57E+00	0.001	1.000	3.24E-03	1	9.89E-01	1.23E+00	1
Si	7.89E+00	0.001	1.000	8.22E-03	1	1.62E+00	1.29E+00	1
Ni	6.76E+00	0.001	1.000	5.60E-03	1	1.26E+00	1.26E+00	1

APPENDIX G

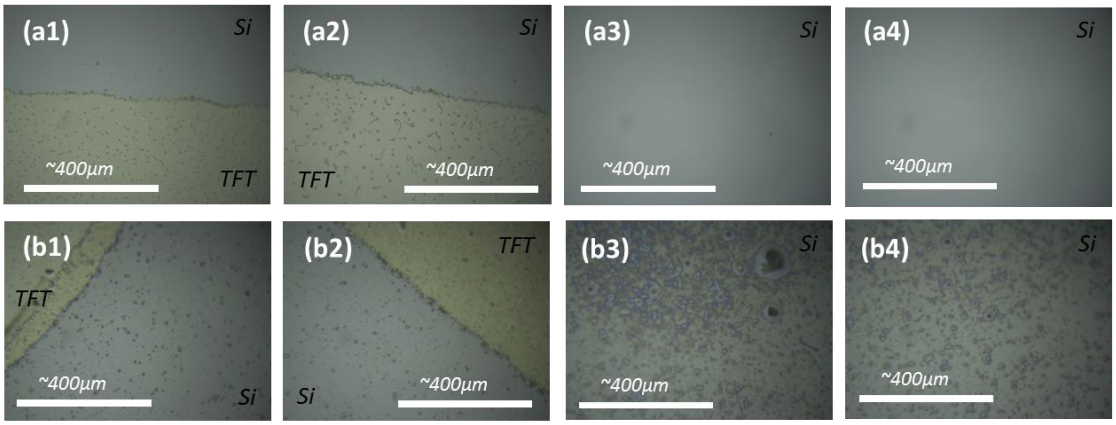

Figure G 1 Images obtained by performing optical microscopy of silicon heaters with patterned nanofins of height 46nm: (a) before boiling experiments, and (b) after boiling experiments.

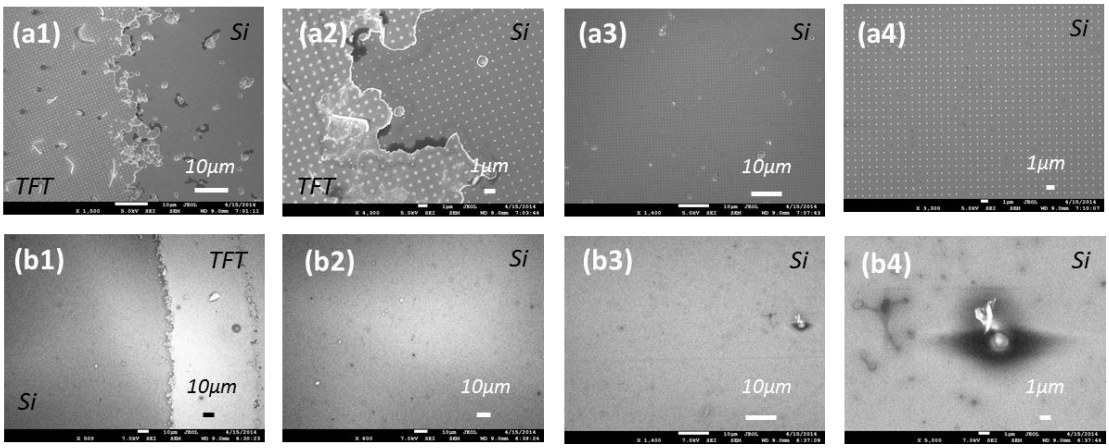

Figure G 2 Images obtained by performing electron microscopy (SEM) of silicon heaters with patterned nanofins of height 46nm: (a) before boiling experiments, and (b) after boiling experiments.

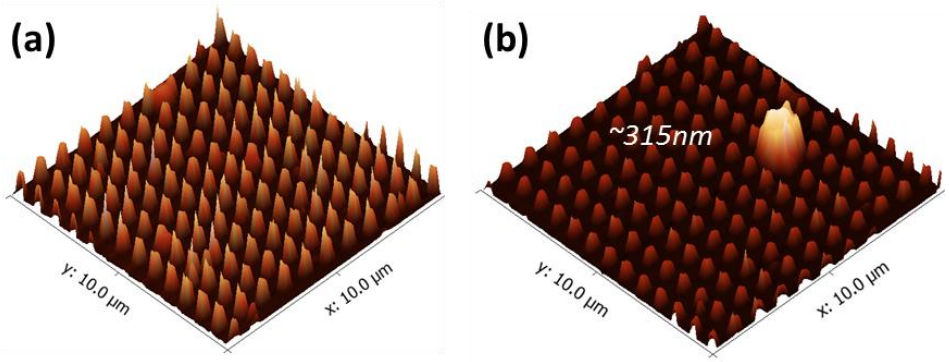

Figure G 3 Images obtained by performing Atomic Force Microscopy (AFM) microscopy of silicon heaters with patterned nanofins of height 46nm: (a) before boiling experiments, and (b) after boiling experiments.

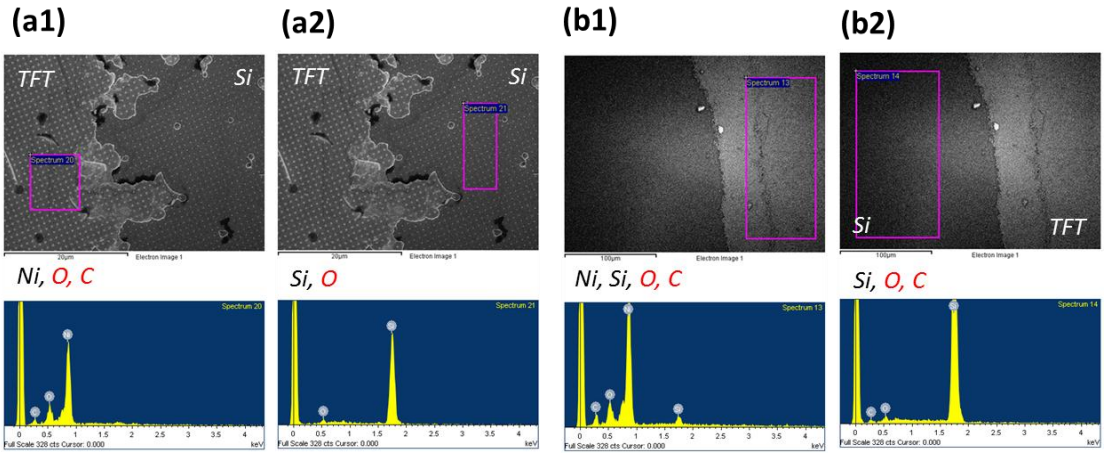

Figure G 4 Images obtained by performing electron microscopy (SEM) along with surface characterization by EDX (Energy Dispersive X-Ray Spectroscopy) of silicon heaters with patterned nanofins of height 46nm for: (a) before boiling experiments, and (b) after boiling experiments.

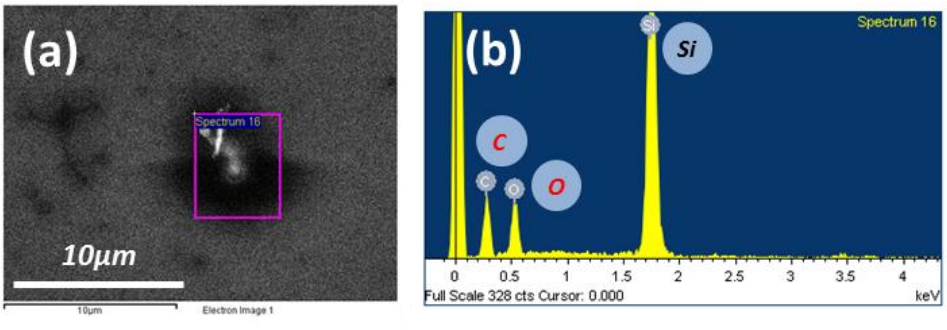

Figure G 5 EDX analysis of residue formed on silicon heater surface (with patterned nanofin of height 46nm) after boiling experiments.

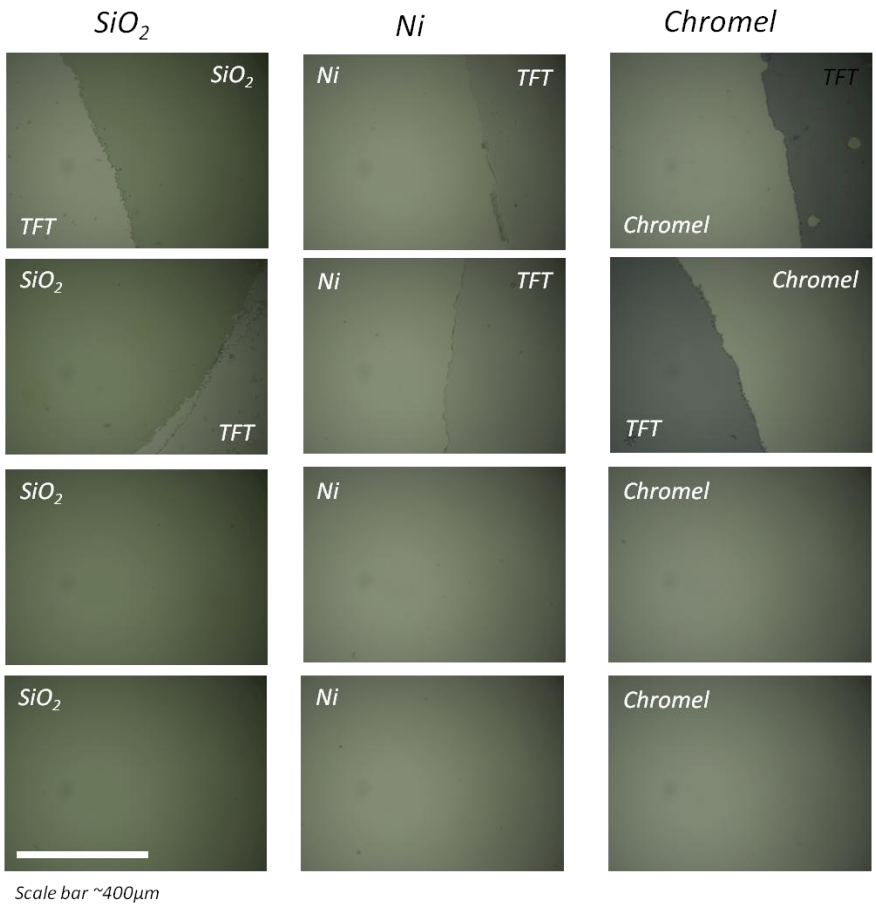

Figure G 6 Optical microscopy images of Silica/Nickel/Chromel heater surfaces (without patterned nanofin surfaces) before boiling experiments.

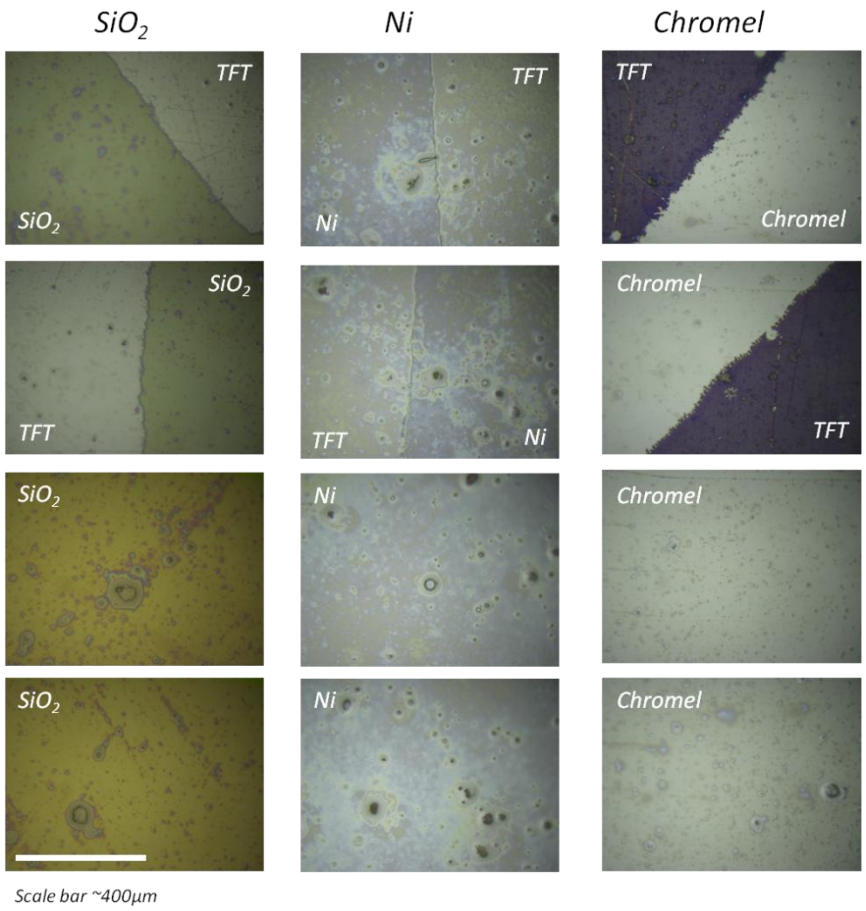

Figure G 7 Optical microscopy images of Silica/Nickel/Chromel heater surfaces (without patterned nanofin surfaces) after boiling experiments.

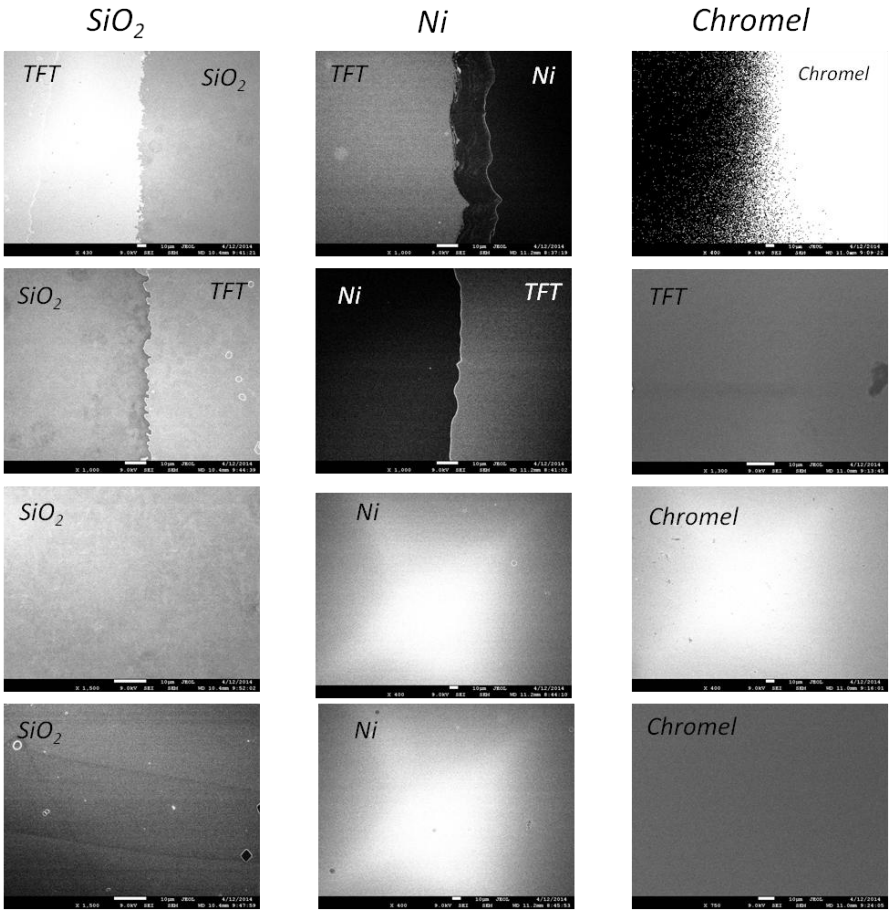

Figure G 8 SEM (Scanning Electron Microscopy) images of the Silica/Nickel/Chromel heater surfaces (without patterned nanofin surfaces) before boiling experiments.

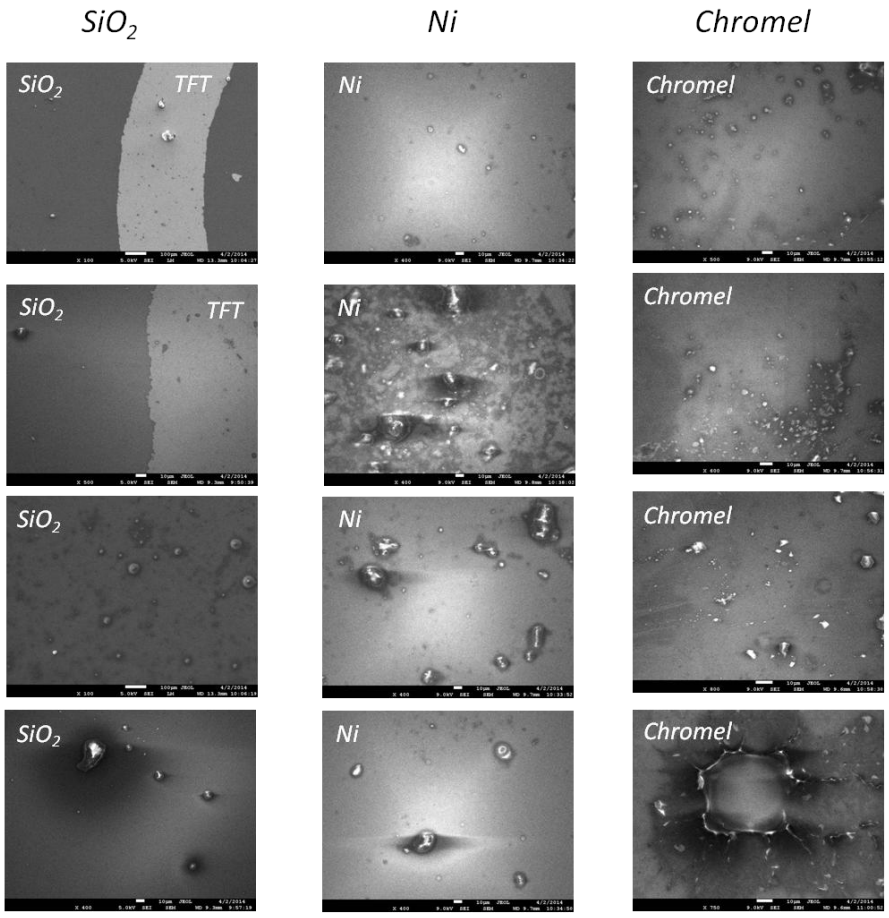

Figure G 9 SEM (Scanning Electron Microscopy) images of Silica/Nickel/Chromel heater surfaces (without patterned nanofin surfaces) after boiling experiments.

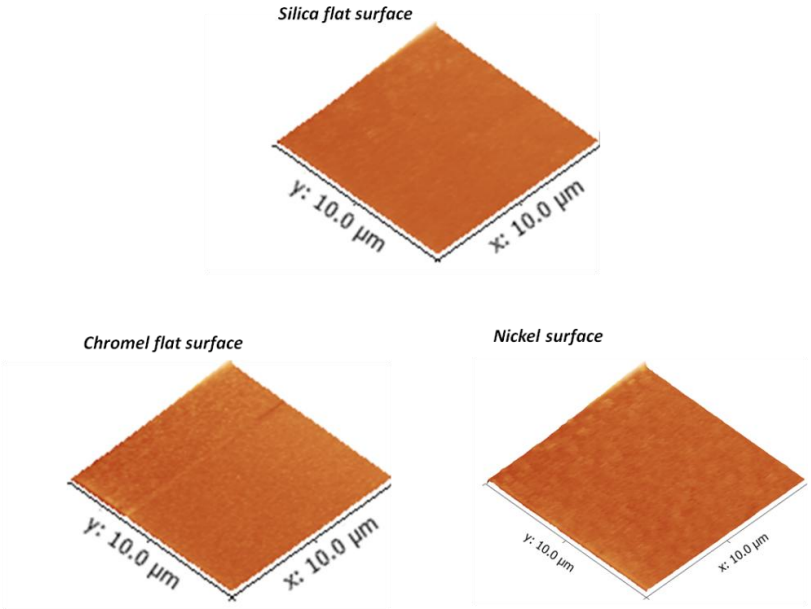

Figure G 10 Images obtained from AFM (Atomic Force Microscopy) of Silica/Nickel/Chromel heater surfaces (without patterned nanofin surfaces) before boiling experiment.

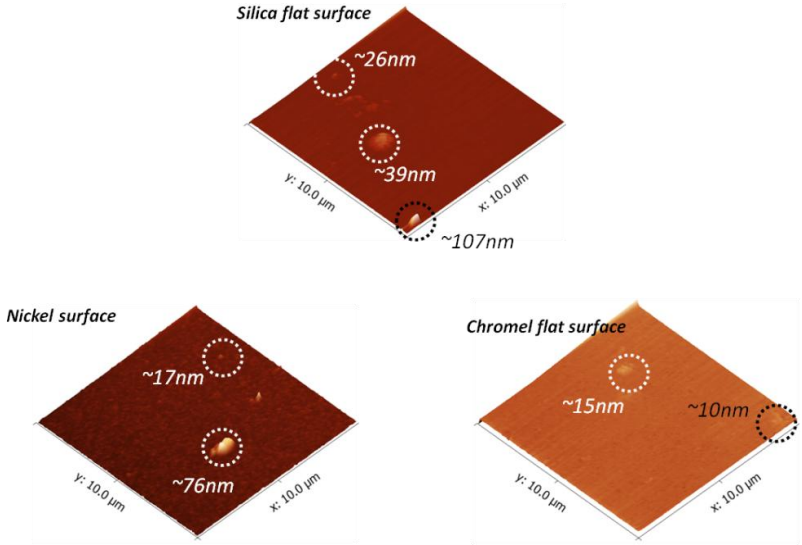

Figure G 11 Images obtained from AFM (Atomic Force Microscopy) of Silica/Nickel/Chromel heater surfaces (without patterned nanofin surfaces) after boiling experiment.

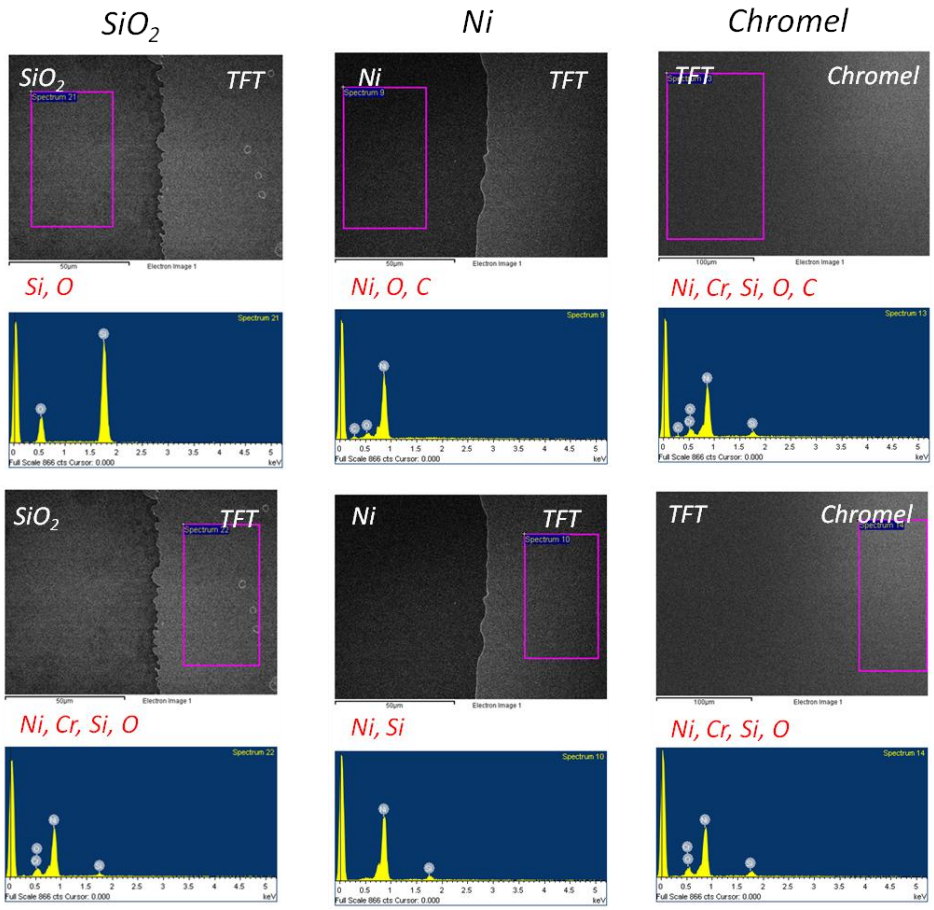

Figure G 12 EDX (Energy Dispersive X-ray spectroscopy) analysis Silica/Nickel/Chromel heater surfaces (without patterned nanofin surfaces) before boiling experiment.

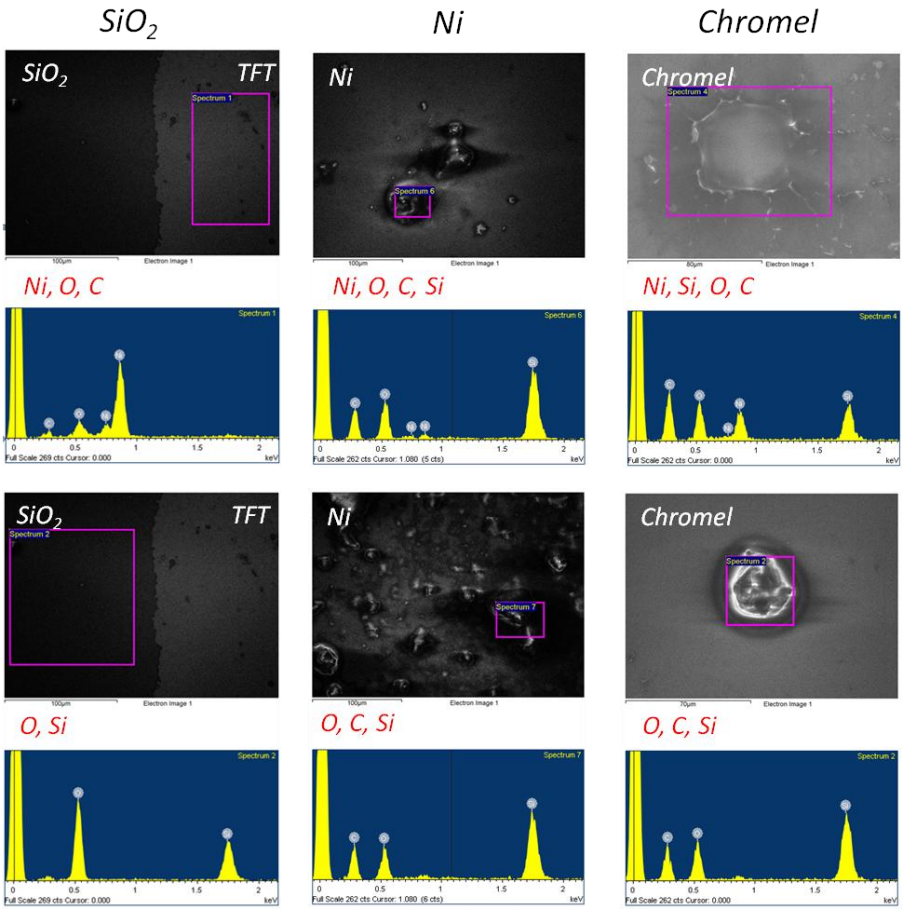

Figure G 13 EDX (Energy Dispersive X-ray spectroscopy) analysis Silica/Nickel/Chromel heater surfaces (without patterned nanofin surfaces) after boiling experiment.

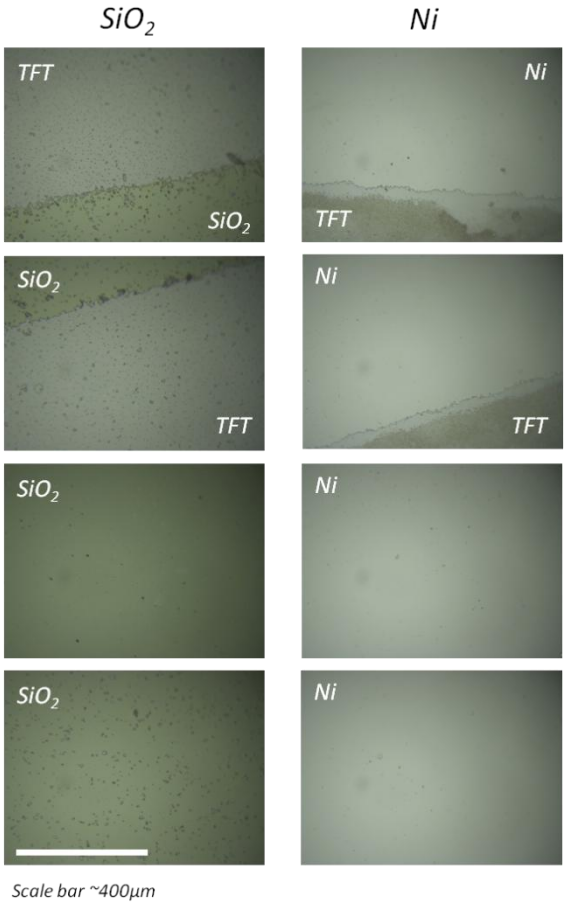

Figure G 14 Images obtained by performing optical microscopy of Silica/Nickel heaters with patterned nanofins of height ~100nm before boiling experiments.

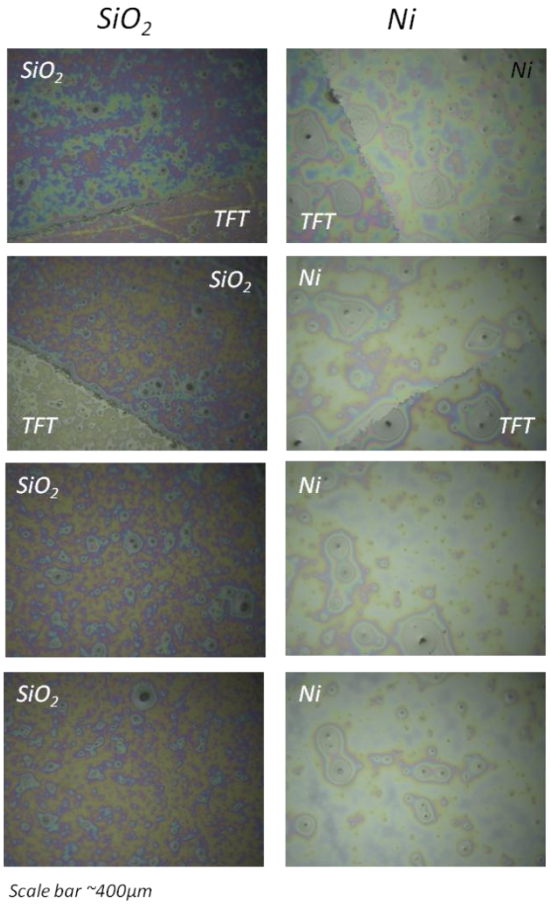

Figure G 15 Images obtained by performing optical microscopy of Silica/Nickel heaters with patterned nanofins of height ~100nm after boiling experiments.

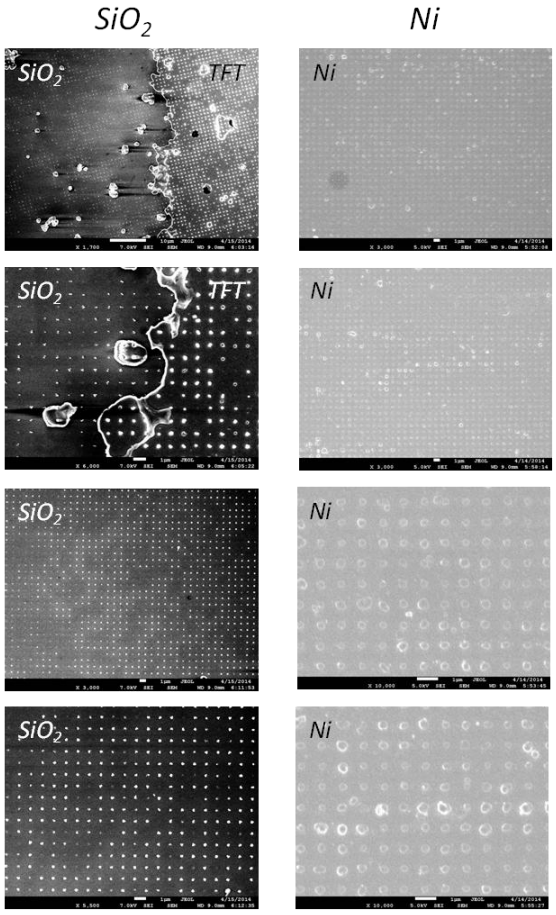

Figure G 16 Images obtained by performing electron microscopy (SEM) of Silica/Nickel heaters with patterned nanofins of height ~100nm before boiling experiments.

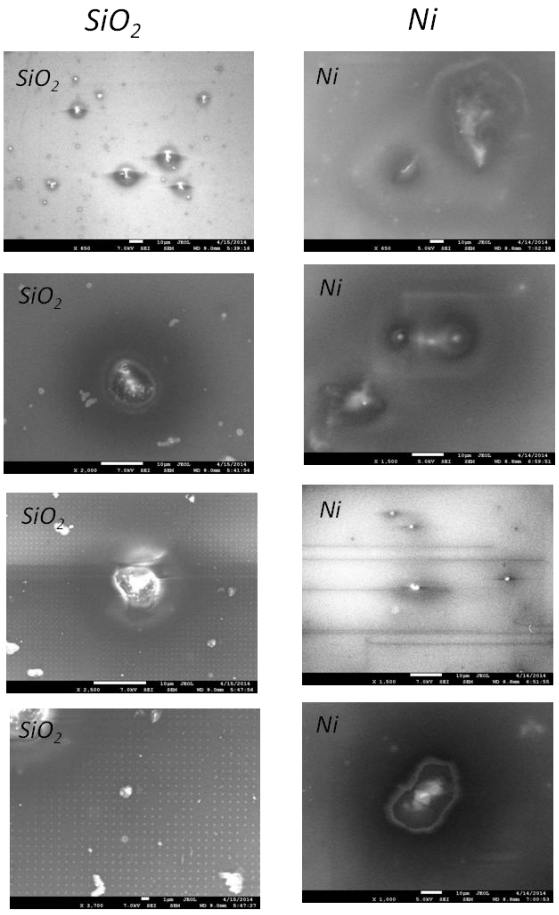

Figure G 17 Images obtained by performing electron microscopy (SEM) of Silica/Nickel heaters with patterned nanofins of height ~100nm after boiling experiments.

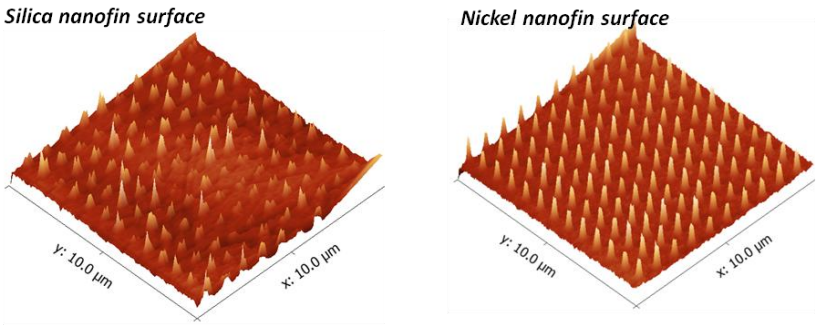

Figure G 18 Images obtained by performing Atomic Force Microscopy (AFM) microscopy of Silica/Nickel heaters with patterned nanofins of height ~100nm before boiling experiments.

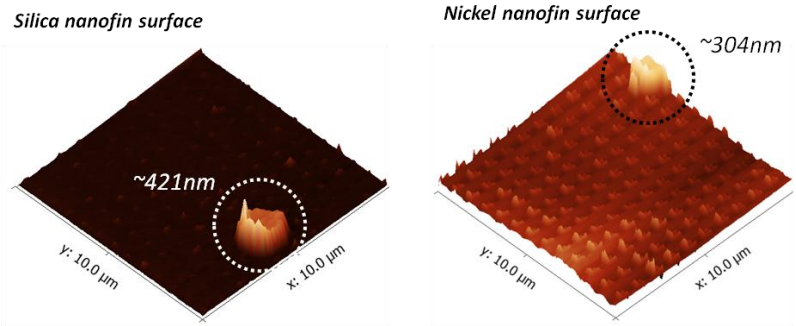

Figure G 19 Images obtained by performing Atomic Force Microscopy (AFM) microscopy of Silica/Nickel heaters with patterned nanofins of height ~100nm after boiling experiments.

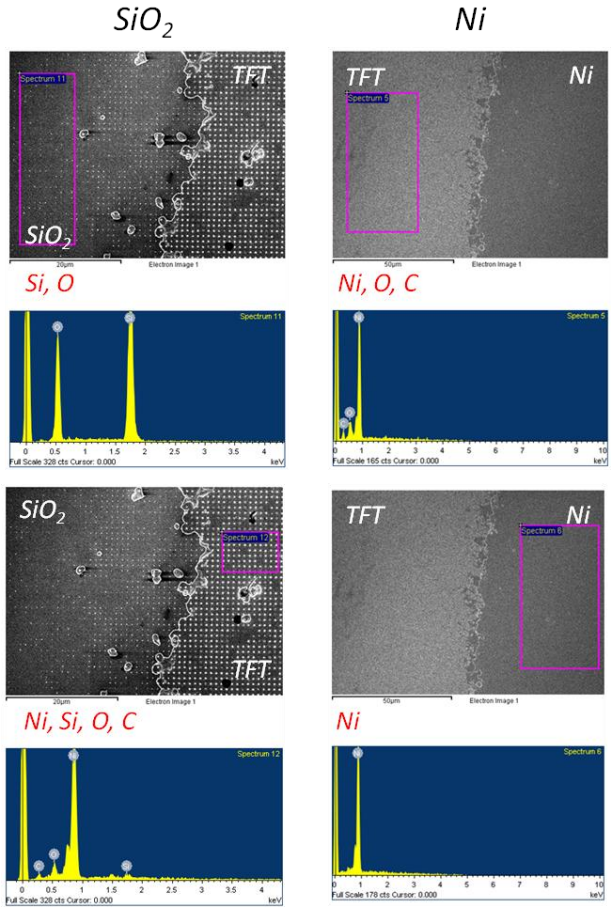

Figure G 20 Images obtained by performing electron microscopy (SEM) along with surface characterization by EDX (Energy Dispersive X-Ray Spectroscopy) of Silica/Nickel heaters with patterned nanofins of height ~100nm before boiling experiments.

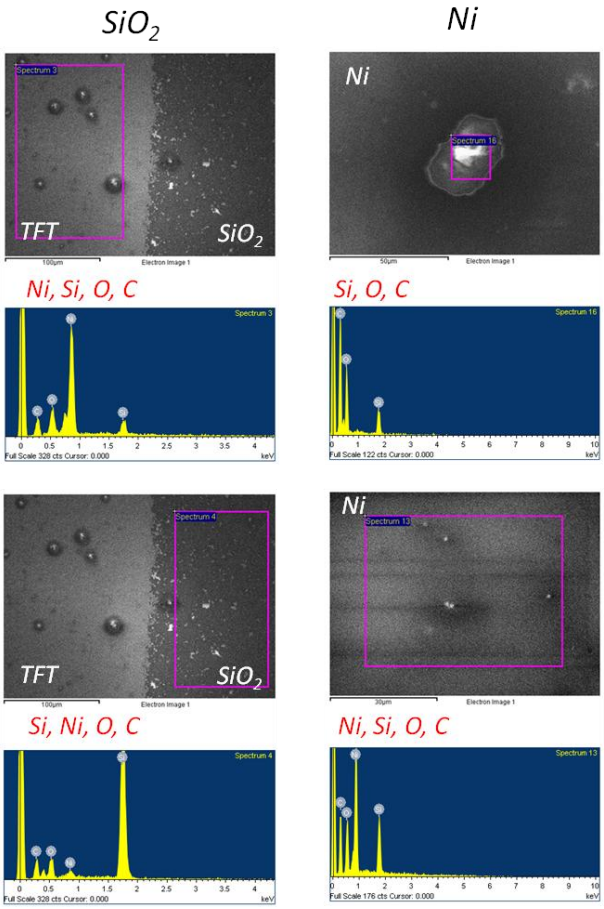

Figure G 21 Images obtained by performing electron microscopy (SEM) along with surface characterization by EDX (Energy Dispersive X-Ray Spectroscopy) of Silica/Nickel heaters with patterned nanofins of height ~100nm after boiling experiments.

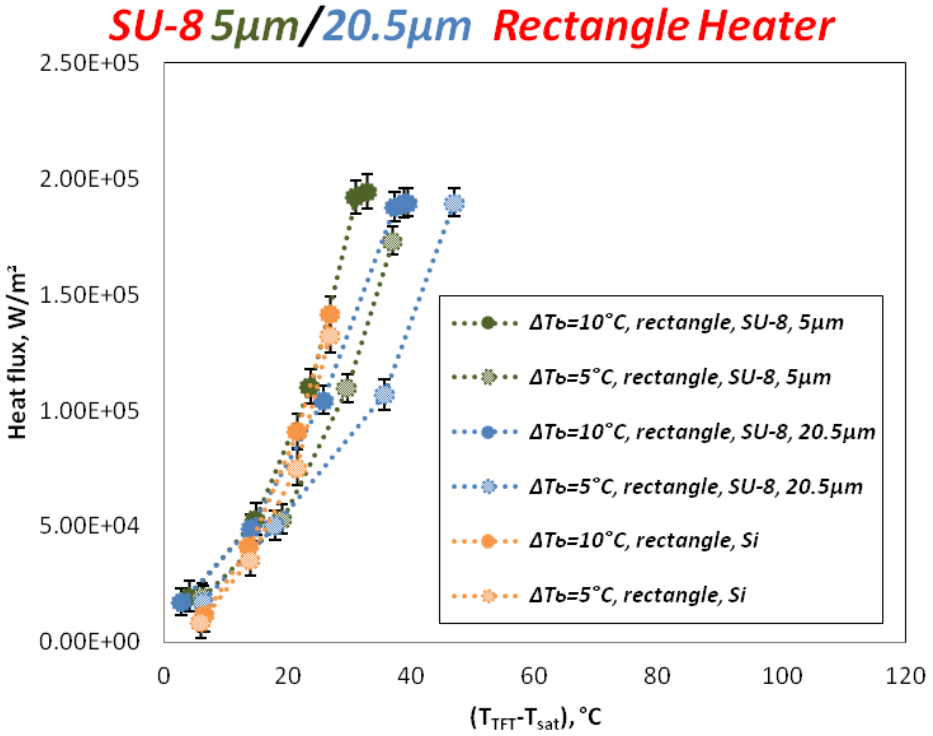

Figure G 22 Pool boiling curve of photoresist coated surface, heat flux is plotted with (T_{TFT}-T_{sat})

Table G 1Summary of heat flux values (CHF) on the heater surface (q_w") with SU-8 photoresist at liquid subcooling values of 10 ^oC and 5 ^oC with uncertainty values

Subcooling 10°C	Critical heat flux			
SU-8 thickness, µm	Wall superheat, °C	Uncertainty	Heat flux, W/m²	Uncertainty
0 µm (Bare Si)	26.8	1.3E-01	1.42E+05	7.4E+03
5 µm	29.5	1.2E-01	1.95E+05	7.6E+03
20.5 µm	25.8	3.1E-01	1.90E+05	6.2E+03
Subcooling 5°C	Critical heat flux			
SU-8 thickness, µm	Wall superheat, °C	Uncertainty	Heat flux, W/m²	Uncertainty
0 µm (Bare Si)	26.8	1.3E-01	1.32E+05	7.5E+03
5 µm	34.1	1.2E-01	1.73E+05	6.0E+03
20.5 µm	33.9	2.3E-01	1.90E+05	6.0E+03